IDENTIFYING THERAPEUTIC TARGETS AND STRATEGIES IN NEUROMYELITIS OPTICA SPECTRUM DISORDERS ASSOCIATED OPTIC NEURITIS THROUGH TEMPORAL WINDOW AND PATHOLOGICAL EVENTS

YANG XIAYIN

PhD

The Hong Kong Polytechnic University

2026

The Hong Kong Polytechnic University

The School of Optometry

Identifying Therapeutic Targets and Strategies in Neuromyelitis Optica Spectrum Disorders associated Optic Neuritis through Temporal Window and Pathological Events

Yang Xiayin

PhD

A thesis submitted in partial fulfilment of the requirements for the degree of Doctor of Philosophy

Aug 2025

A Certificate of Originality

I hereby declare that this thesis is entirely my own work and that, to the best of my knowledge and belief, it reproduces no material previously published or written, nor material that has been accepted for the award of any degree or diploma, except where due acknowledgement has been made in the text.

(signed)

15/6/2025

YANG XIAYIN (Name of student)

Abstract

Background: Neuromyelitis Optica Spectrum Disorder associated with Optic Neuritis (NMOSD-ON) is a devastating autoimmune disorder of the central nervous system that often leads to permanent vision loss. While the disease pathogenesis is known to originate from the binding of pathogenic aquaporin 4-antibodies (AQP4-IgG) to aquaporin 4 (AQP4) proteins on astrocyte endfeet, critical knowledge gaps remain in our understanding of this condition. Key unanswered questions include: (1) the optimal therapeutic window for intervention, (2) the development of safer treatment alternatives to current steroid-based therapies, which often cause significant side effects, and (3) the molecular mechanisms underlying potential therapeutic approaches.

Objectives: We first analyzed disease progression by examining the temporal window of phenotypic development in patients. Using this time window, we observed pathological progression in an animal model. Based on the key pathological deterioration within the time window, we explored potential treatment strategies. Finally, we investigated the underlying mechanisms driving disease progression and therapeutic effects.

Methods: Optical coherence tomography (OCT) was employed to monitor the peripapillary retinal nerve fiber layer (pRNFL) thickness in patients, comparing with Typical optic neuritis Idiopathic Optic Neuritis (IDON) within different time windows to identify the temporal phenotypic characteristics of NMOSD-ON. Immunofluorescence, Western blot, and functional assessments were utilized to analyze the pathology of the NMOSD-ON animal model and corresponding functional alterations in vivo. The therapeutic effects of Lycium barbarum glycopeptide (LBGP) administration on NMOSD-ON were evaluated, while proteomics was used to investigate the

underlying mechanisms. Functional validation of the candidate mediators was subsequently performed.

Results: In the first study, our investigations revealed that NMOSD-ON exhibits early pRNFL thinning in the superior and inferior ETDRS sectors within 0–1 month, a previously unreported temporal distinction from IDON. Within the identified critical window of pathological deterioration (≤1 month), the spatiotemporal progression and sequential phenotypes of each pathological event using our novel animal model were systemically evaluated. A sequential pathology: AQP4-IgG binding and astrocyte disintegration peaked within the first week, followed by secondary demyelination and RGC degeneration at 3–4 weeks was observed, confirming demyelination as a downstream event following the astrocytes damage. In the third study, LBGP treatment demonstrated efficacy in reversing NMOSD-induced optic nerve damage. A subsequent mechanistic study revealed that this neuroprotective effect was mediated through LBGP's selective targeting of Cathepsin Z dependent neuroinflammatory pathways.

Conclusion: Our research began by characterizing NMOSD-ON phenotypes to define the critical time windows for disease onset and progression. Leveraging these temporal insights, we established a novel NMOSD-ON animal model to systematically recapitulate key pathological events. This model subsequently enabled us to investigate both the therapeutic efficacy of LBGP intervention and its underlying mechanisms of action.

Publications arising from the thesis

Publications as the first author

1. **Xiayin Yang**, Xuefen Li, Mengying Lai, Jincui Wang, Shaoying Tan, Henry Ho-Lung Chan. Pain Symptoms in Optic Neuritis. ***Front Pain Res (Lausanne) (Impact factor: 2.7)***, 2022 Apr, DOI: 10.3389/fpain.2022.865032
2. **Xiayin Yang**, Shi-Qi YAO, Henry Ho-Lung Chan, Shaoying Tan. Dynamic characterization of pathological and functional deterioration in a mouse model of optic neuritis related to neuromyelitis optica spectrum disorder. ***Neural Regen Res (Impact factor: 6.7)***, 2025 Jan, DOI: 10.4103/NRR.NRR-D-24-00898
3. **Xiayin Yang,** Jingfang, Bian, Shi-Qi Yao, Thomas Chuen Lam, Kwok-Fai So, Henry Ho-Lung Chan, and Shaoying Tan. Lycium Barbarum Glycopeptide attenuates the Cathepsin Z-mediated apoptosis in refractory optic nerve neuroinflammation. ***PNAS****,* Under review

Publication as the co-author

1. Shi-Qi Yao, **Xiayin Yang**, Ling-Ping Cen, Shaoying Tan. The Role of Gut Microbiota in Neuromyelitis Optica Spectrum Disorder. ***International Journal of Molecular Sciences (IJMS) (Impact factor: 4.9)***, 2024 Mar. DOI: 10.3390/ijms25063179

Oral Presentations

1. **Xiayin Yang**, Xuefen Li, Jincui Wang, Shiqi Yao, Shihui Wei, Shaoying Tan. Peripapillary

retinal nerve fiber layer thickness in idiopathic optic neuritis and neuromyelitis optica spectrum disorder associated optic neuritis. Congress of Chinese Ophthalmological Society (CCOS 2024), September 4-8, 2024, Wuhan, China.

2. **Xiayin Yang**; Shaoying Tan. The Temporal Dynamics of Pathological Profile and Functional Impairment in Neuromyelitis Optica Spectrum Disorders associated Optic Neuritis. The 12th Asian Neuro-Ophthalmology Society Meeting, December 6-8, 2024, Hong Kong, China.
3. **Xiayin Yang**; Henry Ho-Lung Chan; Shaoying Tan. Lycium barbarum glycopeptide promotes neuroinflammation management, remyelination, neuroprotection via lyososmal regulation. Guangdong – Hong Kong – Macao Greater Bay Area Visual Science and Neuroscience Conference (GBA-VSNS 2025), March 1, 2025, Guangzhou, China
4. **Xiayin Yang**; Henry Ho-Lung Chan; Shaoying Tan. Lycium Barbarum Glycopeptide protect the optic nerve in refractory neuroinflammation. Chinese Congress of Research in Vision and Ophthalmology (CCRVO) 2025, July 24-28, 2025, Chongqing, China.

Poster

1. **Xiayin Yang**, Henry Ho-Lung Chan, Shaoying Tan. Neuroprotective Effects of Lycium barbarum Glycopeptide in a Mouse Model of Neuromyelitis Optica Spectrum Disorders associated Optic Neuritis. The International conference of Vision and Eye Research (iCover) 2025, June 7-8, 2025, Tianjing, China.

Awards

1. **School of Optometry in Hong Kong Polytechnic University Three Minute Thesis (3MT) Competition First Runner-up. Xiayin Yang**, Henry Ho-Lung Chan, Shaoying Tan. Neuromyelitis optica spectrum disorders associated optic neuritis (NMOSD-ON) animal model and potential underlying disease mechanisms.
2. **Best Poster Award at iCover 2025. Xiayin Yang**, Henry Ho-Lung Chan, Shaoying Tan. Neuroprotective Effects of Lycium barbarum Glycopeptide in a Mouse Model of Neuromyelitis Optica Spectrum Disorders associated Optic Neuritis. iCover 2025, 2025

Acknowledgements

First and foremost, I would like to show my sincere appreciation to **Dr. Shaoying Tan** and **Prof. Henry CHAN Ho-lung** for their invaluable guidance, support, and the collaborative platform they provided throughout my PhD journey. Together, we built this project from the ground up—from collecting clinical data and developing animal models to exploring treatments and investigating underlying mechanisms. It has been a continuous process of exploration and refining experimental conditions.

Dr. Shaoying Tan, my chief supervisor, has been not only a mentor but also a comrade-in-arms in this four-year endeavor. We worked side by side, pushing the boundaries of research on optic neuritis, a field still largely uncharted and filled with unknowns. Every step forward demanded tremendous effort, and only we truly understand the challenges behind each hard-earned breakthrough. Dr. Tan was unwavering in her commitment, engaging in weekly—sometimes even daily—discussions about our progress. Even when we faced setbacks, she never gave up. Despite limited funding, a small team, and insufficient support in the early stages, we persevered and ultimately succeeded.

I would also like to extend my sincere thanks to **Prof. Henry Chan**, whose support was instrumental in this journey. As my co-supervisor, he generously guided me in lab meetings, providing opportunities to develop my research. When we lacked essential equipment, he went above and beyond to secure critical resources, such as a stereotaxic apparatus. Every manuscript we produced benefited from his meticulous feedback and revisions. Without his dedication, this four-year project

would not have been possible.

Their mentorship, resilience, and belief in our work have been the driving force behind this achievement. For that, I am eternally grateful.

I would also like to express my sincere gratitude to **Prof. Thomas LAM**, from whom I learned essential techniques such as peptide extraction and proteomics analysis during his guided study sessions. These skills greatly contributed to the success of my experiments.

I would like to express my sincere gratitude to our DRC Chair, **Prof. Bin Lin**. Prof. Lin guided me through three DRC meetings with insightful discussions and careful mentorship. He has provided invaluable advice on my project, even offering detailed suggestions on experimental design.

We are extremely grateful to **Mr. KK Li** for his invaluable assistance. As a meticulous technician and lab manager, he has been instrumental in every aspect of our work—from equipment operation and reagent procurement to training in experimental techniques. It has been a true privilege to benefit from his expertise and support.\

I am also deeply thankful to the People's Liberation Army General Hospital and Medical School (301 Hospital) for providing us with invaluable clinical OCT data that made this research possible.

Additionally, I am deeply thankful to **Dr. Jennifer Bian**, **Dr. Samantha Shan**, **Dr. Choi Kai-yip**,

Dr. Yamuna Lakshmanan, **Dr. Francisca Wong**, **Mr. Kirk Patrick**, **Miss Shi-qi YAO**, **Miss Fangyu Xu**, **Miss Mingpu Xu**, and **Mr. Milan Rai** for their invaluable technical support, insightful advice, and the learning opportunities they provided. Their expertise and generosity were instrumental in advancing my research.

I would also like to express my heartfelt gratitude to my family for their quiet yet unwavering support of my work.

Table of contents

List of figures

List of tables

Chapter 1 Introduction

1.1 The visual pathway anatomy

The visual pathway begins from the eyeball, where the complex process of visual signal processing first takes place. When light enters the eye, it undergoes a series of precise optical transformations. Initially, the light rays pass through the cornea, the transparent front layer of the eye, which acts as the primary focusing element. The majority of the eye's focusing ability is provided by the cornea. In fact, cornea is responsible for nearly two-thirds of it, performing the crucial first step in focusing incoming light (De Moraes, 2013).

After passing through the cornea, light continues its journey through the lens. The flexibility of the lens allows it to adjust its shape, fine-tuning the focus for objects at varying distances. The focused light then travels through the vitreous humor, a clear gel-like substance that fills the posterior chamber of the eye, before finally reaching the retina (DelMonte & Kim, 2011) **(Figure 1.1)**.

Interestingly, the structural organization of retina appears counter-intuitive at first glance. The photoreceptor cells, which are responsible for the initial detection of light stimuli, are actually located in the outermost layer of the retina, furthest from incoming light. This arrangement requires light to traverse through multiple retinal layers before reaching the photoreceptors. Upon receiving light stimulation, photoreceptors convert light into electrical signals. Together with the inhibitory function of the horizontal cells, these signals are transmitted to bipolar cells, which then relay the information to amacrine cells and eventually to RGCs. These ganglion cells are crucial as their

axons form the optic nerve fibers, which bundle together becoming the optic nerve. This nerve is the primary conduit for transmitting processed visual information arising from the eyeball to the visual cortex, marking the beginning of the higher-order visual processing pathway (De Moraes, 2013) **(Figure 1.1)**.

The axons of RGCs form the optic nerve posterior to the globe, these fibers enter and become incorporated into the central nervous system (CNS), establishing the optic nerve as a true CNS structure. RGCs send processed visual information through their axons, which form the optic nerve. The optic nerve is surrounded by three layers of protective tissue known as the meninges. The outermost layer, the dura mater, is robust and fibrous, providing primary protection and assisting in maintaining the optic nerve's structural integrity. Beneath this, the arachnoid mater, a web-like intermediate layer, offers cushioning and houses cerebrospinal fluid (CSF) to mitigate shocks and further safeguard the nerve. Lastly, the innermost layer, the pia mater, is thin and delicate, closely adhering to the optic nerve surface, delivering additional support and critical nourishment. Collectively, these layers ensure that the optic nerve is adequately protected and supported within the CNS. The myelin sheath encasing an individual optic nerve fiber enhances the rapid transmission of electrical signals. This sheath is synthesized by oligodendrocytes within the CNS, serving to insulate the axons and augment conduction velocity. The visual signals travel through the optic nerve and reach the lateral geniculate nucleus (LGN) of the thalamus, where initial processing occurs. From the LGN, visual signals are sent to the visual cortex in the occipital lobe of the brain. The visual cortex integrates these signals, allowing us to perceive images, colors, motion, and depth. Through this complex pathway, the visual system transforms light stimuli into meaningful visual

information, enabling us to visualize our surroundings. The interplay between various cell types in the retina and the careful organization of the optic nerve and its protective layers ensure efficient processing and transmission of visual signals to the brain (De Moraes, 2013) **(Figure 1.1)**.

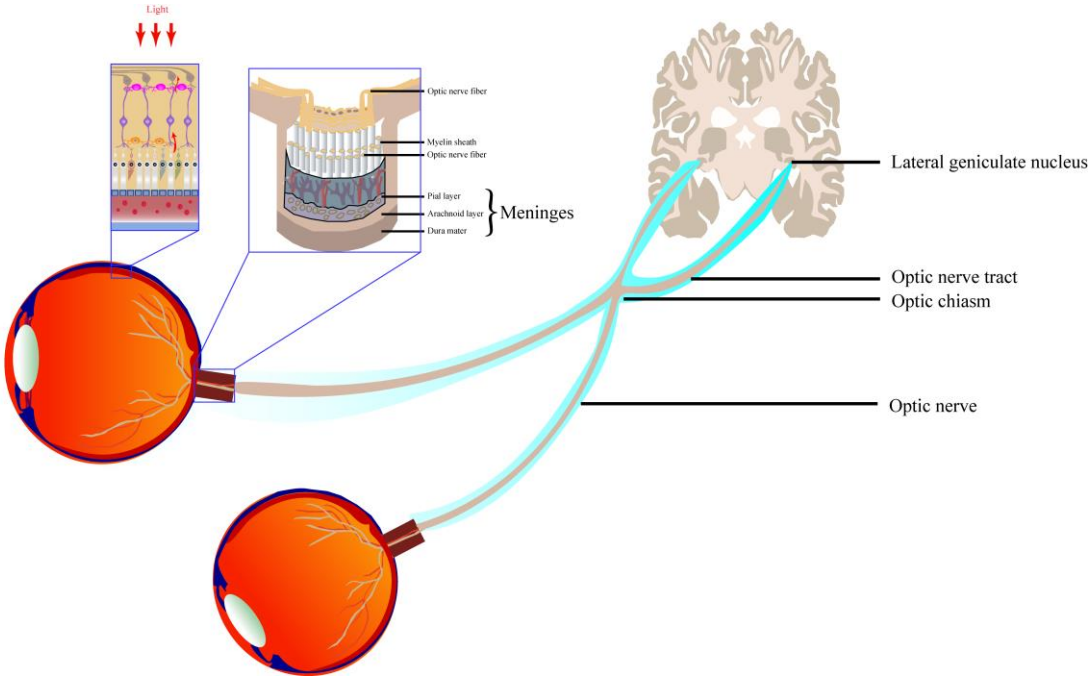

Figure 1.1 The anatomical structure of the optic nerve visual pathway.

After delineating the gross anatomical organization of the optic nerve, our investigation progressed to ultrastructural examination and biomarker profiling of its cellular components.

1.2 Optic nerve cell components and biomarkers

The optic nerve is composed of several essential cellular components that work synergistically to ensure proper visual signal transmission and nerve integrity. While RGC axons constitute the primary signal-conducting elements, the optic nerve functionality depends heavily on its diverse cellular composition (Wong & Benowitz, 2022). The RGC axons are extensively wrapped by myelin sheaths, which are produced and maintained by oligodendrocytes (Butt et al., 2004). These

specialized glial cells can simultaneously myelinate multiple axon segments, creating concentric layers of membrane that enable rapid saltatory conduction of action potentials (Butt et al., 2004). Astrocytes, another crucial glial cell type, perform multiple essential functions within the optic nerve, including providing metabolic support to axons, maintaining ionic homeostasis in the extracellular environment, and contributing to the blood-nerve barrier (Mazumder et al., 2023). These star-shaped cells also produce various growth factors and signaling molecules that support axon survival while helping maintain the optic nerve structure through mechanical support. Microglia, the resident immune cells of the optic nerve, continuously patrol the tissue environment, responding swiftly to injury or infection by initiating inflammatory responses and promoting phagocytosis to remove cellular debris and dead cells (Mazumder et al., 2023). They release both pro- and anti-inflammatory mediators to regulate immune responses and participate in tissue repair and remodeling processes (De Moraes, 2013) **(Figure 1.2)**.

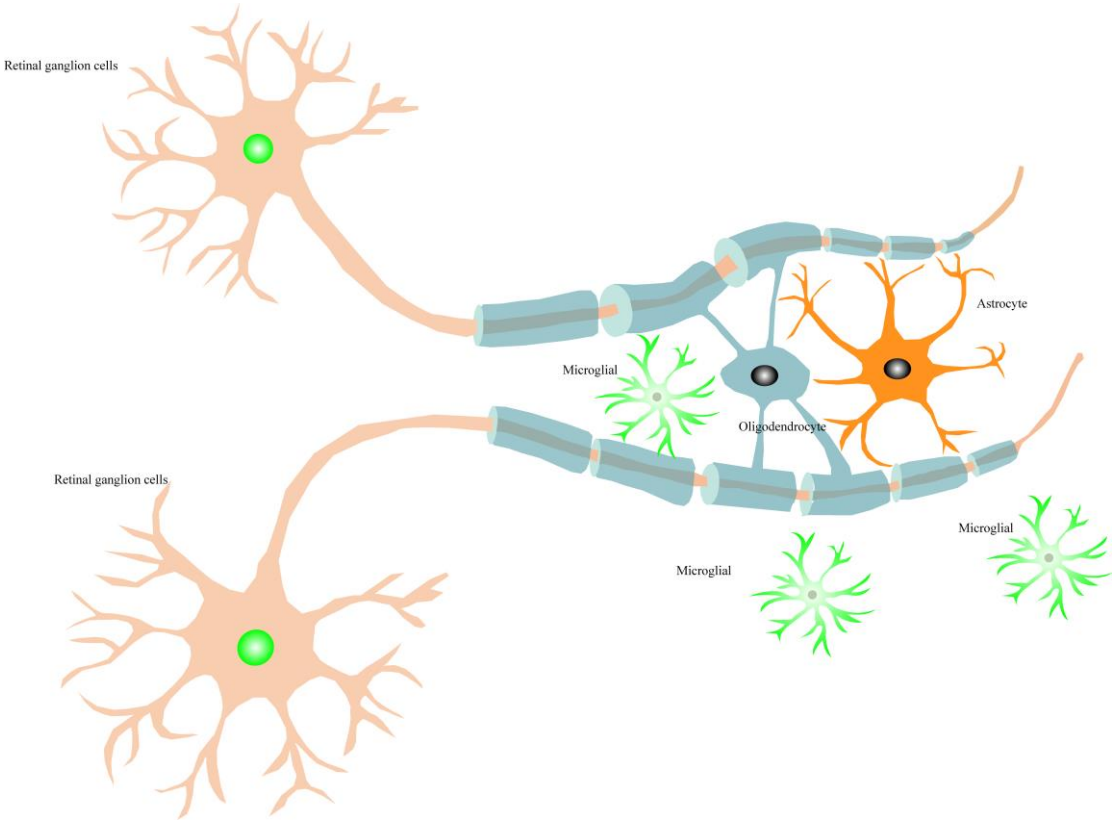

Figure 1.2 The cellular structural framework surrounding the optic nerve.

The optic nerve consists of multiple cellular components, each identifiable through specific molecular biomarkers indicating their identity and functional state. RGCs, the primary neurons of the optic nerve, can be identified through several characteristic markers including RNA-binding protein with multiple splicing (RBPMS), which is specifically expressed in RGC cell bodies, and so does the Brn3 family transcription factors (Brn3a, Brn3b, and Brn3c). The myelin-producing oligodendrocytes express distinct markers at different stages of their development and maturation - Olig2 serves as a key transcription factor throughout their lineage, while mature oligodendrocytes specifically express myelin oligodendrocytes glycopeptide (MOG). Astrocytes, which provide crucial support functions, are characteristically identified by their expression of glial fibrillary acidic protein (GFAP). These cells also express AQP4 water channels, particularly in their endfeet processes contacting blood vessels. Microglial cells, the immune sentinels of the optic nerve,

express several distinctive markers including ionized calcium binding adaptor-1 (Iba-1) molecule. In their activated state, microglia may also express additional markers such as CD68, indicating their phagocytic activity. These molecular markers not only help identify specific cell types but also provide valuable tools for studying optic nerve development, function, and pathology **(Table 1.1)**.

Table 1.1 This table delineates the biomarkers and their corresponding phenotypic manifestations.

Biomarkers	Phenotype
RNA-binding protein with multiple splicing (RBPMS)	Retinal ganglion cells
Brn3 family transcription factors (Brn3a, Brn3b, and Brn3c	Retinal ganglion cells
Myelin oligodendrocytes glycopeptide (MOG)	Myelin sheath
Glial fibrillary acidic protein (GFAP)	Astrocytes
Ionized calcium binding adaptor-1 (Iba-1) molecule	Microglial
CD68	Microglial with phagocytic activity

The immune system plays critical roles in both physiological and pathological development of the optic nerve. Resident microglia and astrocytes - key components of the blood-brain barrier (BBB) within the optic nerve - are particularly important in regulating immune-inflammatory responses. Building on this foundation, we next sought to elucidate the broader mechanisms of immune regulation throughout the CNS.

1.3 The immunoregulation in CNS system

The CNS is distinguished by its immune-privileged nature (Carson et al., 2006; Galea et al., 2007;

Tian et al., 2012; Tian et al., 2009), which limits the infiltration of peripheral immune cells due to the presence of the BBB. Within the CNS, glial cells, particularly microglia and astrocytes, are integral to immune defense, safeguarding against injury and infection. However, excessive or prolonged activation of these glial cells can result in chronic neuronal damage, leading to neuroinflammation and neurodegeneration (Tian et al., 2012).

Microglia, the predominant phagocytic localated within the CNS, are actively engaged in phagocytosis (Rivest, 2009; Tian et al., 2012). Upon activation, microglia transits from a ramified morphology to an amoeboid form (Griffiths et al., 2009; Rivest, 2009; Tambuyzer et al., 2009). This phagocytic activity help clears apoptotic cell debris, thereby averting neuronal damage and loss (Bessis et al., 2007; Napoli & Neumann, 2009). Nevertheless, microglial activation under pathophysiological conditions and excessive phagocytosis can exacerbate neurodegeneration (Butler et al., 2021). Microglia are often described as the macrophage-like population of the CNS. During inflammatory responses, peripheral macrophages can infiltrate the CNS, where they operate in a manner akin to microglia, collaborating to enhance the inflammatory response (Li & Barres, 2018).

Astrocytes, the supportive cells of the CNS, contribute to the immune landscape by modulating the ingress of immune cells through the BBB (Bechmann et al., 2007; Haydon & Carmignoto, 2006). Initially, astrocytes secrete cytokines to facilitate immune cell entry. Upon activation, they can recruit microglia, which may lead to neurodegenerative processes (Schwab & McGeer, 2008). During the complex neurodegenerative processes, the phenomenon of demyelination, characterized

by the loss of myelin sheaths that insulate neuronal axons, leads to significant neuroaxonal impairment. This impairment is primarily attributed to the diminished neurotrophic support provided by oligodendrocytes, which help maintain the survival of neurons. The absence of this support not only disrupts the integrity of the axonal structure but also compromises the overall functionality of the neural circuitry, ultimately result into the neurodegenerative diseases (You et al., 2020). Chemokines and cytokines, including TNF-alpha, IL-1 beta, and IL-6, along with anti-inflammatory cytokines such as TGF-beta, can enter the CNS from the peripheral circulation, participating in neuroimmune interactions. This is particularly relevant given that peripheral immune cells possess a limited capacity to penetrate the CNS (Kerschensteiner et al., 2009; Wahl et al., 2006).

1.4 The autoimmune disorders in CNS

Autoimmune disorders are characterized by the production of autoantibodies, and a broader spectrum of diseases has been identified in recent years as more disease-associated autoantibodies have been discovered (Flanagan, 2019; Graus et al., 2016). The autoantibodies targeting neuronal or glial antigens contributes to disease progression. However, not all autoantibodies can be detected, leading to the occurrence of "seronegative" autoimmune CNS disorders (Graus et al., 2018). This phenomenon may also be attributed to cell-mediated mechanisms.

The breakdown of immune tolerance in the periphery immune system is the origin of autoimmune disorders (Dalmau & Graus, 2018; Ramanathan et al., 2023), primarily due to the elevated concentrations of autoantibodies in the serum (Trewin et al., 2022). As a result, treatments targeting

the peripheral autoantibodies often yield better therapeutic outcomes. However, autoantigen-specific B cells and plasma cells are also found within the intrathecal compartment, indicating that these cells are localized to the CNS rather than the periphery (Zrzavy et al., 2021). This explains why some patients remain resistant to treatment. A defect in the B cell checkpoint may result into the failure to negatively select developing autoreactive B cells. As a result, autoreactive naïve B cells can accumulate in the circulation and present self-antigens to T cells, thereby promoting autoimmunity. This reservoir of autoreactive naïve B cells may also undergo clonal mutations, maturing into fully functional B cells and eventually becoming plasma cells against self-antigens (Meffre & O'Connor, 2019). The direct binding of autoantibodies to cell-surface or synaptic antigens, leading to blockade or internalization of the antigen, is a primary pathogenic mechanism (Dalmau et al., 2017; Hughes et al., 2010; Lai et al., 2009; Sechi & Flanagan, 2021). Alternatively, damage can be mediated through complement activation and cellular cytotoxicity pathways or by disrupting protein-protein interactions (Hinson et al., 2012; Huijbers et al., 2015). Ultimately, these mechanisms result in the disruption of cytoskeletal architecture (Dale et al., 2014; Landa et al., 2020). Autoantibodies targeting oligodendrocytic or astrocytic antigens initially cause demyelination and eventually lead to neuronal loss (Hinson et al., 2008).

This disease spectrum encompasses CNS demyelinating conditions, including multiple sclerosis (MS) and Neuromyelitis optica spectrum disorder (NMOSD), as well as paraneoplastic syndromes, autoimmune encephalomyelitis, and myositis (Bhagavati, 2021).

1.5 NMOSD

1.5.1 The characteristic features of NMOSD

NMOSD is characterized by the frequent bilateral optic neuritis and transverse myelitis; MRI examinations can reveal longitudinally extensive transverse myelitis lesions (LETM) spanning ≥3 vertebral segments in the spinal cord (Wingerchuk et al., 1999). The discovery of detectable serum antibodies targeting the water channel aquaporin-4 (AQP4–immunoglobulin G [IgG]) has expanded the diagnostic criteria for NMOSD (Lennon et al., 2004).

1.5.2 The diagnosis of NMOSD

In terms of diagnostic criteria, the requirements for clinical manifestations have been relaxed, allowing even unilateral optic neuritis or asymptomatic brain MRI lesions to be diagnosed as NMOSD. However, the dual requirement of both myelitis and optic neuritis remains essential (Wingerchuk et al., 2006).

The International Panel for NMO Diagnosis (IPND) has established diagnostic criteria for NMOSD. For AQP4-IgG-positive patients, the diagnosis of NMOSD requires at least one core clinical manifestation, such as unilateral or bilateral optic neuritis, longitudinally extensive transverse myelitis (LETM) spanning more than three vertebral segments, area postrema syndrome, cerebral syndrome, acute diencephalic syndrome, or acute brainstem syndrome. For AQP4-IgG-negative patients, at least one of the following core clinical manifestations is required: optic neuritis, LETM, or area postrema syndrome. If only one of these three manifestations is present, an additional core

clinical manifestation (cerebral syndrome, acute diencephalic syndrome, or acute brainstem syndrome) must also be present to establish the diagnosis. Additionally, MRI findings must demonstrate optic nerve or long-segment LETM involvement, and other diseases must be excluded. For seronegative patients, testing for MOG antibodies is also required (Wingerchuk et al., 2015).

1.5.3 The prevalence of NMOSD

The prevalence of neuromyelitis optica spectrum disorder (NMOSD) varies significantly across different regions worldwide. Recent studies have shown that individuals of African descent in the Caribbean have the highest prevalence, reaching 10 per 100,000, while the lowest prevalence is observed in Australia, at only 0.73 per 100,000 (Papp et al., 2021). Globally, the incidence of NMOSD is estimated to be around 4-5 per 100,000 (Papp et al., 2021; Vaknin-Dembinsky et al., 2014). In Asia, the incidence of multiple sclerosis (MS) is not as high as in Europe or North America. However, the ratio of NMOSD to MS is significantly higher in Asian populations compared to Western regions (Ochi & Fujihara, 2016). This suggests that in Asia, NMOSD should be given a level of attention comparable to that of MS. NMOSD exhibits a strong female predominance (80%), with onset typically occurring in younger individuals (Ransohoff, 2012). The mean age is around 40 years old for NMOSD patients (Kitley et al., 2014). The proportion of NMOSD among demyelinating disorders (including MS, NMOSD, Acute Disseminated Encephalomyelitis) varies significantly by country. Asian nations such as Thailand and India exhibit particularly high prevalence rates, reaching up to 30%, whereas in the U.S., NMOSD accounts for only ~1% of cases

(Pandit et al., 2015). Thus, in Asian populations, NMOSD should be actively considered in the differential diagnosis of demyelinating diseases (Pandit et al., 2015).

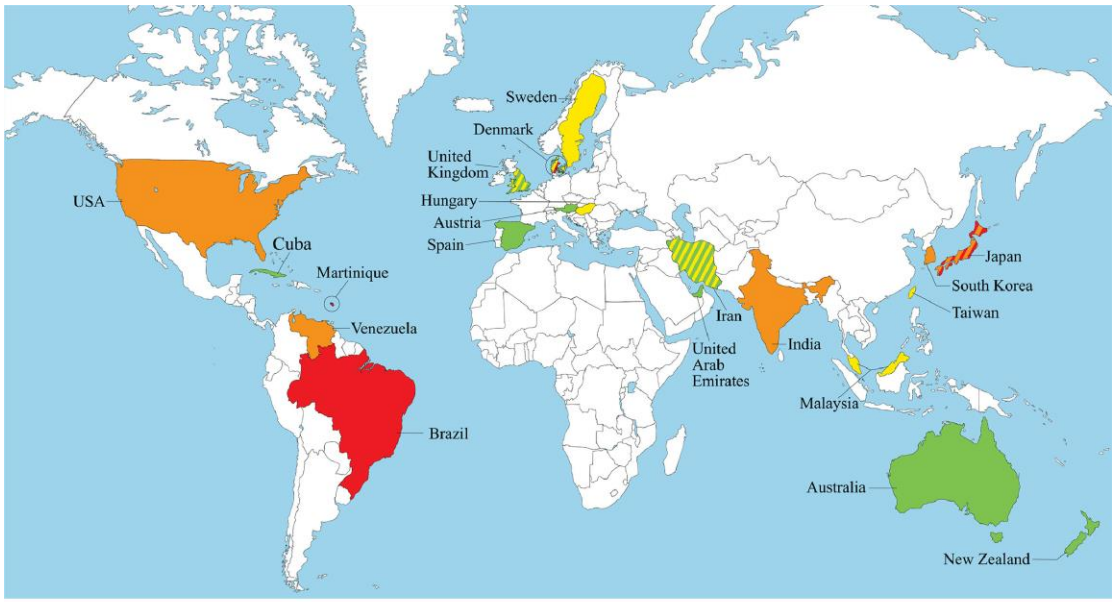

Figure. Global prevalence gradient for neuromyelitis optica spectrum disorders

<1.0: Australia and New Zealand, Austria, Cuba, Denmark (Nationwide), Iran (Tehran), Spain, United Arab Emirates, UK (North West England)

1.0-1.9: Denmark (Nationwide), Hungary, Iran, Malaysia, Sweden, Taiwan, UK (South East Wales)

2-3.9: India, Japan (Nationwide), South Korea, USA, Venezuela

>4.0: Brazil, Denmark (Southern), Japan (Northern), Martinique

Figure 1.3 The world-wide prevalence of NMOSD.

Figure 1.3 adapted from (Lana-Peixoto et al., 2021), illustrates the geographical distribution of NMOSD prevalence across different regions.

1.5.4 Pathogenesis of NMOSD

NMOSD is a type of astrocytopathy, where demyelination occurs secondarily to the astrocytopathy (Carnero Contentti & Correale, 2021; Wingerchuk et al., 2006; Wu et al., 2019a). This is fundamentally different from MS, in which demyelination is the primary pathological process

(Carnero Contentti & Correale, 2021; Wingerchuk et al., 2006).

An autoimmune disease where pathogenic antibodies are the primary driver of pathogenesis, NMOSD was initially characterized by serum AQP4-IgG antibodies entering the CNS and targeting AQP4 proteins on astrocytes (Carnero Contentti & Correale, 2021; Wingerchuk et al., 2006; Wu et al., 2019a). However, it is now recognized that some patients exhibit the core clinical manifestations of NMOSD—optic neuritis, myelitis, and brainstem syndromes—yet test negative for AQP4-IgG. Among these seronegative patients, a subset is positive for anti MOG autoantibodies (MOG-IgG), while others remain negative for both AQP4-IgG and MOG-IgG. As a result, NMOSD now encompasses three distinct patient subgroups: (1) AQP4-IgG seropositive, (2) MOG-IgG seropositive, and (3) double-seronegative (negative for both antibodies) (Uzawa et al., 2024). The mechanisms underlying double-seronegative NMOSD are primarily thought to involve either antibodies targeting unknown antigens or a direct, cell-mediated immune attack orchestrated by T cells (Wu et al., 2023).

The aggregation of orthogonal arrays of particles (OAPs) within the AQP4 protein sequence is a crucial structure for AQP4-IgG recognition of AQP4 epitopes and for complement C1q binding. The M23-AQP4 isoform can form OAPs, whereas the M1-AQP4 isoform, which has 22 additional amino acids at the cytoplasmic N terminus, does not form OAPs and inhibits their formation. AQP4-IgG is more likely to bind to the M23-AQP4 isoform rather than the M1-AQP4 isoform because the M23-AQP4 isoform facilitates OAPs formation (Crane et al., 2009; Crane et al., 2011; Lu et al., 1996; Phuan et al., 2012). The optic nerve and spinal cord are the most susceptible areas for NMOSD

attacks, possibly due to the differing ratio of M23-AQP4 to M1-AQP4 in these tissues compared to other locations (Matiello et al., 2013).

After AQP4-IgG binding, a series of pathological changes can occur. The activation of T and B lymphocytes has been substantiated (Liu et al., 2021). Following astrocyte degradation, microglia and neutrophils are recruited, leading to the production of pro-inflammatory cytokines such as TNF-α; IL-1β, and IL-6, which contribute to the exacerbation of neuroinflammation (Carnero Contentti & Correale, 2021; Yick et al., 2020). This neuroinflammatory response subsequently results in demyelination and axonal degeneration (Carnero Contentti & Correale, 2021; Wingerchuk et al., 2006; Wu et al., 2019a).

Complement deposition is markedly evident in a rat NMOSD model where they passively transfer the AQP4-IgG (Asavapanumas, Ratelade, & Verkman, 2014). It is clear that complement plays a significant role in the pathogenesis of NMOSD (Asavapanumas, Ratelade, & Verkman, 2014). However, even when complement is depleted or inhibited, pathological changes associated with NMOSD persist. This observation suggests the existence of complement-independent mechanisms contributing to the disease process in NMOSD (Asavapanumas, Ratelade, & Verkman, 2014). Antibody-dependent cellular cytotoxicity (ADCC) is likely to be one of the mechanisms involved because, in the absence of ADCC effector function, there is a notable reduction in the lesions associated with NMOSD. This observation suggests that the presence of ADCC may play a critical role in the pathophysiology of NMOSD, influencing the extent and severity of the disease manifestations (Asavapanumas, Ratelade, & Verkman, 2014). The rat model provides unique

benefits for NMOSD research. Its larger size allows for easier optic nerve exposure with reduced risk of vascular damage and hemorrhage. Moreover, its endogenously functional complement system enables robust inflammatory induction without supplemental complement. Drawbacks, however, include higher maintenance demands compared to mice and a narrower selection of commercial knockout models (Yuko Morita et al., 2022). In this particular model they passively transfer the AQP4-IgG to the brain of rats. I added this sentence the main text of thesis.

1.5.5 Treatment options in NMOSD

To date, numerous therapeutic interventions have been employed for NMOSD. During the acute phase of the condition, intravenous administration of methylprednisolone and intravenous immunoglobulin has been utilized to modulate the immune system on a systemic level in the management of NMOSD (Danieli et al., 2025; Shoenfeld & Katz, 2005; Yang et al., 2024). Rituximab inhibits the expression of the CD20 antigen on B cells, thereby preventing the maturation of premature B cells into plasmablasts (Gao et al., 2019) **(Figure 1.3)**. Inebilizumab targets CD19 on cells to obstruct the differentiation of plasmablasts into plasma cells (Bennett et al., 2022) **(Figure 1.3)**. Tocilizumab or satralizumab works therapeutically by inhibiting IL-6, which can weaken the BBB and allow plasma cells and antibodies to enter the central nervous system (CNS) (Araki et al., 2014) **(Figure 1.3)**. Complement activation significantly contributes to the progression of NMOSD; thus, complement inhibition is effective in halting disease advancement (Pittock et al., 2019) **(Figure 1.3)**. The mechanism of steroids involves a generalized suppression of inflammatory mediators and immune cell activation. In contrast, immunosuppressants typically work by inhibiting discrete steps in specific cellular pathways or the cell cycle itself. I added this sentence the main

text of thesis.

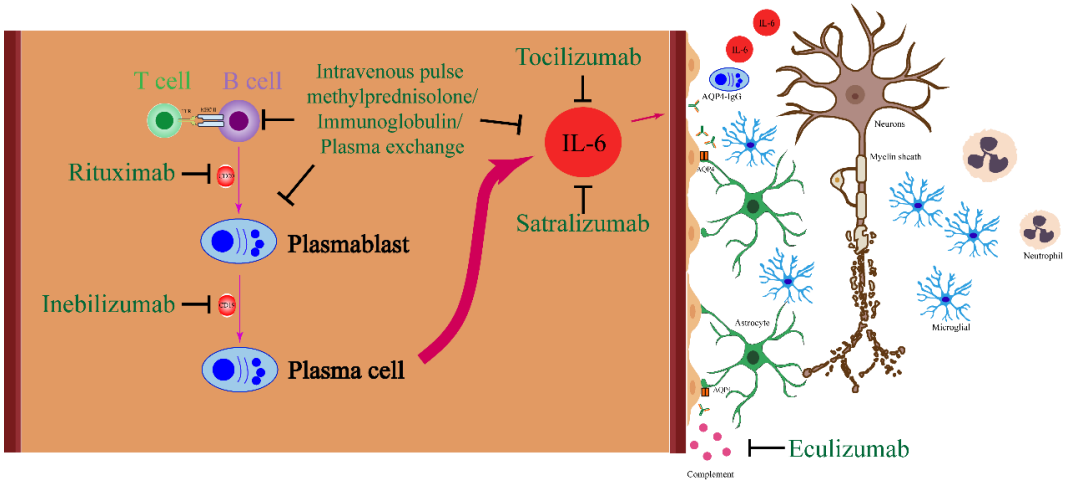

Figure 1.3 Treatment options for NMOSD apart from traditional methylprednisolone and intravenous immunoglobulin administration.

1.6 Neuromyelitis optica spectrum disorder associated optic neuritis

1.6.1 The characteristic features of Neuromyelitis optica spectrum disorder associated optic neuritis

The primary manifestations of NMOSD include optic neuritis, myelitis, and various brain syndromes (Uzawa et al., 2024). In Neuromyelitis optica spectrum disorder associated optic neuritis (NMOSD-ON), the optic nerve is always affected due to interactions between antibodies and antigens. Typically, the binding of AQP-IgG to the AQP4 antigen leads to aquaporin-4 antibody-positive optic neuritis (AQP4-ON) (Naganuma et al., 2021). Meanwhile, the binding of MOG-IgG to the MOG antigen results in myelin oligodendrocytes antibody-positive optic neuritis (MOG-ON)

(Jeyakumar et al., 2024).

Typical optic neuritis, which commonly presents with unilateral involvement, pain with eye movement, and moderate, reversible visual impairment, is primarily associated with MS-related optic neuritis (MS-ON) and idiopathic optic neuritis (IDON) (Abel et al., 2019). The NMOSD-ON, recognized as atypical ON, differs from typical ON (Abel et al., 2019). NMOSD-ON primarily affects the posterior segment of the optic nerve, typically impacting both eyes. This condition often results in significant and irreversible vision loss (Huda et al., 2019). While both MS and NMOSD can cause optic neuritis, NMOSD demonstrates distinct clinical patterns: it more frequently presents with bilateral simultaneous involvement, causes more severe visual impairment at initial onset, and exhibits higher relapse rates. Illustrating this, one cohort study documented 163 ON episodes among 72 affected eyes in NMOSD patients (average 2.26 relapses per eye), compared to only 36 episodes among 23 eyes in MS patients (average 1.57 relapses per eye) - representing a 44% higher relapse frequency in NMOSD (Srikajon et al., 2018).

1.6.2 The optimal therapeutic time window for NMOSD-ON

The treatment of NMOSD-ON requires different therapeutic targets at different stages of the disease process—from the entry of autoantibodies into the CNS to the eventual degeneration of RGCs. Each phase demands a distinct therapeutic approach. In the earliest stage, the focus should be on preventing AQP4-IgG from binding to the optic nerve, which means reducing CNS infiltration of AQP4-IgG. Next, during the inflammatory peak, the priority shifts to targeting neuroinflammation, as this acts as a key driver of disease progression. In the later stages, the critical challenge changes

again. The goal is to promote remyelination and protect RGCs to prevent degeneration. To optimize treatment timing, we first need to determine when NMOSD-ON progresses from acute onset to RGC degeneration and the exact timing of each pathological event in this cascade. Understanding these dynamics is essential for developing stage-specific interventions that precisely address the evolving mechanisms of NMOSD-ON. In the subsequent Chapter 2, OCT analysis of patient retinas revealed that NMOSD-ON primarily targets the nerve fibers of RGCs. Based on this finding, we identified the temporal window of RGC damage in NMOSD-ON. Within this time window, the entire pathological progression in animal models was observed in Chapter 3. By analyzing the sequential changes in these pathological processes, the treatment efficacy was evaluated in Chapter 4 and the underlying mechanisms were investigated in Chapter 5.

Chapter 2 Thinning characteristic of pRNFL thickness in NMOSD-ON

2.1 Introduction and literature reviews

In our clinical practice, distinguishing between typical and atypical ON poses a significant challenge, as the treatments for these two conditions differ markedly (Kraker & Chen, 2023; Saitakis & Chwalisz, 2022). For example, typical ON often responds well to treatments such as high-dose steroids or plasma exchange (Saitakis & Chwalisz, 2022). In contrast, atypical ON may require immunosuppressants, as its treatment response to steroids can be suboptimal (Saitakis & Chwalisz, 2022). The mechanism of steroids involves a generalized suppression of inflammatory mediators and immune cell activation. In contrast, immunosuppressants typically work by inhibiting discrete

steps in specific cellular pathways or the cell cycle itself (Luo et al., 2021). The primary patient group for atypical ON is NMOSD-ON, while IDON and cases that may eventually transition to MS-ON represent a major group of typical ON (Newton et al., 2020; Poonja et al., 2025; Wingerchuk et al., 2015). Our research aims to differentiate between these two conditions, highlighting that AQP4-IgG testing is a crucial indicator for this distinction (Jarius & Wildemann, 2013). If a patient experiences ON and tests positive for AQP4-IgG, they can be diagnosed with NMOSD-ON (Jarius & Wildemann, 2013; Wingerchuk et al., 2015). However, a significant number of NMOSD-ON cases are AQP4-IgG negative, and even MOG-IgG may also be negative (Wu et al., 2023). In such instances, alternative assessment methods become necessary. MRI scans of the cervical spine can serve as one approach, while OCT can also help differentiate between the two types of ON (Oertel et al., 2018; Petzold et al., 2022; Zhao et al., 2018). Many previous studies have focused on the OCT analysis of NMOSD-ON and typical ON, examining the thickness of the RNFL in the macular region (Ayoubi et al., 2022) and around the optic disc (Ratchford et al., 2009), as well as the thickness of the RGC layer (Ayoubi et al., 2022). Their results indicated that both peripapillary retinal nerve fiber layer (pRNFL) and macular retinal nerve fiber layer (mRNFL) were more significantly thinned in NMOSD-ON cases (Ayoubi et al., 2022; Bennett et al., 2015; Ratchford et al., 2009). However, some data suggest that there is no difference in the pRNFL thickness between the two conditions (Manogaran et al., 2016). Moreover, the thinning associated with NMOSD-ON does not persist beyond four years, while MS-ON can continue for a longer duration (Manogaran et al., 2016). This discrepancy is quite controversial (Fernandes et al., 2013; Naismith et al., 2009).

In summary, distinguishing between these two diseases is crucial, especially in geographical regions

where serum AQP4-IgG detection is not widely available or in an era where there are increasing cases of MOG-IgG serum-positivity and double-negative NMOSD. The use of more detailed diagnostic methods is particularly important. OCT is a non-invasive examination technique that provides rapid results, making it especially valuable during acute phases when quick assessment is necessary. Utilizing OCT can significantly enhance our ability to evaluate the condition, allowing for timely treatment before more definitive but time-consuming and costly diagnostic results are available. This highlights the need for a detailed and comprehensive OCT profile that covers multiple timepoints and retinal areas of analysis.

2.2 Objectives

It is important to understand the differences between patients experiencing their first NMOSD-ON or IDON attack over various disease durations. Specifically, the differences between NMOSD-ON and IDON patients, categorized by disease duration, were systematically evaluated. Additionally, by conducting longitudinal comparisons of pRNFL thickness in OCT across different time periods, we aimed to determine how this thickness may change as time progresses. We also particularly interested in whether these trends differ between the two diseases, when these differences occur, and in which specific retinal areas they manifest.

2.3 Methods

2.3.1 Subjects

This clinical cohort study included patients diagnosed with ON between February 2012 and July

2017 in People's Liberation Army General Hospital (PLAGH). Participants were selected based on the initial onset of the condition, which was defined by the first occurrence of visual impairment, disruption of visual function, or related pain symptoms. Informed consent was obtained from all participants, and this study was approved by the ethics committee of the PLAGH.

2.3.2 Inclusion criteria

Individuals diagnosed with ON were chosen according to the specific symptoms and clinical manifestations delineated in the diagnostic criteria established by the Optic Neuritis Treatment Trials (ONTT) ("The clinical profile of optic neuritis. Experience of the Optic Neuritis Treatment Trial. Optic Neuritis Study Group," 1991). Participants in our study were exclusively those who had undergone a solitary episode of ON. Furthermore, the diagnosis of NMOSD-ON was determined based on the presence or absence of AQP4-IgG seropositivity, in accordance with the established clinical criteria (Wingerchuk et al., 2007). AQP4-seropositive patients were included based on verified serum levels of AQP4-IgG. The diagnosis of AQP4-seronegative NMOSD relied on the criteria essential for identifying hallmark clinical manifestations, including ON and myelitis, supported by MRI findings that demonstrate characteristic lesions in the spinal cord or brain. It was imperative to exclude alternative etiologies, such as MS and other autoimmune disorders (Wu et al., 2023). The diagnostic criteria for IDON involve recognizing hallmark symptoms, such as sudden vision impairment and pain during ocular movement. Furthermore, it is essential to rule out differential diagnoses, including NMOSD, MS, systemic lupus erythematosus (SLE), and various forms of arthritis. MRI should demonstrate the absence of lesions typically associated with these disorders, and patients must test seronegative for AQP4-IgG and MOG-IgG. The diagnosis is

confirmed after a solitary episode of ON, with no prior history of demyelinating events (Lee et al., 2018).

2.3.3 Exclusion criteria

In this study, participants with ocular conditions such as retinal detachment, macular degeneration, glaucoma, and non-ON-related ocular injuries were excluded. Furthermore, patients, with ON declined to undergo optical coherence tomography (OCT) scans, or the images obtained were of inadequate quality for subsequent analysis, were also excluded. Among the participants, five ON patients (7 eyes) presented with retinal disorders or glaucoma. Acceptable OCT reports were unavailable for 18 subjects (19 eyes). Additionally, two patients (4 eyes) were under the age of 18 years, resulting in their exclusion from the study. The exclusion criteria are detailed in ***Figure 2.1***.

2.3.4 Subject Classification

Based on the appearance of the optic disc as observed via fundus photographs, the entire population was categorized into two sub-cohorts: the oedematous-optic-disc (EOD) group and the non-oedematous-optic-disc (NEOD) group, reflecting distinct pathological alterations. Additionally, in accordance with clinical guidelines and previous research on the staging of IDON and NMOSD-ON (Duvigneaud et al., 2024), the EOD group was further subdivided into two categories: early stage (within 1 month from onset, 0-30 days) and middle stage (1-3 months, 30-90 days). The NEOD group was also divided into four categories, representing different disease timelines: early stage

(onset within 1 month, 0-30 days), middle stage (1-3 months, 30-90 days), late stage (3-6 months, 90-180 days), and end stage (more than 6 months, over 180 days) following the onset of ON ***(Figure 2.1)***. To stage the disease, the following criteria are used. The acute phase of optic neuritis typically occurs within the first month (Kupersmith et al., 2007). Axonal degeneration then progresses to widespread loss of retinal ganglion cell bodies over approximately 1-3 months (Laviers et al., 2024). The condition generally stabilizes between 3 to 6 months (Beck et al., 1994), after which the disease process becomes largely inactive, allowing for potential visual recovery in some patients (Pineles et al., 2020).

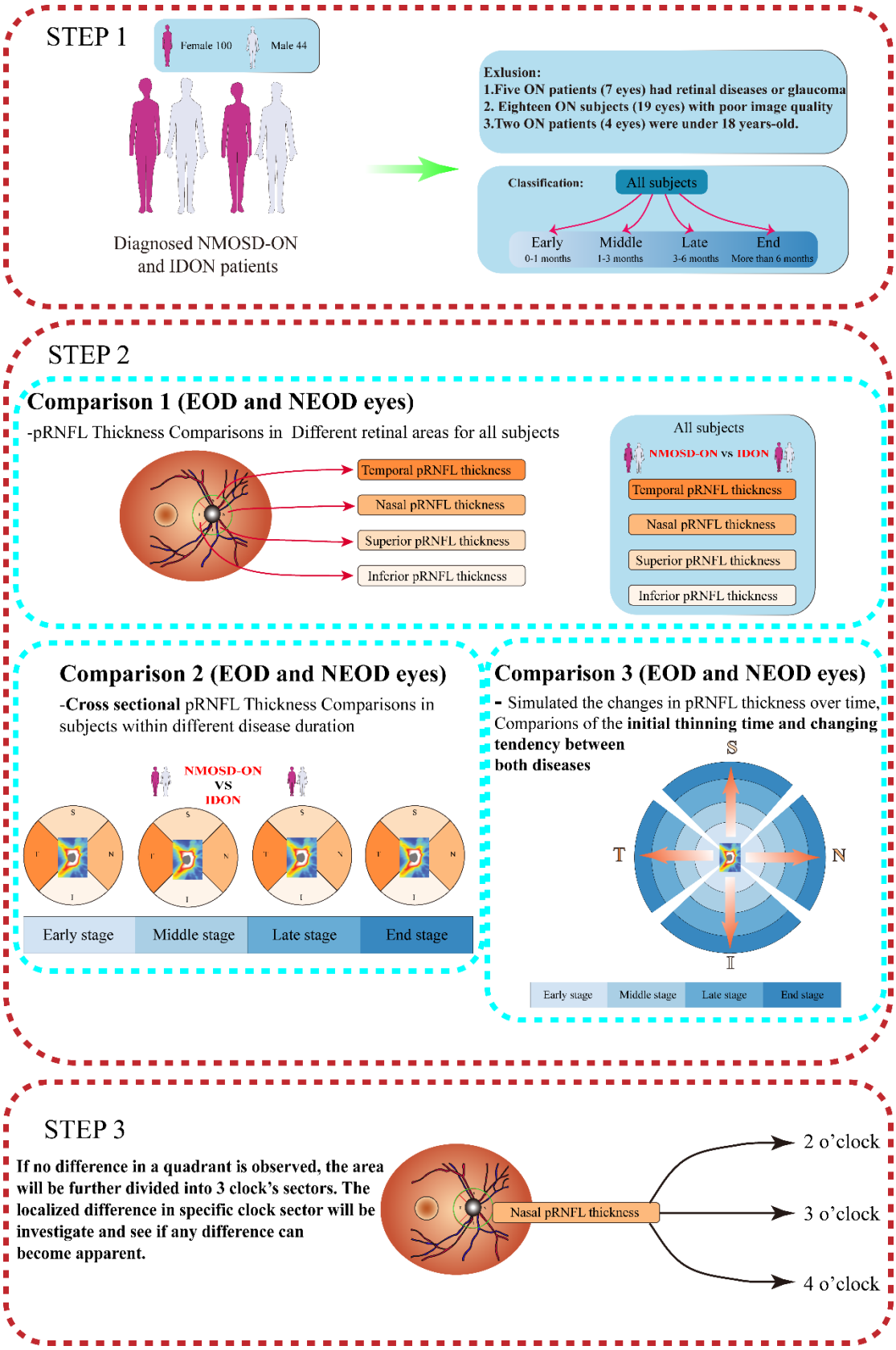

Figure 2.1 This figure illustrates the methodology for selecting subjects, categorizing them, and conducting

spatial and temporal segmentation for analytical purposes. The study employed a flowchart to outline the methodological approach, beginning with the inclusion of male (white) and female (red) patients while excluding those with concurrent retinal diseases, glaucoma, age under 18 years, or inadequate OCT scans. Eligible participants were then stratified according to disease progression stages. The analysis phase involved three sequential comparisons: first, evaluating pRNFL thickness differences between IDON and NMOSD-ON across four retinal quadrants without disease-phase-based distinction; second, comparing pRNFL patterns between the two diseases within the same disease phase; and third, simulating longitudinal thinning trends by analyzing pRNFL changes across adjacent phases for each disease, using directional indicators to contrast progression rates and initial thinning onset. If quadrant-level assessment failed to detect significant inter-disease differences in pRNFL thinning magnitude or timing, a higher-resolution analysis was conducted by subdividing quadrants into three clock-hour sectors for granular evaluation.

2.3.5 Visual acuity evaluation

During the assessments, patients were positioned 2.5 meters from the visual acuity chart. The final visual acuity was determined by averaging the results from three separate examinations conducted three times. The best-corrected visual acuity (BCVA) of participants was evaluated and recorded using decimal notation. All visual acuity results were documented in terms of the logarithm of the minimum angle of resolution (logMAR) (Johnston, 1985). Counting fingers, hand movements, light perception, and no light perception were represented as logMAR 1.40, logMAR 2.70, logMAR 3.70, and logMAR 4.70, respectively (Herrero et al., 2025).

2.3.6 OCT analysis

The Cirrus high-definition OCT system (software version 3.0, model 4000; Carl Zeiss Meditec, Inc., Dublin, CA, USA) was utilized for OCT imaging. This instrument conducted real-time scans, achieving a rapid acquisition rate of 27,000 A-scans per second with an axial resolution of 5 microns. To evaluate retinal nerve fiber layer (RNFL) thickness, the optic disc cube protocol featuring a 3.4 mm-diameter circle centered on the optic disc was employed, and RNFL analysis protocols for both eyes (OU) were implemented. The software algorithm quantified RNFL thickness across the temporal, superior, nasal, and inferior quadrants, as well as twelve clock-hour sectors corresponding to positions from 1 o'clock to 12 o'clock. Furthermore, it computed an overall mean thickness for these quadrants. OCT reports from all participants were collected and analyzed retrospectively.

2.3.7 Statistics

Variations in pRNFL thickness were observed in both the NMOSD with ON and IDON cohorts across multiple retinal regions, independent of disease duration. Receiver operating characteristic (ROC) analysis was performed for each region to assess the diagnostic accuracy of pRNFL thickness in differentiating NMOSD-ON from IDON, quantified by the area under the curve (AUC). To evaluate the influence of disease duration on pRNFL thickness disparities between NMOSD-ON and IDON, generalized estimating equations (GEE) were utilized, with pRNFL thickness as the dependent variable, and disease type, duration, and their interaction as independent variables. Additionally, a Kruskal-Wallis test was employed to compare pRNFL thickness across varying disease durations, accounting for the non-parametric distribution of the data in both groups. Mann-Whitney U tests were conducted to compare pRNFL thickness between NMOSD-ON and IDON at different disease durations.

2.4 Results

2.4.1 Subject Demographics

This study included a total of 146 patients diagnosed with ON, accounting for 192 affected eyes. The mean age of participants was 40.3 ± 12.9years, with an average duration of symptoms recorded at 84.43 ± 244.61 days. The logMAR visual acuity was measured at 1.2 ± 1.17. Among the participants, 101 were female, representing 69.18% ***(Table 2.1)***.

Following allocation, the NEOD group comprised 74 eyes with NMOSD-ON and 57 eyes with IDON, while the EOD group included 14 NMOSD-ON eyes and 47 IDON eyes. In both the NEOD

and EOD groups, age and visual acuity were comparable between NMOSD-ON and IDON (all $p > 0.05$). Notably, the proportion of females in the NMOSD-ON subgroup of the NEOD cohort was significantly higher ($p = 0.006$). Conversely, the gender distribution was similar for both conditions within the EOD group (all $p > 0.05$) ***(Table 2.1)***.

Table 2.1 Demographic profiles of NMOSD-ON and IDON patients within the EOD and NEOD eyes

		NEOD			EOD		
		NMOSD-ON	IDON	p value	NMOSD-ON	IDON	p value
Subjects (N)		74	57	N/A	14	47	N/A
Sex (female in percentage)		83.7%	56.5%	0.006*	40.0%	73.2%	0.065
Age (years, mean ± SD)		42.4 ± 16.1	38.5 ± 10.8	0.172	40.7 ± 9.7	39.7 ± 11.3	0.800
LogMAR visual acuity of NMOSD-ON eyes (median, IQR)		1.4 (0.52 to 2.35)	1.4 (0.40 to 1.52)	0.157	1.4 (0.93 to 2.7)	1.0 (0.1 to 1.4)	0.139
Duration of diseases	Early (N)	22	13	N/A	11	27	N/A
	Middle (N)	22	24	N/A	3	20	N/A
	Late (N)	11	14	N/A	N/A	N/A	N/A
	End (N)	18	6	N/A	N/A	N/A	N/A

An asterisk (*) indicates a statistically significant difference ($p<0.05$, Mann-Whitney U test).

2.4.2 Differentiating NMOSD-ON from IDON in the cohort of all recruited eyes

The receiver operating characteristic (ROC) curve analysis of peripapillary retinal nerve fiber layer (pRNFL) thickness was conducted to distinguish between IDON and NMOSD-ON in NEOD eyes. Average pRNFL thickness were obtained and documented for the temporal, inferior, nasal, and superior quadrants surrounding the optic disc **(Table 2.2)**. The area under the curve (AUC) and corresponding p-values were calculated and are presented in **Table 2.2**. No specific regions in NEOD eyes demonstrated a significant ability to differentiate IDON from NMOSD-ON (All $p>0.05$). Furthermore, there was no notable difference in pRNFL thickness between IDON and NMOSD-ON across the various quadrants surrounding the optic disc in NEOD eyes **(Figure 2.2A and Table 2.2)**. Conversely, in EOD eyes, the temporal pRNFL thickness was identified as a reliable discriminator between IDON and NMOSD-ON, as indicated by the ROC curve ($p=0.018$, AUC=0.709) **(Figure 2.2B and Table 2.2)**. The optimal cut-off value was established at 87.5μm, yielding 100% sensitivity and 38.3% specificity, with a likelihood ratio of 1.621. In contrast, other quadrants exhibited limited discriminatory capacity between IDON and NMOSD-ON (All $p>0.05$) **(Table 2.2)**. Comparative analysis of pRNFL thickness across different sectors surrounding the optic disc in EOD eyes revealed significant thinning in the temporal quadrant ($p=0.017$), particularly at the 9 o'clock and 10 o'clock positions ($p=0.042$, $p=0.008$), in NMOSD-ON cases compared to IDON **(Figure 2.2C and Table 2.2)**.

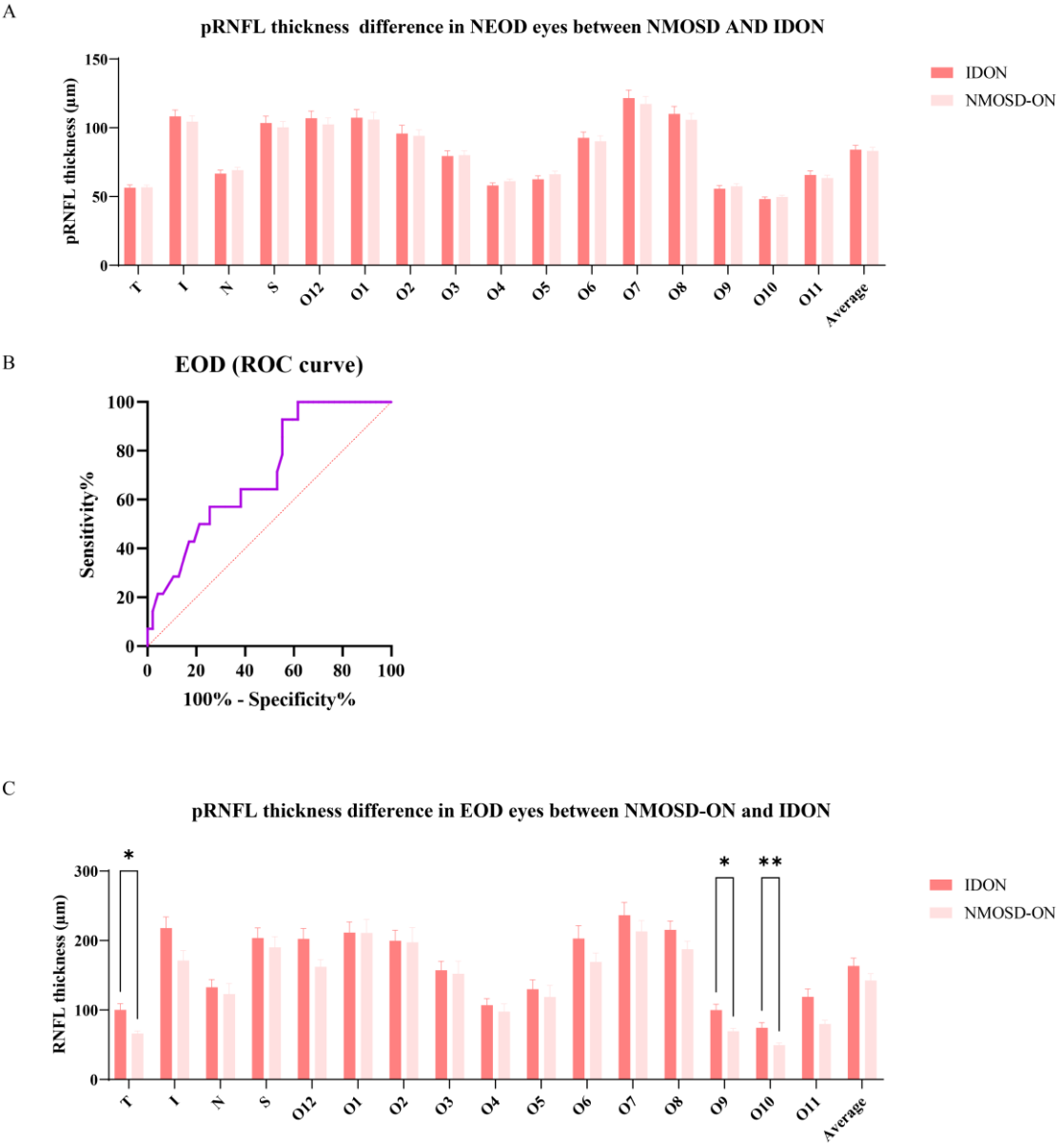

Figure 2.2 This study evaluated the discriminatory potential of peripapillary pRNFL measurements in differentiating IDON from NMOSD-ON using OCT, irrespective of disease duration. **(A)** NEOD Cases: A statistically significant reduction in pRNFL thickness was observed in NMOSD-ON compared to IDON. **(B)** In EOD cases, ROC curve analysis demonstrated moderate diagnostic accuracy in distinguishing the two conditions. **(C)** Further comparison revealed notable pRNFL thinning in NMOSD-ON relative to IDON.

Table 2.2 Measurement of pRNFL thickness (μm) across quadrants (Temporal, Inferior, Nasal, Superior) and twelve-o'clock sectors (O1 to O12) in all affected eyes within both NMOSD-ON and IDON cohorts. All values were expressed as median values with corresponding ranges (lower limit to upper limit).

NEOD eyes	NMOSD-ON	IDON	p value (pRNFL difference)	p value (AUC)
Temporal	54.00 (46.00 to 62.50)	54.00 (46.00 to 65.00)	0.784	0.782
Inferior	104.00 (73.00 to 125.25)	105.00 (85.50 to 125.00)	0.469	0.468
Nasal	65.00 (56.00 to 77.25)	62.00 (53.50 to 76.50)	0.397	0.396
Superior	95.50 (72.25 to 116.25)	106.00 (73.50 to 123.00)	0.548	0.790
12 o'clock	97.00 (68.00 to 124.25)	111.00 (74.00 to 138.50)	0.375	N/A
11 o'clock	58.50 (50.00 to 71.50)	60.00 (48.00 to 79.00)	0.717	N/A
1 o'clock	103.00 (67.00 to 135.25)	102.00 (76.00 to 131.00)	0.780	N/A
2 o'clock	87.00 (64.75 to 112.25)	97.00 (62.00 to 116.50)	0.979	N/A
3 o'clock	72.00 (60.00 to 95.00)	73.00 (59.00 to 96.00)	0.979	N/A
4 o'clock	59.50 (52.00 to 67.25)	56.00 (48.50 to 67.50)	0.221	N/A
5 o'clock	62.00 (52.75 to 74.50)	60.00 (48.00 to 74.00)	0.157	N/A
6 o'clock	82.00 (61.00 to 112.00)	91.00 (72.00 to	0.507	N/A

		113.00)		
7 o'clock	105.50 (76.00 to 157.50)	121.00 (91.50 to 146.00)	0.542	N/A
8 o'clock	102.00 (77.25 to 137.50)	107.00 (73.00 to 137.00)	0.643	N/A
9 o'clock	55.00 (45.00 to 66.25)	55.00 (41.00 to 65.50)	0.509	N/A
10 o'clock	50.00 (42.00 to 56.00)	48.00 (39.50 to 54.50)	0.315	N/A
Average pRNFL	83.00 (95.50 to 66.75)	83.00 (95.50 to 66.50)	0.791	N/A

EOD eyes	**NMOSD-ON**	**IDON**	**p value (pRNFL difference)**	**p value (AUC)**
Temporal	65.50 (56.25 to 79.25)	77.00 (66.00 to 119.00)		
Inferior	187.00 (141.00 to 216.00)	189.00 (147.00 to 255.00)	0.289	0.284
Nasal	110.00 (78.25 to 162.00)	107.00 (77.00 to 164.00)	0.976	0.973
Superior	199.50 (138.75 to 240.50)	173.00 (135.00 to 241.00)	0.796	0.546
12 o'clock	159.50 (122.75 to 192.25)	174.00 (135.00 to 243.00)	0.266	N/A
11 o'clock	79.00 (67.00 to 95.25)	93.00 (77.00 to 147.00)	0.072	N/A
1 o'clock	229.50 (134.00 to 267.00)	187.00 (125.00 to 276.00)	0.608	N/A
2 o'clock	206.50 (125.00 to 241.25)	173.00 (135.00 to	0.776	N/A

		240.00)		
3 o'clock	131.00 (101.00 to 197.00)	131.00 (99.00 to 204.00)	0.970	N/A
4 o'clock	93.50 (64.25 to 118.75)	82.00 (62.00 to 127.00)	0.936	N/A
5 o'clock	100.50 (70.00 to 169.25)	102.00 (76.00 to 143.00)	0.895	N/A
6 o'clock	179.50 (126.00 to 192.75)	175.00 (122.00 to 248.00)	0.829	N/A
7 o'clock	226.00 (156.00 to 248.25)	210.00 (166.00 to 286.00)	0.738	N/A
8 o'clock	185.50 (168.50 to 213.25)	193.00 (158.00 to 233.00)	0.567	N/A
9 o'clock	71.00 (60.75 to 82.00)	82.00 (67.00 to 112.00)	0.042*	N/A
10 o'clock	48.50 (39.00 to 57.25)	62.00 (48.00 to 79.00)	0.008*	N/A
Average pRNFL	154.50 (163.75 to 109.50)	133.00 (120.00 to 197.00)	0.719	0.712

The asterisk (*) denotes statistically significant disparities ($p<0.05$, Mann-Whitney U test).

2.4.3 Differentiating NMOSD-ON from IDON eyes based on pRNFL thickness variations across different disease durations (cross-sectional observation)

In the analysis utilizing the GEE model, the Wald chi-squared statistic indicated elevated values at the position of 12 o'clock (8.692, p=0.034), 2 o'clock (10.074, p=0.018), and 6 o'clock (10.151, p=0.017) for NEOD eyes **(Figure 2.3A)**.

In NEOD eyes, cross-sectional assessments demonstrated that the mean pRNFL thickness **(Figure 2.3B and Table 2.3)**, as well as the temporal, nasal, and superior pRNFL measurements in NMOSD-ON eyes, were consistent with those in IDON eyes across all stages (All p>0.05) **(Figure 2.3C and Table 2.3)**. However, the inferior pRNFL thickness in NMOSD-ON eyes was significantly lower than that in IDON eyes, achieving statistical significance (p=0.047) at the late stage. For other disease durations, no significant differences were observed in inferior pRNFL thickness between NMOSD-ON and IDON eyes **(Figure 2.3C and Table 2.3)**. More specifically, in the analysis across various twelve-hour sectors, the superior quadrant indicated that the 12 o'clock sector exhibited significant pRNFL thinning at the middle stage in NMOSD-ON compared to IDON in the cross-sectional analysis (p=0.046). No significant differences were noted at other timepoints or in other regions within the superior quadrant **(Figure 2.3D, Table 2.3)**. In the nasal quadrant, cross-sectional comparisons revealed significant pRNFL thinning in IDON compared to NMOSD-ON at 2 o'clock (p=0.037 for end stage) and 4 o'clock (p=0.046 for middle stage) **(Figure 2.3D, Table 2.3)**. In the inferior quadrant, pRNFL thickness was notably thinner at both 6 o'clock and 7 o'clock positions in NMOSD-ON compared to IDON in the cross-sectional observation (p=0.007, p=0.047 respectively)

in the late stage **(Figure 2.3D, Table 2.3)**. In the temporal regions, no significant differences were observed at 8 o'clock, 9 o'clock, or 10 o'clock **(Figure 2.3D, Table 2.3)**.

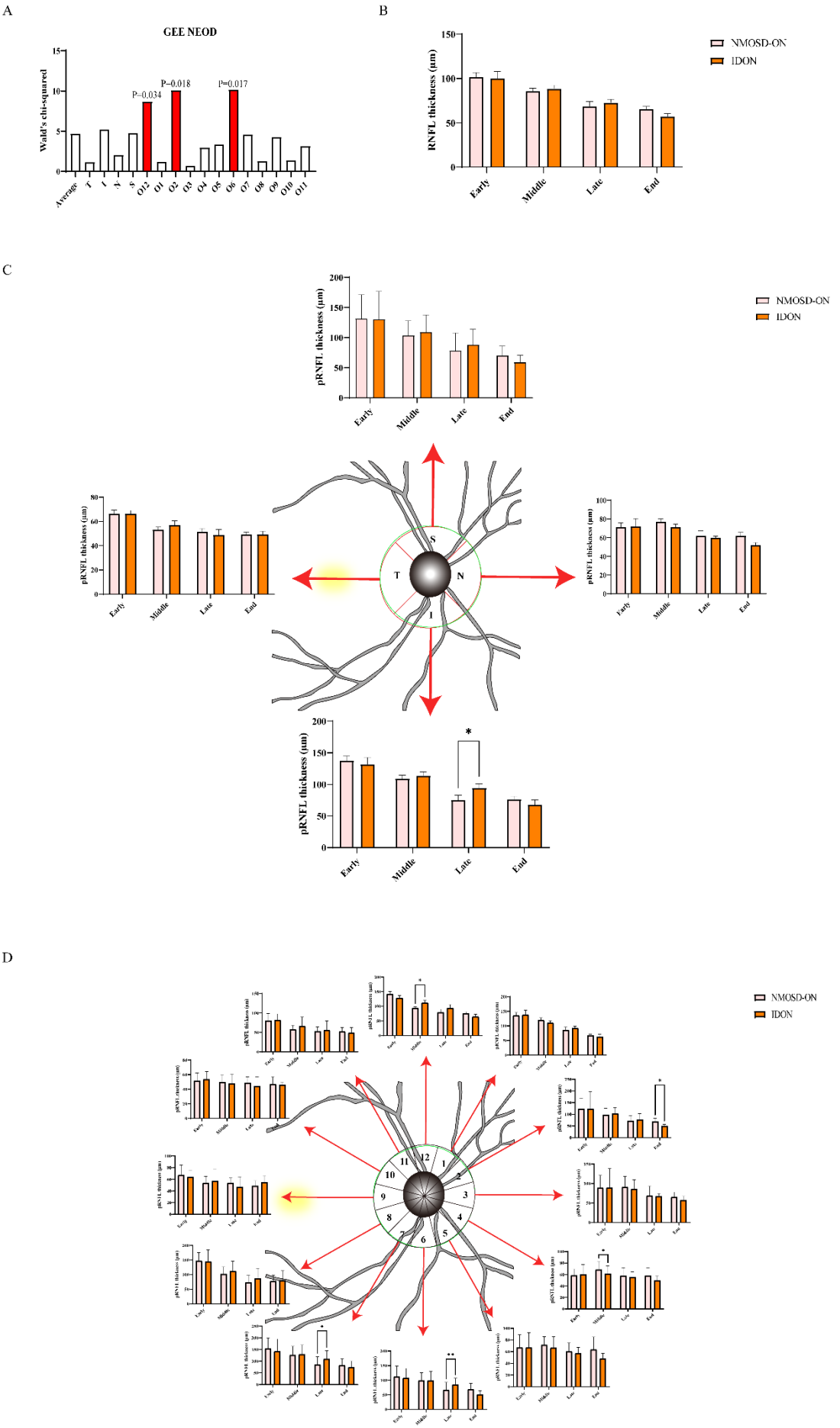
A
GEE NEOD
Wald's chi-squared
P=0.034
P=0.018
P=0.017
Average
T
I
N
S
O12
O1
O2
O3
O4
O5
O6
O7
O8
O9
O10
O11
B
RNFL thickness (μm)
NMOSD-ON
IDON
Early
Middle
Late
End
C
pRNFL thickness (μm)
NMOSD-ON
IDON
S
T
N
I
*
D
NMOSD-ON
IDON
12
1
2
3
4
5
6
7
8
9
10
11

Figure 2.3 The study employed cross-sectional OCT to compare pRNFL thickness profiles between IDON and NMOSD-ON patients with NEOD, stratified by disease progression phases. **(A)** A generalized estimating equations approach examined potential confounding effects of disease duration on the discriminative capacity of pRNFL in NEOD cases. **(B)** Comparative analysis revealed statistically significant differences in mean pRNFL measurements, with NMOSD-ON demonstrating more pronounced axonal loss compared to IDON counterparts. **(C)** Regional assessment across four standard quadrants and twelve clock-hour sectors identified distinct spatial thinning patterns, providing potential anatomical markers for clinical differentiation.

Table 2.3 Measurement of pRNFL thickness (μm) across quadrants—temporal, inferior, nasal, and superior—in NEOD eyes within both NMOSD-ON and IDON cohorts. Cross-sectional analysis presented as median values with range (lower to upper limit), stratified by disease duration.

		Duration	NMOSD-ON	IDON	p value
NEOD	Average	Early	96.00 (87.00 to 114.00)	92.00 (83.00 to 110.00)	0.808
		Middle	86.00 (76.75 to 97.25)	89.00 (80.75 to 100.50)	0.971
		Late	64.00 (54.00 to 80.00)	70.00 (62.25 to 82.25)	0.749
		End	65.00 (55.50 to 73.50)	56.50 (50.50 to 62.00)	0.211
	Temporal	Early	66.50 (55.00 to 76.25)	63.00 (56.50 to 77.00)	0.913
		Middle	52.00 (45.75 to 59.25)	52.00 (46.00 to 69.75)	0.530
		Late	52.00 (41.00 to 59.00)	47.50 (35.75 to 52.50)	0.509
		End	50.00 (41.50 to 56.75)	48.50 (45.75 to 52.00)	0.504
	Inferior	Early	133.50 (114.25 to 156.75)	122.00 (105.00 to 147.00)	0.745
		Middle	112.00 (90.00 to 125.00)	113.00 (96.50 to 132.00)	0.933
		Late	69.00 (57.00 to 86.00)	94.00 (73.25 to 118.50)	0.047*
		End	71.50 (64.00 to 88.50)	66.00 (52.25 to 79.50)	0.699
	Nasal	Early	70.00 (56.75 to 76.25)	67.00 (53.00 to 79.00)	0.999
		Middle	78.00 (64.75 to 91.75)	74.50 (54.50 to 86.00)	0.765
		Late	57.00 (50.00 to 63.00)	60.50 (54.75 to 63.00)	0.435
		End	59.00 (52.75 to 67.50)	52.50 (43.75 to 59.25)	0.336
	Superior	Early	122.00 (107.50 to 151.25)	123.00 (101.00 to 157.50)	0.990
		Middle	104.00 (85.50 to 113.00)	110.00 (86.50 to 126.00)	0.344
		Late	65.00 (62.00 to 104.00)	80.00 (66.50 to 110.25)	0.435
		End	68.00 (56.75 to 81.50)	57.00 (50.25 to 68.75)	0.336

The asterisk (*) denotes statistically significant disparities ($p<0.05$, Mann-Whitney U test).

From the perspective of EOD eyes, the GEE model revealed that the Wald chi-squared statistic peaked at the 1 o'clock position, with a recorded value of 4.050 and a significance level of p=0.044 **(Figure 2.4A)**.

During the middle stage of the disease (beyond 30 days), the thickness reduction in average pRNFL thickness in NMOSD-ON was significantly greater than in IDON (p=0.044) **(Figure 2.4B)**. No significant differences were observed in localized quadrants (temporal, inferior, nasal, superior) across various timepoints (All p>0.05) **(Figure 2.4C, and Table 2.4)**.

In more precise terms, the pRNFL thickness in both conditions (IDON and NMOSD-ON) appeared comparable across all clock hour sectors, with the exception of the 8 o'clock position, which exhibited thinning in NMOSD-ON compared to IDON at more than 30 days in the cross-sectional comparisons (p=0.035) **(Figure 2.4D and Table 2.4)**.

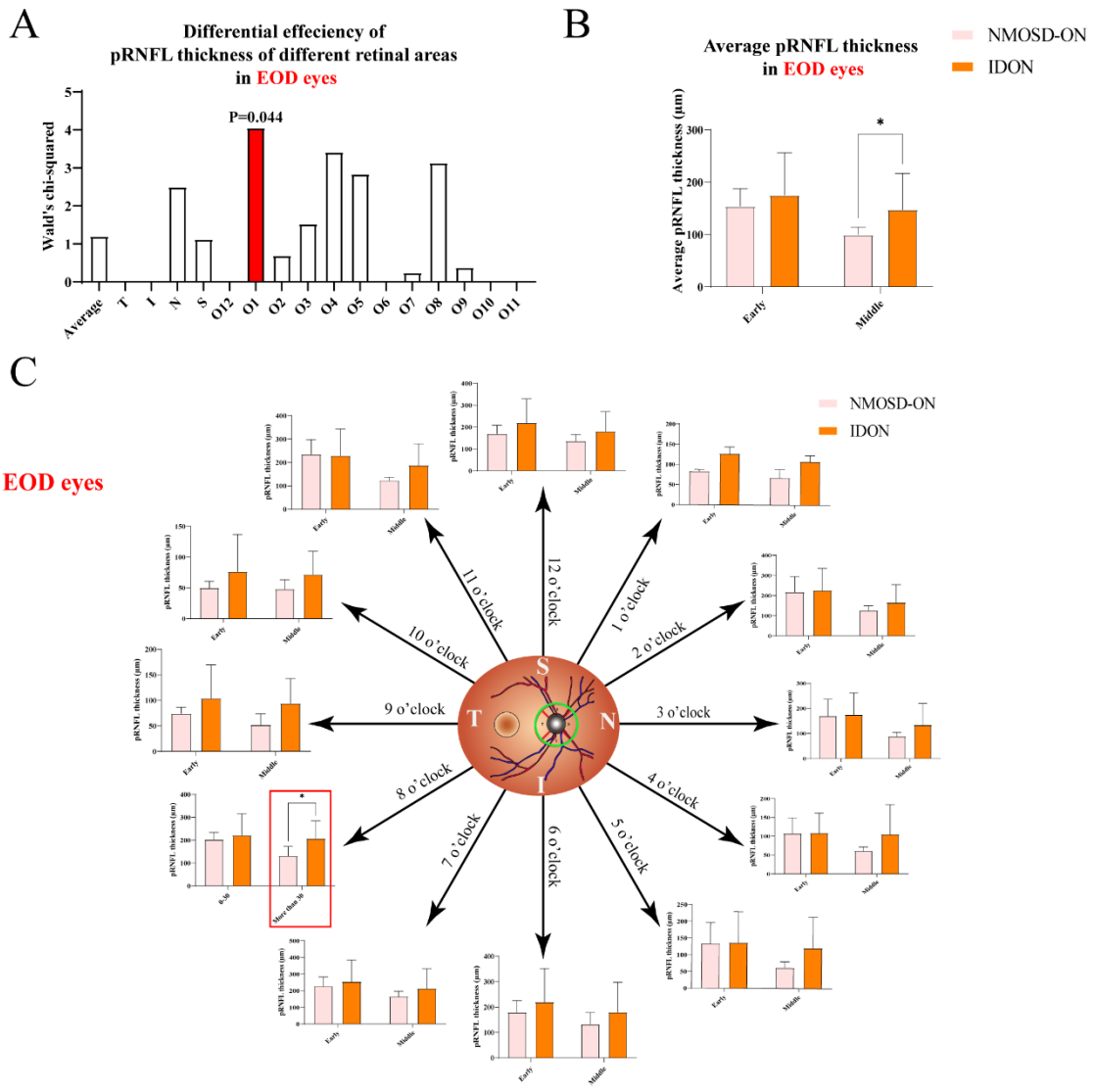

Figure 2.4 Cross-sectional evaluation of pRNFL thickness in IDON versus NMOSD-ON across different stages of disease in eyes with EOD. **(A)** Generalized estimating equations (GEE) model analysis of the impact of disease duration on the differentiation of IDON and NMOSD-ON based on pRNFL thickness in EOD eyes. **(B)** Mean pRNFL thickness disparity between IDON and NMOSD-ON in EOD eyes. **(C)** Sectoral pRNFL thickness differences across four quadrants and clock-hour sectors between IDON and NMOSD-ON in EOD eyes. OCT: optical coherence tomography; ROC: receiver operating characteristic; EOD: edematous optic disc. An asterisk denotes statistically significant differences.

Table 2.4 Measurement of pRNFL thickness (μm) across quadrants—temporal, inferior, nasal, superior—in EOD eyes within both NMOSD-ON and IDON cohorts. Cross-sectional analysis presented as median values with range (lower to upper limit), stratified by disease duration.

		Duration	NMOSD-ON	IDON	p value
EOD	Average	Early	157 (121 to 172)	150 (118 to 210)	0.830
		Middle	102 (84 to 112)	127 (120 to 150.25)	0.044*
	Temporal	Early	67 (60 to 79)	84 (69 to 119)	0.091
		Middle	52 (34 to 81)	74.5 (63 to 116)	0.180
	Inferior	Early	210 (148 to 216)	207 (146 to 289)	0.336
		Middle	141 (115 to 172)	185.5 (149.25 to 218.5)	0.139
	Nasal	Early	128 (87 to 171)	140 (88 to 176)	0.968
		Middle	73 (58 to 80)	104 (65.5 to 110)	0.257
	Superior	Early	221 (164 to 245)	193 (143 to 280)	0.770
		Middle	129 (114 to 142)	159.5 (123.25 to 212.5)	0.304

The asterisk (*) denotes statistically significant disparities ($p<0.05$, Mann-Whitney U test).

2.4.4 Differentiating NMOSD-ON from IDON through monitoring the progressive thinning in pRNFL thickness

The rate of change over the duration of the disease in both NMOSD-ON and IDON eyes is depicted in Figure 4 (NEOD eyes) and Figure 5 (EOD eyes).

In NEOD eyes, the average pRNFL thickness in NMOSD-ON eyes exhibited a significant decrease at the middle stage compared to the early stage (-10.42%, p=0.014) and a further reduction at the late stage compared to the middle stage (-25.58%, p=0.006) **(Figure 2.5A, and Table 2.5)**. Additionally, a significant decline in average pRNFL thickness in IDON eyes was observed in the late stage relative to the middle stage (-21.35%, p=0.016) and in the end stage compared to the late stage (-19.29%, p=0.048) **(Figure 2.5A, and Table 2.5)**. This indicates a delayed thinning of average pRNFL thickness in IDON eyes compared to NMOSD-ON in NEOD eyes **(Figure 2.5A,**

and Table 2.5). Notably, the significant reduction in temporal pRNFL thickness occurred simultaneously in both NMOSD-ON and IDON (middle stage versus early stage, with p=0.006 for NMOSD-ON and p=0.004 for IDON) **(Figure 2.5B and Table 2.5)**. The substantial reduction in pRNFL thickness was observed earlier in both the inferior (middle stage compared to early stage, and late stage compared to middle stage, with p=0.003 and p=0.001 respectively) and superior quadrants (middle stage compared to early stage, and late stage compared to middle stage, with p=0.012 and p=0.015 respectively) among NMOSD-ON patients **(Figure 2.5B and Table 2.5)**. In the superior region of IDON, significant thinning of pRNFL thickness was noted in the late stages of the disease (late stage compared to middle stage, and end stage compared to late stage, p=0.041 and p=0.009, respectively). In contrast, the pRNFL thickness in the inferior region of IDON eyes remained relatively stable over time, showing no significant thinning between adjacent timepoints (All p>0.05) **(Figure 2.5B)**. The nasal quadrant exhibited progressive thinning only in IDON (late stage compared to middle stage, end stage compared to late stage, with p=0.042 and p=0.037, respectively) but not in NMOSD-ON **(Figure 2.5B)**. The early reduction of pRNFL thickness in NMOSD-ON was evident at the 12 o'clock position (p<0.001, middle stage compared to early stage) and at 1 o'clock (p=0.013, late stage compared to middle stage). Conversely, the late thinning in pRNFL thickness in IDON occurred at the 1 o'clock position (p=0.005, end stage compared to late stage) **(Figure 2.5C, Table 2.5)**. The earliest thinning timepoints for pRNFL thickness were consistent, occurring at the middle stage compared to the early stage in both NMOSD-ON and IDON at the 11 o'clock position **(Figure 2.5C, Table 2.5)**. The thinning of the pRNFL in NMOSD occurs earlier at the 2 o'clock position, indicating a middle stage compared to the early stage, with statistical significance (p=0.042), and a late stage compared to the middle stage (p=0.009). Conversely, in

IDON, the reduction in pRNFL thickness exhibited a delayed thinning at the 2 o'clock position, with significant differences noted between the late stage and middle stage (p=0.014) and between the end stage and late stage (p=0.015). Notably, the earlier thinning of pRNFL at the 3 o'clock position was exclusively observed in IDON eyes (p=0.010). The findings regarding pRNFL thickness at the 4 o'clock position are particularly noteworthy, as it remained relatively stable over time in both conditions, showing no significant reduction. However, a significant thickening of pRNFL was recorded in NMOSD-ON when comparing the middle stage to the early stage (p=0.017) **(Figure 2.5C, Table 2.5)**. Longitudinal analysis revealed significant early pRNFL thinning at the 7 o'clock position in NMOSD-ON (p=0.023, comparing the middle stage to the early stage). Further thinning was noted at the 5 o'clock, 6 o'clock, and 7 o'clock positions in NMOSD-ON (p=0.046, p=0.002, p=0.005, respectively). In IDON, the reduction in pRNFL thickness began later at the 6 o'clock and 7 o'clock positions (p=0.012, p=0.030, respectively) **(Figure 2.5C, Table 2.5)**. At the early stage, pRNFL thickness was reduced at the 8 o'clock position in both diseases (NMOSD-ON, p<0.001; IDON, p=0.011). The early thinning of pRNFL thickness at the 9 o'clock position was observed solely in NMOSD-ON (p=0.012), without notable change in IDON (p>0.05). No temporal changes were detected in either NMOSD-ON or IDON at the 10 o'clock position **(Figure 2.5C, Table 2.5)**.

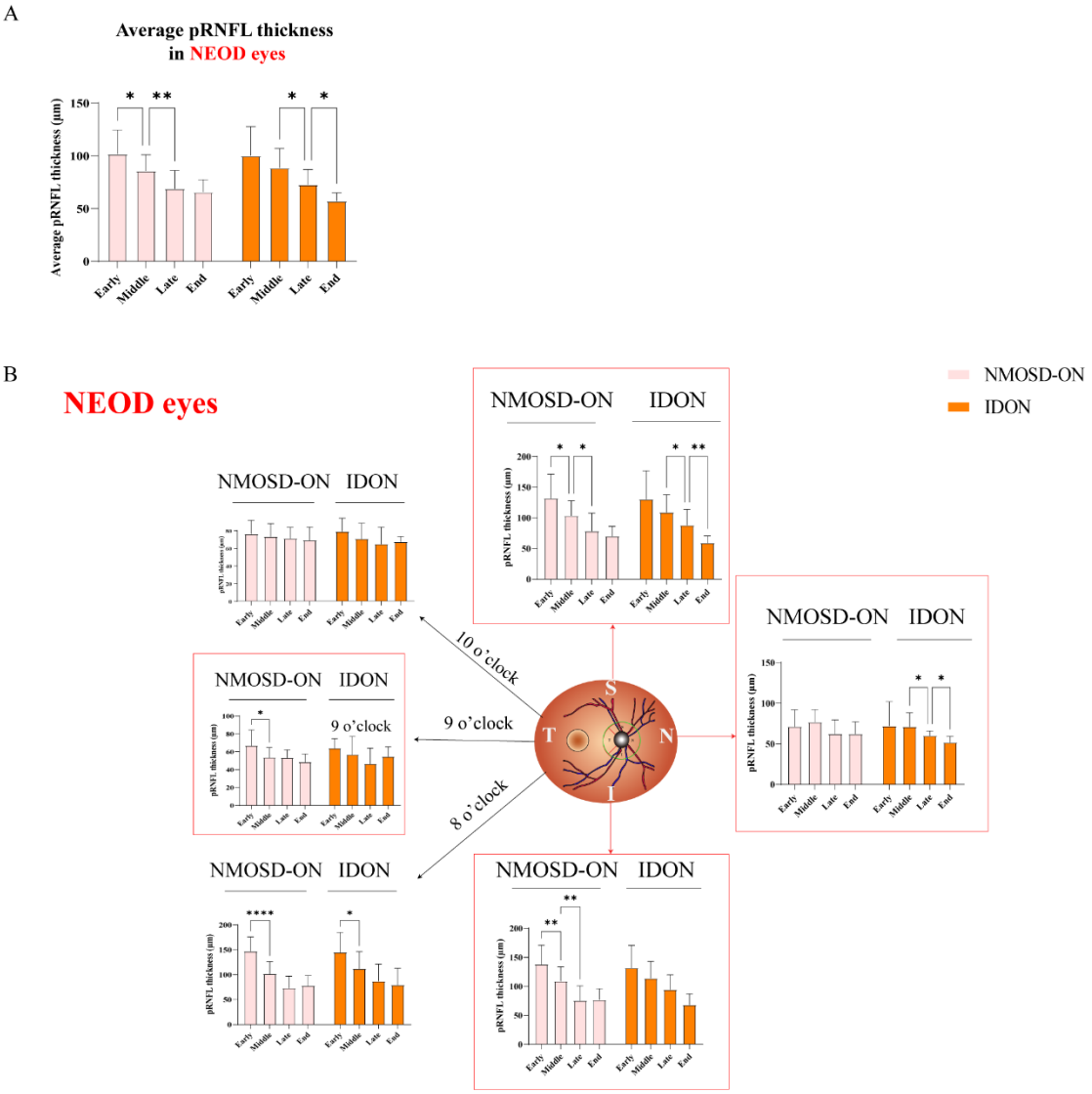

Figure 2.5 This investigation characterized Longitudinal pRNFL Thinning Patterns (Comparisons between adjacent phases) in IDON and NMOSD-ON through serial OCT measurements of NEOD cases. **(A)** Comparative analysis of consecutive timepoints revealed significantly greater progressive pRNFL attenuation in NMOSD-ON versus IDON, suggesting more aggressive axonal degeneration. **(B)** Sector-Specific Degeneration Patterns. OCT mapping demonstrated distinct quadrantal and clock-hour sector thinning profiles, with NMOSD-ON showing more diffuse involvement across all sectors, accelerated superior and inferior quadrant loss , and earlier temporal sector involvement compared to IDON.

In eyes with EOD, the gradual attenuation of edema in the averaged pRNFL thickness and in the four quadrants surrounding the optic disc remained undetectable, as no significant differences were found between adjacent disease durations (middle stage compared to early stage) in both IDON and NMOSD-ON (all $p>0.05$) **(Figure 2.6A and B, Table 2.5)**. When examining temporal changes in both conditions, the oedematous state of pRNFL thickness did not significantly decrease across all clock-hour sectors (all $p>0.05$), with the exception of the 2 o'clock sector in IDON (middle stage compared to early stage, $p=0.039$) **(Figure 2.6C, Table 2.5)**.

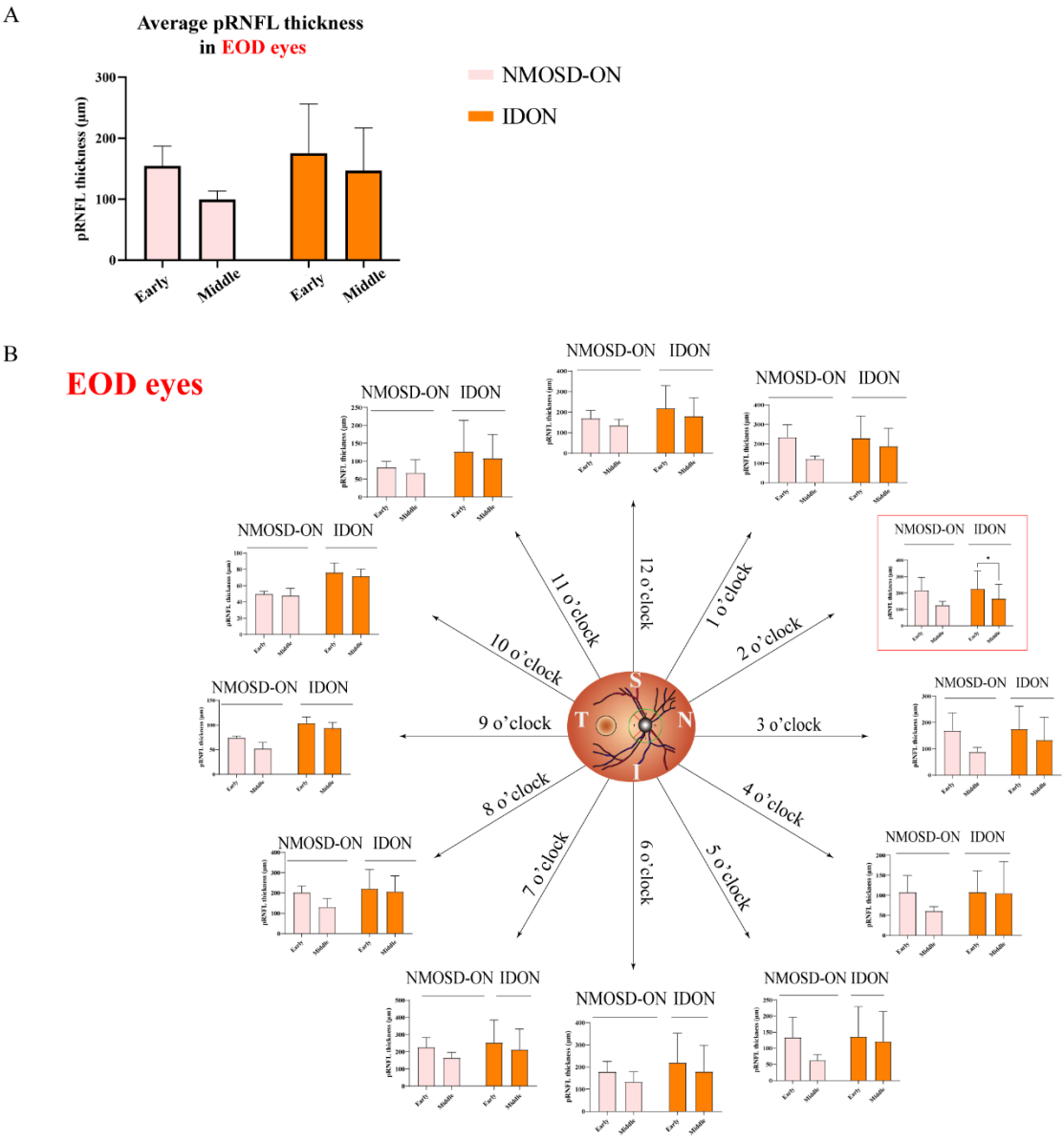

Figure 2.6 Progressive evaluation of pRNFL thickness in eyes with early-onset demyelinating optic neuropathy (EOD eyes) involved comparisons between consecutive time phases in both IDON and NMOSD-ON. **(A)** The observed progressive reduction in mean pRNFL thickness in IDON and NMOSD-ON EOD eyes. **(B)** The sectoral (clock hours) analysis of pRNFL thinning across the four quadrants and clock-hour sectors in IDON and NMOSD-ON EOD eyes.

Table 2.5 Assessment of pRNFL thinning across quadrants (temporal, inferior, nasal, superior) and retinal sectors (O12 to O1) in NEOD and EOD eyes within NMOSD-ON and IDON cohorts. All values were expressed as median percentage reduction relative to previous measurements, with ranges denoting lower and upper limits.

	NEOD eyes						**EOD eyes**	
	NMOSD-ON			IDON			NMOSD-ON	IDON
	Middle	Late	End	Middle	Late	End	Middle	Middle
Average	-10.42%*	-25.58%*	1.56%	-3.26%	-21.35%*	-19.29%*	-35.03%	-15.33%
Temporal	-21.80%*	1.96%	-3.85%	-17.46%*	-8.65%	2.11%	-22.39%	-11.31%
Inferior	-16.10%*	-38.39%*	3.62%	-7.38%	-16.81%	-29.79%	-32.86%	-10.39%
Nasal	11.43%	-26.92%	3.51%	11.19%	-18.79%*	-13.22%*	-42.97%	-25.71%
Superior	-14.75%*	-37.50%*	4.62%	-10.57%	-27.27%*	-28.75%*	-41.63%	-17.36%
12 o'clock	-32.13%*	-23.40%	-6.94%	-9.13%	-32.31%	-22.58%	-19.64%	-20.10%
11 o'clock	-32.93%*	-7.27%	5.88%	-24.36%*	-14.41%	-6.93%	-39.53%	-2.66%
1 o'clock	-4.37%	-44.40%*	-10.45%	-18.32%	-13.55%	-42.70%*	-50.21%	-17.51%
2 o'clock	-16.74%*	-34.39%*	4.84%	-2.97%	-31.12%*	-27.41%*	-48.21%	-11.17%*
3 o'clock	8.54%	-31.46%	6.56%	4.60%	-23.08%*	-17.14%	-53.26%	-29.11%
4co'clock	17.09%*	-19.71%	2.73%	0.89%	1.77%	-9.57%	-40.82%	-24.49%
5 o'clock	15.45%	-22.54%*	5.45%	5.56%	-16.54%	-13.51%	-50.45%	-18.10%
6 o'clock	2.48%	-44.93%*	8.77%	-2.08%	-9.57%	-39.41%*	-34.43%	-9.46%
7 o'clock	-19.18%*	-44.75%*	9.15%	3.52%	-21.51%	-33.65%*	-32.08%	-15.67%
8 o'clock	-31.99%*	37.62%	21.43%	-22.38%*	-34.23%	-11.64%	-30.81%	-1.81%
9 o'clock	-22.22%*	2.86%	-15.74%	-18.46%	-20.75%	32.14%	-24.66%	-9.41%
10 o'clock	-7.77%	5.26%	-6.00%	-6.86%	-17.89%	15.38%	-2.04%	3.28%

The asterisk (*) indicates statistically significant differences ($p<0.05$, Kruskal-Wallis test).

2.5 Discussion

To the best of my knowledge, this is the first study using OCT to measure the diverse four quadrants and twelve-hour sectors of pRNFL thickness, comparing NMOSD-ON and IDON. This research was observed from two perspectives: first, a cross-sectional analysis to understand the differences in pRNFL thickness between the two diseases over various time courses. Second, it examines the differences in pRNFL thickness at different timepoints for NMOSD-ON and IDON separately to infer trends in pRNFL thickness over time. Overall, we compare the trends and rates of thinning in pRNFL thickness for both diseases. This approach may allow us to preliminarily classify patients with first-episode ON as typical or atypical based on their disease course. Subsequently, by monitoring the deterioration trends of pRNFL thickness in specific areas, we can identify which type of ON they are likely experiencing and select the most appropriate treatment as quickly as possible.

In this investigation, we utilized ROC curves to assess the discriminative efficacy of pRNFL thickness across various retinal regions in patients with NMOSD-ON or IDON, without considering the disease duration. Our findings demonstrated that the temporal retinal region was particularly effective in distinguishing NMOSD-ON from IDON, in contrast to other regions in EOD eyes and all regions in NEOD eyes. This suggests that the temporal region may hold unique diagnostic significance warranting further exploration. The lack of differentiation in other regions, particularly for NEOD eyes, highlights the need for targeted evaluations based on specific disease durations. Our preliminary analysis, employing the GEE model, indicated that the differences in pRNFL

thickness between the two conditions at the 12, 2, and 6 o'clock positions in NEOD eyes, as well as at the 1 o'clock position in EOD eyes, may be significantly influenced by disease duration. This observation emphasizes the complexity of analyzing pRNFL metrics and suggests that disease duration must be carefully considered in diagnostic processes. To facilitate further differentiation, we categorized participants based on their disease durations for more comprehensive examinations.

The examination of the progressive thinning trend in the neuro-ophthalmic eyes revealed that both superior and inferior pRNFL thickness decreased earlier in the disease progression of NMOSD-ON eyes. In contrast, IDON exhibited progression in these regions at a later stage. Notably, nasal pRNFL thickness in IDON began to show progressive thinning from the middle stage onward, while NMOSD-ON maintained stability in this area. Early deterioration was observed in both conditions within the temporal sector. A comprehensive analysis across twelve o'clock-hour sectors highlighted a significant thinning trend at the 12 o'clock and 1 o'clock positions, adjacent to the nasal quadrant in NMOSD-ON. Simultaneously, both conditions demonstrated concurrent thinning at the 11 o'clock position, closer to the temporal quadrant. Observations regarding the thinning of pRNFL thickness in the inferior quadrant indicated similar patterns of change. In NMOSD-ON, progressive thinning occurred earlier, subsequently affecting the 5 o'clock, 6 o'clock, and 7 o'clock positions. Conversely, IDON primarily exhibited thinning later, particularly at the 6 o'clock and 7 o'clock positions, nearer to the temporal quadrant. The clock hour analysis of the nasal area revealed some discrepancies; NMOSD-ON progressed earlier at 2 o'clock, while IDON showed earlier thinning at 3 o'clock. The pRNFL thickness in the nasal-inferior region (4 and 5 o'clock) appeared more vulnerable to earlier thinning in IDON. Meanwhile, NMOSD-ON demonstrated an increase in

pRNFL thickness during mid-stage compared to the early stage, a phenomenon that may be associated with potential axonal swelling conditions.

2.6 Conclusion

Early OCT findings reveal that in NEOD eyes, NMOSD-ON is characterized by pronounced and rapid thinning of pRNFL thickness in the superior and inferior quadrants, distinguishing it from typical ON. In contrast, EOD eyes with NMOSD-ON may exhibit nasal-inferior thickening, likely due to inflammatory processes. These patterns could help differentiate NMOSD-ON from IDON at an early stage.

Chapter 3 Development of an optimized NMOSD-ON animal model

3.1 Introduction and literatures review

The complexity of NMOSD necessitates the use of animal models, which play an indispensable role in elucidating the underlying pathophysiological mechanisms of the disease. These models are instrumental in understanding NMOSD's etiology and in the development of new therapeutic agents.

3.1.1 Previous NMOSD animal model

One NMOSD model is based on Experimental Autoimmune Encephalomyelitis (EAE), which serves as an animal model for MS and effectively simulates various phenotypes associated with the disease. This model allows for the delivery of myelin-derived proteins or peptides in conjunction with an adjuvant to induce active immunity within the animal's system. Alternatively, one can directly administer myelin-specific CD4+ T lymphocytes to the animal to induce passive immunity. Both methodologies have proven successful in establishing EAE (Robinson et al., 2014). It was widely acknowledged that the primary challenge in developing an animal model for NMOSD lies in the integrity of the BBB. The AQP4-IgG we aimed to deliver is a large molecule that cannot penetrate this barrier. Therefore, we must consider strategies to weaken the BBB. The EAE model presents a viable solution, as it is characterized by a significantly compromised BBB. Once the barrier is sufficiently weakened, we can perform intraperitoneal injections from the periphery to deliver AQP4-IgG. This approach results in heightened neurological inflammation and demyelination, closely mirroring the pathological features observed in NMOSD (H. Saini et al.,

2013). Another approach involves Ultrasound-Mediated BBB Opening for the delivery of AQP4-IgG. This cutting-edge technique employs the ultrasound employed with low frequency to achieve a reversible opening of the BBB in EAE mice. This process facilitates the peripheral injection of AQP4-IgG and complement, enabling their entry into the central nervous system. Notably, this model necessitates a considerably lower dosage of AQP4-IgG to elicit the characteristic NMOSD pathology in both the thoracic spine and optic nerve. However, it is essential to utilize the EAE model, as it is a critical step in demonstrating the weakening of the BBB. If the objective is to deliver AQP4-IgG from the periphery to induce NMOSD, it is imperative to first establish the EAE model (Luo et al., 2020; Xiang et al., 2021).

In another animal model, the localized administration of AQP4-IgG has the potential to replicate the characteristics of this disease within the cerebral environment of animal models. To effectively simulate the encephalitis associated with NMOSD, both intraventricular and intracerebral injections of AQP4-IgG, in conjunction with complement components, were conducted. This approach can elicit hallmark NMOSD-like pathological alterations, which encompass the depletion of AQP4 and GFAP, demyelination and leukocyte infiltration. However, it is important to note that the mere delivery of AQP4-IgG is insufficient, as the complement system in mice is not sufficiently active. Therefore, it is imperative to concurrently administer human complement to achieve the desired pathological effects (Saadoun et al., 2010). However, the use of human complement in the rat model is unnecessary. Even when AQP4-IgG is delivered in isolation, we can still observe the loss of AQP4 and GFAP within the rat brain. This finding provides compelling evidence that the complement system in rats can indeed be activated, highlighting the relevance of this model in studying the

underlying mechanisms of NMOSD.

The localization of injections and the delivery of AQP4-IgG in the optic nerve present unique challenges due to the anatomical structure of the optic nerve, which is enveloped by the meninges. Direct delivery of AQP4-IgG into the meninges may hinder the interaction between AQP4-IgG and the optic nerve, complicating the establishment of a reliable model for research. Consequently, existing studies have employed a technique involving access through the conjunctival fornix, utilizing blunt dissection to expose the optic nerve, followed by the administration of AQP4-IgG. This method has proven effective in successfully modeling the condition, allowing for the observation of functional impairments associated with the disease (Y. Matsumoto et al., 2014; Zhang et al., 2018).

3.1.2 Limitations of existing NMOSD animal models

Currently, there are numerous limitations associated with animal models of NMOSD. First, it involves systematic modeling, where peripheral delivery of AQP4-IgG allows it to cross the pre-weakened BBB and attack the optic nerve within the CNS (Redler & Levy, 2020) ***(Figure 3.1)***.

One significant issue arises from the use of the EAE model (H. Saini et al., 2013). It is well established that the EAE model inherently induces demyelination and ultimately leads to axonal loss (Harleen Saini et al., 2013). However, it remains unclear whether the demyelination observed is a consequence of astrocyte damage induced by AQP4-IgG or if it is primarily due to the EAE model itself. This uncertainty restricts the applicability of the EAE model in the application of NMOSD research (Duan & Verkman, 2020; Harleen Saini et al., 2013).

An alternative approach may involve the passive immunization method through direct injection of AQP4-IgG into the CNS of mice ***(Figure 3.1)***, which circumvents the need to weaken the BBB as required in EAE models (Duan & Verkman, 2020; Yao & Verkman, 2017; Yick et al., 2018). Direct CNS injection effectively bypasses the BBB, allowing for a more targeted investigation (Harleen Saini et al., 2013; Yao & Verkman, 2017; Yick et al., 2018). However, if the injection is performed in the cerebral cortex or specific brain regions (Harleen Saini et al., 2013; Yao & Verkman, 2017; Yick et al., 2018), it may inadvertently create a model of encephalitis rather than accurately reflecting NMOSD pathology, which predominantly affects the optic nerve and spinal cord. The tissue specificity of NMOSD underscores the importance of focusing our research on the optic nerve and spinal cord, as this could yield more meaningful insights. Moreover, when injecting into brain regions, the insertion of the injection needle may cause localized damage, potentially triggering inflammatory responses. This raises concerns about whether such damage could activate microglia and astrocytes, which we have observed in the context of AQP4 loss. Our primary interest lies in the processes of demyelination and axonal degeneration, as these phenomena are directly linked to behavioral outcomes. Additionally, the model involving localized delivery of AQP4-IgG to the optic nerve presents its own set of limitations (Zhang et al., 2018). Utilizing a conjunctival approach to expose the anterior optic nerve necessitates the removal of the meninges, which introduces a significant risk of optic nerve injury during the surgical procedure. Furthermore, the damage to the meninges raises the question of whether such injury could predispose the optic nerve to degeneration, given the protective and supportive role that the meninges play in maintaining optic nerve integrity. Finally, it is essential to note that NMOSD-ON does not frequently occur in the anterior segment of

the optic nerve; rather, it predominantly manifests in the posterior segment of the optic nerve (Chen et al., 2015; Huda et al., 2019; Khanna et al., 2012; Kim et al., 2015). This distinction is critical for understanding the pathophysiology and clinical implications of NMOSD-ON, as the posterior optic nerve involvement may lead to different visual outcomes and necessitate tailored therapeutic approaches.

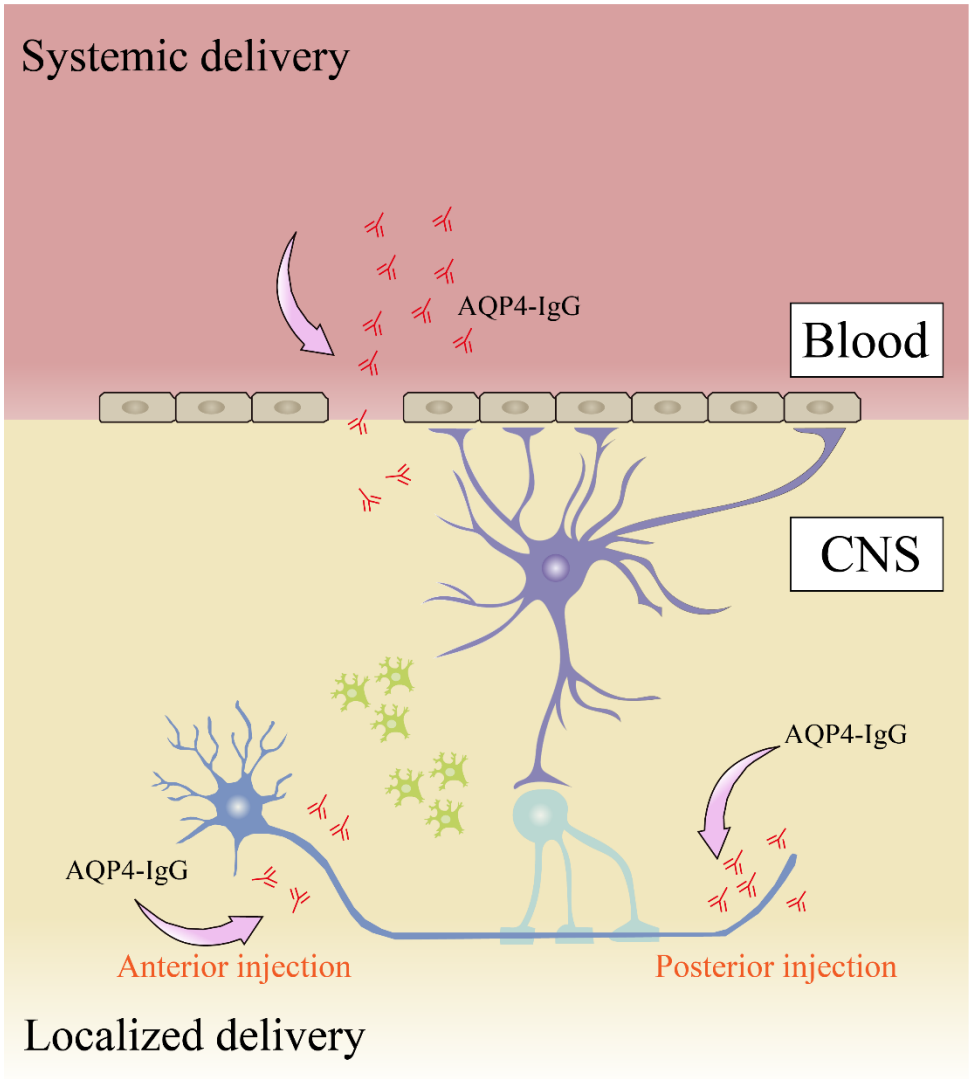

Figure 3.1 The diagram illustrates different animal models of NMOSD-ON established by different established approaches.

A summary of the key characteristics of current mainstream NMOSD-ON animal models is in **Table 3.1**.

Table 3.1 Previous NMOSD-ON animal model characteristics.

Delivery	*Animal*	*characteristics*	*Strength*	*limitation*	*Reference*
Systemic delivery	C57/BL 6 mice	AQP4-IgG delivery after EAE establishment; AQP4 loss and neutrophil infiltration	The operation is straightfor ward and has no technical learning barrier.	With the BBB compromised, peripheral drug trials may show bias, and the myelin sheath could be damaged due to EAE modeling, leading to unreliable experimental results. Demyelination may not necessarily be a consequence of astrocyte damage.	Saini *et al* (H. Saini et al., 2013)
	C57/BL 6 mice	T cell delivery	The process of T cell-induced antibody production by B cells can be simulated.	No destruction of AQP4 and astrocyte was noted.	Sagan *et al (Sagan et al., 2016)*
	C57/BL 6 mice	AQP4-IgG delivery; puls-ed focused ultrasound faci -litate the AQP4-IgG access to CNS	Destructio n of AQP4 and astrocyte	Technical support and potential ultrasound-related injury	Yao *et al* (Yao et al., 2019)
Anterior optic nerve delivery	SD rats	AQP4-IgG delivery; AQP4 loss and astrocyte damage (week 2), demyelination	There is direct contact between the antigen and antibody,	Meningeal stripping may lead to inflammation of the optic nerve, and NMOSD-ON is more commonly seen in the posterior optic nerve.	Matsumoto Y *et al (Yoshiko Matsumoto et al., 2014)*

		and axonal degeneration (week 4)	and secondary demyelination and degeneration of retinal ganglion cells (RGCs) have been observed.		
	SD rats	AQP4-IgG delivery ;AQP 4 loss and astrocyte damage	Comprehensive timeframe with functional recordings		Zhang *et al*(Zhang et al., 2018)
	Lewis rats	AQP4-IgG (E5415A) delivery	The animal is available for Minocycline treatment test		Morita et al (Yuko Morita et al., 2022)
Posterior optic nerve delivery	C57/BL 6 mice	AQP4-IgG (rab53) delivery; AQP4 loss and astrocyte damage	Direct antigen-antibody interaction	There is a lack of a complete timeline framework, and the implantation of the osmotic pump has led to significant inflammation due to foreign body rejection.	Asavapanumas *et al (Asavapanumas, Ratelade, Papadopoulos, et al., 2014)*

3.1.3 Unclear timeline and framework throughout the progression of the disease in the NMOSD-ON animal model

Numerous previous studies have reported various pathological events associated with NMOSD. The

distinctive feature of intracerebral and spinal cord injections is that they allow antibodies to make direct, uninterrupted contact with the target tissues. This characteristic explains why intracerebral injections can lead to the damage of AQP4 and GFAP proteins, with observable loss occurring as early as 12 hours post-injection (Saadoun et al., 2010). Within a week, we can detect demyelination, axonal damage, and the accumulation of inflammatory cells. Similarly, there have been reports of using intracerebral injections to induce NMOSD, where the loss of AQP4 and GFAP, along with demyelination, was observed by day 5 (with only this single timepoint reported). This indicates that NMOSD-like pathology in the brain typically manifests within a week (Asavapanumas, Ratelade, & Verkman, 2014). To address this temporal controversy, a model of NMOSD myelitis (also utilizing passive transfer of AQP4-IgG) employed two-photon imaging to observe pathological events in neuromyelitis optica, revealing that astrocyte and axonal injury can occur as early as 2 hours post-exposure (Herwerth et al., 2016). This finding underscores the rapid destruction of astrocytes following direct contact with antibodies.

What is the temporal sequence of pathological events occurring in the optic nerve? In a model induced by AQP4-IgG via a conjunctival route, a reduction in AQP4 and GFAP within the optic nerve was observed by day 7, followed by the infiltration of inflammatory cells, demyelination, and axonal degeneration by day 14 (Y. Matsumoto et al., 2014). Additionally, this model demonstrated a decrease in VEP amplitude on day 7, although latency remained unchanged. OCT analysis revealed a reduction in RNFL thickness, with day 21 serving as the sole observation point for pathological events, during which astrocytic damage, demyelination, and axonal loss were noted, alongside the presence of an inflammatory response (Zhang et al., 2018). The administration of a

high-affinity AQP4-IgG can facilitate the passive transfer of antibodies, leading to the depletion of AQP4 and GFAP as early as day 2. Additionally, infiltration of neutrophils and microglia was noted on day 2. However, by day 4, the activated neutrophils began to disperse. By day 7, axonal degeneration was evident (Y. Morita et al., 2022).

The temporal sequence of events is significantly influenced by the methodology employed in the induction model. In the case of passive transfer of AQP4-IgG, if systemic induction is utilized, a prolonged duration is anticipated. This is primarily due to the necessity of establishing the EAE model, after which AQP4-IgG can cross the compromised BBB and enter the CNS. Once within the CNS, AQP4-IgG interacts with astrocytes, ultimately leading to the degeneration of the optic nerve. Literature indicates that AQP4-IgG delivery occurs approximately ten days post-EAE model establishment (Remlinger et al., 2023). Furthermore, the involvement of RGCs may not manifest until day 26 to day 29. In contrast, direct injection of AQP4-IgG in localized targeted tissue results in a more rapid onset of associated pathological events. As previously mentioned, RGCs involvement can be observed within seven days, with the latest occurrences observed within three weeks (Duan & Verkman, 2020; Y. Morita et al., 2022).

Consequently, the entire timeline appears rather ambiguous, as each study presented a distinct timeline. Most critically, certain studies only provided a single timepoint for assessment, leaving us in the dark regarding the precise timing of these pathological events throughout the progression of the disease. We remain uncertain about the chronological order of occurrences; for instance, it is unknown whether neuroinflammation precedes or follows astrocytic damage. Additionally, we lack

clarity on whether demyelination coincides with the timing of astrocytic damage or occurs at a different point altogether. These timelines are, in fact, quite unclear.

3.2 Objectives

Simulating NMOSD is of paramount importance, particularly given the higher incidence rates observed among Asian populations (Bagherieh et al., 2023; Briggs & Shaia, 2024; Tian et al., 2020). Although NMOSD is not classified as a highly prevalent disease overall, the consequences of this condition can be profoundly severe, leading to blindness, disability, and potentially fatal outcomes (Duchow et al., 2024; Tian et al., 2020; Wu et al., 2019b). Progress in treatment options has been limited, with current clinical practices predominantly relying on high-dose corticosteroid therapy or plasma exchange (Carnero Contentti & Correale, 2021; Kageyama et al., 2013). Immunomodulators and immunosuppressants also represent significant options for long-term therapeutic strategies in the managing the immune disorders. These agents play a crucial role in modulating the immune response, thereby providing a means to achieve disease control and improve patient outcomes over extended periods (Carnero Contentti & Correale, 2021). However, these approaches are fraught with numerous side effects, and neither corticosteroids nor plasma exchange effectively address the issue of frequent relapses. Such relapses are a critical factor contributing to the serious consequences of the disease (Carnero Contentti & Correale, 2021; Kageyama et al., 2013).

A long-term, continuous follow-up strategy that may necessitate a lifelong treatment regimen could represent the most pragmatic approach to managing NMOSD (Carnero Contentti & Correale, 2021). It is crucial to explore ways to mitigate the side effects associated with pharmacological treatments

in order to extend the duration of therapeutic efficacy. Furthermore, drug trials will undoubtedly require the development of animal models that comprehensively encompass the various pathological events associated with the onset and progression of NMOSD (Duan & Verkman, 2020). Understanding the timing and sequence of these pathological events is essential for establishing a coherent and comprehensive framework for future research and therapeutic interventions.

The previous models require optimization to closely mimic the entire disease process. Initially, we excluded the systemic induction model due to the necessity of establishing an EAE model (Xiang et al., 2021), as EAE itself may induce demyelination (Constantinescu et al., 2011). We also attempted the option of injecting the anterior optic nerve reported in previous literature (Yuko Morita et al., 2022; Zhang et al., 2018); however, this procedure is more suited for rats due to their larger body size, which allows for easier avoidance of blood vessels and facilitates complete exposure of the anterior optic nerve for injection (Yuko Morita et al., 2022; Zhang et al., 2018). Nevertheless, it is well recognized that mouse models are more appealing, particularly because there is a wide array of genetically modified knockout mice available for our research, which greatly aids our subsequent investigations. Regardless of whether we utilize rats or mice, exposing the anterior optic nerve necessitates the removal of a segment of the meninges to adequately expose the optic nerve for drug delivery (Yuko Morita et al., 2022; Zhang et al., 2018). This process of meninges removal and drug administration poses a risk of damaging the optic nerve or disrupting the vascular supply to the retina, which is an outcome we wish to avoid. Our primary focus is on the interaction between antibodies and antigens, as well as the various downstream inflammatory pathways that are triggered, rather than the inflammation resulting from mechanical injury.

Our focus on NMOSD highlights it as a disease characterized by multifocal involvement of the posterior optic nerve. The initiation of this condition is believed to occur at the posterior segment of the optic nerve, subsequently extending along the entire length of the optic nerve and affecting the somatic bodies of RGCs. Variations in the primary lesion can lead to differing timelines for the involvement of these somatic bodies (Duan & Verkman, 2020). Notably, the passive transfer of AQP4-IgG in the anterior segment of the optic nerve likely result in a more rapid onset of somatic body involvement, given its proximity to the retina (Duan & Verkman, 2020; Y. Morita et al., 2022). Furthermore, there are specific histopathological distinctions between the anterior and posterior segments of the optic nerve, which may influence their pharmacological responses (McAllister, 2013). This is particularly relevant when systemic medications must navigate through different vascular supplies, as the responses of the anterior and posterior optic nerves are not uniform (McAllister, 2013).

The implications of whether the modeling occurs in the anterior or posterior optic nerve are significant (McAllister, 2013). Additionally, the methodologies of inducing NMOSD through intracranial or intrathecal injections present challenges; direct cortical injection inherently causes tissue damage, which is an undesirable outcome as it bears no relevance to NMOSD pathology (Asavapanumas, Ratelade, & Verkman, 2014; Duan & Verkman, 2020; Luo et al., 2020; Yuko Morita et al., 2022; Saadoun et al., 2010). Our objective is to propose a comprehensive timeline for an animal model system that accurately simulates the disease. This animal model must be designed to deliver interventions without inflicting any mechanical damage. To achieve this, we utilized a 33-

gauge needle to minimize injury and mitigate intracranial immune rejection responses. Our delivery method avoided direct puncture injections into the optic nerve; instead, a slow-release pump positioned around the posterior optic nerve was applied to gradually administer AQP4-IgG. This approach aimed to maximize the antibody's exposure to AQP4 on astrocytes as quickly as possible. In a previously published article, researchers attempted various modeling and found that only the implantation of an osmotic pump for the sustained release of AQP4-IgG yielded satisfactory modeling results (Asavapanumas, Ratelade, Papadopoulos, et al., 2014). However, considering that the osmotic pump requires implantation and placement within the cranial cavity in a living animal for three days, and given our objective to control inflammation as a primary target, the confounding factors caused by the implantation of the osmotic pump are not desirable. Therefore, we chose two consecutive injections as an alternative to the osmotic pump for delivering AQP4-IgG. In this process, we utilized a syringe pump to regulate the release rate, thereby simulating the gradual binding of AQP4-IgG to the antigen. Rather than that, we could also mitigate mechanical damage. We aimed to investigate the occurrence of various pathological events across multiple timepoints for this model. After establishing a comprehensive timeline and framework, we attempted to identify a candidate therapeutic approach. The neuroprotective effects of LBGP are evident, and the side effects of wolfberry are minimal, making long-term administration for NMOSD-ON a viable option. We utilized this clearly defined timeline model as a reference, conducting assessments of our targeted biomarkers at different stages of disease. Furthermore, it is essential to comprehend the underlying mechanisms that contribute to the observed therapeutic effects. To this end, we employed proteomics methodologies to analyze potential molecular pathways and mediators that facilitate the treatment's efficacy.

In summary, our objective was to establish an NMOSD-ON animal model that encompasses a timeline with multiple timepoints, thereby creating a systematic framework. We utilized this framework to evaluate the effectiveness of LBGP in treating NMOSD-ON and ultimately seek to understand the reasons behind its therapeutic benefits.

3.3 Methods

3.3.1 Animal ethics in this study

This investigation conformed to the ethical principles outlined in the 1964 Declaration of Helsinki and its subsequent amendments. The research protocol received approval from The Hong Kong Polytechnic University's Animal Subjects Ethics Sub-committee (approval No. 20-21/127-SO-R-GRF, approval date: October 7, 2021; approval No. 21-22/152-SO-R-GRF, approval date: February 5, 2024). All animal experimentation adhered to the guidelines set forth by Animal Research: Reporting of In Vivo Experiments (ARRIVE) (Percie du Sert et al., 2020).

3.3.2 Selection of AQP4-IgG for model establishment

The recombinant monoclonal AQP4-IgG rAb53 (Creative Biolabs Inc., Shirley, NY, USA), also referred to as AQP4-IgG, was derived from a clonally expanded population of plasmablasts isolated from the cerebrospinal fluid of a patient diagnosed with neuromyelitis optica spectrum disorder (NMOSD). Its derivation and characteristics have been thoroughly documented in previous studies (Asavapanumas, Ratelade, Papadopoulos, et al., 2014; Bennett et al., 2009; Crane et al., 2011).

Monoclonal recombinant antibodies targeting AQP4 demonstrate superior antigen affinity compared to polyclonal antibodies obtained from the sera of NMOSD patients (Duan & Verkman, 2020). These recombinant monoclonal NMOSD antibodies were generated through the co-transfection of heavy and light chain constructs into HEK293 cells, utilizing plasmablasts clonally expanded from cerebrospinal fluid. The Fab fragment was subsequently isolated via papain digestion of IgG, while the Fc fragment was obtained through protein A affinity purification (Bennett et al., 2009).

3.3.3 Intracranial delivery of AQP4-IgG

All mice were purchased from the Centralized Animal Facilities (CAF) at The Hong Kong Polytechnic University. Adult female C57BL/6 mice (15–22 g, 8–10 weeks) were maintained under a 12/12-hour light/dark cycle with free access to food and water, adhering to the protocols established by the CAF at The Hong Kong Polytechnic University. The selection of female sex in this study is evidenced by the higher predominance of NMOSD in females, a decision that is consistent with previous research (Soerensen et al., 2021), thereby enhancing the validity of our NMOSD findings. Mice with ocular injuries were excluded from the study. All subjects were randomly allocated into NMOSD-ON and control groups. Initially, five mice were euthanized for tissue staining as the baseline. Following the group assignment, five mice from both the NMOSD-ON and control groups were euthanized at designated timepoints: day 2, week 1, week 2, and week 4 for tissue staining. For quantitative reverse transcription polymerase chain reaction (qRT-PCR) analysis, five mice from each group were euthanized at each specified timepoint. Additionally, at week 4, five mice from each group were euthanized for western blot analysis. Thus, each group

consisted of 45 mice, culminating in a total of 95 mice, including the five utilized for baseline analysis ***(Figure 3.1)***.

To induce NMOSD-ON, mice were positioned on a stereotaxic instrument (Portable Stereotaxic Instrument for Mouse, SGL M, Digital. RWD Life Science Co., Ltd., Shenzhen, China) (Asavapanumas, Ratelade, Papadopoulos, et al., 2014) and subjected to intracranial injection of AQP4-IgG (5 μg, rAb53 variant) and human complement (5 μL, Innovative Research Company, Novi, MI, USA). Control group animals received injections of normal IgG (5 μg, Sigma Aldrich Company, Burlington, MA, USA) and human complement (5 μL). The AQP4-IgG/normal IgG and human complement components were combined in a syringe and delivered via a syringe pump (KDS Legato 130 Syringe Pump, RWD Life Science Co., Ltd.). Anesthesia was achieved through intraperitoneal injection of a mixture comprising 100 mg/kg ketamine hydrochloride (Alfasan International B.V. Woerden, Holland) and 20 mg/kg xylazine (Alfasan International B.V. Woerden). For the intracranial injections, the scalp was meticulously disinfected, and an incision was made at the apex of the mouse skull. A 1-mm aperture was drilled into the skull, positioned 1 mm laterally and 1 mm anterior to the bregma, utilizing coordinates defined by the stereotaxic frame. A 33-gauge needle affixed to a 25 μL gas-tight syringe was then inserted 6 mm beneath the dura mater. This methodology ensures precise targeting of the intracranial optic nerve adjacent to the optic chiasm **(Figure 3.1)**.

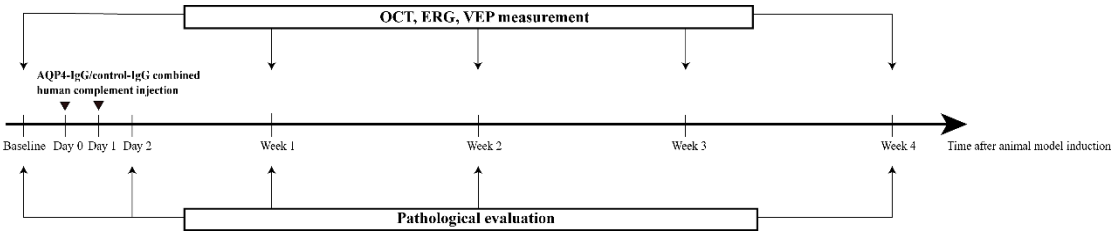

Figure 3.1 The diagram representing the temporal progression of the experimental protocol.

The pump administered the substances at a rate of 1 μL/min into the posterior optic nerve, simulating the gradual accumulation of AQP4-IgG and complement activation. Dosage and volume were informed by prior investigations (Asavapanumas, Ratelade, Papadopoulos, et al., 2014). Immunoreactive regions were subsequently delineated within the intracranial optic nerve ***(Figure 3.2)***.

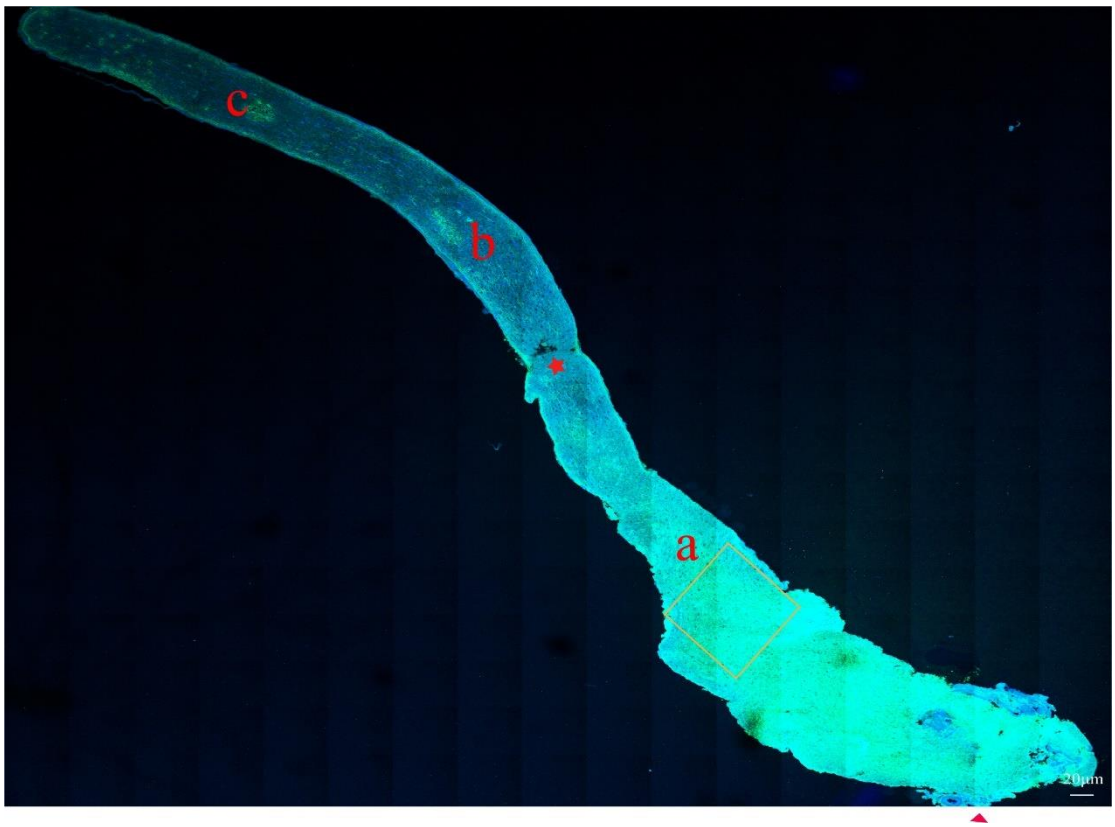

Figure 3.2 The evaluated area where the AQP4-IgG delivered. Deposition of AQP4-IgG (green, stained with anti-human IgG, Alexa fluor 488), indicating delivery to the (a) intracranial optic nerve but not the (b) posterior optic nerve or (c) anterior optic nerve. The asterisk indicates the junction between the posterior optic nerve and the intracranial optic nerve, marking the point at which the optic nerve enters the cranial cavity. The orange frame indicates the area evaluated for quantification of immunoreactivity. The red triangle is adjacent to the optic chiasm. AQP4-IgG: Anti-aquaporin-4 antibodies.

3.2.4 Immunostaining

The immunofluorescence testing follows a standardized protocol, ensuring that each sample is subjected to fluorescence staining using precisely the same methods and reagents. To minimize the impact of blood cells on the morphology and protein expression of neural tissue, we first performed cardiac perfusion to remove blood cells. An anesthetic mixture of ketamine and xylazine was prepared as previously described. Following anesthesia, a needle was inserted into the left ventricle, and an incision was made in the right atrium. Phosphate-buffered saline (PBS) was infused into the left ventricle at a rate of 2 mL/min. Once the perfusion was completed, the entire optic nerve was carefully excised, ensuring its integrity being maintained. The optic nerves and whole-mounted retinas were then fixed in 4% paraformaldehyde (Agar Scientific, Sheffield, UK), embedded in O.C.T. compound (SAKURA, Tokyo, Japan), and sectioned into 14-μm slices utilizing a Leica CM1950 cryostat (Wetzlar, Germany). To prevent non-specific binding during immunostaining, 5% bovine serum albumin in phosphate-buffered saline was utilized for a duration of 1 hour. Following this, the tissue sections were incubated overnight at 4°C with primary antibodies ***(Table 3.1)***.

Table 3.1 Antibodies utilized for immunohistochemistry in optic nerve and retina

	Antibodies (host)	Company	RRID no.	Cat#	Dilution
Primary antibodies	AQP4 (mouse)	Santa Cruz, Dallas, TX, USA	AB_3083097	sc-390488	1:200
	GFAP (rabbit)	Dako, Glostrup, Denmark	AB_10013382	z0334	1:200
	CD68 (rat)	Abcam, Cambridge, UK	AB_869007	ab53444	1:200
	Iba-1 (rabbit)	Wako, Osaka, Japan	AB_839504	019–19741	1:700
	MOG (mouse)	Millipore, Burlington, MA, USA	AB_1587278	MAB5680	1:200
	NF200 (mouse)	Sigma, St. Louis, MO, USA	AB_477257	N0142	1:200
	Brn3a (mouse)	Millipore, Burlington, MA, USA	AB_94166	MAB1585	1:200
	C5b9 (mouse)	Santa Cruz, Dallas, Texas, USA	AB_1119840	sc-66190	1:200
Secondary antibodies	Alexa Fluor 488 IgG (goat anti rabbit)	Invitrogen, Waltham, MA, USA	AB_143165	A11008	1:500
	Alexa Fluor 555 (goat anti mouse)	Invitrogen, Waltham, MA, USA	AB_141822	A21422	1:500
	Alexa Fluor 488 IgG (donkey anti rabbit)	Invitrogen, Waltham, MA, USA	AB_2535792	A21206	1:500
	Alexa Fluor 555 IgG (donkey anti rat)	Abcam, Cambridge, UK	AB_2813834	AB150154	1:500
	Alexa Fluor 488 IgG (goat anti human-IgG)	Invitrogen, Waltham, MA, USA	AB_141360	A11013	1:500

Following primary antibody incubation and three PBS washes, secondary antibodies conjugated to specific fluorophores were applied. Nuclei were counterstained with DAPI (1:1000, Sigma, D8417). The tissue sections of the optic nerve were examined using a Zeiss LSM 800 Upright Confocal Microscope (Carl Zeiss, Oberkochen, Germany). Confocal images were acquired at 10×/0.45 and

20×/0.8 magnifications. Quantitative analysis of protein expression levels was performed and expressed in arbitrary fluorescence intensity units.

3.2.5 Western Blot

All optic nerve tissues harvested from euthanized mice were subjected to denaturation through boiling in SDS sample buffer. An aliquot containing 30 µg of total protein was subsequently loaded onto 10 % sodium dodecyl sulfate polyacrylamide gel electrophoresis (SDS-PAGE) gels. Following electrophoresis (150 minutes at 300 mA), the proteins were transferred to polyvinylidene fluoride (PVDF) membranes. The membranes were blocked overnight at 4°C with 5 % bovine serum albumin in Tris-buffered saline containing Tween® 20. The membranes were then incubated with primary antibodies (anti-NF200, mouse, 1:1000, Sigma, Cat# N0142, RRID: AB_477257 and anti-GAPDH, mouse, 1:1000, Millipore, Cat# CB1001, RRID: AB_2107426) with shaking overnight at 4°C. After three washes in Tris-buffered saline with Tween® 20, the membranes were treated with a secondary antibody (goat anti-mouse IgG, horseradish peroxidase-conjugated, ABclonal, Woburn, MA, USA, Cat# AS003, RRID: AB_2769851) diluted 1:1000 at 22°C for 1 hour. The membranes underwent five additional washes before being exposed to SuperSignal™ West Pico PLUS Chemiluminescent Substrate (Invitrogen, Waltham, MA, USA). The resulting blots were analyzed using a ChemiDoc Imager System (Bio-Rad, Hercules, CA, USA). The intensity was normalized against the reference protein (GAPDH), which served as loading control.

3.2.6 Quantitative reverse transcription polymerase chain reaction (qRT-PCR) analysis

Optic nerves were harvested from euthanized mice at Day 2, Week 1, Week 2, Week 3, Week 4 following the induction of NMOSD-ON, subsequent to transcardial perfusion with ice-cold phosphate-buffered saline, as previously detailed. The tissues were snap-frozen in liquid nitrogen and preserved at -80°C until RNA extraction. Samples were thawed on ice and homogenized in 300 µL of TRIzol (Thermofisher, Waltham, MA, USA) utilizing a mechanical homogenizer. Following a 5-minute incubation, 60 µL of chloroform was introduced, and the samples were centrifuged at 12,000 × g for 15 minutes at 4°C. The RNA-containing aqueous phase was transferred to a new tube and quantified with a NanoDrop spectrophotometer (Thermofisher), targeting an absorbance ratio of ~2.0 at 260/280 nm. RNA was reverse transcribed into complementary DNA using a High-Capacity cDNA Reverse Transcription Kit (Applied Biosystems™, Thermofisher). qRT-PCR was executed with TB Green Premix Ex Taq II (Takara, Kusatsu, Shiga, Japan) and a QuantStudio™ 7 Flex Real-Time PCR System (Thermofisher). Glyceraldehyde-3-phosphate dehydrogenase (GAPDH) served as an internal control for gene expression analysis ($2^{-\Delta\Delta CT}$). All primers employed in the experimental procedures are listed in ***Table 3.2***.

Table 3.2 The primer sequences for the targeted gene

Gene	Forward sequence (5'–3')	Reverse sequence (5'–3')
GAPDH	GGG TCC CAG CTT AGG TTC AT	CTC GTG GTT CAC ACC CAT CA
IL-6	TAT GAA GTT CCT CTC TGC AAG	CTG CAA GTG CAT CAT CGT TGT

	AGA	TC
IL-1β	GGC TGC TTC CAA ACC TTT GA	GAA GAC ACG GAT TCC ATG GT
TNF-α	CAG GCG GTG CCT ATG TCT C	CGA TCA CCC CGA AGT TCA GTA G
CXCL10	GCC GTC ATT TTC TGC CTC AT	GGC CCG TCA TCG ATA TGG
BDNF	TGA CAA CGA CAT CGC ATT AC	TTC AGC CGG TCA GAG AAG
NGF	CAA TAG CTG CCC GAG TGA CA	TCC GGT GAG TCC TGT TGA AAG

BDNF: Brain-derived neurotrophic factor; CXCL10: C-X-C motif chemokine ligand 10; GAPDH: glyceraldehyde-3-phosphate dehydrogenase; IL-1β: interleukin 1β; IL-6: interleukin 6; NGF: nerve growth factor; TNF-α: tumor necrosis factor α

3.2.7 Functional assessment

The retinal activity was evaluated through electroretinography (ERG) recordings, focusing on the positive scotopic threshold response (pSTR), as well as the amplitudes of a-wave and b-wave components of the scotopic ERG response (Perlman, 1995). Full-field Ganzfeld stimulation (Q450; RETI Animal; Roland Consult, Brandenburg an der Havel, Germany) was employed to evoke responses from both the inner and outer retinal layers in experimental mice, following methodologies established in prior research (Lakshmanan et al., 2023). The animal subjects underwent a 12-hour dark adaptation just before testing. Under dim red illumination, the mice were anesthetized using a ketamine and xylazine solution delivered via intraperitoneal injection. Mydrin-P (Santen Pharmaceutical, Osaka, Japan) was utilized for pupil dilation. The mice were positioned on a temperature-regulated platform linked to a warm water bath maintained at 37.8°C. A lubricating gel was applied to the cornea. Recording ring-electrodes (Roland Consult, Brandenburg an der Havel, Germany) were attached to the corneal surface (active electrode), while reference sub-dermal needle electrodes were inserted underneath the skin of the lateral canthi of each eye and the base of

the tail (ground electrode). This configuration facilitated concurrent recordings from both eyes. The pSTR was quantified by an average of 40 responses with a 2-second interstimulus interval. The stimuli comprised 2-ms brief, dim flashes from white light-emitting diodes, with intensities ranging from −5.1 to −4.05 log cd·s/m^2, in increments of 0.15 log cd·s/m^2. Scotopic responses, integrating both rod and cone activity, were recorded using a single flash at an intensity of 1.3 log cd·s/m^2. The acquired signals were processed through a bandpass filter set between 0.1 and 1000 Hz. The pSTR amplitudes (approximately -4.8 log cd·s/m^2), along with the a- and b-wave amplitudes of scotopic responses, were measured and prepared for further analysis. These responses are indicative of functional integrity of the RGCs, photoreceptors, and bipolar cells, respectively (Lakshmanan et al., 2023). Full-field ERG assessments were conducted to evaluate retinal function in both the NMOSD-ON and the Control at baseline, and week 1, 2, 3, and 4.

Visual evoked potential (VEP) recordings, which are non-invasive, were employed to assess the functional integrity of the visual pathway extending from the retina to the visual cortex (Robson et al., 2018). The animals were anesthetized following the protocol established for ERG recordings, and visual stimuli were administered while the active electrode, a sub-dermal needle (Roland Consult), was positioned underneath the skin of the animal head at the midline between the ears. This location corresponds to the cortical area where responsive signals are processed. The non-stimulated eye was occluded with a dark patch. The reference electrode (Roland Consult) was placed beneath the tongue, and the ground electrode (Roland Consult) was inserted into the tail (Sekyi et al., 2021). Full-field (Ganzfeld) stimulation was utilized in conjunction with a computational system (RETI port, Roland Consult). The N1P1 amplitude, N1 latency, and P1 latency of the VEP response

were evaluated to determine the functionality of the visual pathway, as outlined in prior research (Sekyi et al., 2021). The N1 wave represents the primary negative peak, while the P1 wave denotes the initial positive peak. N1 latency indicates the timing of the trough of N1 wave and serves as a marker for myelin sheath integrity of the optic nerve (Zhang et al., 2018). The N1-P1 amplitude was quantified from the trough of the N1 wave to the peak of the P1 wave, reflecting the integrity of the visual pathway, particularly regarding RGCs. P1 latency signifies the duration required for a signal to travel from the retina to the visual cortex. The stimulus and recording parameters were consistent with those employed in earlier studies (Zhang et al., 2018).

3.2.8 OCT

OCT was performed utilizing a Bioptigen Envisu spectral domain OCT system (Model R2210, Leica Microsystems, Morrisville, NC, USA). This imaging technique was employed to quantify the thickness of various retinal layers, including the RNFL, the combined ganglion cell and inner plexiform layer (GCIPL), the inner nuclear layer (INL), and the inner retina (which includes the RNFL, IPL, and INL), thereby providing an indirect *in-vivo* evaluation of axonal integrity within the retina. All mice were anesthetized, and their pupils were pharmacologically dilated. Radial OCT scans were executed (a-/b-scans: 1000 lines; b-scans: 100 scans; frame/b-scans: 10 frames), covering a region of 0.8 mm × 0.8 mm. The optic disc was centrally located within the scan to establish a uniform reference point across different subjects and time intervals. Retinal thickness measurements were analyzed as previously described (Lam et al., 2023). The average thicknesses of the RNFL, GCIPL, INL, and inner retina were captured to monitor structural alterations within

the whole retina (baseline, week 1, week 2, week 3, and week 4).

Data acquisition and analysis were conducted for each experiment (immunostaining intensity, ERG, VEP, and OCT) at baseline and week 1, week 2, week 3, and week 4. Variations in immunoreactivity (AQP4, GFAP, MOG, and NF200), microglial counts (Iba-1 and CD68), RGC counts, ERG parameters (pSTR amplitude, a- and b-wave amplitude and latency), VEP parameters (N1-P1 amplitude, N1 and P1 latency), and OCT measurements (RNFL, IPL, INL thickness) were evaluated using repeated measurements. Data is presented as the mean ± standard error of the mean (SEM). Comparative analyses were executed by unpaired t-tests for two groups and one-way analysis of variance (ANOVA) with Tukey's correction for three or more groups. Two-way ANOVA with post hoc Tukey's correction was employed to detect significant temporal changes and group differences over time. A p-value < 0.05 was considered statistically significant. Analyses were performed by GraphPad Prism (version 9.2.0 for Windows, GraphPad Software, Boston, MA, USA, www.graphpad.com).

3.3 Results

3.3.1 Pathological deterioration over time

3.3.1.1 Early loss of AQP4 and astrocyte damage

We sacrifice mice at different timepoints (day 2, week 1, week 2, week 3, and week 4), followed by sectioning and staining to examine AQP4 immunoreactivity. We compared AQP4 immunoreactivity

with the control or baseline. By day 2, a notable decrease in AQP4 immunoreactivity was already observed at the injection site compared to the control group (p = 0.015) and the baseline group (p = 0.030). This reduction in AQP4 immunoreactivity progressively deteriorated with significant AQP4 loss observed at week 1 (p = 0.031 vs. control and p = 0.038 vs. baseline), week 2 (p = 0.044 vs. control and p = 0.031 vs. baseline), week 3 (p = 0.0094 vs. control and p = 0.058 vs. baseline), and week 4 (p = 0.015 vs. control, though not significantly different from baseline) ***(Figure 3.3A, and B and Figure 3.4)***.

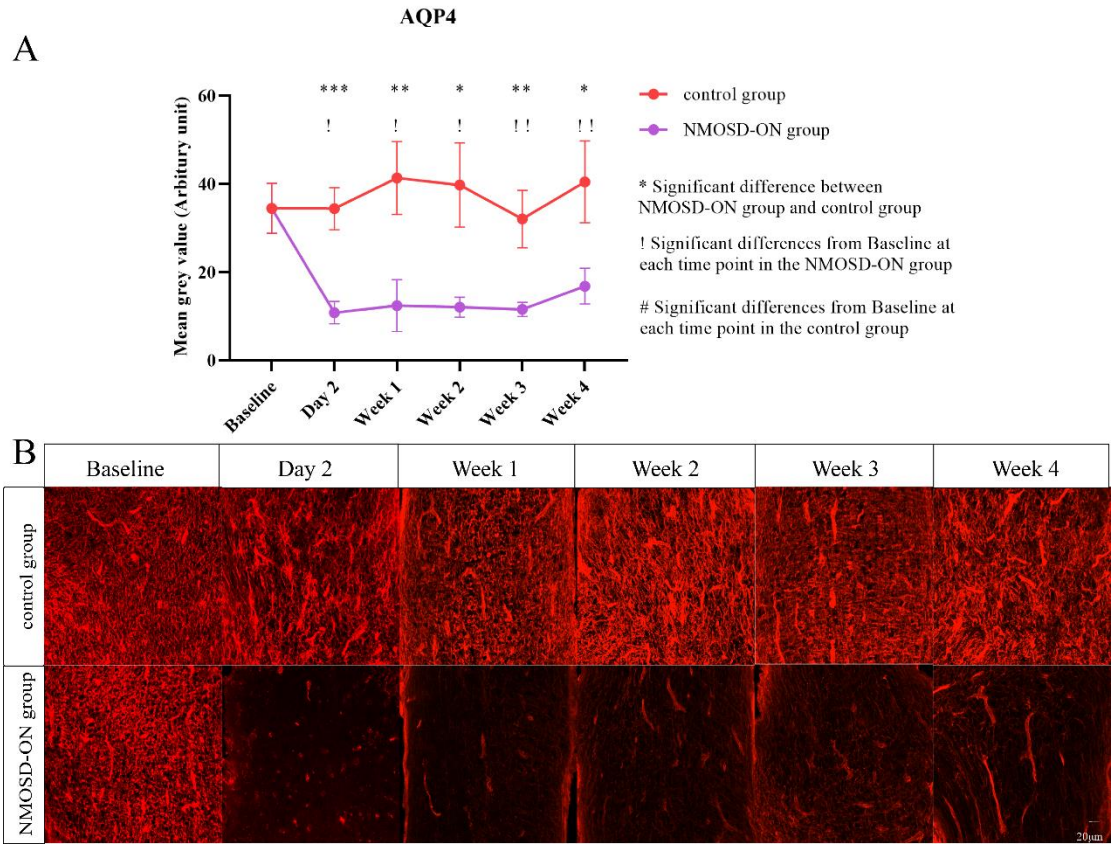

Figure 3.3 The loss of AQP4 protein documented at various time points. **(A)** The quantification of AQP4 immunoreactivity in the optic nerve at various timepoints was conducted, comparing the NMOSD-ON cohort with the control group (n=5 mice per group, ANOVA, *p<0.05; ** p<0.01, ***p<0.001; !p<0.05; !! p<0.01, !!!p<0.001). **(B)** Representative images illustrating

AQP4 loss in both the NMOSD-ON cohort and the control group over various timepoints.

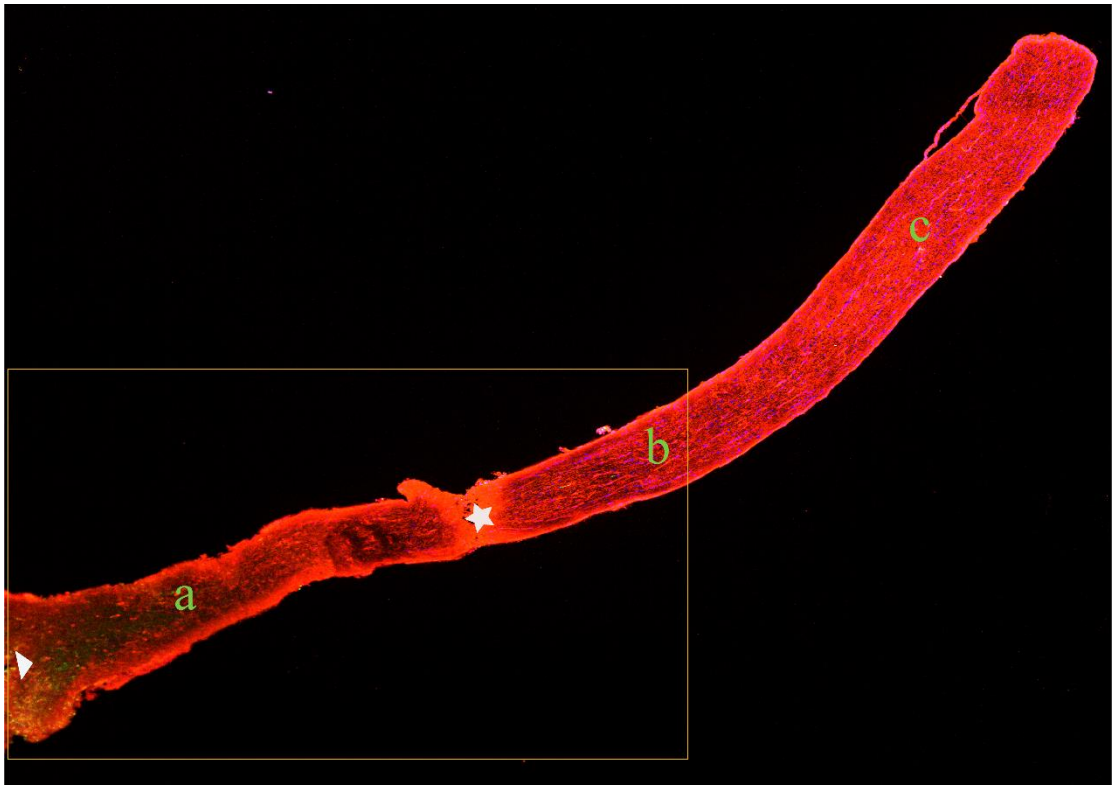

Figure 3.4 Depicts the lesion area of AQP4 protein loss (orange frame). (a) Intracranial optic nerve, corresponding to the injection site, and (b) posterior optic nerve, with no loss observed in (c) anterior optic nerve. The asterisk denotes the junction of the posterior optic nerve and the intracranial optic nerve, where the optic nerve penetrates the intracranial cavity. The triangle highlights the region adjacent to the optic chiasm.

Meanwhile, astrocytes, as indicated by GFAP expression, also showed progressive damage over time compared to baseline and control groups. At day 2, significant damage was observed relative to the baseline ($p = 0.015$), but no significant difference was found compared to the control group. By week 1, significant astrocyte damage occurred relative to the control group ($p = 0.048$) and the baseline ($p = 0.016$). At week 2, this damage persisted, with significant differences observed

compared to the control group (p = 0.043) and the baseline group (p = 0.008). By week 3, astrocyte damage further intensified, showing significant differences relative to the control group (p = 0.005) and the baseline (p = 0.014). By week 4, partial recovery of astrocytes was observed. Although fluorescence remained significantly reduced compared to the baseline (p = 0.001), there was no significant difference compared to the control group ***(Figure 3.5A and B)***.

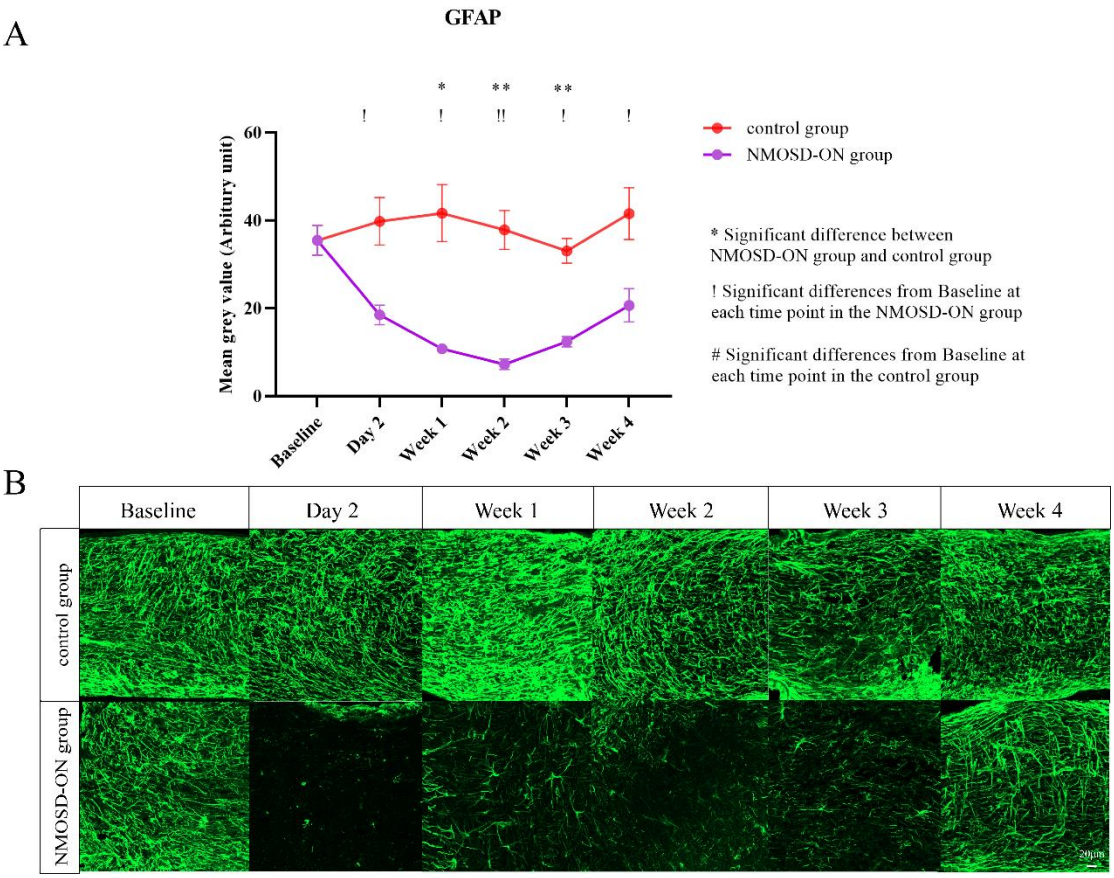

Figure 3.5 Astrocyte (labeled by GFAP) loss at different timepoints. **(A)** The quantification of GFAP expression in the optic nerve at various timepoints was conducted, comparing the NMOSD-ON cohort with the control group across different timepoints (n=5 mice per group, ANOVA, *p<0.05; **p<0.01; !p<0.05; !!p<0.01). **(B)** The representative images in both NMOSD-ON and control.

3.3.1.2 Demyelinating condition in NMOSD

Throughout the disease course, the demyelination process was monitored by assessing the immunoreactivity of MOG, a key component of oligodendrocytes in the myelin sheath. At day 2 and week 1, the myelin sheath remained intact, showing no signs of disruption. However, from week 2 onward, a significant degradation of MOG protein was observed compared to both the baseline and control group (all $p < 0.001$ vs. control). Specifically, MOG immunoreactivity decreased markedly at week 2 ($p = 0.020$ vs. baseline), with further deterioration at week 3 ($p < 0.001$ vs. baseline) and week 4 ($p = 0.009$ vs. baseline). These findings are illustrated in ***Figure 3.6A and B***.

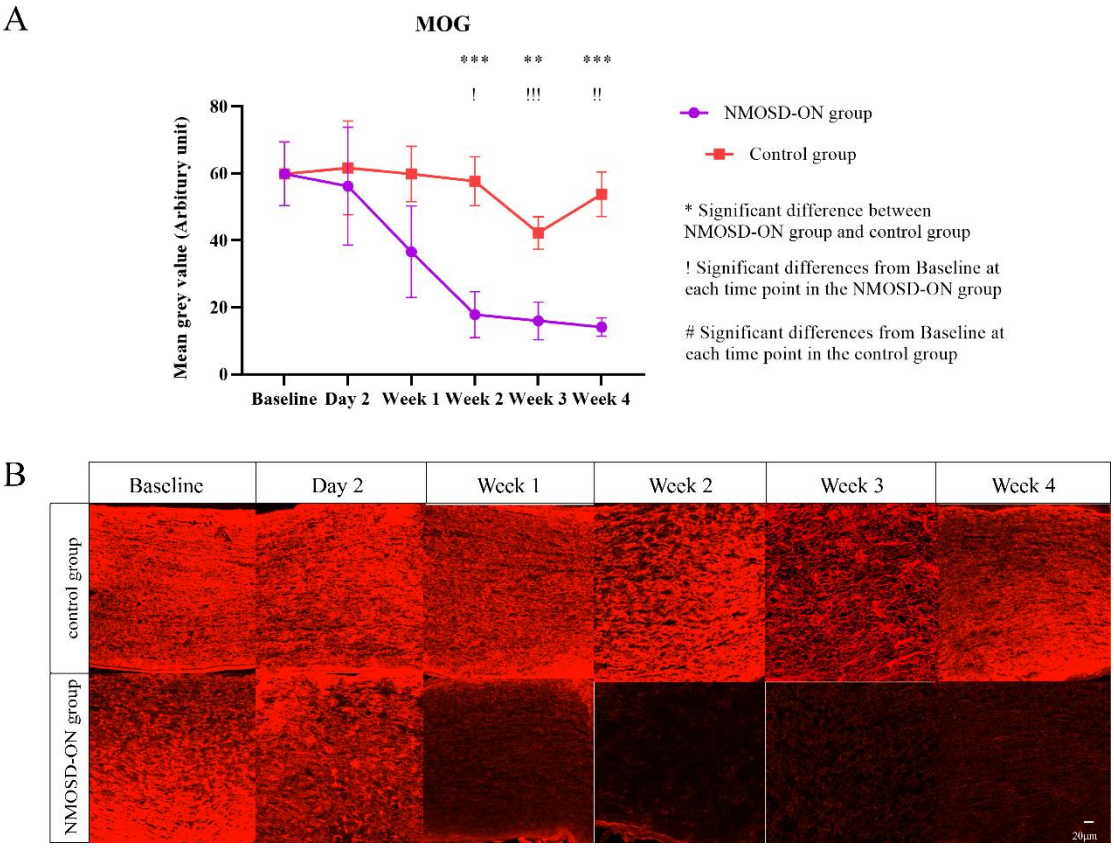

Figure 3.6 Demyelination (loss of MOG protein) at various timepoints. **(A)** The quantification of MOG expression in the optic nerve at various timepoints was conducted, comparing the NMOSD-ON cohort with the control group across different timepoints (n=5 mice per group,

ANOVA, **p<0.01; ***p<0.001; !p<0.05; !!p<0.01; !!!p<0.0001). **(B)** The representative images in both NMOSD-ON and control.

3.3.1.3 RGCs degeneration following NMOSD onset

To evaluate axonal integrity in RGCs over time, the quantitative analysis of NF200 immunoreactivity was performed. The structure of optic nerve fibers is primarily composed of neurofilaments, with NF200 being one of their primary subunit proteins. Our results demonstrated that RGC axons remained largely intact during the first two weeks post-onset, with no significant signs of degeneration (all $p > 0.05$). NF200 expression demonstrated axonal degeneration from week 2 onset (vs control: week 2 $p = 0.033$, week 3 $p = 0.032$, week 4 $p < 0.001$; vs baseline: all $p < 0.001$) ***(Figure 3.7A, B, and Figure 8, Figure 3.8)***. The western blot result confirmed the NF200 expression decreased over 4 weeks in NMOSD-ON optic nerve***(Figure 3.9)***.

A

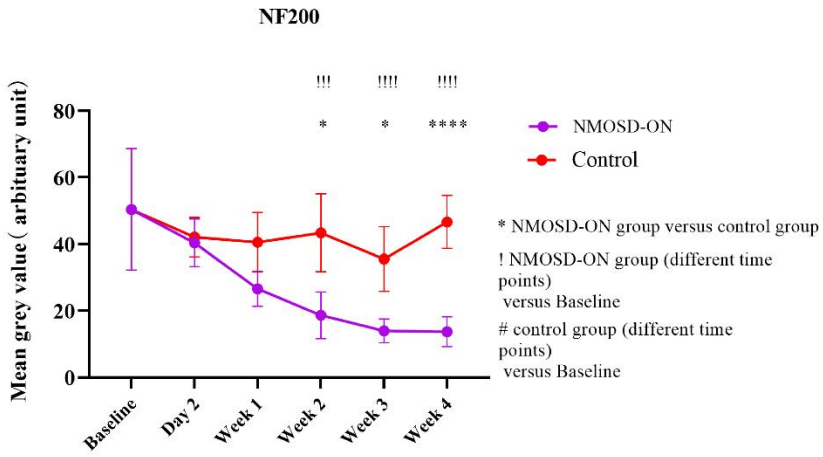

B

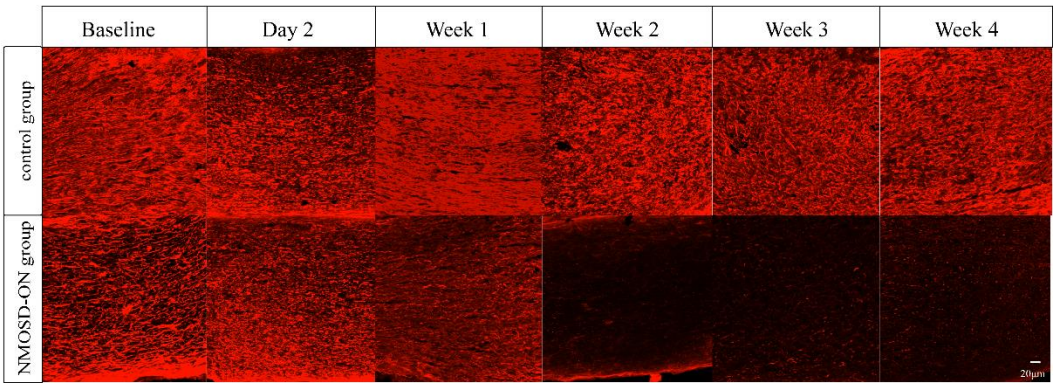

Figure 3.7 Axonal degeneration (NF200 loss) at different timepoints. **(A)** The quantification of NF200 expression in the optic nerve at various timepoints was presented, comparing the NMOSD-ON with control across different timepoints (n=5 mice per group, ANOVA, ***p<0.001; ****p<0.0001; !p<0.05; !!!!p<0.0001). **(B)** The representative images in both NMOSD-ON and control.

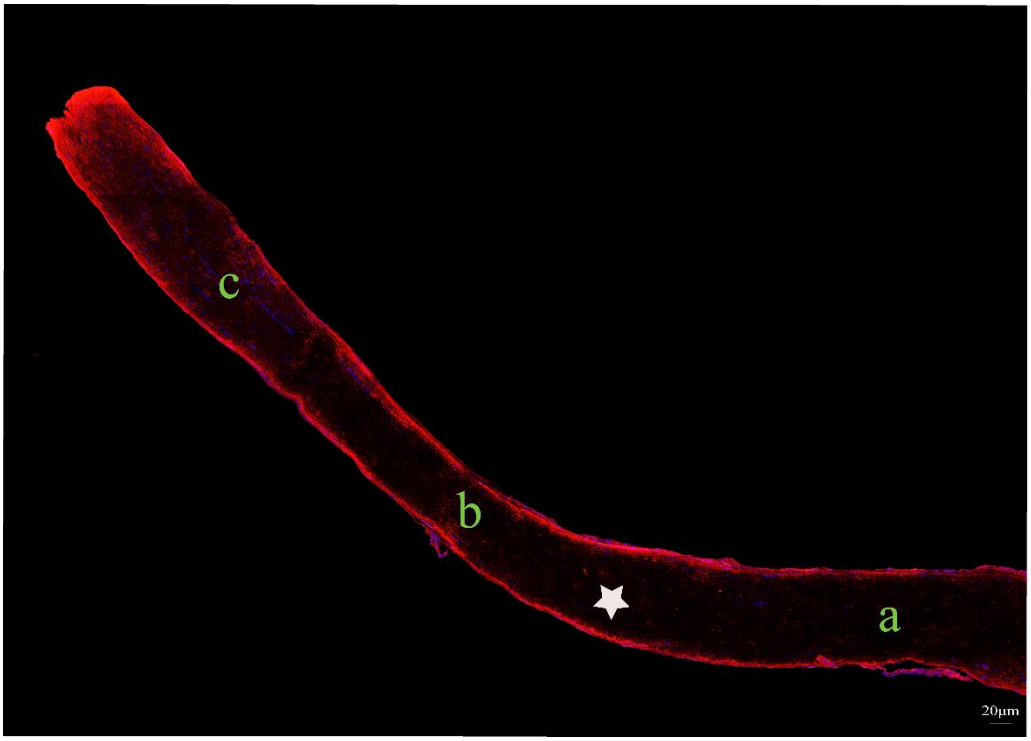

Figure 3.8 The asterisk indicated the lesion area with the NMOSD-ON optic nerve.

Western blot analysis at week 4 confirmed substantial NF200 protein degradation ($p<0.001$), consistent with the immunoreactivity findings (Figure 9A and B).

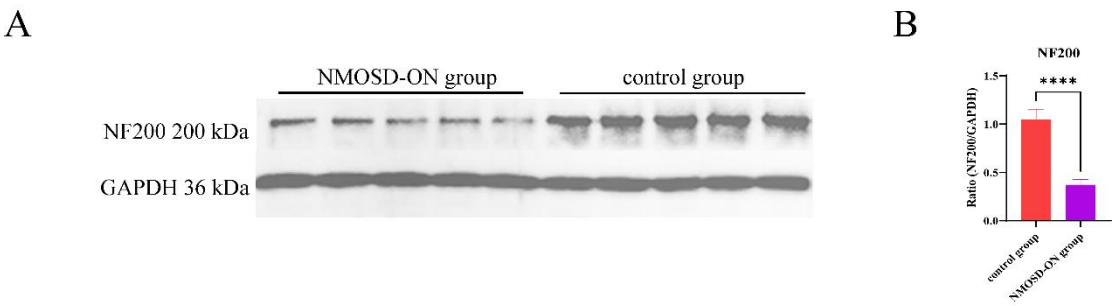

Figure 3.9 The western blot analysis of NF200 expression at week 4. **(A)** The western blot image of NF200 and GAPDH expression. **(B)** The quantification analysis of NF200/GAPDH ratio comparing the NMOSD-ON and control (n=5 mice per group, ANOVA, ****$p<0.0001$).

These results revealed a coordinated temporal pattern of myelin sheath disruption and axonal degeneration beginning in week 2 and progressing through week 4. Our comprehensive evaluation

of RGCs degeneration in NMOSD-ON through whole-mounted retina analysis revealed a distinct temporal progression of neuronal loss. During the initial disease phase (week 1), RGC counts showed no significant reduction compared to either control ($p > 0.05$) or baseline values, indicating preserved neuronal integrity. However, subsequent examination at weeks 2 and 4 demonstrated significant RGC depletion, with marked reductions compared to controls (both $p < 0.001$) and baseline levels (week 2: $p = 0.019$; week 4: $p = 0.009$) ***(Figure 3.10A and B)***.

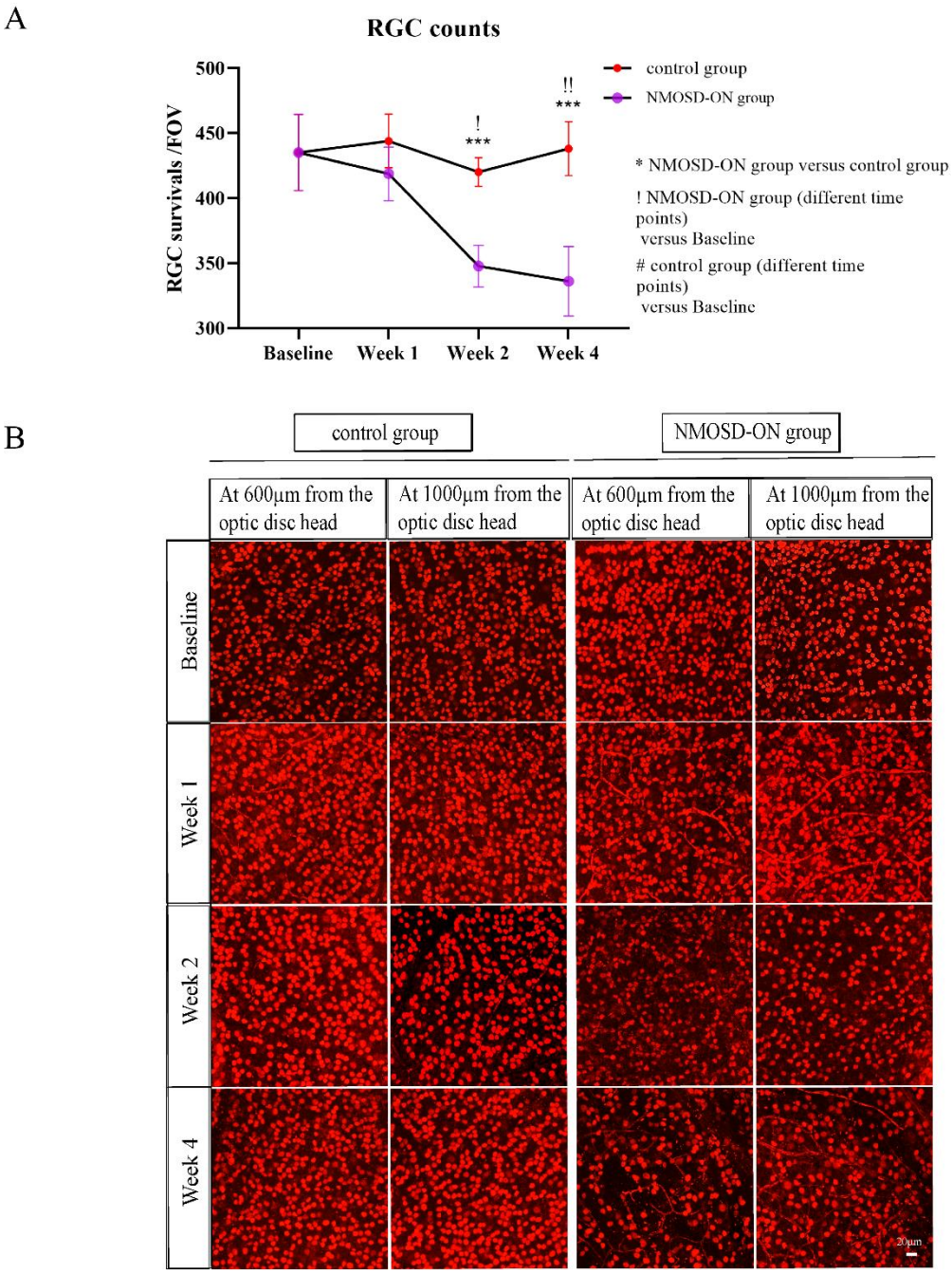

Figure 3.10 The cell counts of RGCs soma bodies. **(A)** The quantification analysis of RGCs soma bodies (Brn3a labeled) comparing the NMOSD-ON and control (n=5 mice per group, ANOVA, ***p<0.001; !p<0.05; !!p<0.01). **(B)** The representative images of RGCs soma bodies in both NMOSD-ON and control.

These findings of somatic degeneration paralleled our observations of concurrent axonal (NF200) and myelin (MOG) damage, collectively demonstrating that NMOSD-ON induces progressive optic neuropathy characterized by synchronous deterioration of neuronal cell bodies, their axonal projections, and associated myelin sheaths, with the degenerative cascade initiating at week 2 post-onset.

3.3.1.4 Microglial activation in NMOSD-ON

In the NMOSD-ON cohort, a temporal profile of microglial activation was observed. While Iba-1, a pan-microglial marker, identifies all microglia, whereas CD68 is associated with microglial phagocytosis. The CD68/Iba-1 ratio reflects the proportion of activated microglia (Ohsawa et al., 2004). Compared to the control group, CD68+ cell counts exhibited a significant increase at week 1 ($p = 0.012$) and week 2 ($p = 0.011$). The CD68+/Iba-1+ cell ratio also demonstrated a significant increase at week 1 ($p = 0.001$) and week 2 ($p = 0.009$) compared with the control group ***(Figure 3.11 A and B)***.

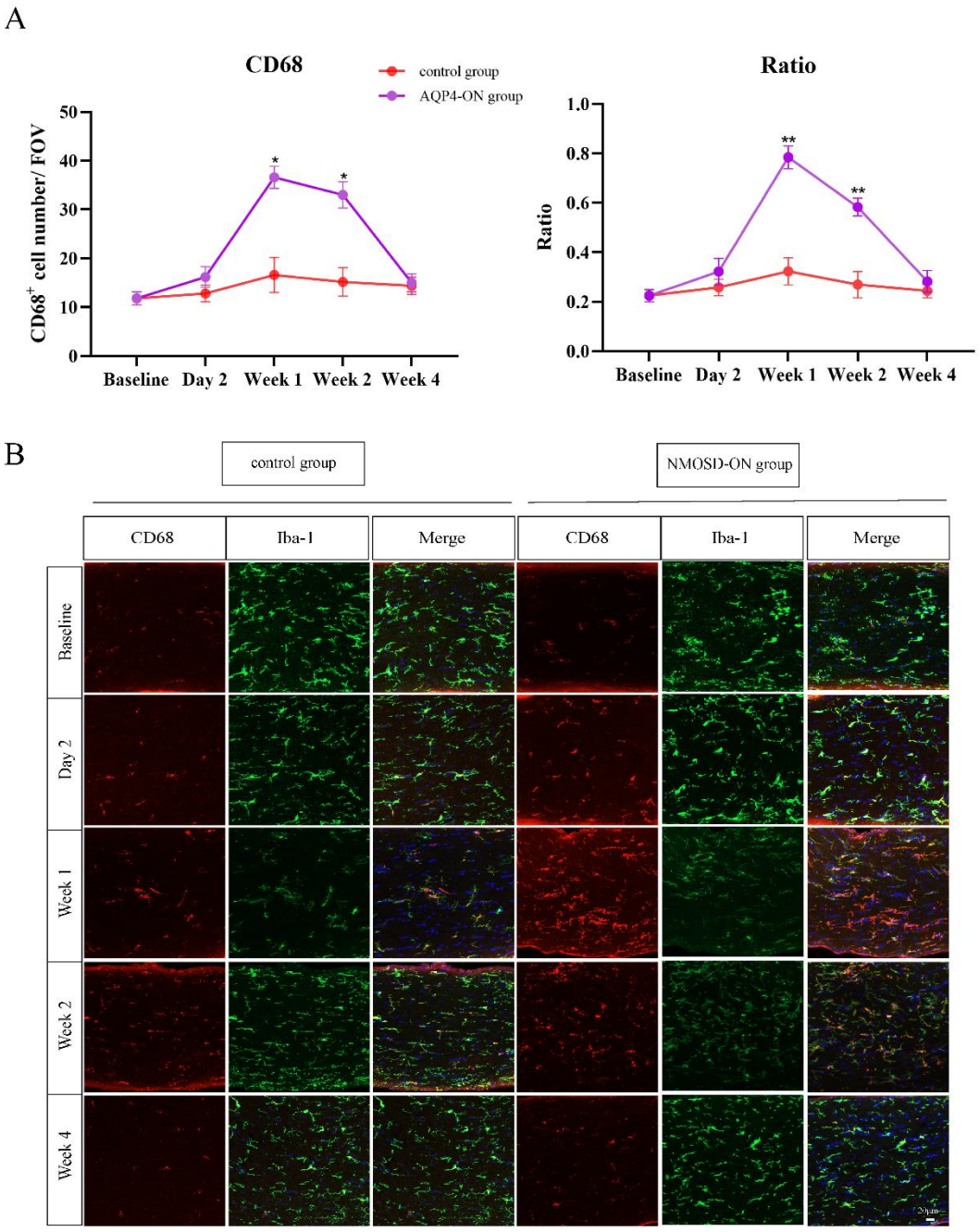

Figure 3.11 The microglial activation in NMOSD-ON. **(A)** The quantification of CD68 labeled microglial in NMOSD-ON over time (n=5 mice per group, ANOVA, *p<0.05). **(B)** The quantification of CD68/Iba-1 ratio in NMOSD-ON over time (n=5 mice per group, ANOVA, **p<0.01). **(C)** The representative images in NMOSD-ON over time.

3.3.1.5 The pro-inflammatory cytokines in NMOSD-ON

Alongside the microglial activation, the cytokine associated with inflammation IL-1β, IL-6, TNF-α, CXCL10, and BDNF ($p = 0.034$, $p = 0.047$, $p = 0.004$, $p < 0.001$, and $p = 0.009$, respectively) remained unchanged in the NMOSD-ON optic nerve as compared to control at day 2 **(Figure 3.12. A)**. However, the significance can be reached at week 1 as for IL-1β, IL-6, TNF-α, CXCL10, and BDNF ($p = 0.034$, $p = 0.047$, $p = 0.004$, $p < 0.001$, and $p = 0.009$, respectively) **(Figure 3.12 B)**. Following that, no observed difference was found at week 2 and week 4 ($p > 0.05$) **(Figure 3.12 C and D)**. In autoimmune diseases, BDNF is secreted by immune cells, and its expression is closely linked to lymphocyte survival and proliferation (Calabrese et al., 2014).

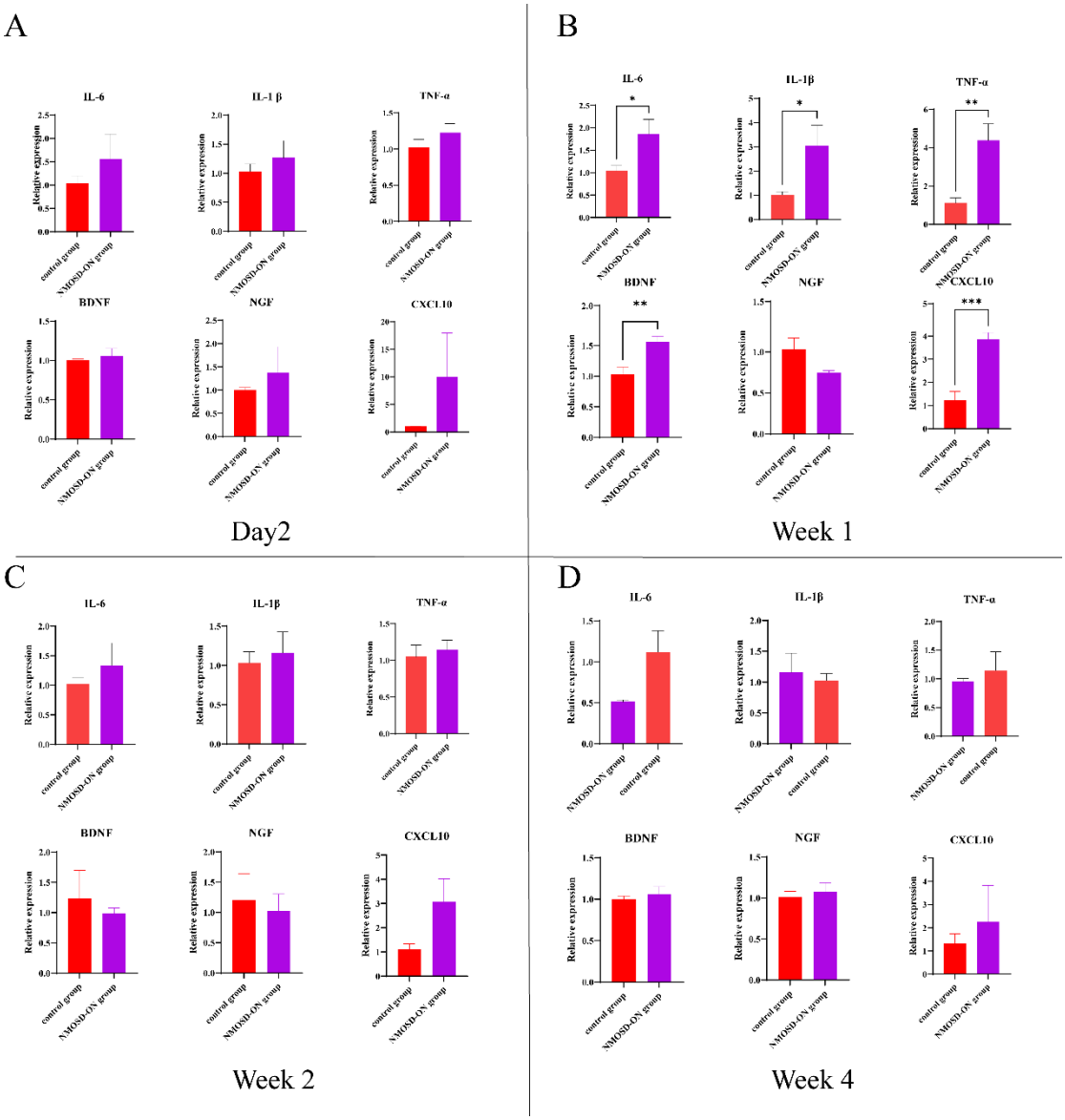

Figure 3.12 The pro-inflammatory cytokines in NMOSD-ON over time. **(A)** The difference between NMOSD-ON and control at day 2 (n=5 mice per group, ANOVA). **(B)** The difference between NMOSD-ON and control at week 1 (n=5 mice per group, ANOVA, *p<0.05; **p<0.01; ***p<0.001). **(C)** The difference between NMOSD-ON and control at week 2 (n=5 mice per group, ANOVA). **(D)** The difference between NMOSD-ON and control at week 4 (n=5 mice per group, ANOVA).

3.3.2 OCT measurement over time in NMOSD-ON

Longitudinal OCT monitoring of retinal layer thickness following NMOSD-ON onset revealed selective vulnerability of neural structures. Quantitative analysis demonstrated significant thinning of the RNFL beginning at week 2 compared to controls (week 2: $p = 0.018$; week 3: $p = 0.002$; week 4: $p = 0.021$), indicating progressive axonal loss. This RNFL thinning correlated temporally with both the observed RGC soma bodies degeneration and previously documented NF200 protein degradation. In contrast, other retinal layers including the GCIPL, INL, and outer retinal structures showed no significant thickness changes throughout the observation period (all $p > 0.05$) ***(Figure 3.13 A and B)***. These OCT findings provided *in-vivo* structural confirmation of the histological and molecular data, demonstrating preferential degeneration of RGC axons (RNFL thinning) beginning at week 2, preservation of non-RGCs retinal structures, and excellent correlation with cellular markers of neurodegeneration ***(Figure 3.13 A, C, D, and E)***.

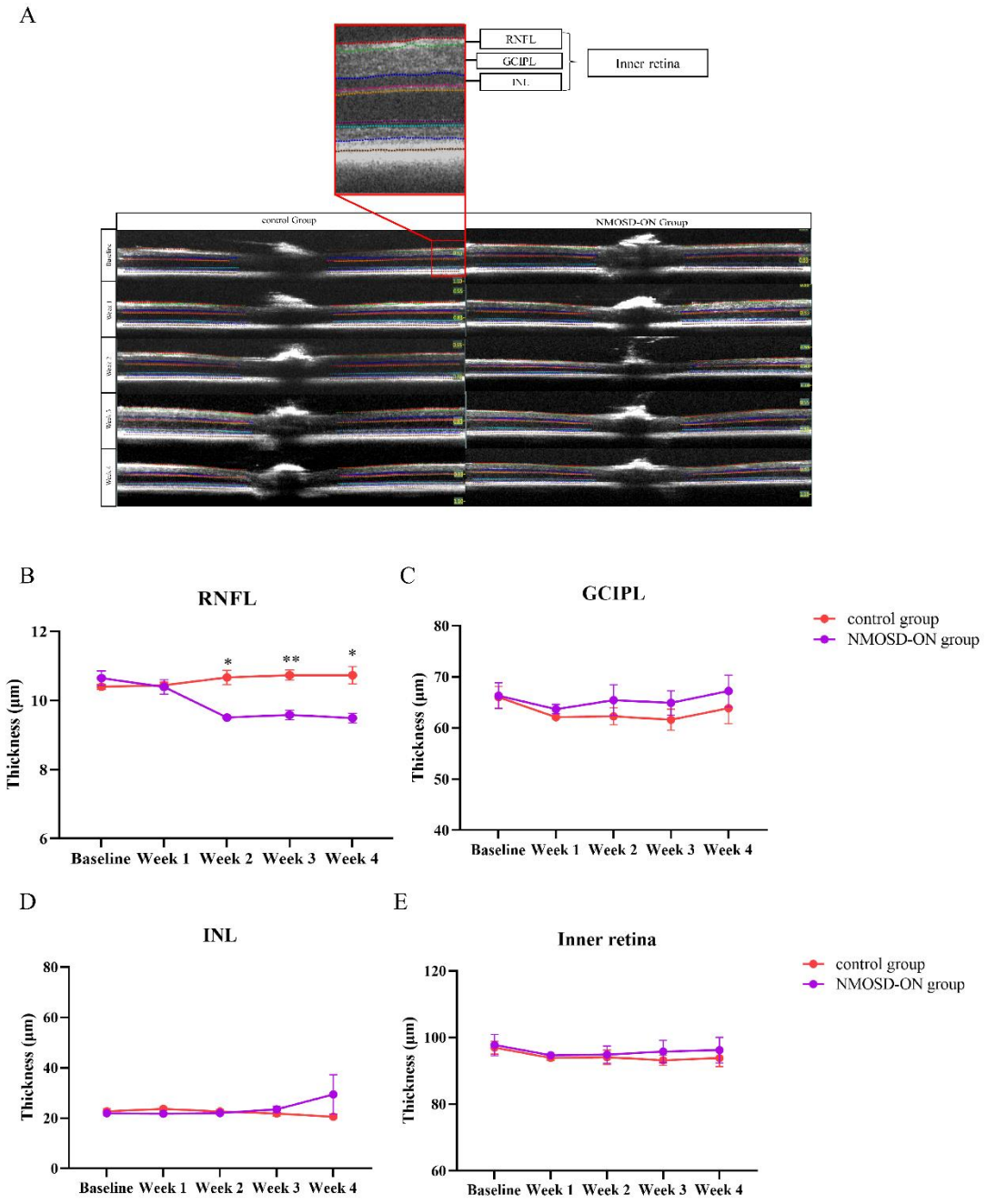

Figure 3.13 The OCT analysis of retinal layers. **(A)** The representative images of retinal images in OCT. **(B)** The quantification of RNFL layers thickness across different timepoints (n=5 mice per group, ANOVA, *p<0.05; **p<0.01). **(C, D, and E)** The quantification of GCIPL, INL, and Inner retina layers thickness across different timepoints (n=5 mice per group, ANOVA).

3.3.3 The observation of deteriorated visual impairment by VEP and ERG in NMOSD-ON

Functional impairment of the visual pathway was further evaluated using longitudinal VEP recordings in NMOSD-ON. The analysis revealed progressive deterioration in visual signal processing, characterized by significant reductions in N1-P1 amplitude, reflecting diminished overall photic responsiveness at week 2 ($p < 0.001$), week 3 ($p = 0.002$), and week 4 ($p = 0.013$) compared to the control group ***(Figure 3.14A, and D)***. Concurrently, progressively delayed N1 latency was observed, indicative of impaired conduction velocity likely related to demyelination, which reached statistical significance at week 2 ($p = 0.017$) and week 4 ($p = 0.010$), with a marginal delay at week 3 ($p = 0.052$) ***(Figure 3.14B, and D)***. In contrast, P1 latency remained almost unchanged throughout the study period (All $p > 0.05$) ***(Figure 3.14C, and D)***.

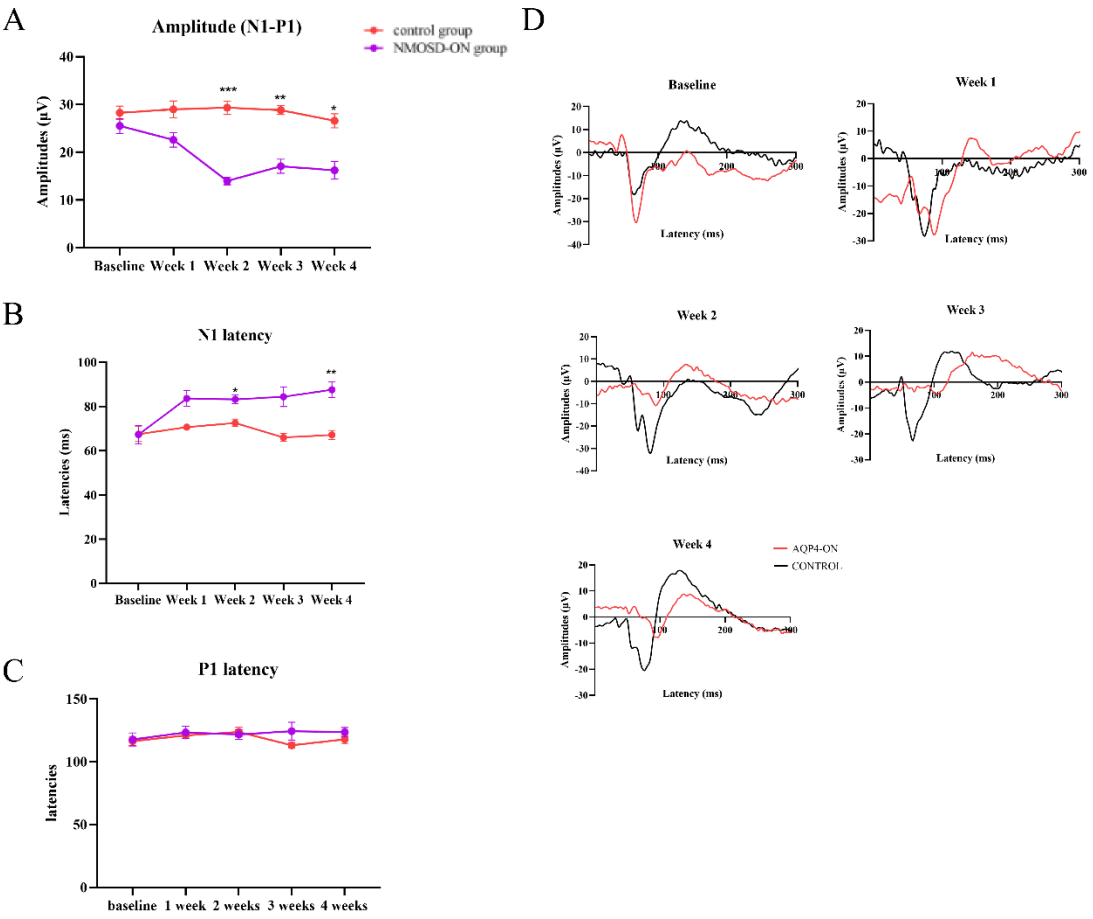

Figure 3.14 VEP analysis of NMOSD-ON across different timepoints. **(A)** The quantification of N1-P1 amplitude across different timepoints (n=5 mice per group, ANOVA, *p<0.05; **p<0.01; ***p<0.001). **(B)** The quantification of N1 latency across different timepoints (n=5 mice per group, ANOVA, *p<0.05; **p<0.01). **(C)** P1 latency quantification across different timepoints (n=5 mice per group, ANOVA). **(D)** Representative images across different timepoints.

ERG was also employed to specifically assess RGCs phototransduction function in the NMOSD-ON animal model. Longitudinal ERG recordings demonstrated significant reduction in the pSTR amplitude compared to controls at week 2 ($p < 0.001$), week 3 ($p = 0.002$), and week 4 ($p < 0.001$) ***(Figure 3.15A, and D)***, indicating progressive impairment of RGC-mediated signaling. In contrast,

dark-adapted a-wave and b-wave parameters (both amplitude and latency) remained unchanged throughout the observation period, demonstrating preserved photoreceptor (a-wave) and bipolar cell (b-wave) function (Figure B, C, and D). These findings provided electrophysiological evidence that NMOSD-ON primarily affected RGCs and their axonal projections while sparing outer retinal structures, consistent with our histological and OCT observations of inner retinal pathology. The photopic negative response (pSTR) primarily reflects the function of the inner retinal layers. Meanwhile, the a- and b-wave amplitudes elicited by light adaptation are indicators of photoreceptor and bipolar cell activity, respectively. In contrast, while the pattern electroretinogram (PERG) can also assess retinal ganglion cell (RGC) function, it more specifically reflects the activity of localized RGCs in the human macular region(Wang et al., 2021).

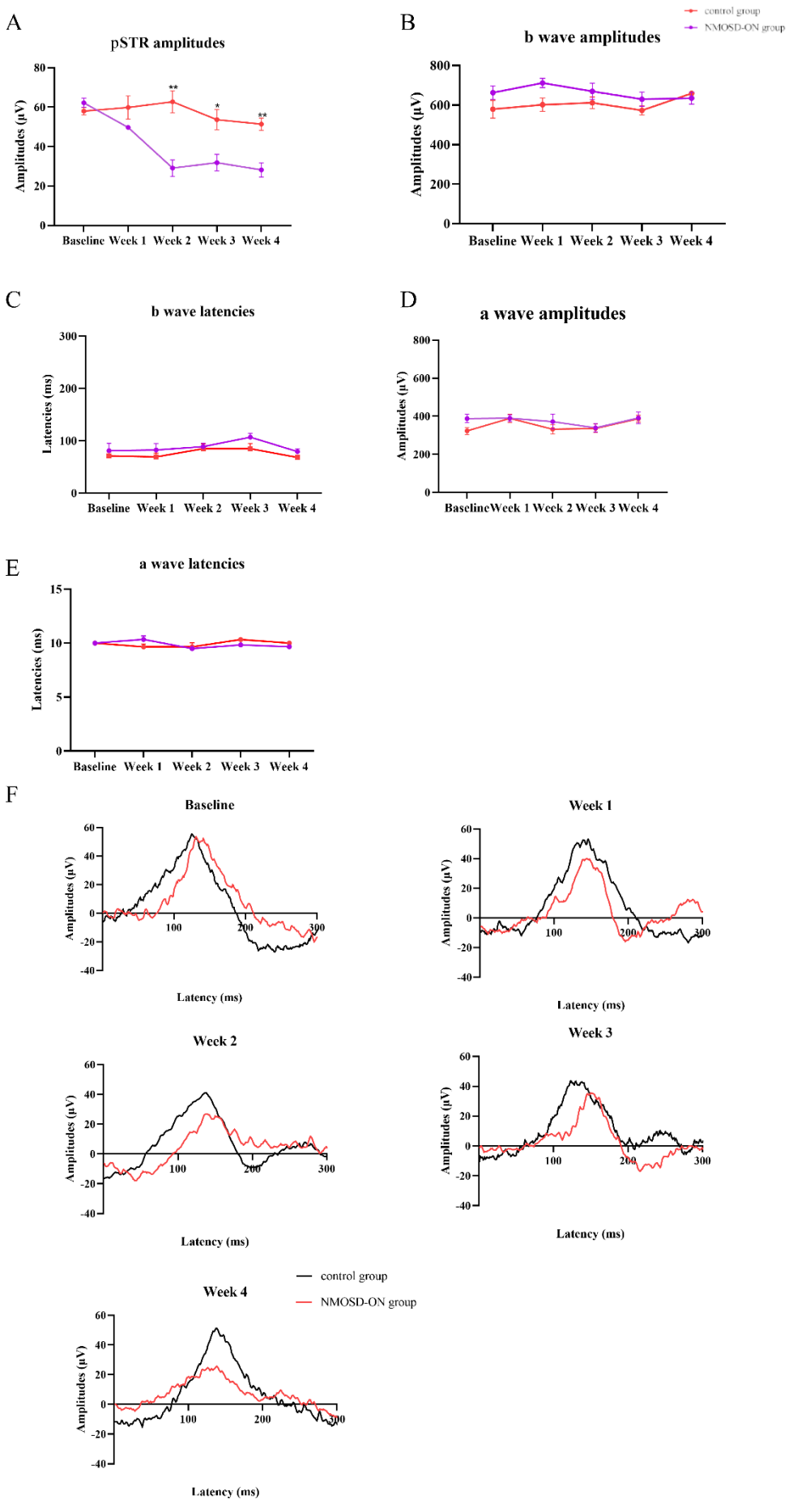
A
pSTR amplitudes
Amplitudes (μV)
Baseline Week 1 Week 2 Week 3 Week 4
B
b wave amplitudes
control group
NMOSD-ON group
C
b wave latencies
Latencies (ms)
D
a wave amplitudes
E
a wave latencies
F
Baseline
Week 1
Week 2
Week 3
Week 4
Latency (ms)

Figure 3.15 ERG analysis of NMOSD-ON across different timepoints. **(A)** The quantification of pSTR amplitude across different timepoints (n=5 mice per group, ANOVA, *p<0.05; **p<0.01). **(B, C, D, E)** The quantification of b-wave amplitude and latency, a-wave amplitude and latency across different timepoints (n=5 mice per group, ANOVA). **(F)** representative images across different timepoints.

3.4 Discussion

Our study first established a novel NMOSD-ON animal model and developed a time-dependent multi-timepoint framework, integrating both pathological and functional assessments to lay the foundation for future therapeutic interventions. This allows us to determine the optimal timepoints for specific treatments. Throughout the study, a series of disease progression changes was identified. In the earliest phase (day 2), significant AQP4 protein lysis was observed. By week 1, secondary changes emerged, including astrocytic damage, microglial activation, and inflammatory progression, which were closely linked to astrocyte injury but occurred later than AQP4 disruption — indicating a primary inflammatory injury originating from astrocytes. After week 2, ongoing deterioration was observed, including demyelination and RGCs degeneration, which were secondary to AQP4 and astrocyte damage. Functional and *in-vivo* structural (OCT) findings corroborated these pathological changes, providing robust evidence and offering valuable *in-vivo* monitoring references for future interventions. For example, the N1 latency in VEP reflects visual signal transmission speed, which is associated with myelin sheath integrity, thus serving as an *in-vivo* indicator of myelin damage. Meanwhile, the N1-P1 amplitude reflects photo-response capacity, offering insights into axonal degeneration. OCT provides a window into RGC soma bodies. These examinations, combined with

pathological findings, contribute to a more comprehensive framework.

For the establishment of the animal model, we first focused on developing a posterior optic nerve-targeted model, as this approach better simulates NMOSD-ON while avoiding nerve damage caused by meningeal dissection or excessive tissue exposure (Y. Morita et al., 2022). Moreover, our approach preserves BBB integrity. Unlike systemic NMOSD models (Xu et al., 2024), ours does not require prior induction of EAE, thereby avoiding BBB disruption. It is critical because a compromised BBB could artificially enhance drug penetration into CNS, confounding the objective assessment of systemic drug effects on CNS lesions. To achieve optimal AQP4-IgG enrichment in the optic nerve, a syringe pump was utilized for slow, controlled infusion, allowing gradual antibody accumulation. A stereotaxic frame was employed to precisely locate the injection site along the optic nerve, ensuring accurate antibody delivery. When The solution was also administered slowly by injecting with a 33-gauge fine needle. If intracranial bleeding is observed during the procedure, it may indicate large vessel damage. This can compromise the reliability of the results due to BBB disruption. Therefore, those animals exhibiting such bleeding were excluded from the study.

In this pilot study, we compared single versus double injections and found that double injections were necessary for sufficient AQP4-IgG deposition, as quantified by mean gray value and percentage of affected area ($p < 0.001$ vs. control group and single injection group, ***Figure 3.16A and C***). Additionally, C5b9 complement deposition was significantly elevated at the lesion site two days after double injections ($p = 0.005$ vs. control group; $p = 0.030$ vs. single injection, ***Figure 3.16B and C***). To track disease progression, anti-human secondary antibodies was used to label the

site of antibody deposition, which was consistently localized in the posterior optic nerve, closely adjacent to the optic chiasm. This approach provided a reliable reference for subsequent fluorescence intensity-based assessment.

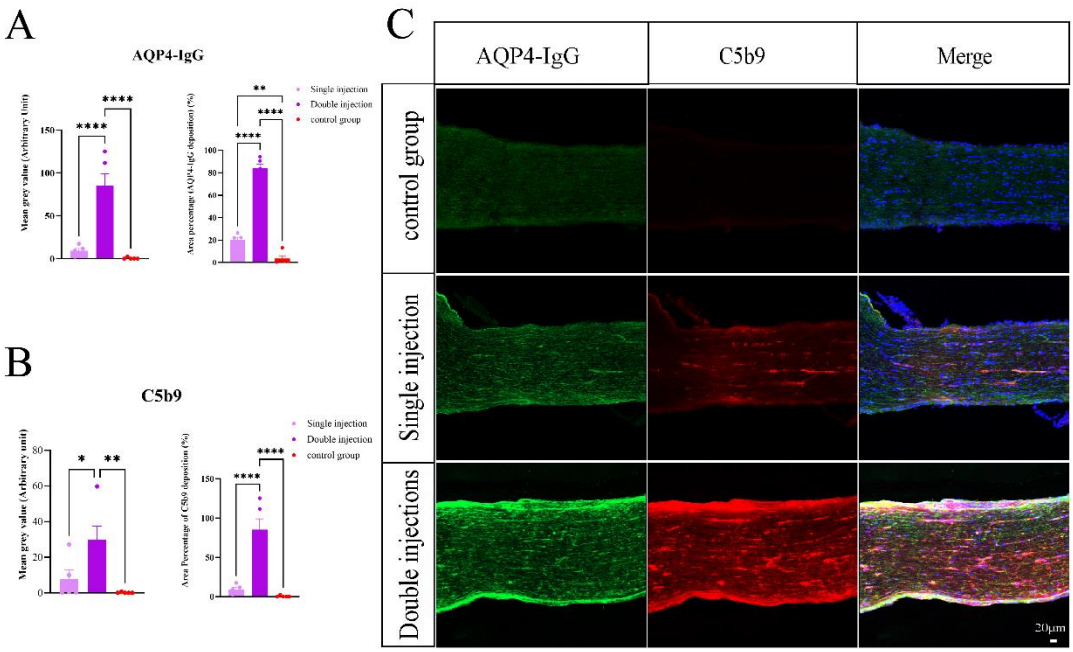

Figure 3.16 The binding of AQP4-IgG and C5b9 to the optic nerve. **(A)** Comparative analysis between one single injection and double injections as for AQP4-IgG binding (n=5 mice per group, ANOVA, ****p<0.0001). **(B)** Comparative analysis between one single injection and double injections as for C5b9 binding (n=5 mice per group, ANOVA, **** p<0.0001). **(C)** Representative images of AQP4 binding and C5b9 binding.

Our analysis revealed that AQP4 loss, a well-established pathological biomarker of NMOSD, was detectable as early as day 2 in our model — a finding consistent with observations in human autopsy samples (Lucchinetti et al., 2014) and prior NMOSD animal studies (Y. Morita et al., 2022). The timing of AQP4 loss critically depends on the method of AQP4-IgG delivery: direct CNS-targeted administration (e.g., intracranial, intrathecal, or optic nerve sheath injection) induces rapid and pronounced AQP4 depletion (Asavapanumas, Ratelade, Papadopoulos, et al., 2014; Y. Morita et al.,

2022; Soerensen et al., 2021; Zhang et al., 2018), whereas systemic models relying on peripheral antibody injection exhibit delayed AQP4 loss due to the additional step of BBB penetration (Bennett et al., 2009; Kinoshita & Nakatsuji, 2012). The choice of AQP4-IgG further influences this timeline — heterogeneous antibodies from NMOSD patient sera often yield variable and inefficient AQP4 depletion (Duan & Verkman, 2020), while recombinant engineered AQP4-IgG, with superior binding affinity and specificity, accelerates complement activation (Lennon et al., 2004; Phuan et al., 2012) and thus AQP4 loss. Importantly, across all models, AQP4 loss precedes other pathological changes, marking the earliest detectable event in disease initiation (Duan & Verkman, 2020).

We also examined pathological changes in astrocytes (labeled by GFAP). Astrocytic alterations emerged at week 1, secondary to AQP4 disruption, with partial recovery observed by week 4 — a pattern consistent with previously reported NMOSD pathology (Asavapanumas, Ratelade, Papadopoulos, et al., 2014; Saadoun et al., 2013; Zhang et al., 2018). These findings suggested that effective astrocyte protection must be targeted within the first week to prevent progression to irreversible damage. The observed partial GFAP recovery demonstrated astrocytes' intrinsic capacity for regeneration, though this appeared insufficient to fully protect against axonal injury. Nevertheless, this endogenous recovery mechanism may reveal potential therapeutic targets (Lucchinetti et al., 2014).

The process of demyelination is as follows: Oligodendrocytes, which utilize MOG as a biomarker (Tea et al., 2019), are structural proteins and supporting cells for the myelin sheath (Felix et al.,

2016). In contrast to multiple sclerosis, NMOSD-related demyelination arises from astrocyte damage and inflammation rather than being directly induced by inflammatory processes, with astrocytes being the primary cells affected (Marignier et al., 2021). These findings align with human demyelination data (Lucchinetti et al., 2014). A progressive loss of MOG protein from the second to the fourth week marks the worsening of demyelination (Lagumersindez-Denis et al., 2017).

In our animal model, the observed degeneration of RGC axons and soma bodies aligns with findings from other animal models (Duan & Verkman, 2020). This is consistent with the eventual involvement of RGCs in NMOSD-ON (Lucchinetti et al., 2014). The absence of detectable neuronal damage in the early stages matches clinical-pathological observations, as the disease does not initially affect RGCs (Asavapanumas, Ratelade, Papadopoulos, et al., 2014; Zhang et al., 2018).

In-vivo retinal structural monitoring allows us to observe changes in RGCs within the retina, with thinning thickness serving as a key indicator of RGC degeneration (Ratchford et al., 2009). Our findings revealed that the RNFL of RGCs began to thin by the second week, consistent with previous reports (Zhang et al., 2018), further supporting the feasibility of *in-vivo* monitoring of RGC degeneration in our model. However, no changes were observed in the thickness of the INL and GCIPL layers, indicating that they cannot serve as reliable biomarkers for detection.

ERG and VEP serve as effective tools for evaluating functional impairment at the retinal and whole visual pathway levels, respectively, while also providing prognostic assessment of therapeutic interventions (Hamilton, 2021). In our animal model, we observed progressive deterioration of the

pSTR, reflecting dysfunction of RGCs soma bodies, which correlated with pathological RGC damage (Lakshmanan et al., 2023). The photopic negative response (pSTR) primarily reflects the function of the inner retinal layers. Meanwhile, the a- and b-wave amplitudes elicited by light adaptation are indicators of photoreceptor and bipolar cell activity, respectively. In contrast, while the pattern electroretinogram (PERG) can also assess retinal ganglion cell (RGC) function, it more specifically reflects the activity of localized RGCs in the human macular region(Wang et al., 2021). The absence of changes in a- and b-waves suggests relative preservation of outer retinal function, as inner retinal layers are typically less affected in optic neuritis (Zheng et al., 2022).

VEP measurements revealed progressive decline in N1-P1 amplitude, indicative of worsening axonal integrity in NMOSD-ON (Zhang et al., 2018). Furthermore, delayed N1 latency reflected ongoing demyelination, marking disease progression (You et al., 2011). These functional parameters establish a reliable framework for longitudinal monitoring of disease progression and evaluation of therapeutic efficacy in preclinical studies.

Our animal model possesses several unique advantages compared to other existing models. First, most current approaches require systemic delivery of AQP4-IgG following prior induction of Experimental Autoimmune Encephalomyelitis (EAE) to weaken the BBB (Bennett et al., 2009). However, since EAE itself, as a MS disease model, can cause demyelination, this confounding factor makes it difficult to determine whether disease progression stems from EAE pathology or direct AQP4-IgG attack (Duan & Verkman, 2020).

Additionally, BBB disruption in these models may complicate the evaluation of systemic drug efficacy, as compromised barrier function allows easier CNS penetration of therapeutic agents. In contrast, our model avoids BBB disruption and more accurately mimics targeted antigen-antibody interactions at specific sites, with demyelination occurring secondarily following astrocyte injury — better recapitulating human NMOSD pathology. Furthermore, conventional systemic models often fail to reproduce RGC soma body damage (H. Saini et al., 2013; Zeka et al., 2016), whereas our model successfully replicates this key pathological feature. This makes our model particularly valuable for longitudinal *in-vivo* monitoring of neuronal injury progression and therapeutic interventions.

Our study has several limitations that warrant discussion. While our model offers novel insights, there remains important unanswered questions regarding potential intercellular communication through inflammatory mediators and how these signaling pathways may influence disease progression. Furthermore, our observation period was relatively short — although we detected emerging trends of astrocyte recovery, it remains unclear whether this regeneration continues over longer timeframe and achieves more complete restoration. Critical questions persist about whether naturally occurring astrocyte recovery in later stages could fully rescue RGC degeneration and lead to functional visual recovery. These knowledge gaps represent important directions for future research to better understand the therapeutic potential of enhancing astrocyte regeneration in NMOSD pathogenesis.

3.5 Conclusion

Based on previously established animal models of NMOSD-ON, we have developed our own optimized NMOSD-ON animal model by refining key experimental conditions. Using this model, the temporal dynamics of pathological and functional changes was systematically investigated, with a particular focus on cell-specific responses and inflammatory progression. Our findings reveal a well-defined sequence of events that provide critical insights into the precise timing of cellular damage and degeneration.

Specifically, we observed that AQP4 protein is rapidly disrupted at the earliest stage, immediately following antibody exposure, indicating an acute attack on astrocytic integrity. Subsequently, astrocytes undergo secondary destruction and trigger a robust inflammatory response, mediated by complement activation, cytokine release, and immune cell infiltration. Importantly, myelin sheath breakdown and axonal degeneration occur later, following astrocytic damage, suggesting that oligodendrocyte dysfunction and neuronal injury are downstream consequences of the initial astrocyte-targeted pathology.

This chronological cascade is crucial for guiding therapeutic interventions. For anti-inflammatory strategies, early-stage monitoring (within hours to days) is essential, as this is when AQP4 loss and astrocyte-driven inflammation are most active. For myelin protection and neural repair, interventions should target the intermediate to late phases (days to weeks), when oligodendrocyte vulnerability and axonal degeneration become prominent. By delineating these critical time

windows, our study not only enhances the understanding of NMOSD-ON pathogenesis but also provides a framework for precision timing of therapeutic interventions, whether aimed at suppressing acute inflammation or promoting long-term neuroprotection and regeneration.

Chapter 4 Evaluating the LBGP treatment in NMOSD-ON animal model

4.1 Introduction and literature reviews

NMOSD-ON frequently induces severe refractory neurodegeneration in the optic nerve, which can result in permanent visual dysfunction. Given the crucial involvement of neutrophils (Iwamoto et al., 2022), microglia (T. Chen et al., 2020), and their associated inflammatory mediators in the disease pathogenesis, therapeutic agents capable of effectively modulating these immune cells may represent promising treatments for this condition.

Conventional treatments (e.g., steroids, immunosuppressants) may cause various side effects, limiting their widespread and long-term use (Carnero Contentti & Correale, 2021). This compels us to explore alternative approaches, such as Traditional Chinese Medicine (TCM). Wolfberry and its isolated compounds have demonstrated anti-inflammatory (Lan et al., 2024), antioxidative and neuroprotective effects (Y. Dai et al., 2023) in various animal models. Additionally, its ability to modulate multiple immune cells, including neutrophils (Yan et al., 2025) and microglia (Ni et al., 2024), suggests it as a potential and effective treatment for NMOSD-ON.

Wolfberry, the fruit of the Lycium barbarum (LB) plant, is frequently utilized for its neuroprotective effects in various neurotoxic conditions leading to neuronal injury. Initially, in Alzheimer's disease models, we observed that it reduces the levels of the apoptosis-related protein caspase-3, subsequently inhibiting the elevation of inflammation-related pathway proteins phosphorylated-ERK (p-ERK) and phosphorylated-JNK (p-JNK) (Ho et al., 2010) while simultaneously upregulated Bcl-2 for apoptosis prevention (Qi et al., 2022). In the context of utilizing pre-treatment of wolfberry as a therapeutic agent in the Partial Optic Nerve Transection animal model, multifocal electroretinography (mfERG) assessments have revealed a notable restoration of retinal function corresponding to the optic nerve injury (Chu et al., 2013). Lycium barbarum glycopeptide (LBGP), an extract derived from the wolfberry, has also been utilized in models of glaucoma induced by vascular dysregulation, demonstrating significant protective effects (Lakshmanan et al., 2024). The authors observed notable vasodilation within the retinal vasculature, accompanied by an increase in vascular supply. Furthermore, the RGCs exhibited both morphological and functional preservation, underscoring the potential therapeutic benefits of LBGP in mitigating the adverse effects associated with glaucoma (Lakshmanan et al., 2024). In the context of animal models for both acute ocular and chronic ocular hypertension (Chan et al., 2007), the protective effects of wolfberry on retinal ganglion cells (RGCs) are notably significant. Furthermore, in patients with normal-tension glaucoma, we have identified that wolfberry effectively protects against the thinning of the RNFL (Lai et al., 2022; Lakshmanan et al., 2023). These findings underscore the potential of Wolfberry in promoting neuroprotective effects and facilitating functional recovery in optic nerve damage (Qi et al., 2022).

4.2 Objectives

The primary objective of this study was to investigate the therapeutic potential of LBGP in NMOSD-ON. Specifically, we aimed to determine the following issues.

1. What is the recommended approach for LBGP in NMOSD-ON, including ideal dosage and timing (pre-treatment vs. post-treatment)?
2. Whether LBGP exerts its effects primarily on astrocytes (to mitigate AQP4 degradation and secondary inflammation), oligodendrocytes (to promote remyelination), or microglia/macrophages (to modulate neuroinflammation).
3. Whether LBGP treatment leads to measurable improvements in visual function, including optic nerve conduction (evaluated via VEP, and ERG).

By addressing these questions, this study seeked to establish LBGP as a novel, cell-specific therapeutic strategy for NMOSD-ON, with potential applications in both acute neuroprotection (early-phase intervention) and chronic repair (late-phase recovery).

4.3 Methods

4.3.1 Animal ethics in this study

Please refer to **Section 3.2.1** within the **Methods subsection** of **Chapter 3**.

4.3.2 Delivered AQP4-IgG

Please refer to **Section 3.2.2** within the **Methods subsection** of **Chapter 3**. The animal model in this study was established using the recombinant rab53 (AQP4-IgG) as outlined in Chapter 3.

4.3.3 LBGP feeding

LBGP was provided by Ningxia Tianren Goji Biotechnology Co., Ltd. Separation and purification of LBGP, employing gel filtration chromatography and ion exchange chromatography, yielded a product with a purity of 93%(Y. Wu et al., 2025). LBGP is a glycoconjugate composed of various monosaccharides—such as arabinose, galactose, and glucose—covalently linked to a protein moiety, with the protein content approximately 30% by composition . It typically exists as a peptidoglycan with a short peptide backbone and a complex, branched glycan structure (Y. Wu et al., 2025). LBGP was fed to the mice by nasogastric gavage.

4.3.4 The identical animal model as previous study for assessing the effectiveness of LBGP

Please refer to **Section 3.2.3** within the **Methods subsection** of **Chapter 3**. To assess the efficacy of LBGP, the same animal model reported in **Chapter 3** was reproduced.

4.3.5 Immunostaining

Please refer to **Section 3.2.4** within the **Methods subsection** of **Chapter 3**.

4.3.6 Western blot

Please refer to **Section 3.2.5** within the **Methods subsection** of **Chapter 3**.

The list of antibodies used in this chapter is as follows.

Table 4.2 Antibodies used for western blotting in the optic nerve

	Antibodies (host)	Company	RRID no.	Cat#	Dilution
Primary antibodies	GAPDH (Mouse)	Millipore, Burlington, MA, USA	AB_2107426	CB1001	1:1000
	GFAP (Rabbit)	Dako, Glostrup, Denmark	AB_10013382	z0334	1:1000
	MOG (Mouse)	Millipore, Burlington, MA, USA	AB_1587278	MAB5680	1:1000
	NF200 (Mouse)	Sigma, St. Louis, MO, USA	AB_477257	N0142	1:1000
Secondary antibodies	Goat anti mouse-HRP	ABclonal, Woburn, MA, USA	AB_2769851	AS003	1:1000
	Goat anti rabbit-HRP	Cell signaling technology, Danvers, Massachusetts, USA	AB_2099233	7074S	1:1000

4.3.7 Functional evaluation

4.3.7.1 OKR measurement

The mouse was placed on a circular central platform, surrounded by screens displaying rotating black-and-white grating stimuli. The gratings could rotate either clockwise or counterclockwise around the mouse. The width of the grating stripes corresponded to the spatial frequency of the stimulus.

To assess the mouse's visual acuity, we observed whether it exhibited a tracking response (head movement) in response to different grating stripe widths. The presence or absence of this optomotor reflex at varying spatial frequencies allowed us to determine the mouse's ability to perceive the visual stimulus.

4.3.7.2 ERG, VEP measurements

Please refer to **Section 3.2.7** within the **Methods subsection** of **Chapter 3**.

4.3.8 *In-vivo* structural measurement

Please refer to **Section 3.2.8** within the **Methods subsection** of **Chapter 3**.

4.4 Results

Previous studies have demonstrated that pre-treatment with LBGP one week before disease onset exerts therapeutic effects in NMOSD-ON (Kong et al., 2024). To optimize the treatment regimen, we first evaluated different doses of LbGp (20, 50, and 100 mg/kg) by pre-treating animals and measuring optic nerve Interleukin-6 (IL-6) levels one week post-onset, given IL-6's critical role in disease progression (Carnero Contentti & Correale, 2021). The results showed that while 20 mg/kg failed to significantly suppress IL-6 elevation, both 50 mg/kg ($p < 0.001$) and 100 mg/kg ($p < 0.001$) effectively inhibited IL-6 levels, leading to select 50 mg/kg as the optimal dose to balance efficacy and potential side effects ***(Figure 4.1)***. There are two possible explanations for why the 50mg/kg dose appears more effective than the 100mg/kg dose. 1.While the 50 mg/kg dose of LBGP may provide a beneficial stimulatory effect that enhances its anti-inflammatory capacity, the 100 mg/kg dose might induce cellular stress or mild toxicity. This adverse effect could counteract its primary intended action, leading to a reduced ability to suppress IL-6. 2. It is possible that at the 50 mg/kg dose, the target receptors responsible for the IL-6 inhibition are already nearly fully saturated. Consequently, increasing the dose to 100 mg/kg does not produce a linear increase in therapeutic

effect. Instead, the excessive stimulation can trigger receptor desensitization, where the cell's response to the drug is blunted. This mechanism can result in a diminished effect at the higher dose.

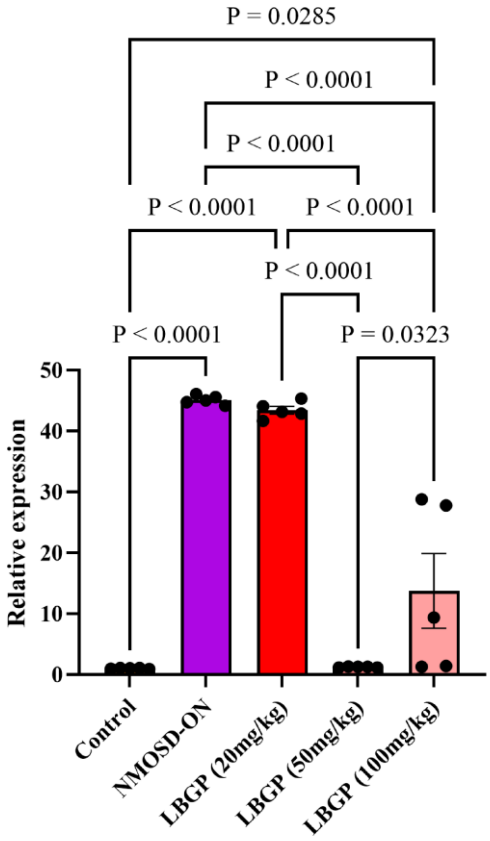

Figure 4.1 IL-6 inhibitory effect was used to determine the dosage. RT-qPCR analysis was performed to assess IL-6 expression one week after the animal model was induced, with varying doses of LBGP treatment. Compared to the AQP4-ON group, the 20 mg/kg dosage did not significantly suppress IL-6 levels. However, the 50 mg/kg and 100 mg/kg dosages showed a significant reduction in IL-6 expression. (n=5 mice per group, ANOVA, *p<0.05, **p<0.01, ***p<0.001, ****p<0.0001).

We next investigated whether 50mg/kg LBGP could be administered after disease onset rather than as pre-treatment as previously reported. Assessment of IL-6 levels one week post-onset revealed that post-treatment did not significantly suppress IL-6 ($p > 0.05$), whereas pre-treatment maintained

its inhibitory effect (p = 0.005) ***(Figure 4.2A)***. Similarly, evaluation of retinal ganglion cell (RGC) axon protection through NF200 expression demonstrated that post-treatment failed to preserve axons (p > 0.05 vs. NMOSD-ON), while pre-treatment significantly maintained NF200 levels (p = 0.044) ***(Figure 4.2B)***.

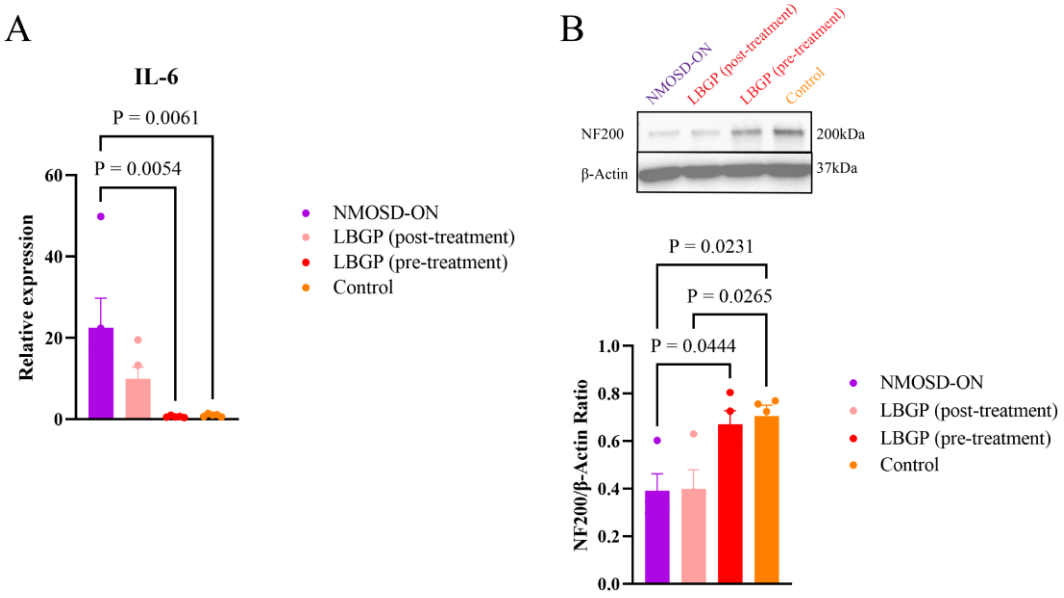

Figure 4.2 Pre-treatment is the only effective approach in NMOSD-ON. **(A)** The pre-treatment significantly reduces elevated IL-6 levels. **(B)** The pre-treatment significantly preserves NF200 expression (n=5 mice per group, ANOVA, *p<0.05, **p<0.01).

To rule out potential neurotoxic effects of LBGP on the optic nerve, we treated animals with 50 mg/kg LBGP for five weeks and examined changes of key markers over time, including AQP4 protein ***(Figure 4.3A, and 4.3B)***, GFAP-labeled astrocytes ***(Figure 4.3A and 4.3C)***, MOG-marked oligodendrocytes ***(Figure 4.3D and 4.3E)***, and NF200-labeled RGC axonal integrity ***(Figure 4.3F and 4.3G)***, confirming no adverse effects as compared to PBS-treated animals (all p > 0.05).

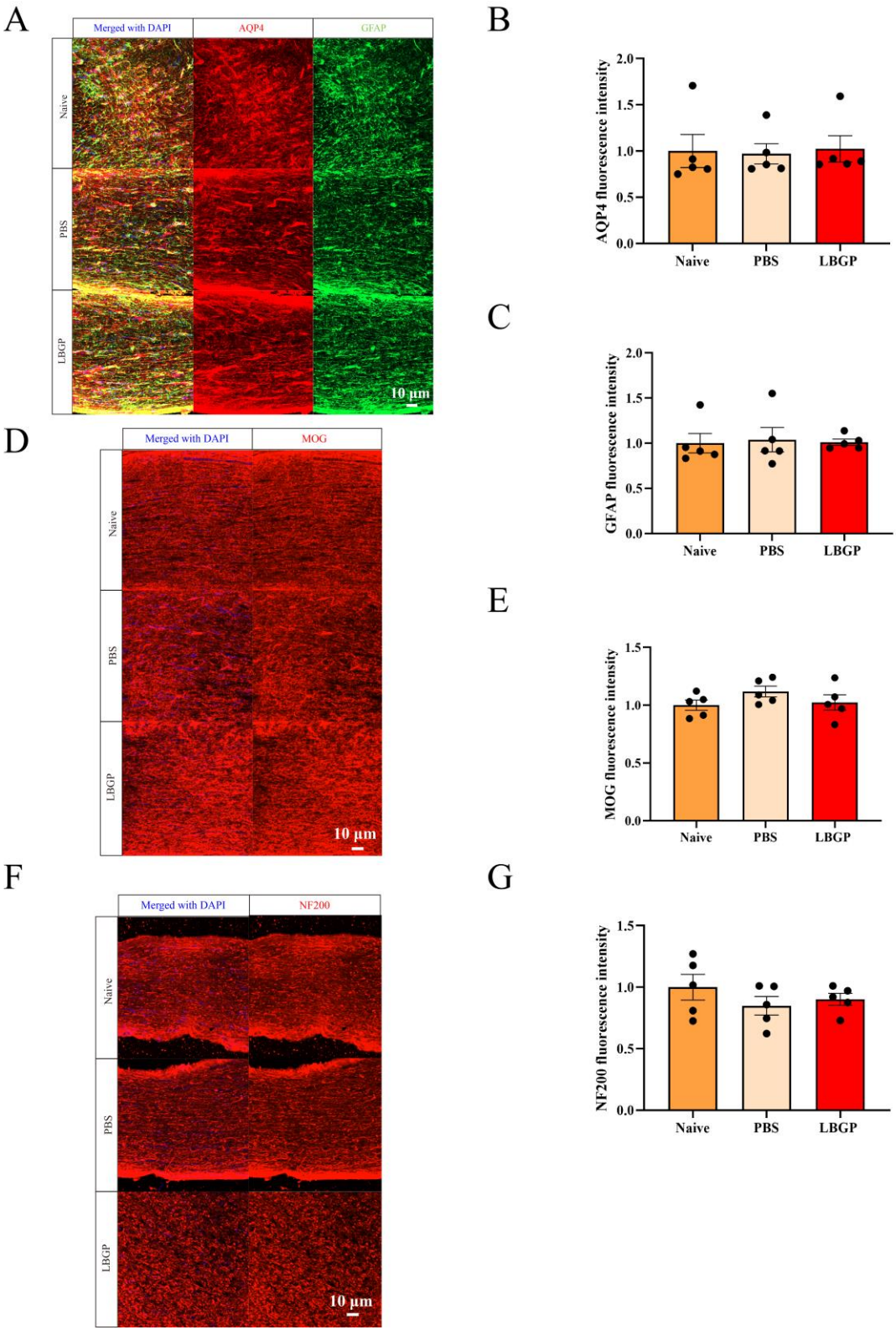

Figure 4.3 Drug toxicity evaluation based on AQP4, GFAP, MOG, and NF200 immunoreactivity.

The immunoreactivities of AQP4, GFAP, MOG, and NF200 were evaluated in PBS-treated,

LBGP-treated, and naïve mice one week after drug administration. No significant differences were detected among the three groups in AQP4 and GFAP expression **(A)**. The quantification of AQP4 and GFAP immunoreactivity was presented in **B** and **C** (n=5 mice per group, ANOVA). Similarly, no significant difference was observed across three groups in MOG expression in representative images **(D)**. The quantification of MOG expression was presented in E (n=5 mice per group, ANOVA). No significant difference was observed across three groups in MOG expression in representative images **F**. The quantification of MOG expression was presented in **G** (n=5 mice per group, ANOVA).

To investigate whether LBGP could mitigate astrocyte damage in NMOSD-ON, we assessed its effects at week 1 and 4 post-disease onset. LBGP (50 mg/kg) was administered one week prior to NMOSD-ON induction, and optic nerve samples were collected at different timepoints for immunofluorescence analysis ***(Figure 4.4)***.

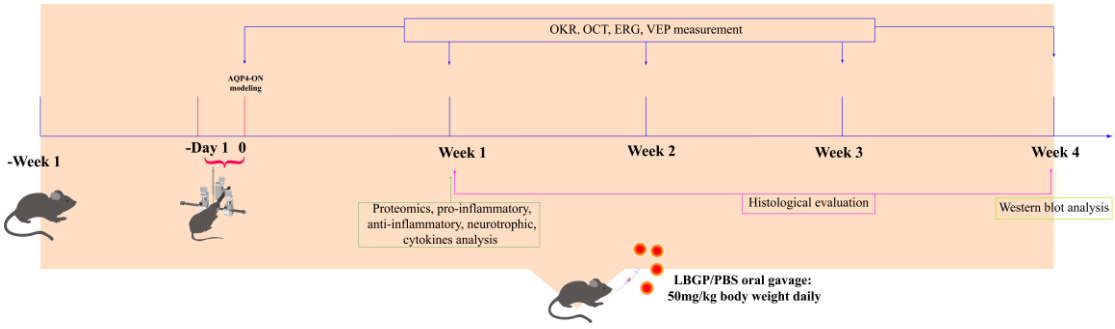

Figure 4.4 Experimental timeline illustrating the LBGP feeding, samples collection for histological evaluation, cytokines measurement.

First, we examined whether LBGP could reduce the binding of delivered AQP4-IgG (labeled by an anti-human antibody) and complement (labeled by anti-C5b-9) to the optic nerve. At week 1, LBGP treatment did not significantly decrease the attachment of AQP4-IgG or complement deposition

(Figure 4.5A, B, and C).

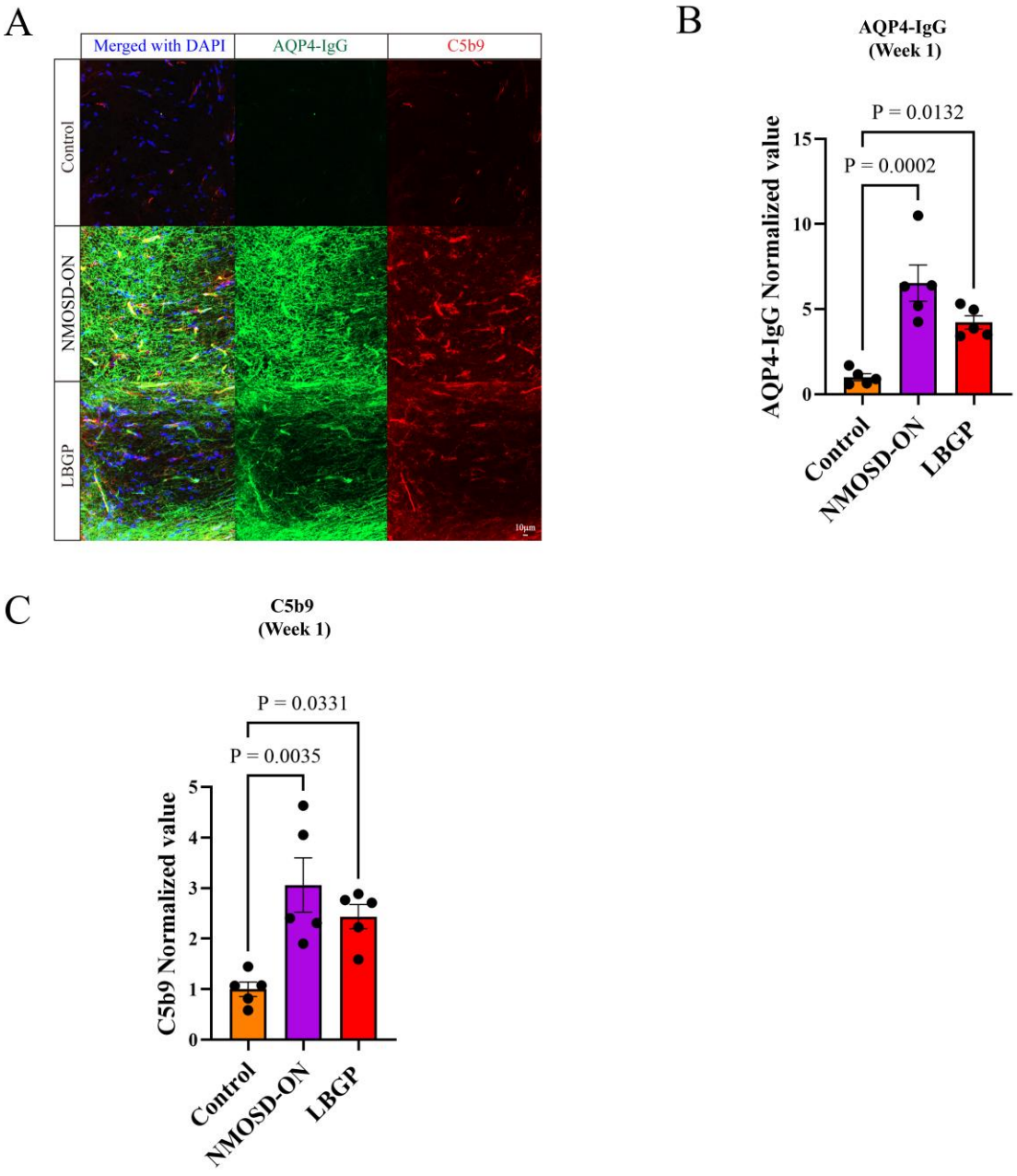

Figure 4.5 LBGP cannot reduce the binding of AQP4-IgG and complement to the optic nerve. **(A)** The representative images illustrating the binding of AQP4-IgG and complement to the optic nerve. **(B)** Quantification of AQP4-IgG (labeled by anti-human antibodies) showed that the LBGP cannot reduce the binding of AQP4-IgG to the optic nerve (n=5 mice per group, ANOVA,

*p<0.05, ***p<0.001). **(C)** Quantification of C5b9 showed that the LBGP treatment cannot reduce the complement (labeled by C5b9 antibody) deposition on the optic nerve (n=5 mice per group, ANOVA, *p<0.05, **p<0.05).

We also evaluated whether early-stage (week 1 post-onset) AQP4 and astrocytes (labeled by GFAP) were damaged. LBGP was shown not able to attenuate the extent of AQP4-IgG-mediated AQP4 protein degradation ***(Figure 4.6A and B)***. Similarly, LBGP failed to mitigate NMOSD-ON-induced astrocyte damage in the early phase (one week post-onset) ***(Figure 4.6A and C)***.

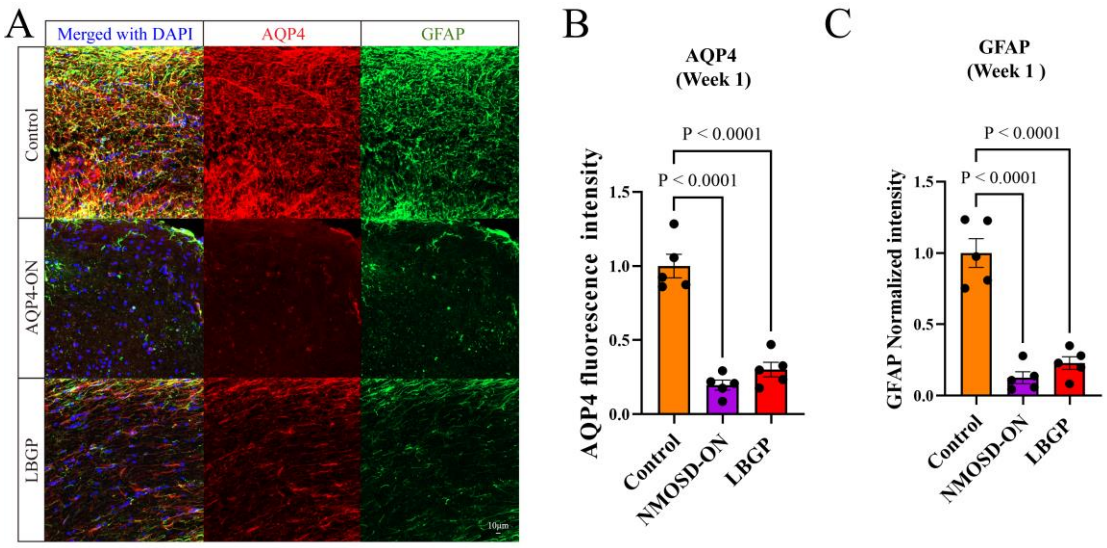

Figure 4.6 The LBGP cannot attenuate the astrocyte pathology at Week 1. **(A)** The representative of AQP4 (red, labeled by anti-AQP4 antibody), and astrocyte (green, labeled by GFAP antibody). **(B)** The quantification of AQP4 protein at week 1 showed that the LBGP treatment cannot reduce the AQP4 protein damage (n=5 mice per group, ANOVA, ****p<0.0001). **(C)** The quantification of GFAP protein at week 1 showed that the LBGP treatment cannot ameliorate the astrocyte damage (n=5 mice per group, ANOVA, ****p<0.0001).

At four weeks post-onset (after five weeks of LBGP treatment), the therapeutic effects of LBGP were further evaluated. While LBGP still did not significantly reduce AQP4 degradation ***(Figure 4.7A and B)***, it demonstrated a clear protective effect on astrocytes (labeled by GFAP) (p = 0.002) ***(Figure 4.7A and C)***.

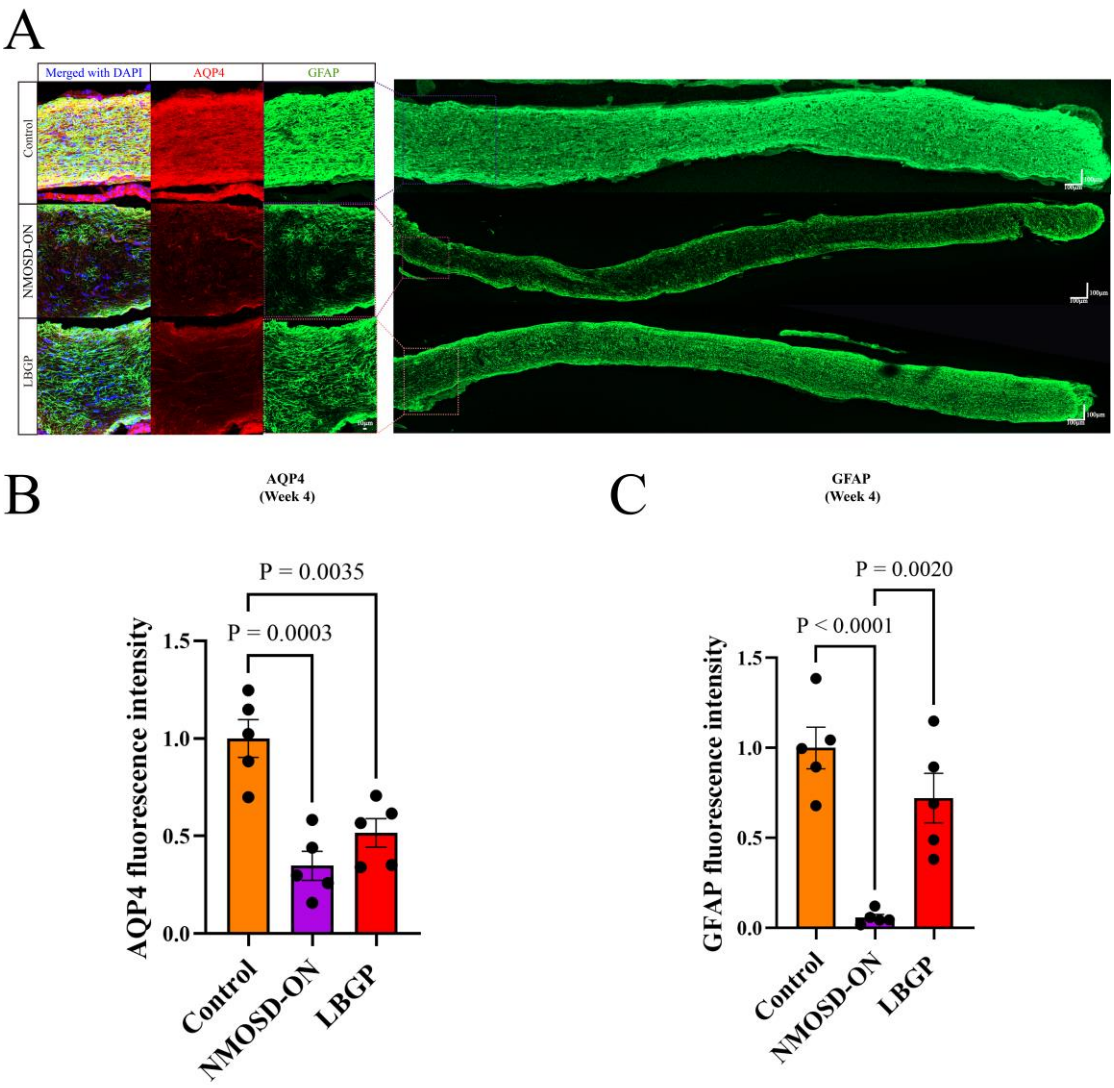

Figure 4.7 The LBGP cannot attenuate the AQP4 protein damage but protect the astrocyte integrity in NMOSD-ON. **(A)** The representative images of AQP4 and GFAP at week 4 in NMOSD-ON optic nerve **(B)** The quantification of AQP4 protein at week 4 revealed no

significant recovery of AQP4 protein in NMOSD-ON (n=5 mice per group, ANOVA, **p<0.01, ***p<0.001). **(C)** The quantification of GFAP protein at week 4 revealed significant recovery of astrocytes in NMOSD-ON (n=5 mice per group, ANOVA, **p<0.01, ****p<0.0001).

We also examined whether LBGP could safeguard the myelin sheath, composed of oligodendrocytes (labeled by MOG), at week 4. Strikingly, LBGP treatment significantly preserved myelin integrity ($p < 0.0001$) ***(Figure 4.8A and B)***.

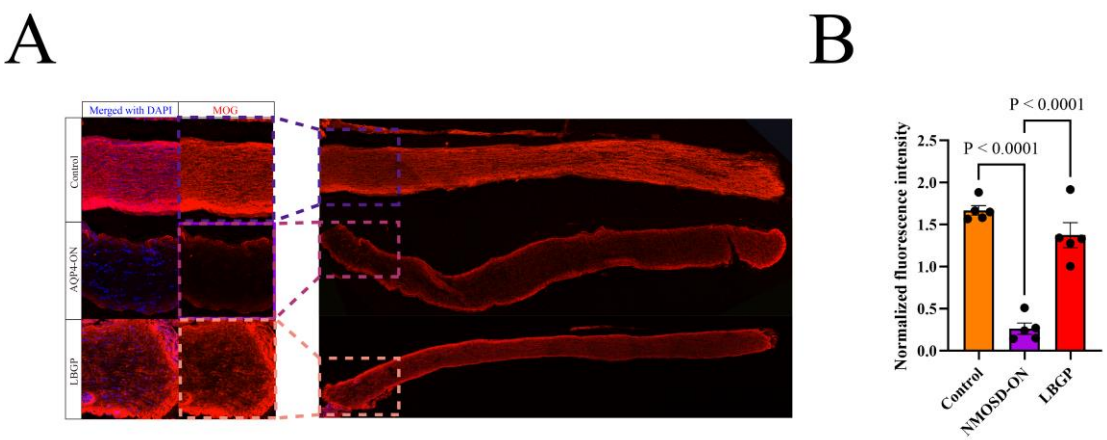

Figure 4.8 The LBGP protects the myelin sheath at week4. **(A)** The representative images of myelin sheath (labeled by MOG antibody). **(B)** The quantification of MOG protein revealed that the LBGP treatment cannot protect the myelin sheath effectively (n=5 mice per group, ANOVA, ****p<0.0001).

The astrocyte preservation was further confirmed by Western blot, showing a significant increase in GFAP levels ($p = 0.005$) ***(Figure 4.9A and B)***.

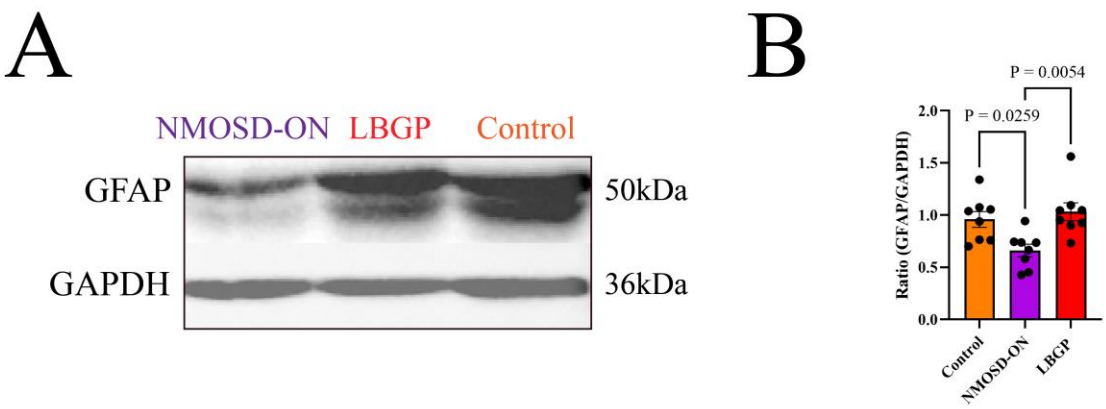

Figure 4.9 The western blot analysis validated the recovery of GFAP expression after LBGP treatment. **(A)** The representative western blot image illustrates the higher GFAP protein expression after LBGP treatment. **(B)** The quantitative analysis of GFAP expression in western blot revealed the recovery of astrocyte damage after LBGP treatment (n=5 mice per group, ANOVA, *p<0.05; **p<0.01).

The finding of MOG protein protection was also corroborated by Western blot analysis ($p < 0.0001$) ***(Figure 4.10 H and I)***.

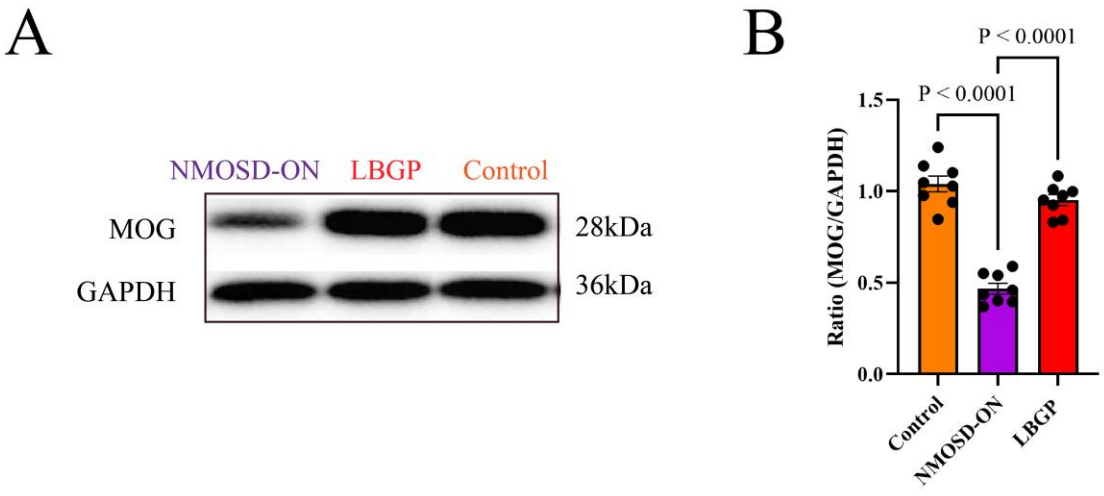

Figure 4.10 The myelin sheath of optic nerve was preserved following the LBGP treatment. **(A)** The representative image of western blot showed the protective role of LBGP in myelin sheath

integrity (labeled by MOG protein). **(B)** The quantitative analysis revealed the significant increase of MOG/GAPDH ratio in western blot analysis (n=5 mice per group, ANOVA; ****p<0.0001).

Collectively, these results suggest that by the fourth week post-onset (five weeks of LBGP treatment), LBGP successfully reverses NMOSD-ON-induced damage, particularly in protecting astrocytes and myelin sheaths. To further investigate whether LBGP could rescue RGCs degeneration in NMOSD-ON, we first observed that RGCs axons (labeled by NF200) were significantly restored by LBGP treatment at week 4 post-onset (p = 0.009) ***(Figure 4.11A and B)***.

Figure 4.11 LBGP treatment protects the axons of RGCs. **(A)**The representative images of axons of RGCs labeled by NF200 revealed the protective effect of LBGP on RGCs axons. **(B)** The quantitative analysis of NF200 expression revealed the significant recovery of RGCs axons after LBGP treatment (n=5 mice per group, ANOVA; **p<0.01, ***p<0.001).

This protective effect was further confirmed by Western blot analysis (p < 0.0001) ***(Figure 4.12A and B)***.

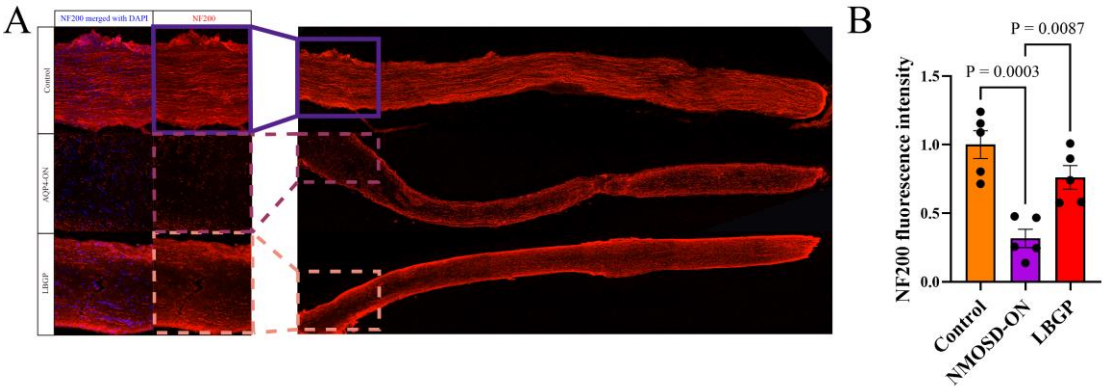

Figure 4.12 The recovery of NF200 after LBGP treatment was confirmed in western blot analysis

in NMOSD-ON. **(A)** The representative western blot image of NF200 expression revealed the increased NF200 blot intensity. **(B)** The quantitative result showed the significant recovery of NF200 expression after LBGP treatment (n=5 mice per group, ANOVA; **p<0.01, ***p<0.001).

Additionally, quantification of RGC soma bodies within the retina revealed that LBGP treatment significantly preserved their numbers ($p < 0.001$) ***(Figure 4.13A and B)***.

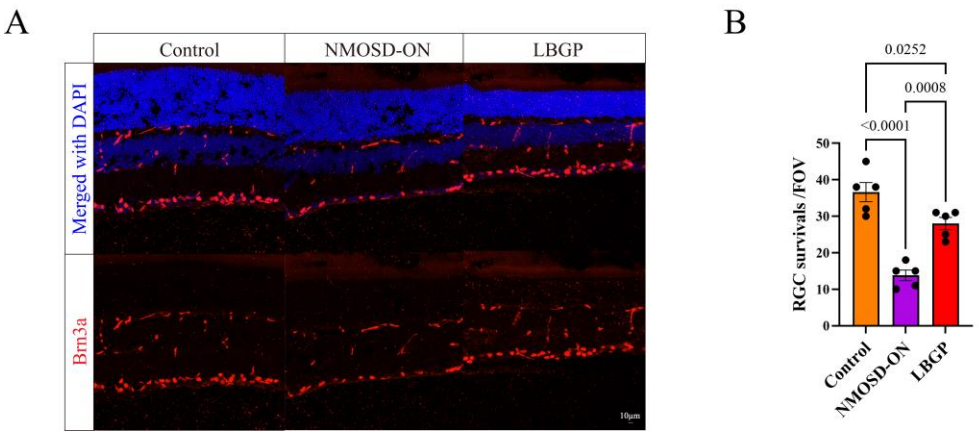

Figure 4.13 LBGP rescues the RGCs degeneration in NMOSD-ON at week 4. **(A)** Representative images illustrating the RGCs (labeled by Brn3a, red) loss in NMOSD-ON and the treatment effect of LBGP. **(B)** The quantitative results confirmed the significant recovery of RGCs soma bodies survival in NMOSD-ON (n=5 mice per group, ANOVA, *; p<0.05; ***p<0.001, ****p<0.0001).

RT-qPCR results at the RNA level supported these findings, demonstrating a marked recovery in the relative expression of POU Domain, Class 4, Transcription Factor 1 (Pou4f1) transcripts, representing the RGCs soma bodies, following LBGP treatment ($p = 0.032$) ***(Figure 4.14)***.

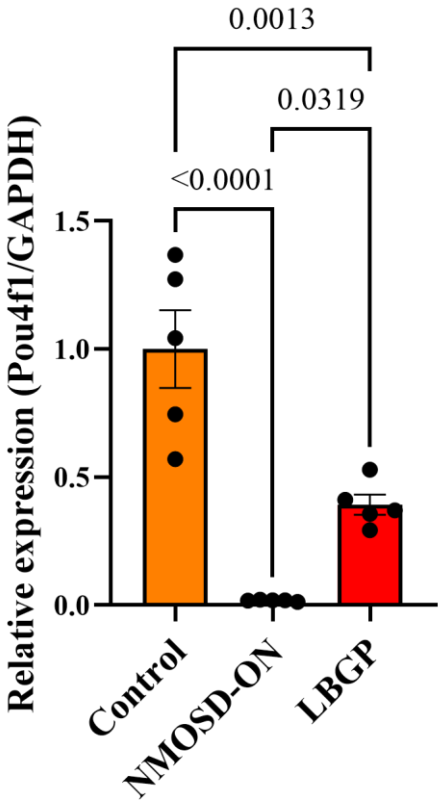

Figure 4.14 The RT-qPCR results illustrate the transcripts of RGCs soma bodies (Pou4f1). Pou4f1 increased after LBGP treatment (n=5 mice per group, ANOVA, *p< 0.05; **p<0.01; ****p<0.0001).

Taken together, these results indicate that LBGP treatment effectively mitigates RGCs degeneration in NMOSD-ON, preserving both axonal integrity and neuronal survival.

We employed OCT to monitor degenerative changes in the optic nerve by measuring the thickness of the retinal nerve fiber layer (RNFL) and the retinal ganglion cell (RGC) layer ***(Figure 4.15A)***, with longitudinal follow-up at multiple timepoints. The LBGP treatment was demonstrated to significantly preserve RNFL thickness against degenerative changes in NMOSD-ON at week 2 ($p = 0.005$). This protective effect on RNFL thickness also remained statistically significant at week 3 ($p = 0.003$) and week 4 ($p = 0.028$) post-onset ***(Figure 4.15B and C)***. However, no significant

changes were observed in the thickness of the ganglion cell-inner plexiform layer (GCIPL) throughout the observation period ***(Figure 4.15B and D)***.

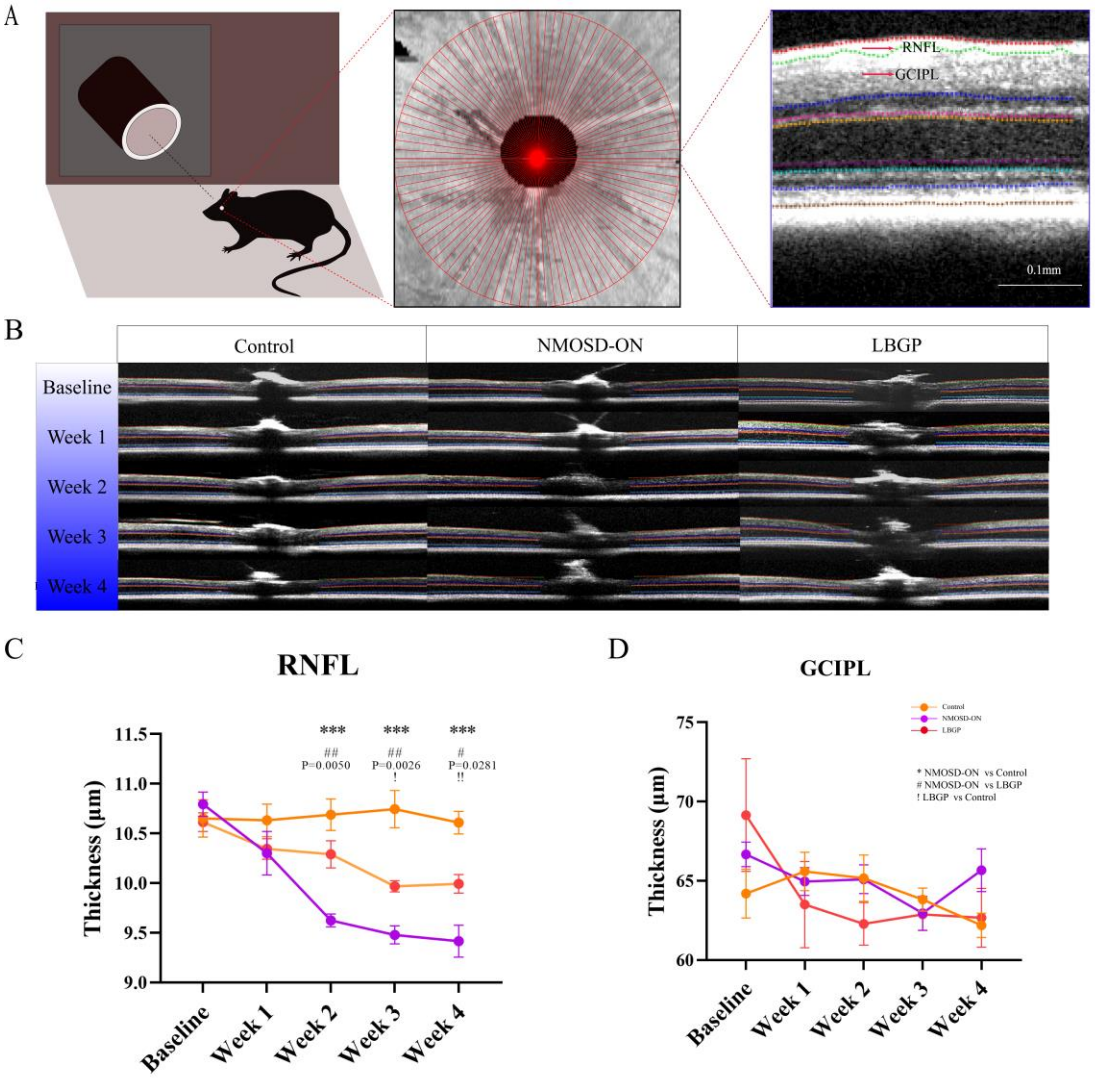

Figure 4.15 The OCT observation across different timepoints showed the RGCs recovery in NMOSD-ON. **(A)** The retinal OCT provides multi-directional scans across different axis after aligning the optic disc. The segmentation offers measurements of different retinal layers. **(B)** The representative images of OCT scans illustrate the recovery of RNFL thickness recovery after LBGP treatment. **(C)** The quantitative analysis elucidates the RNFL thickness increased significantly (n=7 mice per group, ANOVA, ***p<0.001 in AQP4-ON compared to control,

#p<0.05; ##p<0.01 in LBGP compared to AQP4-ON, !p<0.05; !!p<0.01 in LBGP compared to control). **(D)** The quantitative analysis shows no significant changes as for the GCIPL (n=7 mice per group, ANOVA).

Visual function in NMOSD-ON animals was evaluated using the optokinetic response (OKR) test as an objective measure of visual acuity. All animals were exposed to rotating striped stimuli, and their tracking responses were recorded to assess visual acuity ***(Figure 4.16A)***. Our findings demonstrated that LBGP treatment significantly restored visual acuity in NMOSD-ON animals by week 2 ($p < 0.001$). This visual improvement remained statistically significant at week 3 ($p = 0.008$) and persisted through week 4 ($p = 0.001$) ***(Figure 4.16B)***.

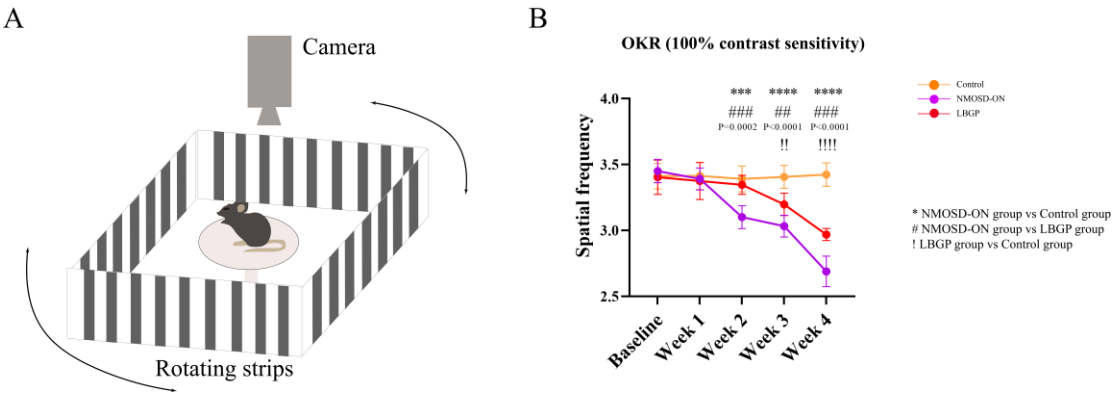

Figure 4.16 The OKR evaluation elucidates the visual acuity recovery after LBGP treatment. **(A)** The OKR setting was illustrated. **(B)** The quantitative results showed the recovery of visual acuity after LBGP treatment (n=7 mice per group, ANOVA, **p<0.01; ***p<0.001 in NMOSD-ON compared to control, ###p<0.001; ####p<0.0001 in LBGP to NMOSD-ON, !!p<0.01; !!!!p<0.0001 in LBGP compared to control).

We further conducted ERG examinations using standard flashlight stimuli to assess retinal light responses ***(Figure 4.17A)***. The pSTR, which reflects retinal ganglion cell (RGC) function, showed significant amplitude recovery in LBGP-treated NMOSD-ON animals by week 2 ($p = 0.025$). This

improvement persisted at week 3 (p = 0.036) and became more pronounced by week 4 (p = 0.003) ***(Figure 4.17B)***. In contrast, the a-wave and b-wave amplitudes, representing photoreceptor and bipolar cell function respectively, remained unchanged following disease induction and LBGP treatment ***(Figure 4.17C and D)***. Representative waveform characteristics of pSTR and a/b-waves are illustrated in ***Figure 4.17E***.

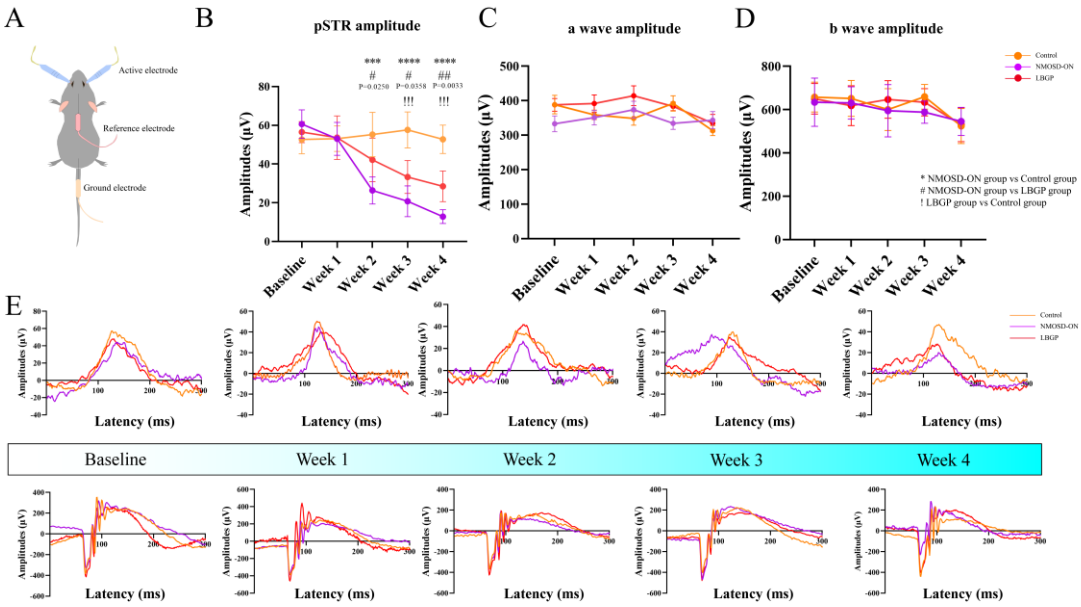

Figure 4.17 The ERG evaluation across different timepoints revealed the functional recovery after LBGP treatment. **(A)** The electrodes placement for ERG measurement was shown. **(B)** The quantitative results showed the significant recovery of pSTR amplitude after the LBGP treatment （n=7 mice per group, ANOVA, ***p<0.001; ****p<0.0001 in NMOSD-ON compared to control, #p<0.05; ##p<0.01 in LBGP compared to NMOSD-ON, !!!p<0.001 in LBGP compared to control. **(C)** No significant changes across different timepoints were observed as for a-wave amplitude (n=7 mice per group, ANOVA). **(D)** No significant changes were observed across different timepoints was observed as for b-wave amplitude (n=7 mice per group, ANOVA).

We also recorded the VEP process of LBGP treatment for NMOSD-ON at different timepoints.

Using flashlight as a stimulus, cortical responses were recorded to evaluate functional impairment along the entire visual pathway. The electrode setup used for recording is shown in ***Figure 4.18A***. The N1 latency was measured to reflect myelin sheath integrity, while the N1-P1 amplitude was used to assess axonal integrity. At week 1, LBGP treatment restored the N1 latency delay in NMOSD-ON animals, with the N1 trough appearing earlier ($p = 0.016$). By week 2, the N1 latency was significantly shortened ($p = 0.009$). At week 3, this therapeutic effect persisted, with a further significant reduction in N1 latency ($p = 0.012$). By week 4, the N1 latency remained significantly shortened ($p=0.015$) ***(Figure 4.18B)***.

We also examined the N1-P1 amplitude and found that at week 1, it showed significant recovery ($p = 0.05$). By week 2, the N1-P1 amplitude was significantly increased ($p = 0.022$). At week 3, the amplitude continued to improve markedly ($p = 0.003$). By week 4, the N1-P1 amplitude remained significantly elevated ($p = 0.017$) ***(Figure 4.18C)***. The waveforms of VEP are illustrated in ***Figure 4.18D***.

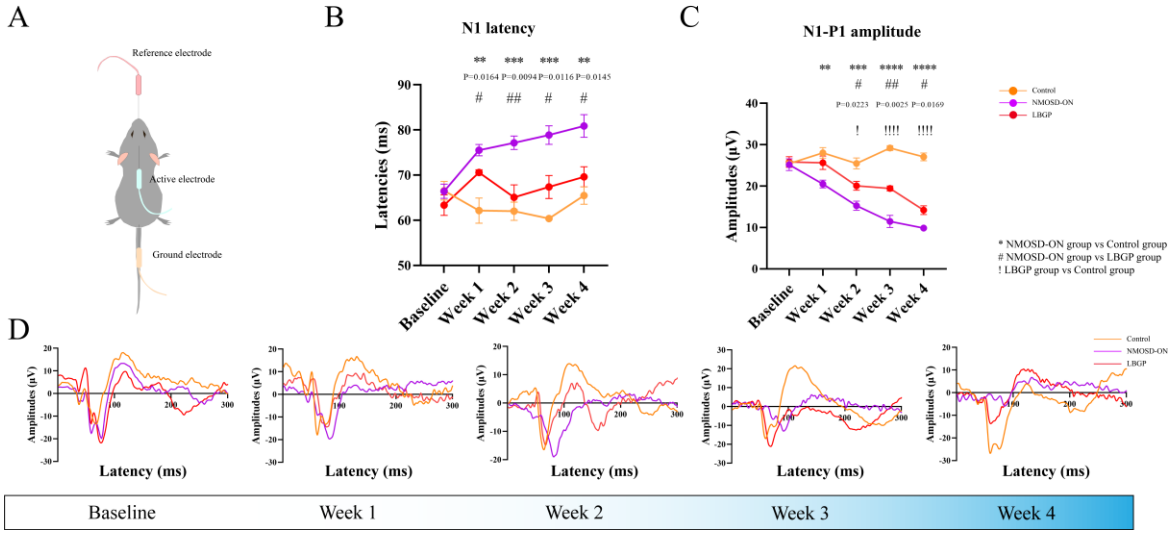

Figure 4.18 The LBGP restores the VEP response in NMOSD-ON. **(A)** The figure shows the electrode placements of VEP. **(B)** The quantitative results of N1 latency in VEP showed the recovery of N1 latency after LBGP treatment n=7 mice per group, ANOVA, **p<0.01; ***p<0.001 in NMOSD-ON compared to control, #p<0.05; ##p<0.01 in LBGP compared to NMOSD-ON. **(C)** The quantitative analysis of N1-P1 amplitude in VEP illustrates the recovery of functional impairment in NMOSD-ON (n=7 mice per group, ANOVA, **p<0.01; ***p<0.001; ****p<0.0001 in NMOSD-ON compared to control, #p<0.05; ##p<0.01 in LBGP compared to NMOSD-ON, !p<0.05; !!!!p<0.0001 in LBGP compared to control). **(D)** The representative VEP waveform illustrates the recovery of visual function in NMOSD-ON after LBGP treatment.

4.5 Discussion

Wolfberry and its bioactive components are widely recognized for their neuroprotective effects, with particularly notable benefits in optic nerve protection (Y. Dai et al., 2023). As the optic nerve is a cranial nerve situated behind the BBB, it remains unclear whether peripherally administered drugs can effectively cross the BBB to exert therapeutic effects on the optic nerve. This study evaluated the therapeutic efficacy of LBGP, a bioactive component of wolfberry, in treating NMOSD-ON while maintaining BBB integrity.

First, LBGP did not reduce the deposition of AQP4-IgG and complement components on the optic nerve in the early stages. Certain drugs, such as aquaporumab and small molecules, can effectively diminish AQP4-IgG accumulation on the optic nerve (Akaishi & Nakashima, 2017). However, since LBGP lacks high affinity for astrocytes in the optic nerve, it could not significantly reduce AQP4-IgG deposition. Additionally, LBGP failed to prevent the destruction of AQP4 protein in NMOSD-ON. Once AQP4-IgG infiltrates astrocytes in the optic nerve, it rapidly triggers AQP4 protein degradation (Carnero Contentti & Correale, 2021) — an acute and severe process for LBGP's therapeutic components to counteract in time. During the first week of treatment, LBGP also could not provide protective effects for astrocytes overall. We attribute this to the fact that astrocytes, being the primary target cells of NMOSD-ON (Carnero Contentti & Correale, 2021), sustained severe damage early in the disease course, making short-term LBGP intervention insufficient for recovery.

At week 4 post-induction (five weeks after LBGP treatment initiation), a significant proliferation and recovery of astrocytes (labeled by GFAP) was observed, which serve as the initiating cells for remyelination and neuronal regeneration (Li et al., 2022), thereby promoting nerve fiber restoration. Correspondingly, marked improvements in key neural markers including MOG, NF200, and the RGC-specific marker Brn3a, were shown, and those findings are consistent with previous literature (Yelin Dai et al., 2023). Our *in-vivo* structural assessments using OCT revealed protective effects of LBGP treatment on RNFL and GCIPL thickness — two parameters known to be affected in optic neuritis (Manogaran et al., 2018). Functional visual testing demonstrated that LBGP treatment significantly restored impaired visual acuity detected by OKR from week 2 onward. ERG evaluations showed substantial recovery by improved RGCs function through enhanced pSTR amplitudes, while VEP recordings also demonstrated shortened N1 latency (reflecting promoted remyelination and myelin sheath protection) (Liu et al., 2022) and increased N1-P1 amplitude (indicating restored visual pathway signal conduction) (Liu et al., 2022), collectively confirming both structural and functional preservation of the visual system following LBGP intervention.

4.6 Conclusion

This study evaluated the therapeutic effects of LBGP by examining cellular recovery across multiple cell types in NMOSD-ON optic nerve tissue, elucidating through which specific cell populations LBGP exerted its therapeutic action, while functional recovery assessments validated these cellular restoration effects.

Chapter 5 Unraveling the mechanisms of LBGP treatment on NMOSD-ON

5.1 Introduction and literature reviews

Understanding the therapeutic mechanisms and identifying molecular targets/pathways is crucial for developing effective treatments for neurological disorders. This knowledge not only reveals how interventions work at cellular and molecular levels but also helps optimize treatment strategies and discover novel therapeutic approaches.

The precise mechanisms through which LBGP exerts its neuroprotective effects remain to be fully elucidated. While existing literature reports multiple potential mechanisms of action, LBGP is likely to achieve inflammation control through multi-pathway and multi-target approaches. In a spinal cord injury model treated with LBGP, the therapeutic effects were primarily attributed to the suppression of the MAPKs/NF-κB signaling pathway and inhibition of pyroptosis (Jiang et al., 2023). Treatment efficacy in DEHP-induced nephrotoxicity and testicular injury models operated through dual mechanisms: SIRT1/FoxO3a-dependent apoptosis/autophagy regulation and p38 MAPK inflammation control (Zhou et al., 2022). In a neomycin-induced ototoxicity animal model, the protective mechanism was found to be mediated through tryptophan hydroxylase-regulated serotonin biosynthesis (Yunhao Wu et al., 2025).

5.2 Objectives

A key question this study aimed to address is which specific inflammatory control mechanisms play the most critical role in its therapeutic effects on NMOSD-ON. In our study, the temporal effects of

LBGP treatment were systematically investigated at both early and late phases. Given that NMOSD-ON pathogenesis is driven by immune cell infiltration and subsequent neuroinflammation, we specifically focused on the identified peak of neuroinflammation (week 1) to elucidate LBGP's therapeutic mechanisms against NMOSD-ON. This approach allowed us to precisely examine how LBGP modulates the disease process during its most active inflammatory phase.

5.3 Methods

5.3.1 Animal ethics in this study

Please refer to **Section 3.2.1** within the **Methods subsection** of **Chapter 3**.

5.3.2 Delivered AQP4-IgG

Please refer to **Section 3.2.2** within the **Methods subsection** of **Chapter 3**. In this study, the recombinant rab53 (AQP4-IgG) described in Chapter 3 was utilized to establish the animal model.

5.3.3 Replication of the NMOSD-ON animal model

Please refer to **Section 3.2.3** within the **Methods subsection** of **Chapter 3**. This study employed the recombinant rab53 (AQP4-IgG), detailed in Chapter 3, to generate the animal model.

5.3.4 Proteomics analysis

One-week post-induction, optic nerve tissues from NMOSD-ON, control, and LBGP cohorts (n=5 per group) were excised, flash-frozen, and stored at -80°C. Tissue homogenization was performed in lysis buffer, followed by protein extraction, quantification via BCA assay, and enzymatic

digestion with trypsin after reduction and alkylation. Peptide purification was achieved using EasyPep™ columns, and samples were analyzed by LC-MS/MS on a TimsTOF Pro 2 mass spectrometer coupled with an Evosep One system, employing a 25 cm reverse-phase column with a 60-minute acetonitrile gradient. Mass spectrometric data were acquired in dia-PASEF mode (100–1700 m/z) and processed with Spectronaut™ 19 against the Mus musculus UniProt database. Differentially expressed proteins (DEPs) were identified based on a fold change >1.5, Q-value <0.05, and at least two peptides per protein. Bioinformatics analyses included Ingenuity Pathway Analysis (IPA) for pathway enrichment, DAVID for KEGG pathway mapping, and STRING (v12.0) for protein-protein interaction network construction, with visualization performed in R and online platforms. Analytical parameters maintained a 1% false discovery rate (FDR) at both peptide and protein levels, with subsequent functional annotation emphasizing neuroinflammatory and neurodegenerative pathways pertinent to NMOSD-ON pathogenesis.

5.3.5 Immunostaining

Please refer to **Section 3.2.4** within the **Methods subsection** of **Chapter 3**.

The list of antibodies used in this chapter is as follows.

Table 5.1 Antibodies utilized for immunohistochemistry in optic nerve and retina.

	Antibodies (host)	Company	RRID no.	Cat#	Dilution
Primary antibodies	AQP4 (mouse)	Santa Cruz, Dallas, TX, USA	AB_3083097	sc-390488	1:200
	GFAP (rabbit)	Dako, Glostrup, Denmark	AB_10013382	z0334	1:200
	CD68 (rat)	Abcam, Cambridge, UK	AB_869007	ab53444	1:200
	Iba-1 (rabbit)	Wako, Osaka, Japan	AB_839504	019–19741	1:700
	MOG (mouse)	Millipore, Burlington, MA, USA	AB_1587278	MAB5680	1:200
	NF200 (mouse)	Sigma, St. Louis, MO, USA	AB_477257	N0142	1:200
	Brn3a (mouse)	Millipore, Burlington, MA, USA	AB_94166	MAB1585	1:200
	C5b9 (mouse)	Santa Cruz, Dallas, Texas, USA	AB_1119840	sc-66190	1:200
	MPO (rabbit)	Abcam, Cambridge, UK	AB_307322	Ab9535	1:50
	LAMP1(rabbit)	Beyotime, Shanghai, China	AB_2843793	AF7353	1:50
Secondary antibodies	Alexa Fluor 488 IgG (goat anti rabbit)	Invitrogen, Waltham, MA, USA	AB_143165	A11008	1:500
	Alexa Fluor 555 (goat anti mouse)	Invitrogen, Waltham, MA, USA	AB_141822	A21422	1:500
	Alexa Fluor 488	Invitrogen, Waltham, MA,	AB_2535792	A21206	1:500

IgG (donkey anti rabbit)	USA			
Alexa Fluor 555 IgG (donkey anti rat)	Abcam, Cambridge, UK	AB_2813834	AB150154	1:500
Alexa Fluor 488 IgG (goat anti human-IgG)	Invitrogen, Waltham, MA, USA	AB_141360	A11013	1:500

5.3.6 Western blot

Please refer to **Section 3.2.5** within the **Methods subsection** of **Chapter 3**.

The list of antibodies used in this chapter is as follows.

Table 5.2 Antibodies used for western blotting in the optic nerve.

	Antibodies (host)	Company	RRID no.	Cat#	Dilution
Primary antibodies	GAPDH (Mouse)	Millipore, Burlington, MA, USA	AB_2107426	CB1001	1:1000
	Bax (Rabbit)	Beyotime, Shanghai, China	AB_3668655	AF1270	1:500
	CYTC (Mouse)	Beyotime, Shanghai, China		AC909	1:200
	c-caspase-3 (Rabbit)	Cell Signaling Technology, Danvers, Massachusetts, USA	AB_2341188	9661T	1:500
	CTSZ (Mouse)	R and D Systems	AB_2088116	AF1033	1:1000
Secondary antibodies	Goat anti mouse-HRP	ABclonal, Woburn, MA, USA	AB_2769851	AS003	1:1000
	Goat anti rabbit-HRP	Cell signaling technology, Danvers, Massachusetts, USA	AB_2099233	7074S	1:1000

5.3.7 RT-qPCR

Please refer to **Section 3.2.6** within the **Methods subsection** of **Chapter 3**.

The list of primers used in this chapter is as follows.

Table 5.3 This table lists the primer sequences identified for the gene expression analysis targeted during the RT-qPCR experiment.

Gene	Forward sequence	Reverse sequence
GAPDH	GGGTCCCAGCTTAGGTTCAT	CTCGTGGTTCACACCCATCA
IL-6	TATGAAGTTCCTCTCTGCAAGAGA	CTGCAAGTGCATCATCGTTGTTC
IL-1β	GGCTGCTTCCAAACCTTTGA	GAAGACACGGATTCCATGGT
TNF-α	CAGGCGGTGCCTATGTCTC	CGATCACCCCGAAGTTCAGTAG
CXCL10	GCCGTCATTTTCTGCCTCAT	GGCCCGTCATCGATATGG
BDNF	TGACAACGACATCGCATTAC	TTCAGCCGGTCAGAGAAG
Pou4f1	CTCCCTGAGCACAAGTACCC	CTGGCGAAGAGGTTGCTC
TGF-β	AGGAGGTTTATAAAATCGACATGC	TGTAACAACTGGGCAGACAGTTT
TMEM119	GTGTCTAACAGGCCCCAGAA	AGCCACGTGGTATCAAGGAG
CTSZ	CCTGTCCGGGAGGGAGAA	TGGTTGATAACGGCCTGGTC
Cd68	TGGCGGTGGAATACAATGTGTC	GAGAGAGCAGGTCAAGGTGAACAG
Rac2	GACAGTAAGCCGGTGAACCT	CGTACCTCAGGGAACCACTTG
Ncf2	CTTGGGTCCTCCCTGCATAA	GGAACTGACGCATAAATTCAAGG
Itgb2	CTGGTGCCAGAAGCTGAACT	TGCTCCTGGGGTCCATGATA
Inpp5d	CTGGCTTGGGGATCTCAACTAC	GGCCAGAAGGTCTGAATACTGC
MCP-1	TGATCCCAATGAGTAGGCTGGAG	ATGTCTGGACCCATTCCTTCTTG
Vit1a	ACGGATCGCCTACAGTGACG	GGCCGATTTGCTCAGTCTCC
Rab7b	CGAGGAATACCAGACCACACT	GGCTGGCCAGAACCTCAAAGG

Atp6v0a1	AGAGGACGCAGAAGAGCCTA	CTCAATGGTGTGGATGGCCT
P53	TCCGAAGACTGGATGACTGC	GATCGTCCATGCAGTGAGGT

5.3.8 Functional evaluation

Please refer to **Section 3.2.7** within the **Methods subsection** of **Chapter 3**.

5.3.9 in-vivo structural measurement

Please refer to **Section 3.2.8** within the **Methods subsection** of **Chapter 3**.

5.4 Results

5.4.1 Proteomics analysis

To elucidate the underlying mechanisms of AQP4-ON pathogenesis, optic nerve samples (n=5) were collected during the peak inflammatory phase (week 1) of AQP4-ON and performed proteomic analysis comparing them with control. 446 upregulated and 185 downregulated differentially expressed proteins (DEPs) were identified ***(Figure 5.1 A)***. Using IPA (Ingenuity Pathway Analysis) to examine canonical pathways, the top-ranked pathway was "Neutrophil Degranulation," which is associated with lysosomal activity and was predicted to be activated in AQP4-ON. Additionally, other immune-related pathways involving neutrophils and macrophages/microglia were identified, including "Phagosome Maturation", "Neutrophil Extracellular Trap Signaling Pathway", "Fcγ Receptor-mediated Phagocytosis in Macrophages and Monocytes", "Production of Nitric Oxide and Reactive Oxygen Species in Macrophages". These pathways are all linked to lysosomal activity ***(Figure 5.1 B)***. The IPA summary graph further highlighted key inflammatory functions and cytokines associated with lysosomal activity, such as "cell movement," "chemotaxis," "FGF2," and "TNF," suggesting their potential activation ***(Figure 5.1 C)***.

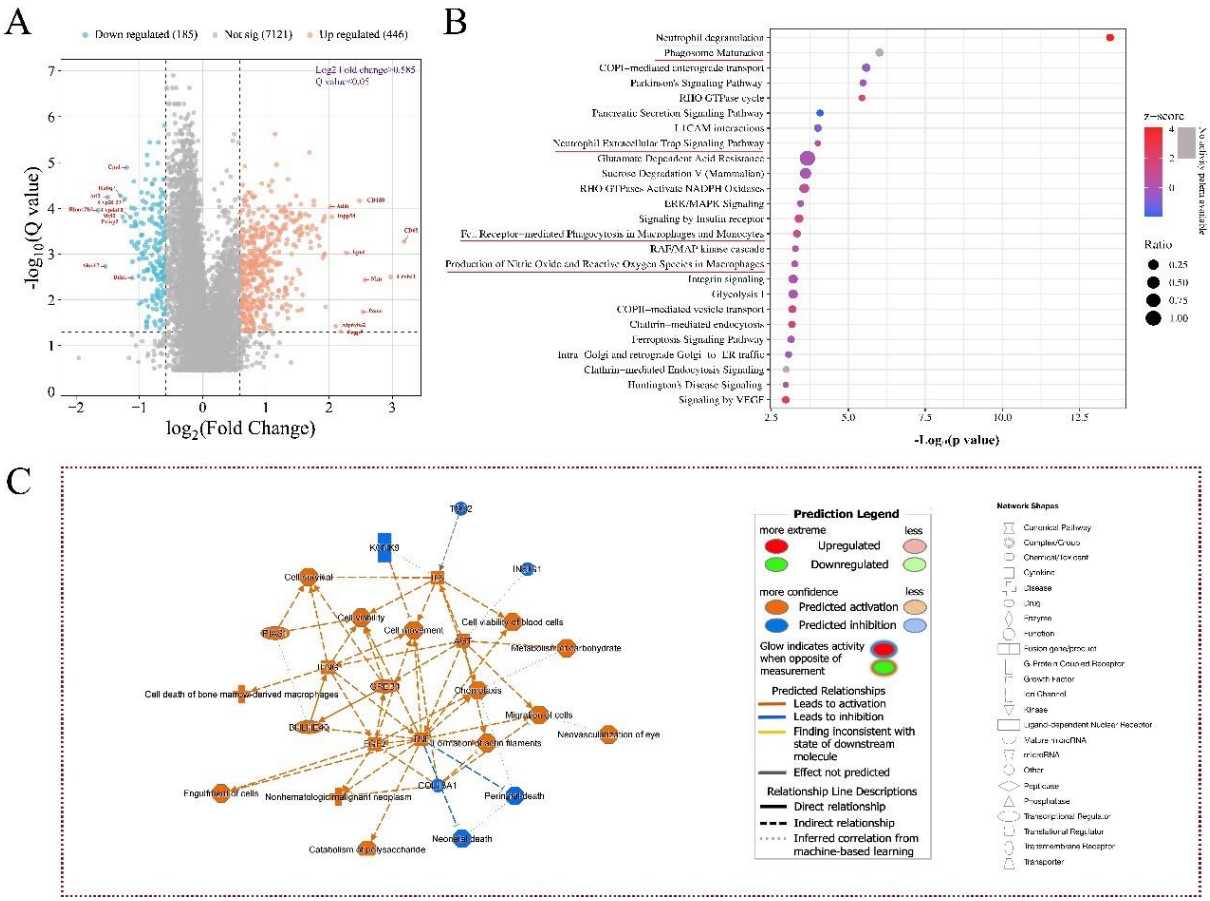

Figure 5.1 Proteomics and Bioinformatic analysis of AQP4-ON disease dataset. **(A)** The volcano plot displays DEPs in NMOSD-ON compared to Control, revealing 446 upregulated and 185 downregulated proteins. **(B)** The bubble plot depicts canonical pathways enriched in the NMOSD-ON disease dataset, as determined by IPA. **(C)** The summary graph illustrates predicted key proteins, pathways, and biological function, along with their interactions. "TNF" and "FGF2" emerge as central regulators, suggesting the neuroinflammation driven by microglial/macrophages and neutrophils likely contributes to disease progression.

Based on these findings, we propose that excessive lysosomal activity, particularly in neutrophils and microglia/macrophages, may be a major driver of inflammation in AQP4-ON. To explore protein-protein interactions (PPIs) among the DEPs enriched in these pathways, we used STRING and identified key node proteins located at central hubs with multiple interactions, which are considered critical to disease pathogenesis ***(Figure 5.2 A)***. The fold changes (FC) of these key node proteins are displayed in ***Figure 5.2B***. In summary, our data suggested that dysregulated lysosomal activity in immune cells (neutrophils and microglia/macrophages) contributed significantly to the inflammatory response in AQP4-ON ***(Figure 5.2 B)***.

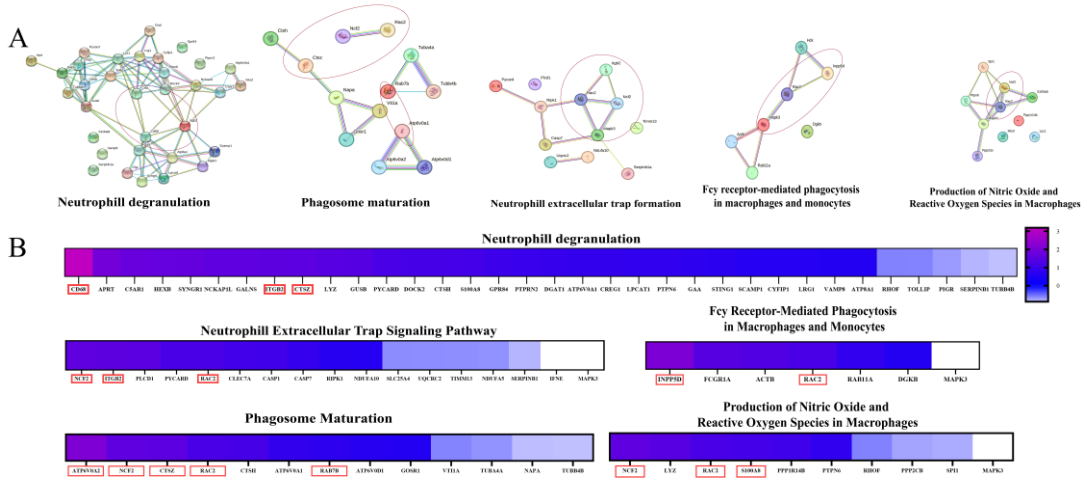

Figure 5.2 Key nodes proteins in pathways of interest. **(A)** The STRING network analysis maps protein-protein interactions (PPIs) within the pathways of interest, with red circles highlighting core node proteins critical to these pathways. **(B)** The heat-map presents log2 fold changes of proteins clustered according to their associated canonical pathways.

Analysis of the LBGP Treatment Dataset Reveals Modulation of Key Inflammatory Pathways. In the LBGP treatment dataset, 545 downregulated and 379 upregulated differentially expressed proteins (DEPs) were identified ***(Figure 5.3A)***. IPA analysis of these DEPs revealed that the top-

ranked canonical pathway was "Neutrophil Degranulation", which was predicted to be inhibited following LBGP treatment ***(Figure 5.3B)***. Other relevant pathways showing involvement included "Phagosome Maturation", "Neutrophil Extracellular Trap Signaling Pathway" "Fcγ Receptor-mediated Phagocytosis in Macrophages and Monocytes" "Production of Nitric Oxide and Reactive Oxygen Species in Macrophages". Notably, the IPA summary analysis indicated suppression of both "TNF" and "immune response of macrophage" ***(Figure 5.3C)***, collectively demonstrating that the hyperactive lysosomal activity observed in AQP4-ON was effectively suppressed by LBGP treatment. Additionally, significant activation of the Myelination Signaling Pathway was also observed, suggesting LBGP may promote reparative processes in addition to its anti-inflammatory effects.

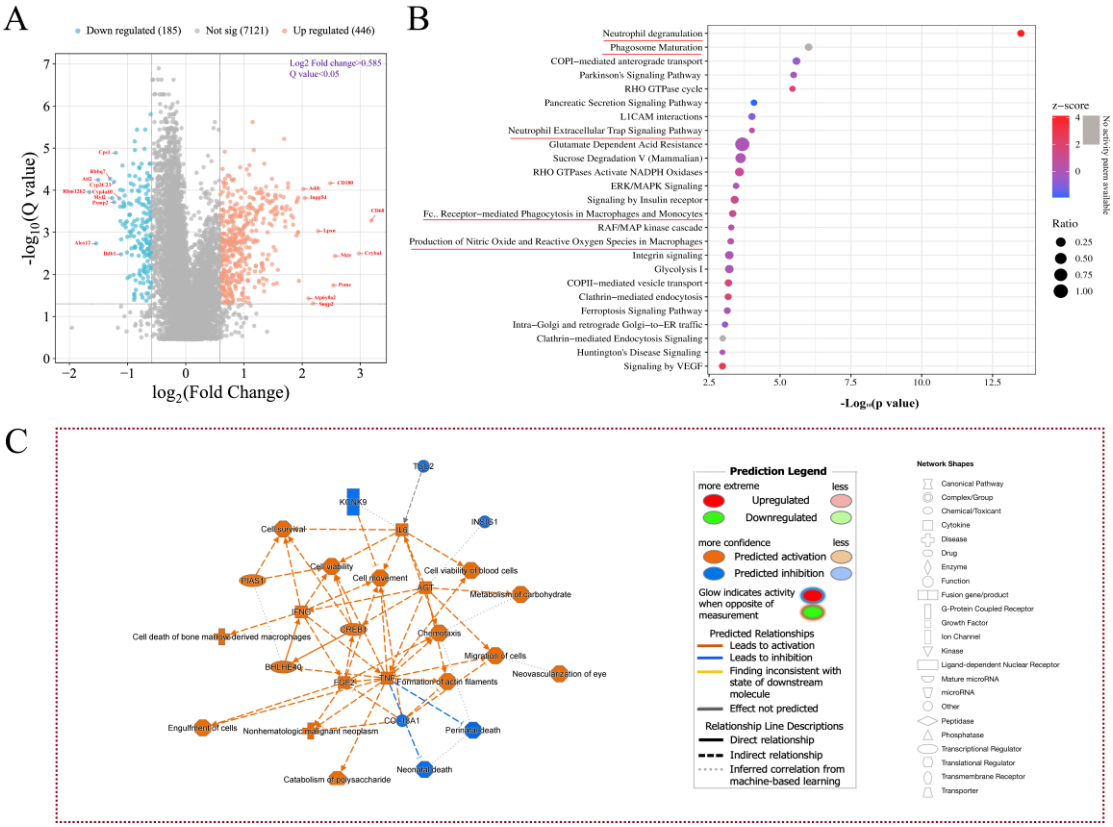

Figure 5.3 Proteomic and bioinformatic analysis of the LBGP treatment dataset. **(A)** Volcano plot showing differentially expressed proteins (DEPs) in LBGP versus AQP4-ON, with 379

upregulated and 545 downregulated proteins. **(B)** Bubble plot of IPA-enriched canonical pathways in the LBGP-treated group, highlighting significantly modulated pathways. **(C)** Summary interaction network of predicted key proteins, pathways, and biological functions. TNF and "Immune response of macrophage" were identified as central regulators, implicating microglia/macrophage- and neutrophil-driven neuroinflammation in disease progression.

To explore the potential therapeutic targets of LBGP in treating AQP4-ON, we first identified 172 overlapping proteins between the upregulated proteins in the AQP4-ON disease dataset and the downregulated proteins in the LBGP treatment dataset ***(Figure 5.4A)***. These overlapping proteins were most significantly enriched in the lysosome pathway (top 1 KEGG pathway, ***Figure 5.4A***), further supporting the involvement of lysosomal activity in the mechanism of LBGP treatment for AQP4-ON.

To pinpoint the key molecular targets, we examined whether LBGP treatment could modulate key node proteins known to play critical roles in AQP4-ON pathogenesis. Mpeg1, Cd68, Ctsz, Itgb2, S100a8, Atp6v0a1, and Ncf2 were found to be regulated by LBGP. Although Rac2 and Rab7b were not identified as significantly modulated in the proteomics analysis, we included them for further validation due to their established importance in disease progression ***(Figure 5.4B)***.

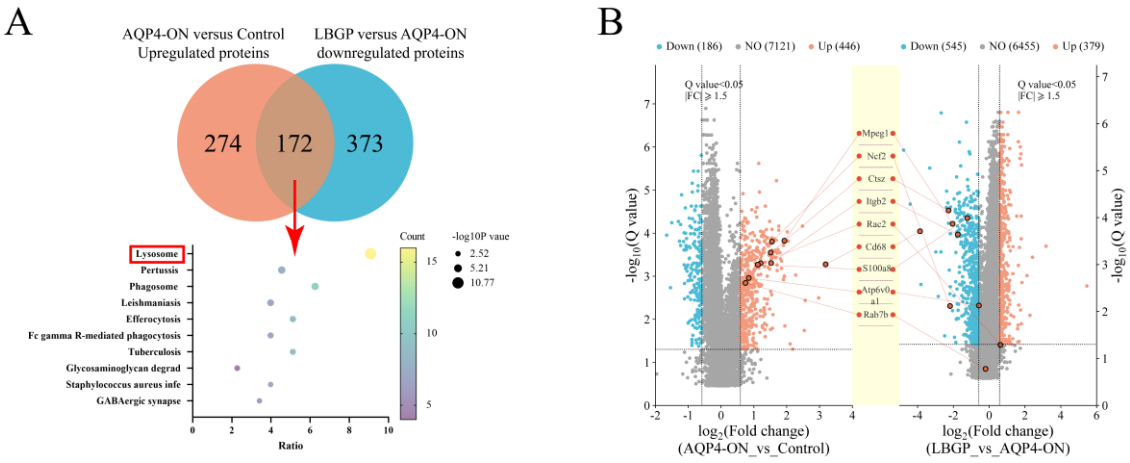

Figure 5.4 Identification of LBGP-Targeted Inflammatory Proteins in AQP4-ON Pathogenesis. **(A)** Among the upregulated proteins in AQP4-ON, 172 were downregulated following LBGP treatment. KEGG pathway analysis revealed that these overlapping proteins were most

significantly enriched in the "lysosome" pathway (ranked as the top one). **(B)** Key node proteins identified in the AQP4-ON dataset—Mpeg1, Ctsz, Cd68, Itgb2, S100a8, Atp6v0a1, and Ncf2 — were significantly suppressed by LBGP treatment, further supporting its regulatory role in lysosomal activity.

Using RT-qPCR, the regulation of Ctsz, Cd68, Mpeg1, S100a8, Ncf2, and Itgb2 by LBGP was successfully validated ***(Figure 5.5A)***. These findings confirmed that lysosome-related pathways—including "Neutrophil Degranulation," "Neutrophil Extracellular Trap Signaling Pathway," "Phagosome Maturation," "Fcγ Receptor-mediated Phagocytosis in Macrophages and Monocytes," and "Production of Nitric Oxide and Reactive Oxygen Species in Macrophages" areinvolved in both disease pathogenesis and LBGP treatment.

However, PLP and MBP, which are associated with the "Myelinating Signaling Pathway," could not be validated ***(Figure 5.5B)***, suggesting that at this early time-point (week 1), LBGP does not yet exhibit a significant pro-remyelination effect.

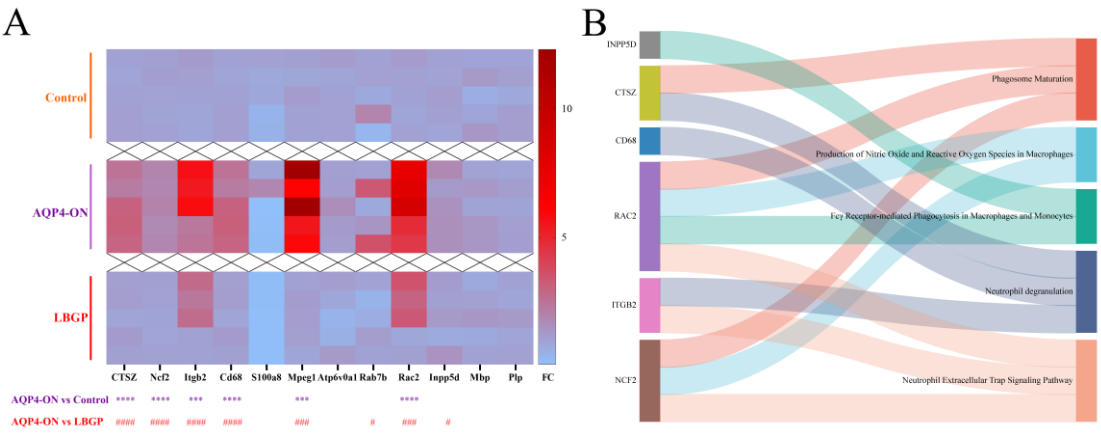

Figure 5.5 Validation of key node proteins. **(A)** RT-qPCR validation (n = 5 mice per group) confirmed the expression changes of key node proteins from the AQP4-ON dataset, as well as

proteins potentially involved in Myelination Signaling Pathway activation post-LBGP treatment. Statistical significance: AQP4-ON vs. Control: ***p<0.001; ****p<0.0001; LBGP vs. AQP4-ON: #p<0.05; ###p<0.001; ####p<0.0001 (ANOVA). **(B)** A Sankey plot integrated the validated proteins with their associated lysosomal activity-related pathways, demonstrating that each pathway contained multiple experimentally confirmed targeted proteins.

5.4.2 Lysosome activities underscoring disease pathogenesis and LBGP treatment

In the proteomics analysis, both disease progression and LBGP-mediated treatment were found to be closely associated with lysosomal activity in immune cells. Targeting the over-activation of lysosomal function can suppress the initiation and progression of inflammation. Therefore, we used Lysosomal Associated Membrane Protein 1 (LAMP1) as a marker to assess lysosomal activation (Furuta et al., 2001). Our results showed that LBGP treatment significantly suppressed lysosomal hyperactivity ($p < 0.001$) ***(Figure 5.6 A and B)***.

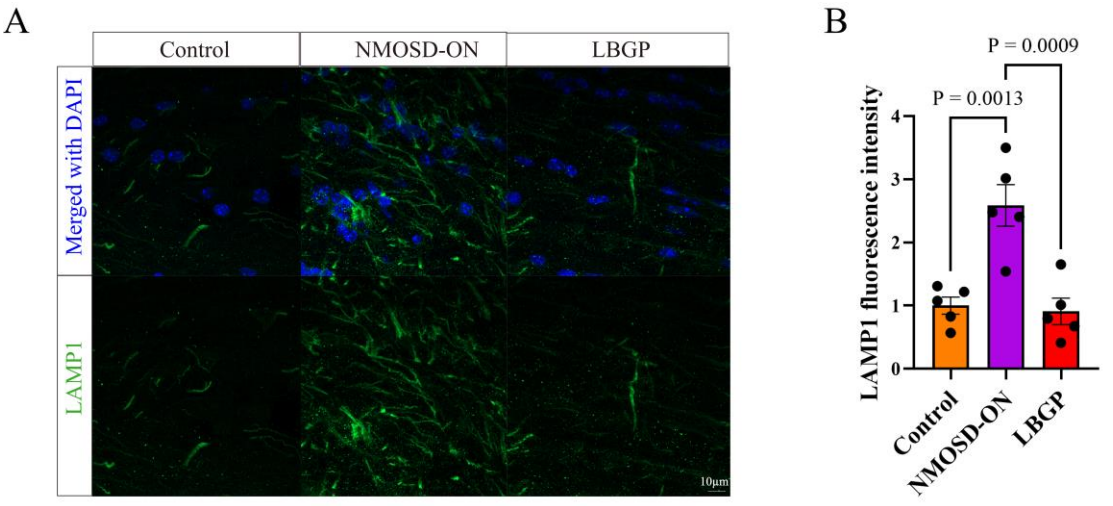

Figure 5.6 LBGP treatment alleviates the lysosomal activities in NMOSD-ON. **(A)** The

representative image of LAMP1 expression. **(B)** The quantitative result illustrates the LAMP1 expression reduces after the LBGP treatment (n=5 mice per group, ANOVA, **p<0.01, ***p<0.001).

Our proteomics analysis further revealed that "Neutrophil degranulation" and the "Neutrophil Extracellular Trap Signaling Pathway", both closely linked to lysosomal activity, played a key role in disease pathogenesis and served as critical targets of LBGP treatment. Therefore, we first investigated whether LBGP modulates immune neutrophils infiltration (Ly6G+ cells) (Kleinholz et al., 2021), in NMOSD-ON. Flow cytometry analysis demonstrated that LBGP significantly reduced neutrophil accumulation in the optic nerve of NMOSD-ON mice ($p < 0.0001$) ***(Figure 5.7A and B)***.

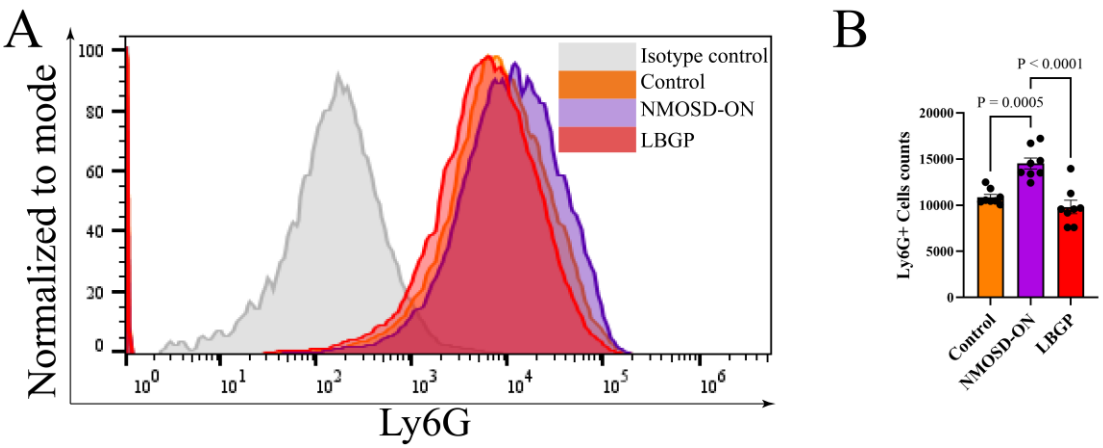

Figure 5.7 The NMSOD-ON neutrophils recruitment was reduced after LBGP treatment. **(A)** The flow cytometry histogram showed neutrophil recruitment labeled by Ly6G antibody in NMOSD-ON optic nerve. **(B)** Quantitative results showed the significant reduction of Ly6G+ cells after LBGP treatment (n=7 mice per group, ANOVA, ***p<0.001, ****p<0.0001).

Additionally, since Myeloperoxidase (MPO) is stored in lysosome-associated azurophilic granules and releases upon neutrophil degranulation or extracellular trap formation, we used MPO as a marker for lysosome-related neutrophil activity (Kleinholz et al., 2021). Our results showed that LBGP treatment significantly suppressed MPO release in NMOSD-ON ($p = 0.040$) ***(Figure 5.8A and B)***. We further validated the regulatory effect of LBGP on NMOSD-ON pathogenesis by performing 63× confocal microscopy to quantify MPO release. Consistent with our previous findings, LBGP treatment significantly reduced the area of MPO release ($p < 0.0001$) ***(Figure 5.8 C and D)***, reinforcing its suppressive role in neutrophil-mediated lysosomal activity.

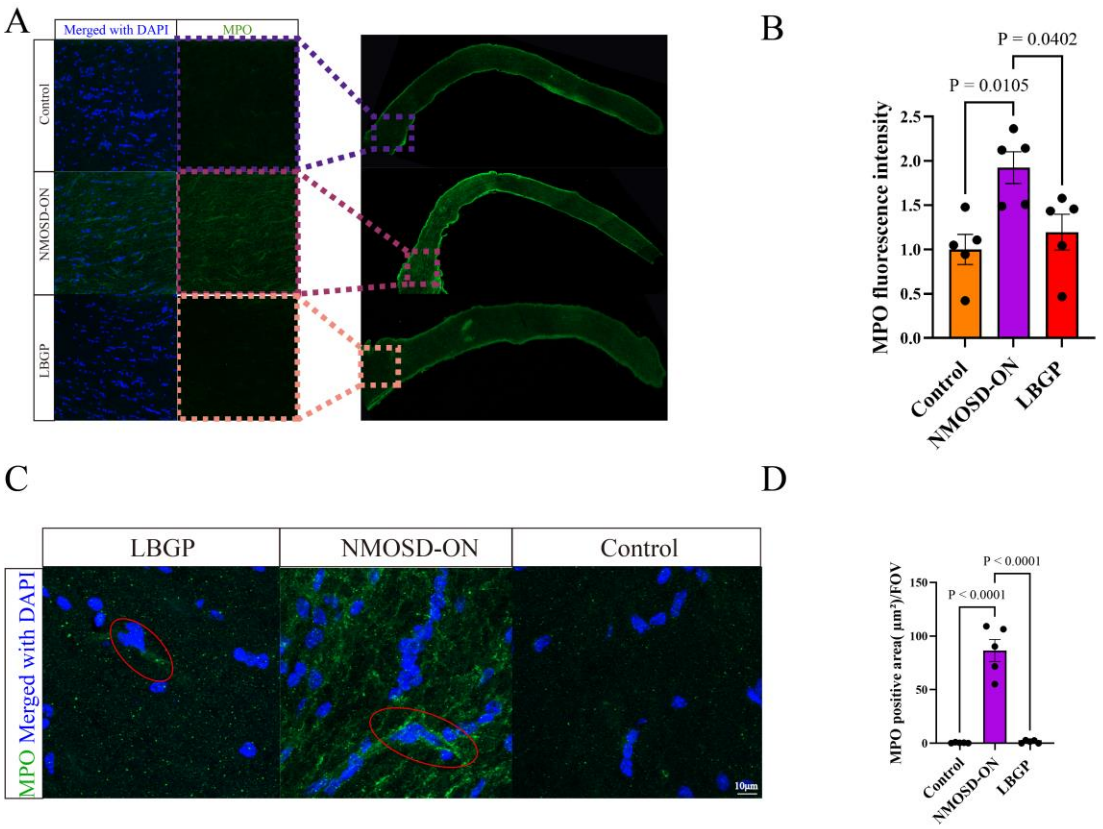

Figure 5.8 The LBGP treatment reduces the lysosomal enzyme release. **(A)** The representative images of MPO expression under 20x microscope. **(B)** The quantitative result

shows that the MPO expression significantly decreased after LBGP treatment (n=5 mice per group, ANOVA, *p<0.05). **(C)** The 63x enlarged image shows that the MPO released area reduced after LBGP treatment. **(D)** The quantitative result shows the MPO releases area reduced after LBGP treatment (n=5 mice per group, ANOVA, ****p<0.0001).

Our proteomics analysis further revealed that microglial/macrophage-mediated lysosomal activities, including "Phagosome Maturation," "Fcγ Receptor-mediated Phagocytosis in Macrophages and Monocytes," and "Production of Nitric Oxide and Reactive Oxygen Species in Macrophages", served as key targets for LBGP in modulating neuroinflammation in NMOSD-ON. Given that excessive phagocytic activity in NMOSD-ON may be a critical therapeutic target of LBGP, we first examined whether total microglia/macrophages (Iba-1+ cells) accumulate in the optic nerve and are suppressed by LBGP treatment. Interestingly, while LBGP did not significantly reduce the total number of Iba-1+ microglia/macrophages ($p > 0.05$) ***(Figure 5.9A and B)***, it markedly decreased the CD68+ population, a marker of phagocytic active microglia/macrophages ($p = 0.003$) ***(Figure 5.9A and C)***. Consistent with this, the ratio of CD68+ area to Iba-1+ area was also downregulated post-LBGP treatment ***(Figure 5.9A and D)***. High-resolution 63× confocal microscopy further demonstrated that LBGP significantly reduced the lysosomal area within microglia ($p = 0.017$) ***(Figure 5.9E and F)***. Additionally, Transmembrane Protein 119 (TMEM-119), a molecule upregulated during microglial/macrophage phagocytosis, was suppressed by LBGP ($p = 0.006$) ***(Figure 5.9G)***, reinforcing its role in curbing lysosome-associated phagocytic overactivation.

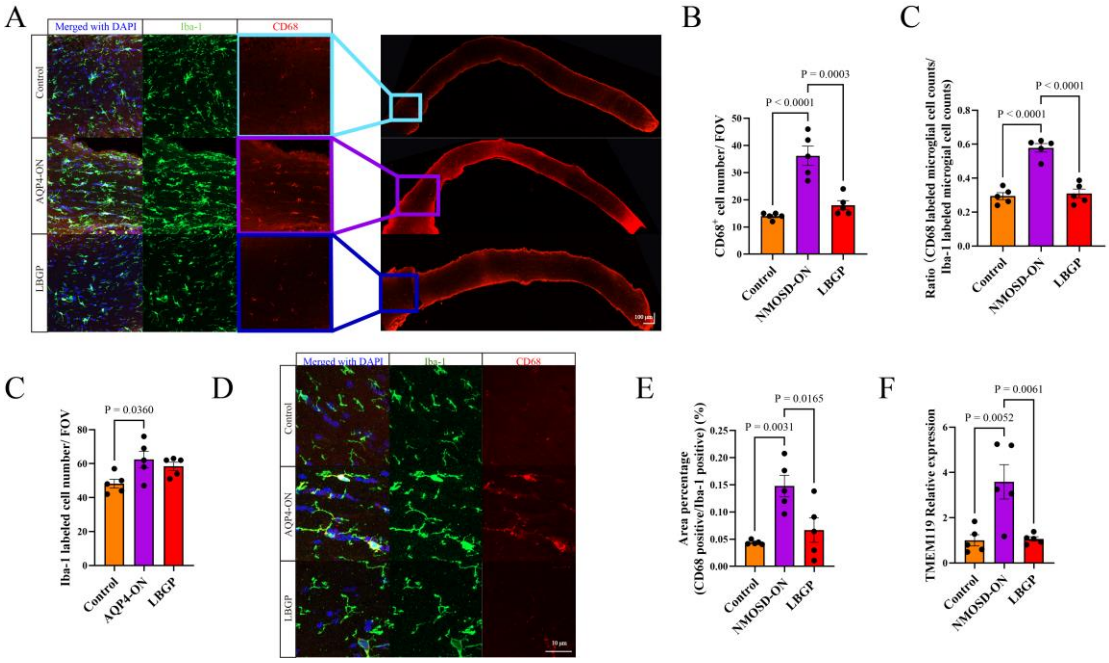

Figure 5.9 The phagocytotic activities reduced after LBGP treatment. **(A)** The representative image of Iba-1 expression showed the recruitment of microglial/macrophages in NMOSD-ON and the representative image of CD68 showed the microglial/macrophages with phagocytotic function. **(B)** The quantitative results showed that the CD68-labeled microglial/macrophages reduced significantly after LBGP treatment (n=5 mice per group, ANOVA, ***p<0.001, ****p<0.0001). **(C)** The quantitative results showed that the ratio of CD68/Iba-1 reduced after LBGP treatment (n=5 mice per group, ANOVA, ****p<0.0001). **(D)** The quantitative results showed no significant reduction of Iba-1-labeled pan-microglial after LBGP treatment (n=5 mice per group, ANOVA). **(E)** CD68-labeled lysosome within microglia/macrophage captured by 63x confocal microscope. **(F)** Quantitative result of area percentage of CD68 labeled lysosome over Iba-1 labeled microglial area showed the significant reduction of CD68+/Iba-1 + area in NMOSD-ON after LBGP treatment. **(G)** The quantification result of RT-qPCR shows that the RNA transcripts of TMEM119 (phagocytotic microglial marker) reduced significantly after LBGP treatment (n=5 mice per group, ANOVA, **p<0.01).

Although these cytokines were not identified as LBGP-regulated inflammatory factors in the proteomics analysis, we further analyzed them via RT-qPCR due to their potential association with lysosomal activity (Bai et al., 2014; Yuan et al., 2002; Zhang et al., 2017). Relative expression of tumor necrosis factor-alpha (TNF-α) was significantly downregulated by LBGP treatment ($p < 0.0001$). Interleukin-6 (IL-6) levels were markedly reduced by post-LBGP ($p = 0.007$). No significant downregulation of Chemokine (C-X-C motif) ligand 10 (CXCL10) was observed, possibly due to its inherent stability. Monocyte Chemoattractant Protein-1 (MCP-1) expression was strongly suppressed by LBGP ($p < 0.0001$). Tumor Protein p53 (P53) showed reduced expression after treatment ($p = 0.002$). TGF-β remained unaffected by LBGP ($p > 0.05$). Interleukin-1β (IL-1β) exhibited significant downregulation ($P < 0.0001$). However, Brain-Derived Neurotrophic Factor (BDNF) expression remained unchanged ***(Figure 5.10)***.

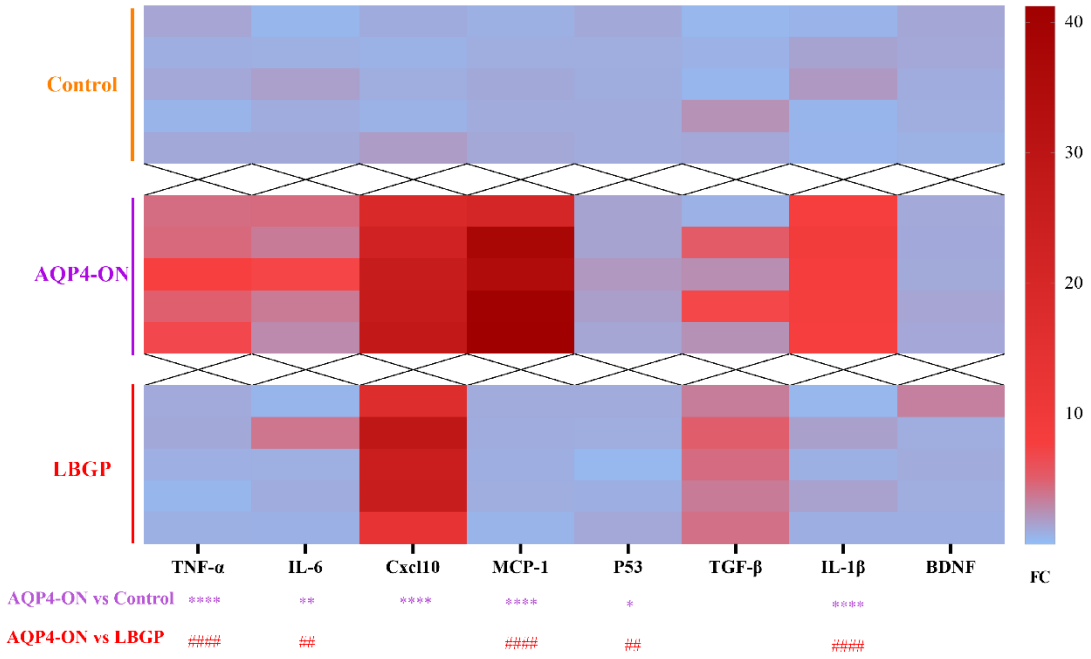

Figure 5.10 RT-qPCR result indicated the comparisons of lysosome-related cytokines TNF-α, IL-6,

MCP-1, P53 , and IL-1β. The LBGP downregulated lysosome-related cytokines (n=5 mice per group, ANOVA, *p<0.05; **p<0.01; ****p<0.0001 when AQP4-ON compared to Control; ##p<0.01; ####p<0.0001 when LBGP compared to AQP4-ON).

5.4.3 CTSZ plays a critical role in LBGP modulation

Our proteomics analysis identified "Neutrophil degranulation" as the top-ranked pathway, with Cathepsin Z (CTSZ) — a lysosomal enzyme critical for lysosomal activity — occupying a central position in PPI of STRING. Notably, CTSZ was also enriched in the "Phagosome Maturation" pathway. Given that RT-qPCR confirmed LBGP-mediated downregulation of CTSZ at the transcriptional level, we further investigated whether this effect extends to the protein level. Consistent with our hypothesis, LBGP treatment significantly reduced CTSZ protein expression ($p < 0.001$) ***(Figure 5.11A and B)***, reinforcing its role in modulating lysosome-associated enzymatic activity in NMOSD-ON.

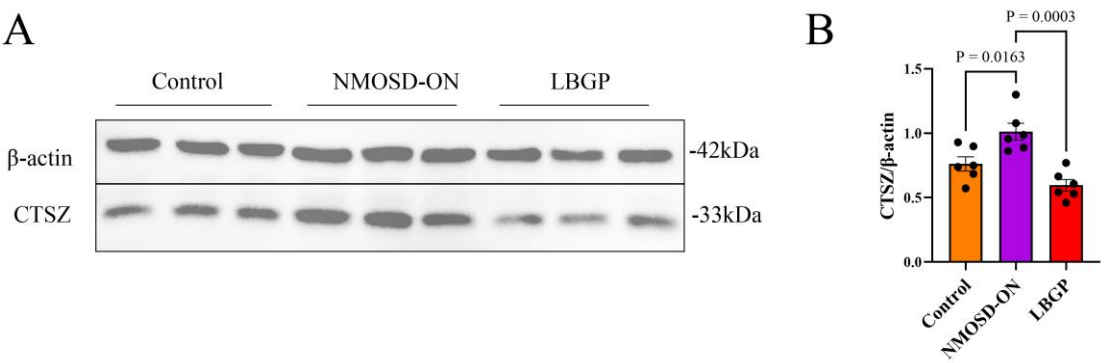

Figure 5.11 The western blot confirmed the CTSZ inhibition after LBGP treatment in NMOSD-ON optic nerve. **(A)** The western blot band showed the reduced band intensity in CTSZ after

LBGP treatment. **(B)** The quantitative result showed the significant reduction of CTSZ band intensity (n=5 mice per group, ANOVA, *p<0.05; ***p<0.001).

Since we know that LBGP can target CTSZ to suppress NMOSD-ON inflammation, two methods of inhibiting CTSZ expression were applied to confirm the mediating role of CTSZ as a mediator, and observe whether it could replicate the therapeutic effects of LBGP.

The first method involved using the general cysteine protease inhibitor, Aloxistatin (E64d), administered via oral gavage to inhibit CTSZ (control group received DMSO solution), while the second method employed intracranial injection to deliver siRNA for CTSZ knockdown (control group received siCTR).

First, the mice one week after disease onset were sacrificed and the optic nerve tissue was collected to measure CTSZ expression via RT-qPCR ***(Figure 5.12A)***. Our results showed that E64d did not effectively suppress CTSZ expression ($p > 0.05$), whereas siCTSZ significantly inhibited CTSZ expression ($p = 0.011$) ***(Figure 5.12B)***.

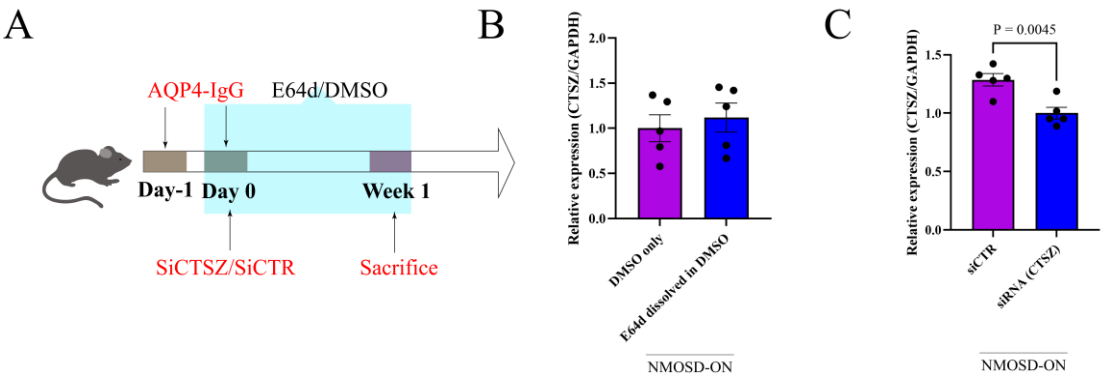

Figure 5.12 Comparative analysis of E64d and siCTSZ efficacy in inhibiting CTSZ activity. **(A)**

Schematic of the experimental protocol detailing the administration of AQP4-IgG, E64d, and siCTSZ. **(B)** Quantitative assessment indicating that E64d treatment did not significantly decrease CTSZ expression levels (n=5 mice for each group, ANOVA). **(C)** Quantitative analysis demonstrated a significant reduction in CTSZ expression following siRNA-mediated knockdown (n=5 mice for each group, ANOVA, **p<0.01).

Based on this finding, we proceeded with siCTSZ-mediated knockdown to investigate the possible mechanism of LBGP. In the experimental design, three groups were compared: (1) The CTSZ knockdown (CTSZKD) group received PBS feeding for one week prior to animal model induction, followed by immediate siCTSZ injection post-modeling; (2) The NMOSD-ON group underwent the same PBS pretreatment but received siCTR after modeling; (3) The CTSZKD+LBGP group was pretreated with LBGP for one week before induction, followed by siCTSZ administration. This third experimental setup served a critical purpose. If LBGP treatment in the CTSZKD+LBGP group failed to show additional therapeutic benefits beyond those achieved by CTSZ knockdown alone, it would strongly suggest that LBGP exerts its anti-inflammatory effects in NMOSD-ON primarily through CTSZ regulation. This approach allows us to determine whether CTSZ is indeed the key mediator through which LBGP controls neuroinflammation in this disease model ***(Figure 5.13)***.

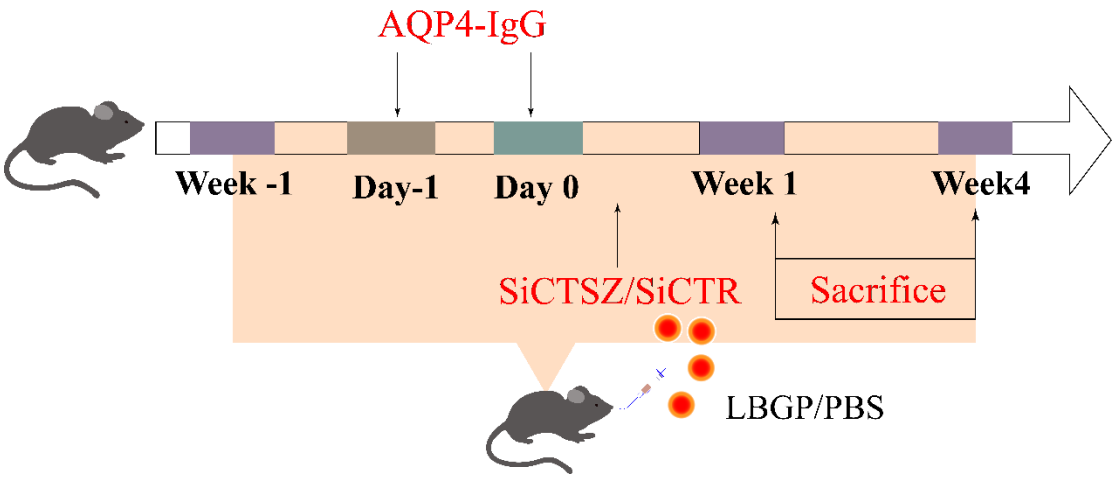

Figure 5.13 The experimental timeline identifying the role of CTSZ in LBGP treatment. The timeline including the delivery of AQP4-IgG, the feeding of LBGP/PBS, the delivery of siCTSZ/siCTR and animal sacrifice.

Our results demonstrate that CTSZKD exerts significant effects on neutrophil recruitment and microglial activity. At week 1, siCTSZ treatment markedly reduced neutrophil infiltration regardless of LBGP co-treatment status ($P < 0.0001$) ***(Figure 5.14 A and B)***.

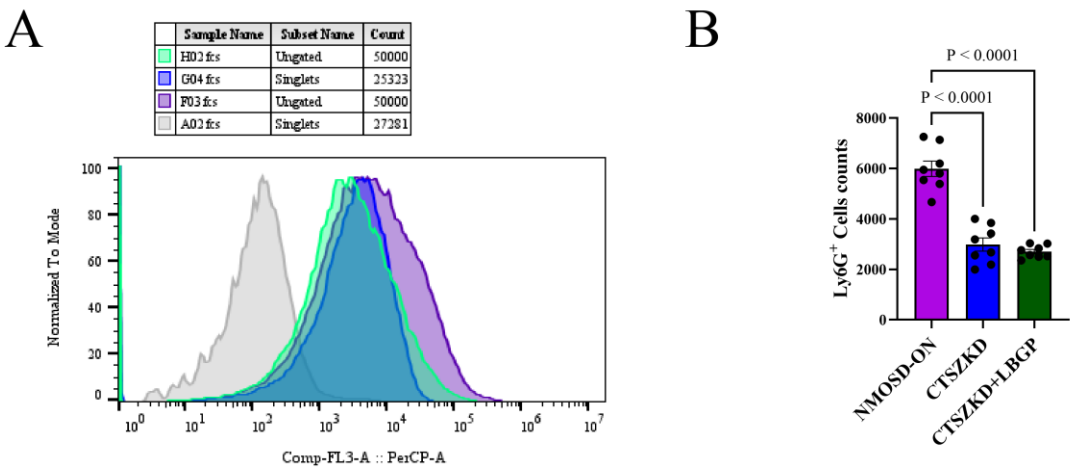

Figure 5.14 Flow cytometry analysis of Ly6G labeled cells counts in NMOSD-ON optic nerve.

(A) The histogram illustrating the CTSZKD and CTSZKD+LBGP reduced the infiltration of Ly6G labeled neutrophils infiltration. **(B)** The quantitative analysis showed the CTSZKD and CTSZKD+LBGP treatment significantly reduced the Ly6G positive cells counts in NMOSD-ON optic nerve.

This reduction in neutrophil presence was accompanied by a significantly decrease of MPO release in both the CTSZKD ($p = 0.004$) and the CTSZKD+LBGP ($p = 0.009$) ***(Figure 5.15 A and B)***.

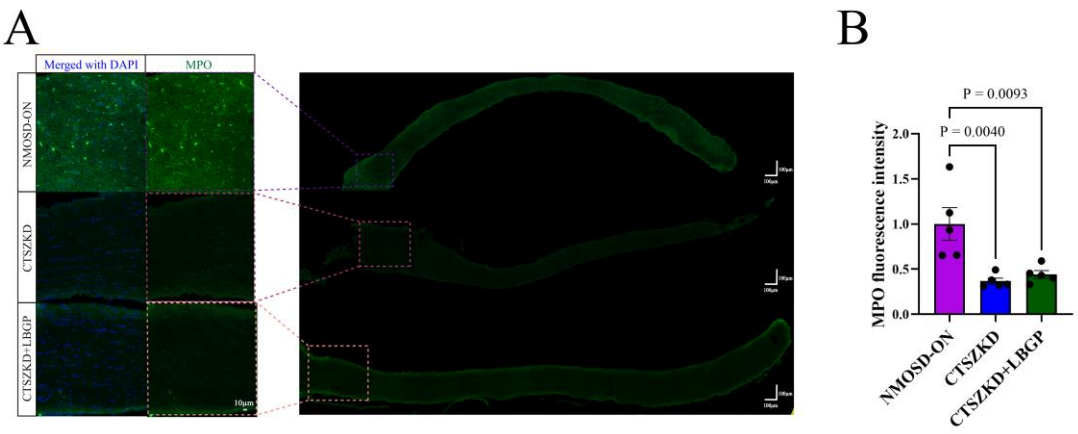

Figure 5.15 The CTSZKD and CTSZKD+LBGP reduced neutrophil-associated lysosomal enzyme in NMOSD-ON. **(A)** The representative image of MPO staining in NMOSD-ON with CTSZKD or CTSZKD+LBGP treatment. **(B)** The quantitative result shows that both CTSZKD and CTSZKD+LBGP significantly reduced MPO staining intensity (n=5 mice per group, ANOVA, **p<0.01).

Further examination of microglial phagocytic activity, as assessed by CD68 labeling, revealed that CTSZKD alone reduced both CD68-positive microglia ($p < 0.0001$) and the CD68/Iba-1 ratio ($p < 0.001$), with similar reductions observed in the CTSZKD+LBGP ($p < 0.001$ and $p = 0.001$,

respectively) ***(Figure 5.16)***.

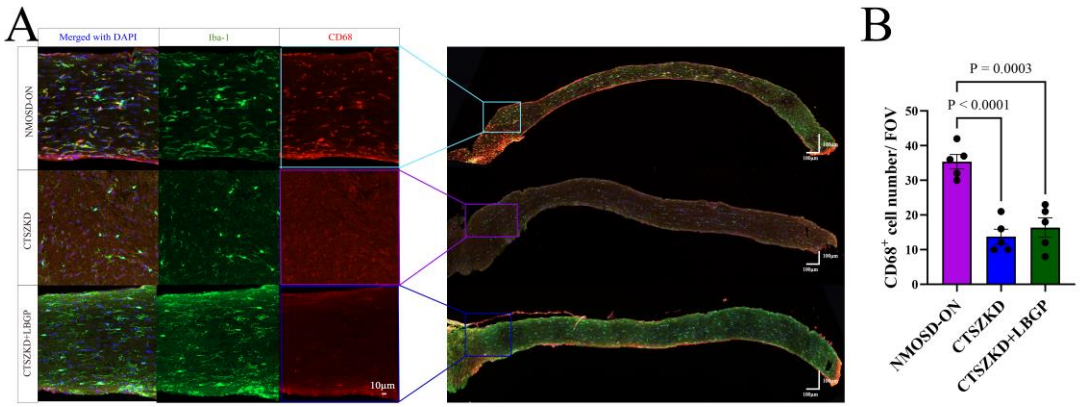

Figure 5.16 The phagocytotic microglial were reduced after CTSZKD or CTSZKD+LBGP treatment. **(A)** The representative images of Iba-1 (green) and CD68 (red) labeled microglial showed the reduced phagocytotic microglial (labeled by CD68) after LBGP treatment. **(B)** The CTSZKD or CTSZKD+LBGP treatment significantly reduced CD68 labeled microglial in the quantitative analysis (n=5 mice per group, ANOVA, ***p<0.001; ****p<0.0001).

Gene expression analysis of lysosome-related and inflammatory markers showed that CTSZKD significantly downregulated multiple pro-inflammatory mediators, including IL-1β ($p < 0.0001$), TNF-α ($p < 0.0001$), IL-6 ($p = 0.045$), Cd68 ($p = 0.008$), Mpeg1 ($p = 0.016$), and Rac2 ($p < 0.0001$), with comparable effects shown in the CTSZKD+LBGP ($p < 0.0001$, $p < 0.0001$, $p = 0.048$, $p = 0.002$, $p = 0.017$, and $p < 0.0001$ respectively). The treatment also reduced expression of MCP-1 ($p < 0.0001$), Cxcl10 ($p < 0.0001$), and Itgb2 ($p < 0.0001$) in both experimental groups ***(Figure 5.17)***.

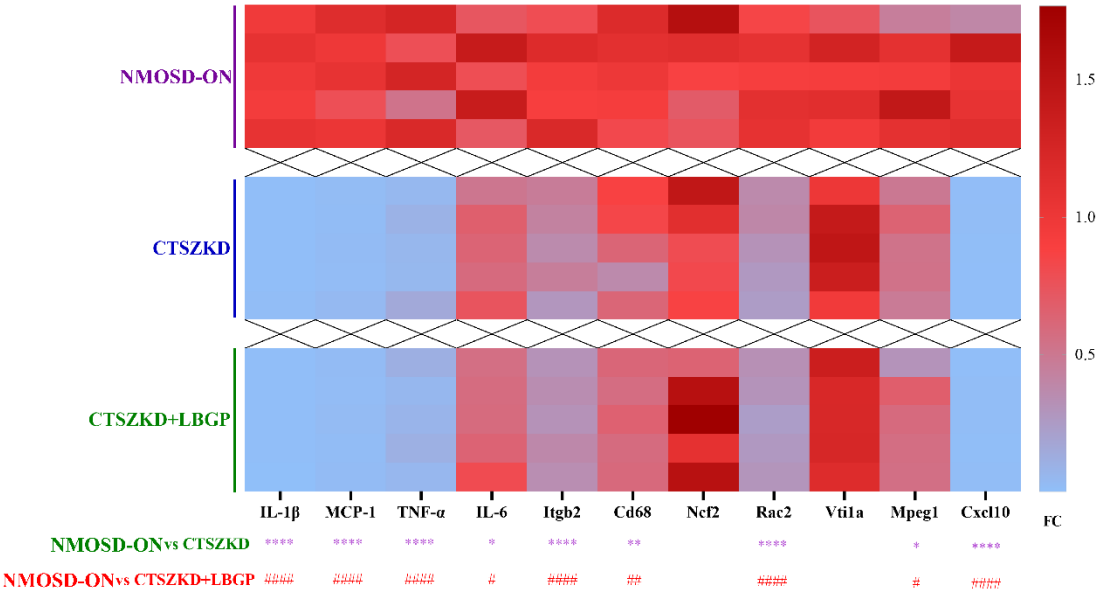

Figure 5.17 Downregulation of lysosomal-activities-associated cytokines. IL-1β, MCP-1, TNF-α, IL-6, Itgb2, Cd68, Rac2, Mpeg1, Cxcl10 were downregulated after CTSZKD or CTSZKD+LBGP treatment (n=5 mice per group, ANOVA, *p<0.05; **p<0.01; ****p<0.0001 when CTSZKD compared to NMOSD-ON; #p<0.05; ##p<0.01; ####p<0.0001 when CTSZKD+LBGP compared to NMOSD-ON).

At the 4-week timepoint, we evaluated whether CTSZKD could provide similar protective effects as LBGP treatment on myelin sheath preservation and RGCs survival in the NMOSD-ON model. Both CTSZ KD alone and CTSZ KD + LBGP treatment significantly restored astrocytes ($p = 0.005$ and $p = 0.024$, respectively). Importantly, myelin sheath integrity was effectively preserved in both the CTSZKD ($p = 0.001$) and CTSZKD+LBGP ($p = 0.003$) groups, demonstrating robust protection against NMOSD-ON-induced damage ***(Figure 5.18)***.

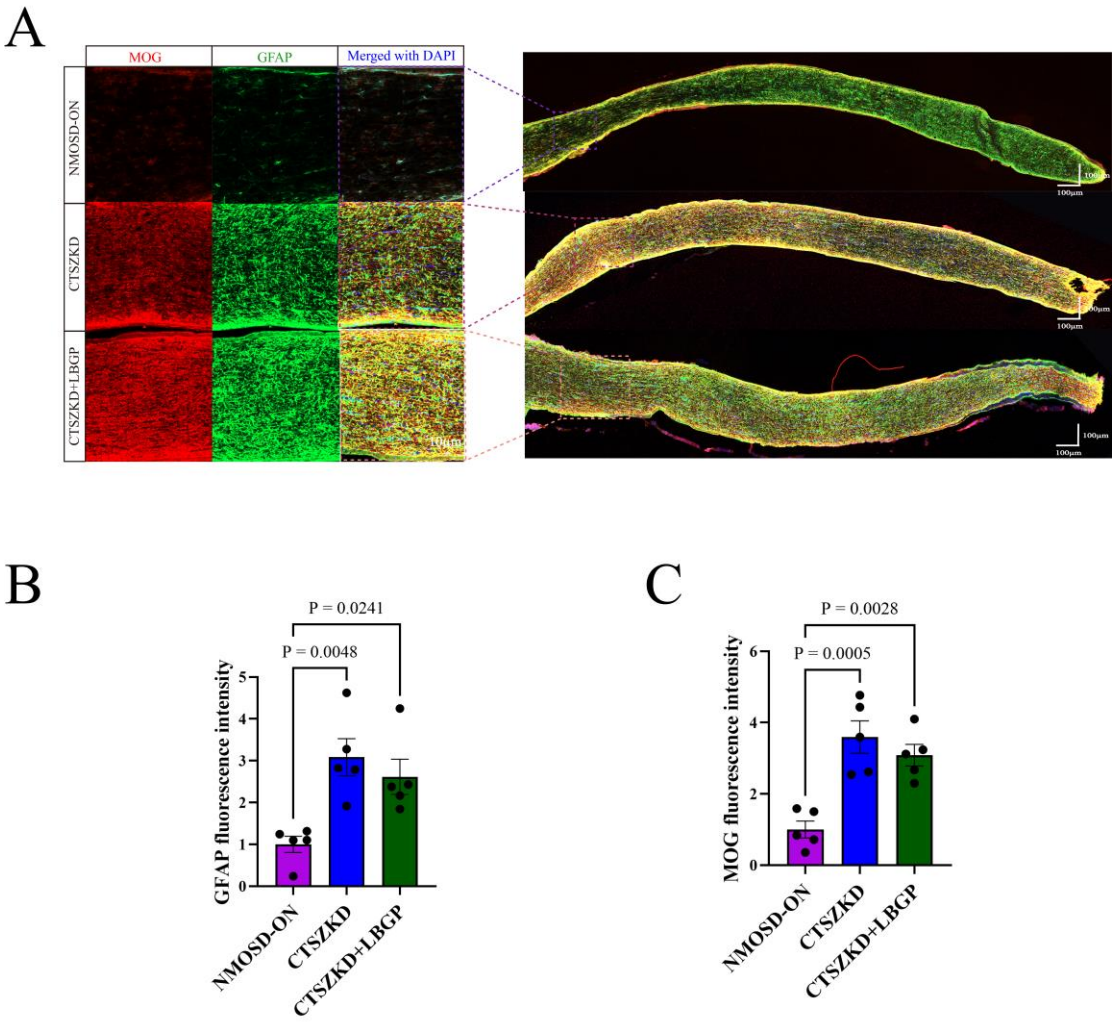

Figure 5.18 The protection of astrocyte and myelin sheath in NMOSD-ON after LBGP treatment. **(A)** The representative image shows that the CTSZKD and CTSZKD+LBGP reduces the damage of MOG protein and GFAP protein expression in NMOSD-ON optic nerve. **(B)** The quantitative analysis shows the GFAP protein was significantly higher after CTSZKD and CTSZKD+LBGP treatment (n=5 mice per group, ANOVA, *p<0.05; **p<0.01, ***p<0.001). **(C)** The MOG protein expression is significantly higher after CTSZKD or CTSZKD+LBGP treatment (n=5 mice per group, ANOVA, **p<0.01, ***p<0.001).

Further analysis revealed that CTSZKD and CTSZKD+LBGP provided strong neuroprotection for

optic nerve axonal fibers, significantly reducing NMOSD-ON degeneration (both $p < 0.0001$) ***(Figure 5.19)***.

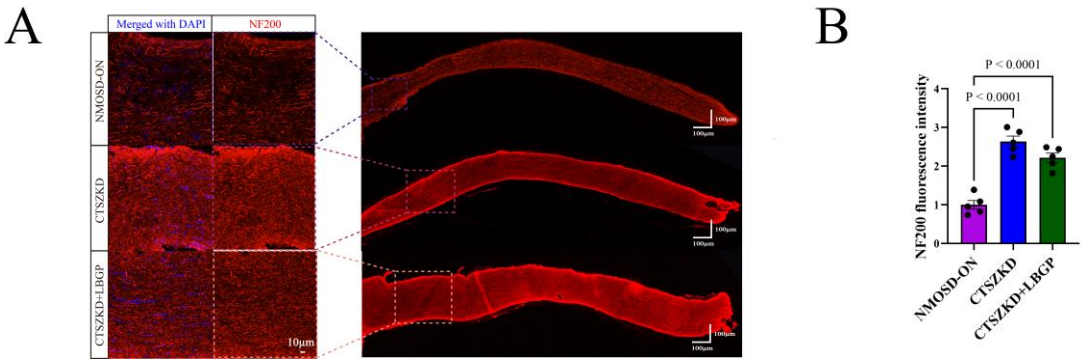

Figure 5.19 The NF200 protein expression after CTSZKD or CTSZKD+LBGP treatment. **(A)** The representative images of NF200. **(B)** The quantitative results show the significant higher NF200 expression after CTSZKD or CTSZKD+LBGP treatment (n=5 mice per group, ANOVA, ****p<0.0001).

Similarly, RGC soma bodies survival was significantly improved in both treatment groups ($p = 0.006$ for CTSZKD; $p = 0.001$ for CTSZKD+LBGP) ***(Figure 5.20)***.

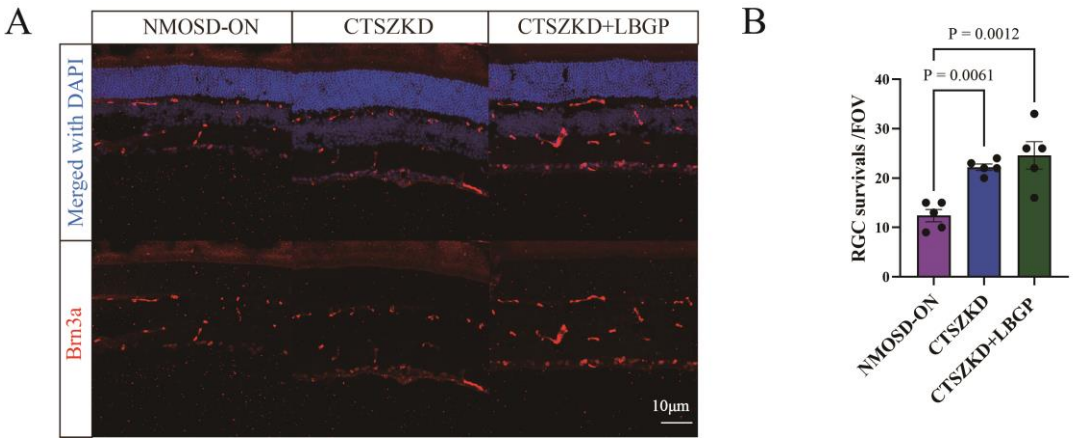

Figure 5.20 The recovery of RGCs soma bodies after CTSZKD or CTSZKD+LBGP treatment. **(A)** The representative images showing the Brn3a-labeled RGCs soma bodies increased after

CTSZKD or CTSZKD+LBGP treatment. **(B)** The quantitative result shows the significant increased RGCs survivals after CTSKZD or CTSZKD+LBGP treatment (n=5 mice per group, ANOVA, ****p<0.0001).

To evaluate visual pathway function, we measured VEP and found the reduced N1 latency (indicating improved signal transmission) in both CTSZKD (p = 0.006) and CTSZKD+LBGP (p = 0.002) groups. Increased N1-P1 amplitude (reflecting enhanced neuronal response) were also observed in both CTSZKD and CTSZKD+LBGP (both p < 0.0001) ***(Figure 5.21)***.

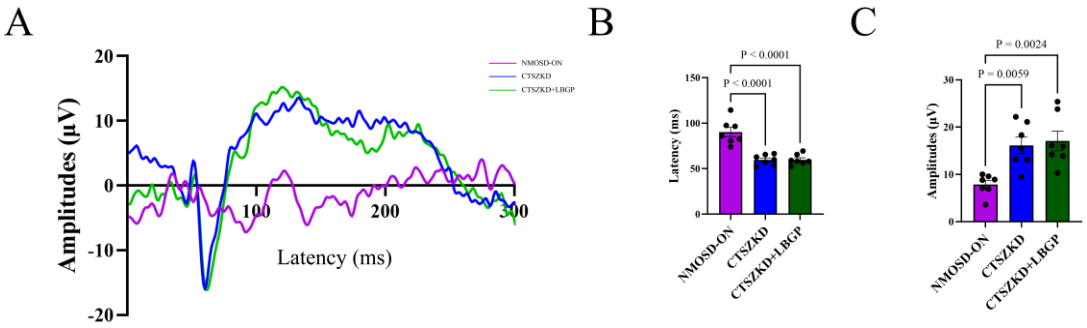

Figure 5.21 The functional impairment was reversed by CTSZKD or CTSZKD+LBGP in NMOSD-ON. **(A)** The representative waveforms elucidate the better VEP responses after CTSZKD or CTSZKD+LBGP treatment. **(B)** The quantitative result shows the significant shortened N1 latency after CTSZKD or CTSZKD+LBGP treatment (n=5 mice per group, ANOVA, ****p<0.0001). **(C)** The quantitative result shows the significant higher N1-P1 amplitude after CTSZKD or CTSZKD+LBGP treatment (n=5 mice per group, ANOVA, **p<0.01).

These findings demonstrate that CTSZ knockdown alone provides neuroprotective effects

comparable to LBGP treatment, preserving myelin integrity, axonal fibers, and RGC survival, while also improving visual functional recovery in the NMOSD-ON model. The combination of CTSZKD+LBGP further enhances these protective effects, suggesting a potential synergistic therapeutic strategy for NMOSD-ON damage.

5.4.4 Mitochondrial-mediated apoptosis prevention is the downstream molecular pathway in LBGP treatment

Our results demonstrate that LBGP treatment regulates both P53 and CTSZ expression. Previous studies have established that P53 can induce the secretion of cathepsins from lysosomes, subsequently activating mitochondria-dependent apoptotic pathways. Given these findings, we investigated whether LBGP-mediated modulation of P53 and CTSZ influences this lysosomal-mitochondrial apoptotic cascade in our experimental model ***(Figure 5.22)***.

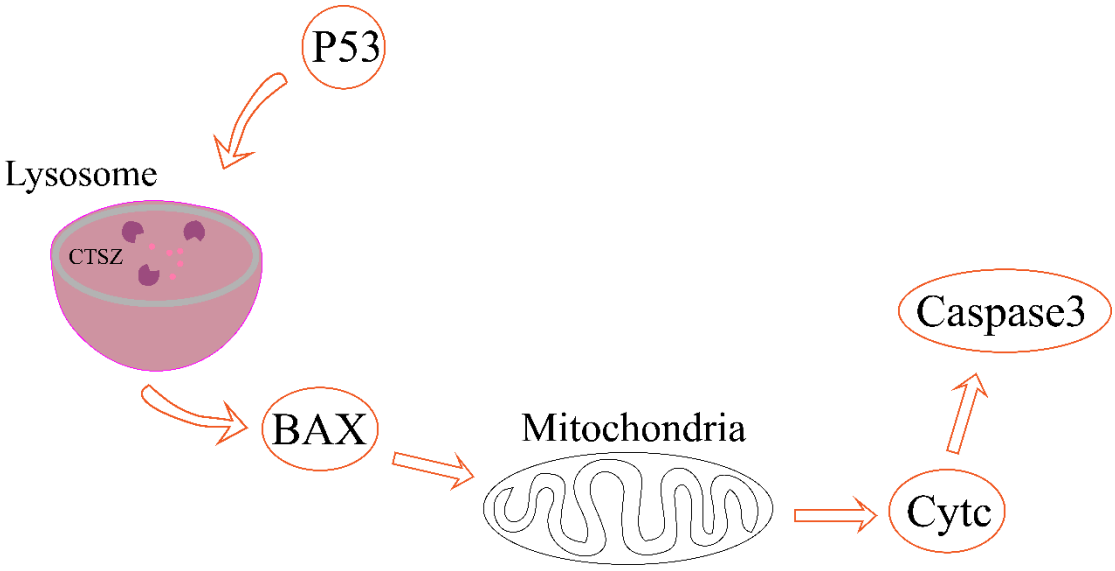

Figure 5.22 This image illustrates how the CTSZ involved in a mitochondria-dependent

apoptosis pathway

In NMOSD-ON, RGCs apoptosis primarily occurs in the inner retinal layer where RGCs soma bodies reside. We quantitatively evaluated apoptotic RGC soma bodies using Terminal deoxynucleotidyl transferase dUTP nick-end labeling (TUNEL) assay. At week 4, LBGP significantly reduced the number of apoptotic RGCs soma bodies (p = 0.006) ***(Figure 5.23)***.

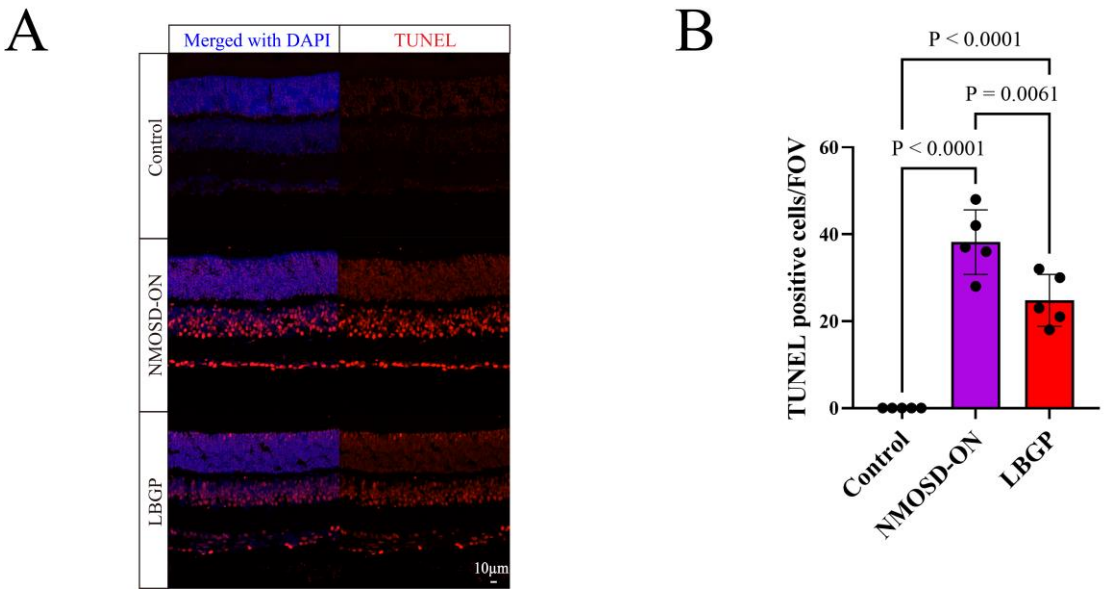

Figure 5.23 The apoptosis prevention after LBGP treatment. **(A)** The representative image of TUNEL labeled apoptotic RGCs soma bodies revealed the reduced apoptotic RGCs soma bodies after LBGP treatment. **(B)** The quantitative result shows the significant reduction of RGCs soma bodies after LBGP treatment (n=5 mice per group, ANOVA, ** p<0.01, ****p<0.0001).

Given that CTSZ is a downstream target of LBGP, CTSZ was further investigated if its knockdown could similarly attenuate apoptotic RGCs soma bodies. Flow cytometric analysis of retinal cell suspensions revealed that CTSZKD alone significantly decreased early apoptotic cells ($p = 0.003$), with comparable effects observed in the combination treatment group (CTSZKD+LBGP, $p=0.006$). However, neither intervention significantly affected late apoptotic cell populations ***(Figure 5.24)***.

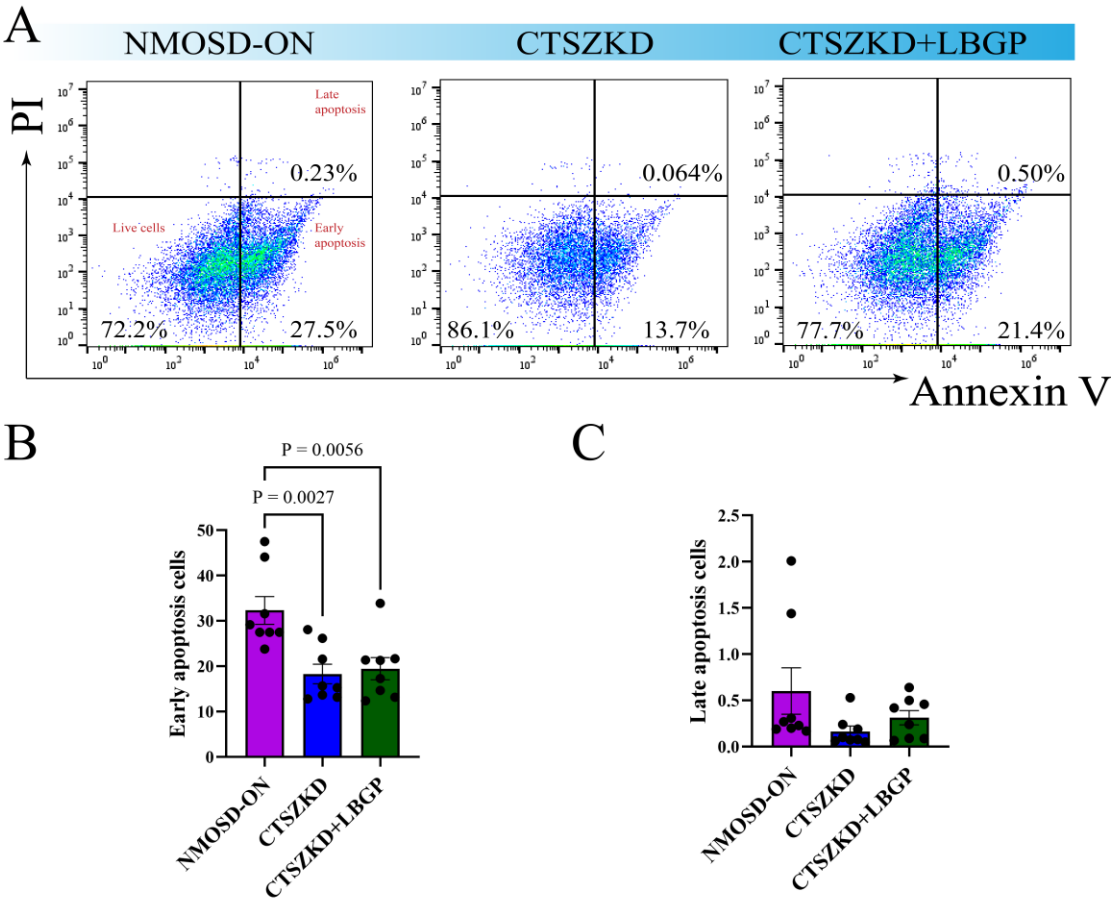

Figure 5.24 The CTSZKD or CTSZKD+LBGP reduced the apoptosis of RGCs. **(A)** Flow cytometry shows that the apoptotic cell population labeled by Annexin V and PI. The Annexin V

(+) and PI (-) indicated early apoptotic cell population while the Annexin V (+) and PI (+) indicated the late apoptotic cells. **(B)** The early apoptotic cell population reduced significantly after CTSZKD or CTSZKD+LBGP treatment (n=5 mice per group, ANOVA, ** p<0.01). **(C)** The late apoptotic cell population did not change significantly (n=5 mice per group, ANOVA).

To establish whether apoptosis represents the final downstream pathway in LBGP-mediated neuroprotection against NMOSD-ON, the apoptosis inhibitor pifithrin-α (PFT-α) was administered via optic nerve injection ***(Figure 5.25 A)***. Our results demonstrated successful inhibition of RGC soma apoptosis ($p < 0.001$) following PFT-α treatment ***(Figure 5.25 B and C)***.

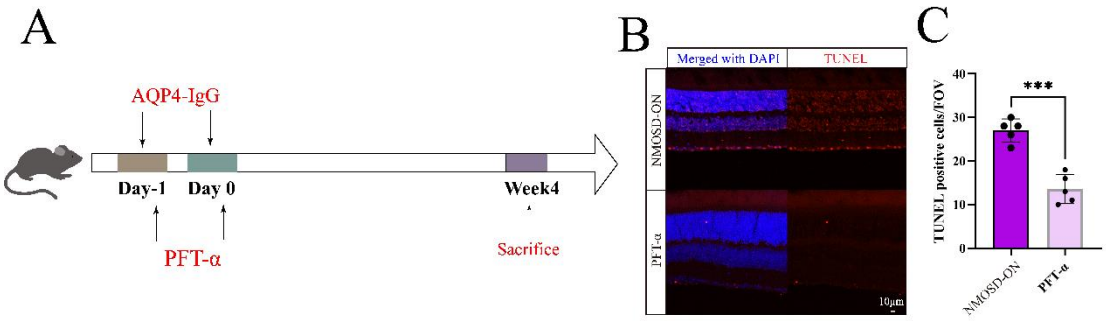

Figure 5.25 Successful inhibition of apoptosis in RGCs soma bodies. **(A)** Timeline elucidating the delivery of AQP4-IgG and apoptotic inhibitory drug PFT-α. **(B)** Reduced apoptotic RGCs soma bodies after delivery of PFT-α in representative image. **(C)** The quantitative analysis shows the significant reduction of TUNEL-labeled RGCs soma bodies (n=5 mice per group, ANOVA, *** p<0.001).

Subsequent evaluation of key neuropathological markers at 4 weeks post-onset revealed. No significant rescue of GFAP expression decline ($p > 0.05$) ***(Figure 5.26 A and B)***, but significant

protection against MOG protein degradation was found (p = 0.002) ***(Figure 5.26 A and C)***.

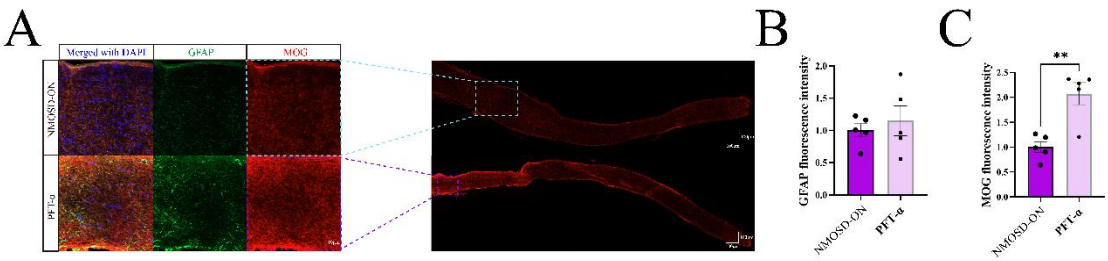

Figure 5.26 PFT-α protects the myelin sheath but not the astrocyte. **(A)** The representative image shows the astrocyte (labeled by GFAP, green), and myelin sheath (labeled by MOG, red) integrity after the PFT-α treatment. **(B)** The quantitative result shows the GFAP expression did not change after PFT-α treatment. **(C)** The quantitative result shows the MOG expression is significantly higher after PFT-α treatment.

Effective prevention of NF200 expression reduction was found (p < 0.001) ***(Figure 5.27 A and B)***, and marked preservation of RGC soma integrity was also observed (p < 0.001) ***(Figure 5.28 A and B)***.

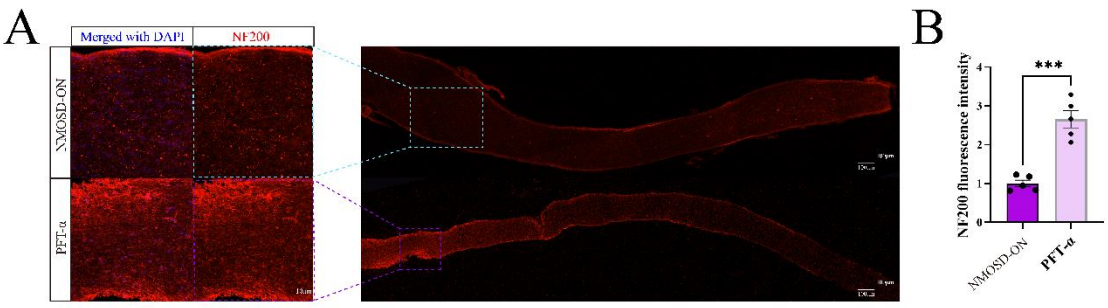

Figure 5.27 Axonal degeneration was rescued by PFT-α treatment. **(A)** The representative image of NF200 illustrates that the PFT-α delivery reduces the reduction of NF200 expression. **(B)** The quantitative result showed the significant increase of NF200 after PFT-α delivery (n=5 mice per group, ANOVA, *** p<0.001).

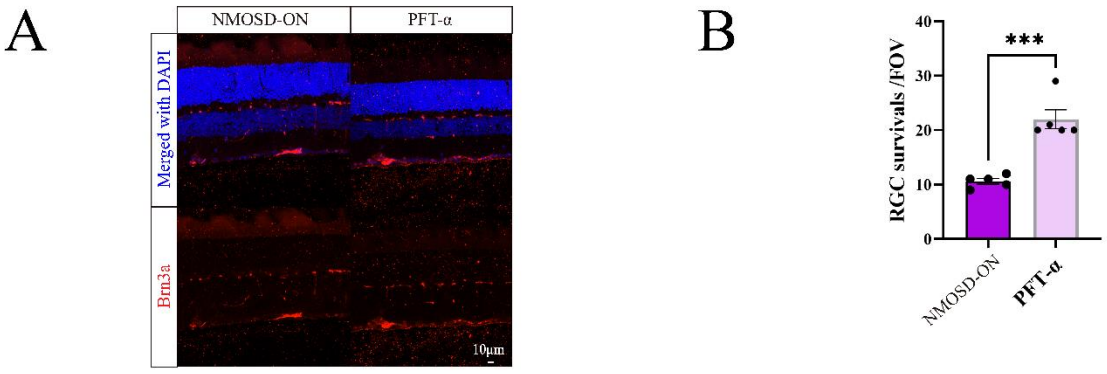

Figure 5.28 The PFT-α delivery rescues the survivals of RGCs soma bodies in NMOSD-ON. **(A)** The representative images of Brn3a-labeled RGCs soma bodies show the increased RGCs soma bodies after PFT-α treatment. **(B)** The quantitative result shows the significant increase in RGCs survivals after PFT-α treatment (n=5 mice per group, ANOVA, *** $p<0.001$).

These findings collectively suggest that while apoptotic inhibition doesn't affect astrogliosis (as reflected by GFAP), it provides substantial protection for myelin integrity (MOG), axonal structure (NF200), and RGC survival in NMOSD-ON.

5.5 Discussion

Exploring the mechanism of action and mediating targets of LBGP treatment in animal models of NMOSD-ON is currently of paramount importance. First, it is important to understand the molecular basis of LBGP's therapeutic effects and then determine whether novel drug candidates can be developed by targeting these mediating proteins.

This study initially employed proteomics to investigate the molecular and protein-level changes associated with NMOSD-ON pathogenesis and LBGP treatment. Subsequently, potential mechanistic pathways were validated, identifying the excessive secretion of lysosomal enzymes as a key mechanism underlying LBGP's therapeutic effect in NMOSD-ON. Among these lysosomal enzymes, CTSZ plays a critical mediating role, as it was significantly downregulated by LBGP following NMOSD-ON onset. Functional validation of CTSZ, along with analysis of its downstream apoptotic pathways (Ding et al., 2022), further supports this finding.

Our proteomics data revealed several neutrophil-related pathways, including "Neutrophil degranulation" (ranked as the top 1 pathway) and "Neutrophil Extracellular Trap Signaling Pathway," consistent with prior literature establishing neutrophil infiltration as a key mechanism in NMOSD pathogenesis (S. Saadoun et al., 2012). Notably, both pathways depend on enzyme secretion to execute their functions.

Additionally, microglial/macrophage-associated pathways such as "Phagosome Maturation," "Fcγ Receptor-mediated Phagocytosis in Macrophages and Monocytes," and "Production of Nitric Oxide and Reactive Oxygen Species in Macrophages" were identified. These pathways are linked to phagosome formation and phagocytic activity, processes previously implicated in NMOSD-ON and modulated by LBGP treatment. Crucially, lysosomal enzyme secretion is required to support phagocytosis (Zimmerli et al., 1996).

Taken together, these findings suggest that lysosomal enzyme regulation serves as a critical

mechanism underlying LBGP's therapeutic effects in NMOSD-ON. CTSZ has been previously implicated in CNS autoimmune disorders, particularly in EAE, an animal model of MS, where it plays a significant pathogenic role (Allan et al., 2017).

In this study, functional validation of CTSZ was performed through siRNA-mediated knockdown, achieving a 30% reduction in CTSZ protein expression. Notably, this partial knockdown produced a neuroprotective effect comparable to LBGP treatment, supporting CTSZ's involvement in NMOSD-ON pathogenesis. Further investigation revealed that CTSZ mediates downstream apoptosis pathways, and key apoptotic proteins were similarly modulated by LBGP treatment. Ultimately, our findings determined that the CTSZ-regulated apoptotic pathway serves as a critical therapeutic target of LBGP in NMOSD-ON.

5.6 Conclusion

In this study, proteomic data at the peak of inflammation revealed that lysosome regulation is likely the targeted pathway through which LBGP modulates the treatment of NMOSD-ON. Among the findings, we identified CTSZ as a key mediator. Through functional validation and confirmation of downstream apoptotic pathways, we further verified this target.

Chapter 6 Summary of this project

My project systematically unravels the pathogenesis and treatment of NMOSD-ON through a continuum of interconnected discoveries. Beginning with clinical observations in human patients, OCT analysis demostrated that NMOSD-ON exhibits more rapid and severe RNFL thinning within one month compared to IDON, in non-edematous eyes, suggesting an aggressive early neurodegenerative process. This clinical insight prompted us to develop an optimized animal model featuring direct AQP4-IgG injection into the optic nerve within one-month observation, which faithfully recapitulated the human disease timeline: AQP4 loss by day 2, inflammatory peak and astrocyte disintegration in week 1, followed by secondary demyelination and RGC degeneration (weeks 2-4), while maintaining BBB integrity for clinically relevant therapeutic testing. This animal model with a comprehensive framework has been published in ***Neural Regeneration Research*** (Yang et al., 2025). Building upon this robust experimental framework, LBGP was investigated as a potential therapeutic intervention due to its neuroprotective and immunoregulatory effects (Kong

et al., 2024). Excitingly, LBGP treatment at week 4 effectively rescued astrocyte loss, preserved myelin integrity, and restored RGC function as evidenced by improved VEP and ERG responses. These therapeutic outcomes naturally initiates to explore the underlying mechanisms, where we discovered LBGP's ability to modulate lysosomal enzyme secretion, with particular emphasis on its targeted downregulation of CTSZ and associated apoptosis pathways.

Our research addresses several key issues in NMOSD-ON. First, we characterized optic nerve degeneration and found that it can occur at the earliest disease stages, suggesting the critical window for inflammation control and neuroprotection may be within the first month. While preventing relapse has been the primary focus after early remission, It was demonstrated that even a single NMOSD-ON attack can cause irreversible optic nerve damage, emphasizing the importance of early intervention. Our animal model revealed that inflammatory peaks involving CNS microglial activation coincide with AQP4 breakdown and astrocyte damage. Interestingly, astrocytes not only provide structural support and blood-brain barrier maintenance but also actively participate in immune responses. Subsequent astrocyte recovery was observed, potentially contributing to neural repair. When testing LBGP, a compound with known anti-inflammatory and neuroprotective properties, we found it effectively prevented retinal ganglion cell degeneration in our NMOSD-ON model, suggesting its potential as either an alternative or adjunct to current first-line therapies. Mechanistically, the lysosomal enzyme CTSZ was identified as LBGP's therapeutic target, with CTSZ knockdown replicating LBGP's benefits. This discovery unveils cathepsin inhibition as a promising novel treatment strategy for NMOSD-ON, opening new avenues for clinical development.

Chapter 7 Limitations and Future Directions

While our study and existing literature collectively demonstrate the involvement of multiple immune cell types (neutrophils, microglia, and dendritic cells) in NMOSD-ON pathogenesis, the precise hierarchy of their contributions remains unresolved. Some studies emphasize microglial-astrocyte interactions through complement-mediated signaling as disease amplifiers (Tingjun Chen et al., 2020), whereas our proteomics data and other reports highlight neutrophils (Samira Saadoun et al., 2012) as potentially dominant players, with additional evidence implicating dendritic cells (Flórez-Grau et al., 2018).

To address this fundamental question, we will first conduct single-cell RNA sequencing of optic nerve tissue to definitively determine which immune cell population shows the most significant infiltration and activation during disease progression. Should neutrophils emerge as the predominant pathogenic cell type, we will employ Switching Mechanism at the 5' end of RNA Template

(SMART)-RNA sequencing technology to perform neutrophil-specific transcriptomic profiling, enabling precise identification of neutrophil recruitment and activation pathways. This will be followed by targeted functional validation using two complementary approaches: (1) neutrophil depletion experiments using Ly6G antibodies to assess therapeutic potential, and (2) cell-specific genetic manipulation via Cre-lox systems to selectively delete neutrophil chemoattractants from either astrocytes or microglia, which will allow us to determine whether disrupting neutrophil infiltration can mitigate disease pathology. This comprehensive strategy will not only clarify the primary immune driver in NMOSD-ON but also identify novel cell-specific therapeutic targets for intervention.

Building on our mechanistic discoveries, we are advancing LBGP therapy through an integrated preclinical-clinical pipeline. First, we are systematically isolating and characterizing LBGP's bioactive components using advanced phytochemical separation techniques combined with functional screening assays, aiming to identify the key neuroprotective and immunomodulatory constituents responsible for its therapeutic effects. This bioactive optimization will be complemented by pharmacological refinement to enhance bioavailability and target specificity while maintaining the formula's holistic therapeutic profile.

Concurrently, we are preparing for clinical translation by establishing standardized quality control protocols for LBGP production and designing investigator-initiated trials to evaluate its safety and efficacy on NMOSD-ON patients. This therapeutic development program bridges our fundamental research findings with real-world clinical applications, with the ultimate goal of providing an

evidence-based, targeted phytotherapeutic option that addresses both the inflammatory and neurodegenerative aspects of NMOSD-ON while minimizing the side effects associated with current immunosuppressive regimens. The dual focus on mechanistic refinement and clinical implementation positions LBGP as a promising candidate for next-generation NMOSD therapeutics.

Reference

Abel, A., McClelland, C., & Lee, M. S. (2019). Critical review: Typical and atypical optic neuritis. *Surv Ophthalmol*, *64*(6), 770-779. https://doi.org/10.1016/j.survophthal.2019.06.001

Akaishi, T., & Nakashima, I. (2017). Efficiency of antibody therapy in demyelinating diseases. *Int Immunol*, *29*(7), 327-335. https://doi.org/10.1093/intimm/dxx037

Allan, E. R., Campden, R. I., Ewanchuk, B. W., Tailor, P., Balce, D. R., McKenna, N. T., Greene, C. J., Warren, A. L., Reinheckel, T., & Yates, R. M. (2017). A role for cathepsin Z in neuroinflammation provides mechanistic support for an epigenetic risk factor in multiple sclerosis. *Journal of Neuroinflammation*, *14*, 1-11.

Araki, M., Matsuoka, T., Miyamoto, K., Kusunoki, S., Okamoto, T., Murata, M., Miyake, S., Aranami, T., & Yamamura, T. (2014). Efficacy of the anti-IL-6 receptor antibody tocilizumab in neuromyelitis optica: a pilot study. *Neurology*, *82*(15), 1302-1306. https://doi.org/10.1212/wnl.0000000000000317

Asavapanumas, N., Ratelade, J., Papadopoulos, M. C., Bennett, J. L., Levin, M. H., & Verkman, A. S. (2014). Experimental mouse model of optic neuritis with inflammatory demyelination produced by passive transfer of neuromyelitis optica-immunoglobulin G. *J Neuroinflammation*, *11*, 16. https://doi.org/10.1186/1742-2094-11-16

Asavapanumas, N., Ratelade, J., & Verkman, A. S. (2014). Unique neuromyelitis optica pathology produced in naïve rats by intracerebral administration of NMO-IgG. *Acta Neuropathol*, *127*(4), 539-551. https://doi.org/10.1007/s00401-013-1204-8

Ayoubi, N. K. E., Moussa, H., Younes, A., Haddad, R., & Khoury, S. J. (2022). Use of retinal optical coherence tomography to differentiate suspected neuromyelitis optica spectrum disorder from multiple sclerosis: A cross-sectional study. *Mult Scler Relat Disord*, *68*, 104160. https://doi.org/10.1016/j.msard.2022.104160

Baghereih, S., Afshari-Safavi, A., Vaheb, S., Kiani, M., Ghaffary, E. M., Barzegar, M., Shaygannejad, V., Zabeti, A., & Mirmosayyeb, O. (2023). Worldwide prevalence of neuromyelitis optica spectrum disorder (NMOSD) and neuromyelitis optica (NMO): a systematic review and meta-analysis. *Neurol Sci*, *44*(6), 1905-1915. https://doi.org/10.1007/s10072-023-06617-y

Bai, X., Jing, L., Li, Y., Li, Y., Luo, S., Wang, S., Zhou, J., Liu, Z., & Diao, A. (2014). TMEPAI inhibits TGF-β signaling by promoting lysosome degradation of TGF-β receptor and contributes to lung cancer development. *Cellular signalling*, *26*(9), 2030-2039.

Bechmann, I., Galea, I., & Perry, V. H. (2007). What is the blood-brain barrier (not)? *Trends Immunol*, *28*(1), 5-11. https://doi.org/10.1016/j.it.2006.11.007

Beck, R. W., Cleary, P. A., & Backlund, J. C. (1994). The course of visual recovery after optic neuritis. Experience of the Optic Neuritis Treatment Trial. *Ophthalmology*, *101*(11), 1771-1778. https://doi.org/10.1016/s0161-6420(94)31103-1

Bennett, J. L., Aktas, O., Rees, W. A., Smith, M. A., Gunsior, M., Yan, L., She, D., Cimbora, D., Pittock, S. J., Weinshenker, B. G., Paul, F., Marignier, R., Wingerchuk, D., Cutter, G., Green, A., Hartung, H. P., Kim, H. J., Fujihara, K., Levy, M., . . . Cree, B. A. C. (2022). Association between B-cell depletion and attack risk in neuromyelitis optica spectrum disorder: An exploratory analysis from N-MOmentum, a double-blind, randomised, placebo-controlled, multicentre phase 2/3

trial. *EBioMedicine*, *86*, 104321. https://doi.org/10.1016/j.ebiom.2022.104321

Bennett, J. L., de Seze, J., Lana-Peixoto, M., Palace, J., Waldman, A., Schippling, S., Tenembaum, S., Banwell, B., Greenberg, B., Levy, M., Fujihara, K., Chan, K. H., Kim, H. J., Asgari, N., Sato, D. K., Saiz, A., Wuerfel, J., Zimmermann, H., Green, A., . . . Paul, F. (2015). Neuromyelitis optica and multiple sclerosis: Seeing differences through optical coherence tomography. *Mult Scler*, *21*(6), 678-688. https://doi.org/10.1177/1352458514567216

Bennett, J. L., Lam, C., Kalluri, S. R., Saikali, P., Bautista, K., Dupree, C., Glogowska, M., Case, D., Antel, J. P., Owens, G. P., Gilden, D., Nessler, S., Stadelmann, C., & Hemmer, B. (2009). Intrathecal pathogenic anti-aquaporin-4 antibodies in early neuromyelitis optica. *Ann Neurol*, *66*(5), 617-629. https://doi.org/10.1002/ana.21802

Bessis, A., Béchade, C., Bernard, D., & Roumier, A. (2007). Microglial control of neuronal death and synaptic properties. *Glia*, *55*(3), 233-238. https://doi.org/10.1002/glia.20459

Bhagavati, S. (2021). Autoimmune Disorders of the Nervous System: Pathophysiology, Clinical Features, and Therapy. *Front Neurol*, *12*, 664664. https://doi.org/10.3389/fneur.2021.664664

Briggs, F. B., & Shaia, J. (2024). Prevalence of neuromyelitis optica spectrum disorder in the United States. *Mult Scler*, 13524585231224683. https://doi.org/10.1177/13524585231224683

Butler, C. A., Popescu, A. S., Kitchener, E. J. A., Allendorf, D. H., Puigdellívol, M., & Brown, G. C. (2021). Microglial phagocytosis of neurons in neurodegeneration, and its regulation. *J Neurochem*, *158*(3), 621-639. https://doi.org/10.1111/jnc.15327

Butt, A. M., Pugh, M., Hubbard, P., & James, G. (2004). Functions of optic nerve glia: axoglial signalling in physiology and pathology. *Eye*, *18*(11), 1110-1121. https://doi.org/10.1038/sj.eye.6701595

Calabrese, F., Rossetti, A. C., Racagni, G., Gass, P., Riva, M. A., & Molteni, R. (2014). Brain-derived neurotrophic factor: a bridge between inflammation and neuroplasticity. *Front Cell Neurosci*, *8*, 430. https://doi.org/10.3389/fncel.2014.00430

Carnero Contentti, E., & Correale, J. (2021). Neuromyelitis optica spectrum disorders: from pathophysiology to therapeutic strategies. *J Neuroinflammation*, *18*(1), 208. https://doi.org/10.1186/s12974-021-02249-1

Carson, M. J., Doose, J. M., Melchior, B., Schmid, C. D., & Ploix, C. C. (2006). CNS immune privilege: hiding in plain sight. *Immunol Rev*, *213*, 48-65. https://doi.org/10.1111/j.1600-065X.2006.00441.x

Chan, H.-C., Chang, R. C.-C., Ip, A. K.-C., Chiu, K., Yuen, W.-H., Zee, S.-Y., & So, K.-F. (2007). Neuroprotective effects of Lycium barbarum Lynn on protecting retinal ganglion cells in an ocular hypertension model of glaucoma. *Experimental neurology*, *203*(1), 269-273.

Chen, T., Lennon, V. A., Liu, Y. U., Bosco, D. B., Li, Y., Yi, M.-H., Zhu, J., Wei, S., & Wu, L.-J. (2020). Astrocyte-microglia interaction drives evolving neuromyelitis optica lesion. *The Journal of clinical investigation*, *130*(8), 4025-4038.

Chen, T., Lennon, V. A., Liu, Y. U., Bosco, D. B., Li, Y., Yi, M. H., Zhu, J., Wei, S., & Wu, L. J. (2020). Astrocyte-microglia interaction drives evolving neuromyelitis optica lesion. *J Clin Invest*, *130*(8), 4025-4038. https://doi.org/10.1172/jci134816

Chen, Z., Lou, X., Liu, M., Huang, D., Wei, S., Yu, S., & Ma, L. (2015). Assessment of Optic Nerve Impairment in Patients with Neuromyelitis Optica by MR Diffusion Tensor Imaging. *PLoS One*, *10*(5), e0126574. https://doi.org/10.1371/journal.pone.0126574

Chu, P. H., Li, H. Y., Chin, M. P., So, K. F., & Chan, H. H. (2013). Effect of lycium barbarum (wolfberry)

polysaccharides on preserving retinal function after partial optic nerve transection. *PLoS One*, *8*(12), e81339. https://doi.org/10.1371/journal.pone.0081339

The clinical profile of optic neuritis. Experience of the Optic Neuritis Treatment Trial. Optic Neuritis Study Group. (1991). *Arch Ophthalmol*, *109*(12), 1673-1678. https://doi.org/10.1001/archopht.1991.01080120057025

Constantinescu, C. S., Farooqi, N., O'Brien, K., & Gran, B. (2011). Experimental autoimmune encephalomyelitis (EAE) as a model for multiple sclerosis (MS). *Br J Pharmacol*, *164*(4), 1079-1106. https://doi.org/10.1111/j.1476-5381.2011.01302.x

Crane, J. M., Bennett, J. L., & Verkman, A. S. (2009). Live cell analysis of aquaporin-4 m1/m23 interactions and regulated orthogonal array assembly in glial cells. *J Biol Chem*, *284*(51), 35850-35860. https://doi.org/10.1074/jbc.M109.071670

Crane, J. M., Lam, C., Rossi, A., Gupta, T., Bennett, J. L., & Verkman, A. S. (2011). Binding affinity and specificity of neuromyelitis optica autoantibodies to aquaporin-4 M1/M23 isoforms and orthogonal arrays. *J Biol Chem*, *286*(18), 16516-16524. https://doi.org/10.1074/jbc.M111.227298

Dai, Y., Guo, J., Zhang, B., Chen, J., Ou, H., He, R.-R., So, K.-F., & Zhang, L. (2023). Lycium barbarum (Wolfberry) glycopeptide prevents stress-induced anxiety disorders by regulating oxidative stress and ferroptosis in the medial prefrontal cortex. *Phytomedicine*, *116*, 154864.

Dai, Y., Guo, J., Zhang, B., Chen, J., Ou, H., He, R. R., So, K. F., & Zhang, L. (2023). Lycium barbarum (Wolfberry) glycopeptide prevents stress-induced anxiety disorders by regulating oxidative stress and ferroptosis in the medial prefrontal cortex. *Phytomedicine*, *116*, 154864. https://doi.org/10.1016/j.phymed.2023.154864

Dale, R. C., Tantsis, E. M., Merheb, V., Kumaran, R. Y., Sinmaz, N., Pathmanandavel, K., Ramanathan, S., Booth, D. R., Wienholt, L. A., Prelog, K., Clark, D. R., Guillemin, G. J., Lim, C. K., Mathey, E. K., & Brilot, F. (2014). Antibodies to MOG have a demyelination phenotype and affect oligodendrocyte cytoskeleton. *Neurol Neuroimmunol Neuroinflamm*, *1*(1), e12. https://doi.org/10.1212/nxi.0000000000000012

Dalmau, J., Geis, C., & Graus, F. (2017). Autoantibodies to Synaptic Receptors and Neuronal Cell Surface Proteins in Autoimmune Diseases of the Central Nervous System. *Physiol Rev*, *97*(2), 839-887. https://doi.org/10.1152/physrev.00010.2016

Dalmau, J., & Graus, F. (2018). Antibody-Mediated Encephalitis. *N Engl J Med*, *378*(9), 840-851. https://doi.org/10.1056/NEJMra1708712

Danieli, M. G., Antonelli, E., Gammeri, L., Longhi, E., Cozzi, M. F., Palmeri, D., Gangemi, S., & Shoenfeld, Y. (2025). Intravenous immunoglobulin as a therapy for autoimmune conditions. *Autoimmun Rev*, *24*(1), 103710. https://doi.org/10.1016/j.autrev.2024.103710

De Moraes, C. G. (2013). Anatomy of the visual pathways. *Journal of glaucoma*, *22*, S2-S7.

DelMonte, D. W., & Kim, T. (2011). Anatomy and physiology of the cornea. *J Cataract Refract Surg*, *37*(3), 588-598. https://doi.org/10.1016/j.jcrs.2010.12.037

Ding, X., Zhang, C., Chen, H., Ren, M., & Liu, X. (2022). Cathepsins Trigger Cell Death and Regulate Radioresistance in Glioblastoma. *Cells*, *11*(24). https://doi.org/10.3390/cells11244108

Duan, T., & Verkman, A. S. (2020). Experimental animal models of aquaporin-4-IgG-seropositive neuromyelitis optica spectrum disorders: progress and shortcomings. *Brain Pathol*, *30*(1), 13-25. https://doi.org/10.1111/bpa.12793

Duchow, A., Bellmann-Strobl, J., Friede, T., Aktas, O., Angstwurm, K., Ayzenberg, I., Berthele, A., Dawin, E., Engels, D., Fischer, K., Flaskamp, M., Giglhuber, K., Grothe, M., Havla, J., Hümmert, M. W., Jarius, S., Kaste, M., Kern, P., Kleiter, I., . . . Häußler, V. (2024). Time to Disability Milestones and Annualized Relapse Rates in NMOSD and MOGAD. *Ann Neurol*, *95*(4), 720-732. https://doi.org/10.1002/ana.26858

Duvigneaud, Z., Lardeux, P., Verrecchia, S., Benyahya, L., Marignier, R., & Froment Tilikete, C. (2024). Diagnostic criteria for optic neuritis in the acute and subacute phase: clinical uses and limitations. *J Neurol*, *271*(8), 5629-5636. https://doi.org/10.1007/s00415-024-12540-9

Felix, C. M., Levin, M. H., & Verkman, A. S. (2016). Complement-independent retinal pathology produced by intravitreal injection of neuromyelitis optica immunoglobulin G. *J Neuroinflammation*, *13*(1), 275. https://doi.org/10.1186/s12974-016-0746-9

Fernandes, D. B., Raza, A. S., Nogueira, R. G., Wang, D., Callegaro, D., Hood, D. C., & Monteiro, M. L. (2013). Evaluation of inner retinal layers in patients with multiple sclerosis or neuromyelitis optica using optical coherence tomography. *Ophthalmology*, *120*(2), 387-394. https://doi.org/10.1016/j.ophtha.2012.07.066

Flanagan, E. P. (2019). Neuromyelitis Optica Spectrum Disorder and Other Non-Multiple Sclerosis Central Nervous System Inflammatory Diseases. *Continuum (Minneap Minn)*, *25*(3), 815-844. https://doi.org/10.1212/con.0000000000000742

Flórez-Grau, G., Zubizarreta, I., Cabezón, R., Villoslada, P., & Benitez-Ribas, D. (2018). Tolerogenic dendritic cells as a promising antigen-specific therapy in the treatment of multiple sclerosis and neuromyelitis optica from preclinical to clinical trials. *Frontiers in immunology*, *9*, 1169.

Furuta, K., Ikeda, M., Nakayama, Y., Nakamura, K., Tanaka, M., Hamasaki, N., Himeno, M., Hamilton, S. R., & August, J. T. (2001). Expression of lysosome-associated membrane proteins in human colorectal neoplasms and inflammatory diseases. *Am J Pathol*, *159*(2), 449-455. https://doi.org/10.1016/s0002-9440(10)61716-6

Galea, I., Bechmann, I., & Perry, V. H. (2007). What is immune privilege (not)? *Trends Immunol*, *28*(1), 12-18. https://doi.org/10.1016/j.it.2006.11.004

Gao, F., Chai, B., Gu, C., Wu, R., Dong, T., Yao, Y., & Zhang, Y. (2019). Effectiveness of rituximab in neuromyelitis optica: a meta-analysis. *BMC Neurology*, *19*(1), 36. https://doi.org/10.1186/s12883-019-1261-2

Graus, F., Escudero, D., Oleaga, L., Bruna, J., Villarejo-Galende, A., Ballabriga, J., Barceló, M. I., Gilo, F., Popkirov, S., Stourac, P., & Dalmau, J. (2018). Syndrome and outcome of antibody-negative limbic encephalitis. *Eur J Neurol*, *25*(8), 1011-1016. https://doi.org/10.1111/ene.13661

Graus, F., Titulaer, M. J., Balu, R., Benseler, S., Bien, C. G., Cellucci, T., Cortese, I., Dale, R. C., Gelfand, J. M., Geschwind, M., Glaser, C. A., Honnorat, J., Höftberger, R., Iizuka, T., Irani, S. R., Lancaster, E., Leypoldt, F., Prüss, H., Rae-Grant, A., . . . Dalmau, J. (2016). A clinical approach to diagnosis of autoimmune encephalitis. *Lancet Neurol*, *15*(4), 391-404. https://doi.org/10.1016/s1474-4422(15)00401-9

Griffiths, M. R., Gasque, P., & Neal, J. W. (2009). The multiple roles of the innate immune system in the regulation of apoptosis and inflammation in the brain. *J Neuropathol Exp Neurol*, *68*(3), 217-226. https://doi.org/10.1097/NEN.0b013e3181996688

Hamilton, R. (2021). Clinical electrophysiology of vision—commentary on current status and future prospects. *Eye*, *35*(9), 2341-2343. https://doi.org/10.1038/s41433-021-01592-0

Haydon, P. G., & Carmignoto, G. (2006). Astrocyte control of synaptic transmission and neurovascular coupling. *Physiol Rev*, *86*(3), 1009-1031. https://doi.org/10.1152/physrev.00049.2005

Herrero, A., Berrada, H., Barraquer, R. I., & Michael, R. (2025). Quantification of visual acuity: "Counting fingers" and "Hand movement" with the Berkeley Rudimentary Vision Test. *J Optom*, *18*(1), 100531. https://doi.org/10.1016/j.optom.2024.100531

Herwerth, M., Kalluri, S. R., Srivastava, R., Kleele, T., Kenet, S., Illes, Z., Merkler, D., Bennett, J. L., Misgeld, T., & Hemmer, B. (2016). In vivo imaging reveals rapid astrocyte depletion and axon damage in a model of neuromyelitis optica-related pathology. *Ann Neurol*, *79*(5), 794-805. https://doi.org/10.1002/ana.24630

Hinson, S. R., Roemer, S. F., Lucchinetti, C. F., Fryer, J. P., Kryzer, T. J., Chamberlain, J. L., Howe, C. L., Pittock, S. J., & Lennon, V. A. (2008). Aquaporin-4-binding autoantibodies in patients with neuromyelitis optica impair glutamate transport by down-regulating EAAT2. *J Exp Med*, *205*(11), 2473-2481. https://doi.org/10.1084/jem.20081241

Hinson, S. R., Romero, M. F., Popescu, B. F., Lucchinetti, C. F., Fryer, J. P., Wolburg, H., Fallier-Becker, P., Noell, S., & Lennon, V. A. (2012). Molecular outcomes of neuromyelitis optica (NMO)-IgG binding to aquaporin-4 in astrocytes. *Proc Natl Acad Sci U S A*, *109*(4), 1245-1250. https://doi.org/10.1073/pnas.1109980108

Ho, Y. S., Yu, M. S., Yang, X. F., So, K. F., Yuen, W. H., & Chang, R. C. (2010). Neuroprotective effects of polysaccharides from wolfberry, the fruits of Lycium barbarum, against homocysteine-induced toxicity in rat cortical neurons. *J Alzheimers Dis*, *19*(3), 813-827. https://doi.org/10.3233/jad-2010-1280

Huda, S., Whittam, D., Bhojak, M., Chamberlain, J., Noonan, C., & Jacob, A. (2019). Neuromyelitis optica spectrum disorders. *Clin Med (Lond)*, *19*(2), 169-176. https://doi.org/10.7861/clinmedicine.19-2-169

Hughes, E. G., Peng, X., Gleichman, A. J., Lai, M., Zhou, L., Tsou, R., Parsons, T. D., Lynch, D. R., Dalmau, J., & Balice-Gordon, R. J. (2010). Cellular and synaptic mechanisms of anti-NMDA receptor encephalitis. *J Neurosci*, *30*(17), 5866-5875. https://doi.org/10.1523/jneurosci.0167-10.2010

Huijbers, M. G., Querol, L. A., Niks, E. H., Plomp, J. J., van der Maarel, S. M., Graus, F., Dalmau, J., Illa, I., & Verschuuren, J. J. (2015). The expanding field of IgG4-mediated neurological autoimmune disorders. *Eur J Neurol*, *22*(8), 1151-1161. https://doi.org/10.1111/ene.12758

Iwamoto, S., Itokazu, T., Sasaki, A., Kataoka, H., Tanaka, S., Hirata, T., Miwa, K., Suenaga, T., Takai, Y., Misu, T., Fujihara, K., & Yamashita, T. (2022). RGMa Signal in Macrophages Induces Neutrophil-Related Astrocytopathy in NMO. *Ann Neurol*, *91*(4), 532-547. https://doi.org/10.1002/ana.26327

Jarius, S., & Wildemann, B. (2013). Aquaporin-4 antibodies (NMO-IgG) as a serological marker of neuromyelitis optica: a critical review of the literature. *Brain Pathol*, *23*(6), 661-683. https://doi.org/10.1111/bpa.12084

Jeyakumar, N., Lerch, M., Dale, R. C., & Ramanathan, S. (2024). MOG antibody-associated optic neuritis. *Eye*, *38*(12), 2289-2301. https://doi.org/10.1038/s41433-024-03108-y

Jiang, Z., Zeng, Z., He, H., Li, M., Lan, Y., Hui, J., Bie, P., Chen, Y., Liu, H., Fan, H., & Xia, H. (2023). Lycium barbarum glycopeptide alleviates neuroinflammation in spinal cord injury via modulating docosahexaenoic acid to inhibiting MAPKs/NF-kB and pyroptosis pathways. *J*

Transl Med, *21*(1), 770. https://doi.org/10.1186/s12967-023-04648-9

Johnston, A. W. (1985). Near visual acuity tests using Chinese characters and the logMAR principle. *Singapore Med J*, *26*(6), 448-455.

Kageyama, T., Komori, M., Miyamoto, K., Ozaki, A., Suenaga, T., Takahashi, R., Kusunoki, S., Matsumoto, S., & Kondo, T. (2013). Combination of cyclosporine A with corticosteroids is effective for the treatment of neuromyelitis optica. *J Neurol*, *260*(2), 627-634. https://doi.org/10.1007/s00415-012-6692-2

Kerschensteiner, M., Meinl, E., & Hohlfeld, R. (2009). Neuro-immune crosstalk in CNS diseases. *Neuroscience*, *158*(3), 1122-1132. https://doi.org/10.1016/j.neuroscience.2008.09.009

Khanna, S., Sharma, A., Huecker, J., Gordon, M., Naismith, R. T., & Van Stavern, G. P. (2012). Magnetic resonance imaging of optic neuritis in patients with neuromyelitis optica versus multiple sclerosis. *J Neuroophthalmol*, *32*(3), 216-220. https://doi.org/10.1097/WNO.0b013e318254c62d

Kim, H. J., Paul, F., Lana-Peixoto, M. A., Tenembaum, S., Asgari, N., Palace, J., Klawiter, E. C., Sato, D. K., de Seze, J., Wuerfel, J., Banwell, B. L., Villoslada, P., Saiz, A., Fujihara, K., & Kim, S. H. (2015). MRI characteristics of neuromyelitis optica spectrum disorder: an international update. *Neurology*, *84*(11), 1165-1173. https://doi.org/10.1212/wnl.0000000000001367

Kinoshita, M., & Nakatsuji, Y. (2012). Where Do AQP4 Antibodies Fit in the Pathogenesis of NMO? *Mult Scler Int*, *2012*, 862169. https://doi.org/10.1155/2012/862169

Kitley, J., Waters, P., Woodhall, M., Leite, M. I., Murchison, A., George, J., Küker, W., Chandratre, S., Vincent, A., & Palace, J. (2014). Neuromyelitis optica spectrum disorders with aquaporin-4 and myelin-oligodendrocyte glycoprotein antibodies: a comparative study. *JAMA Neurol*, *71*(3), 276-283. https://doi.org/10.1001/jamaneurol.2013.5857

Kleinholz, C. L., Riek-Burchardt, M., Seiß, E. A., Amore, J., Gintschel, P., Philipsen, L., Bousso, P., Relja, B., Schraven, B., Handschuh, J., Mohr, J., & Müller, A. J. (2021). Ly6G deficiency alters the dynamics of neutrophil recruitment and pathogen capture during Leishmania major skin infection. *Sci Rep*, *11*(1), 15071. https://doi.org/10.1038/s41598-021-94425-9

Kong, Q., Han, X., Cheng, H., Liu, J., Zhang, H., Dong, T., Chen, J., So, K. F., Mi, X., Xu, Y., & Tang, S. (2024). Lycium barbarum glycopeptide (wolfberry extract) slows N-methyl-N-nitrosourea-induced degradation of photoreceptors. *Neural Regen Res*, *19*(10), 2290-2298. https://doi.org/10.4103/1673-5374.390958

Kraker, J. A., & Chen, J. J. (2023). An update on optic neuritis. *J Neurol*, *270*(10), 5113-5126. https://doi.org/10.1007/s00415-023-11920-x

Kupersmith, M. J., Gal, R. L., Beck, R. W., Xing, D., & Miller, N. (2007). Visual function at baseline and 1 month in acute optic neuritis: predictors of visual outcome. *Neurology*, *69*(6), 508-514. https://doi.org/10.1212/01.wnl.0000267272.60714.42

Lagumersindez-Denis, N., Wrzos, C., Mack, M., Winkler, A., van der Meer, F., Reinert, M. C., Hollasch, H., Flach, A., Brühl, H., Cullen, E., Schlumbohm, C., Fuchs, E., Linington, C., Barrantes-Freer, A., Metz, I., Wegner, C., Liebetanz, D., Prinz, M., Brück, W., . . . Nessler, S. (2017). Differential contribution of immune effector mechanisms to cortical demyelination in multiple sclerosis. *Acta Neuropathol*, *134*(1), 15-34. https://doi.org/10.1007/s00401-017-1706-x

Lai, J. S. M., Chan, H. H. L., Chan, J. C. H., Lo, A. C. Y., Lee, J. W. Y., Chang, R. C. C., & So, K. F. (2022). Neuroprotective effects of wolfberry in normal tension glaucoma: abridged secondary

publication. *Hong Kong Med J*, *28 Suppl 1*(1), 46-47.

Lai, M., Hughes, E. G., Peng, X., Zhou, L., Gleichman, A. J., Shu, H., Matà, S., Kremens, D., Vitaliani, R., Geschwind, M. D., Bataller, L., Kalb, R. G., Davis, R., Graus, F., Lynch, D. R., Balice-Gordon, R., & Dalmau, J. (2009). AMPA receptor antibodies in limbic encephalitis alter synaptic receptor location. *Ann Neurol*, *65*(4), 424-434. https://doi.org/10.1002/ana.21589

Lakshmanan, Y., Wong, F. S. Y., So, K.-F., & Chan, H. H.-L. (2024). Lycium barbarum glycopeptide promotes neuroprotection in ET-1 mediated retinal ganglion cell degeneration. *Journal of Translational Medicine*, *22*(1), 727. https://doi.org/10.1186/s12967-024-05526-8

Lakshmanan, Y., Wong, F. S. Y., So, K. F., & Chan, H. H. (2023). Potential role of Lycium barbarum polysaccharides in glaucoma management: evidence from preclinical in vivo studies. *Neural Regen Res*, *18*(12), 2623-2632. https://doi.org/10.4103/1673-5374.355977

Lam, C. H.-I., Zou, B., Chan, H. H.-L., & Tse, D. Y.-Y. (2023). Functional and structural changes in the neuroretina are accompanied by mitochondrial dysfunction in a type 2 diabetic mouse model. *Eye and Vision*, *10*(1), 37. https://doi.org/10.1186/s40662-023-00353-2

Lan, T., Duan, G., Qi, Y., Almezgagi, M., Fan, G., & Ma, Y. (2024). Exploration of chemical compositions in different germplasm wolfberry using UPLC-MS/MS and evaluation of the in vitro anti-inflammatory activity of quercetin. *Front Pharmacol*, *15*, 1426944. https://doi.org/10.3389/fphar.2024.1426944

Lana-Peixoto, M. A., Talim, N. C., Pedrosa, D., Macedo, J. M., & Santiago-Amaral, J. (2021). Prevalence of neuromyelitis optica spectrum disorder in Belo Horizonte, Southeast Brazil. *Mult Scler Relat Disord*, *50*, 102807. https://doi.org/10.1016/j.msard.2021.102807

Landa, J., Gaig, C., Plagumà, J., Saiz, A., Antonell, A., Sanchez-Valle, R., Dalmau, J., Graus, F., & Sabater, L. (2020). Effects of IgLON5 Antibodies on Neuronal Cytoskeleton: A Link between Autoimmunity and Neurodegeneration. *Ann Neurol*, *88*(5), 1023-1027. https://doi.org/10.1002/ana.25857

Laviers, H., Petzold, A., & Braithwaite, T. (2024). How far should I manage acute optic neuritis as an ophthalmologist? A United Kingdom perspective. *Eye (Lond)*, *38*(12), 2238-2245. https://doi.org/10.1038/s41433-024-03164-4

Lee, H.-J., Kim, B., Waters, P., Woodhall, M., Irani, S., Ahn, S., Kim, S.-J., & Kim, S.-M. (2018). Chronic relapsing inflammatory optic neuropathy (CRION): a manifestation of myelin oligodendrocyte glycoprotein antibodies. *Journal of Neuroinflammation*, *15*(1), 302. https://doi.org/10.1186/s12974-018-1335-x

Lennon, V. A., Wingerchuk, D. M., Kryzer, T. J., Pittock, S. J., Lucchinetti, C. F., Fujihara, K., Nakashima, I., & Weinshenker, B. G. (2004). A serum autoantibody marker of neuromyelitis optica: distinction from multiple sclerosis. *Lancet*, *364*(9451), 2106-2112. https://doi.org/10.1016/s0140-6736(04)17551-x

Li, Q., & Barres, B. A. (2018). Microglia and macrophages in brain homeostasis and disease. *Nature Reviews Immunology*, *18*(4), 225-242. https://doi.org/10.1038/nri.2017.125

Li, W., Mandeville, E. T., Durán-Laforet, V., Fukuda, N., Yu, Z., Zheng, Y., Held, A., Park, J. H., Nakano, T., Tanaka, M., Shi, J., Esposito, E., Niu, W., Xing, C., Hayakawa, K., Lizasoain, I., van Leyen, K., Ji, X., Wainger, B. J., . . . Lo, E. H. (2022). Endothelial cells regulate astrocyte to neural progenitor cell trans-differentiation in a mouse model of stroke. *Nat Commun*, *13*(1), 7812. https://doi.org/10.1038/s41467-022-35498-6

Liu, S., Xiang, K., Lei, Q., Qiu, S., Xiang, M., & Jin, K. (2022). An optimized procedure to record visual evoked potential in mice. *Experimental Eye Research*, *218*, 109011.

Liu, Y., Zhang, H., Zhang, T. X., Yuan, M., Du, C., Zeng, P., Huang, Z., Jia, D., Yang, G., Shi, F. D., & Zhang, C. (2021). Effects of Tocilizumab Therapy on Circulating B Cells and T Helper Cells in Patients With Neuromyelitis Optica Spectrum Disorder. *Front Immunol*, *12*, 703931. https://doi.org/10.3389/fimmu.2021.703931

Lu, M., Lee, M. D., Smith, B. L., Jung, J. S., Agre, P., Verdijk, M. A., Merkx, G., Rijss, J. P., & Deen, P. M. (1996). The human AQP4 gene: definition of the locus encoding two water channel polypeptides in brain. *Proc Natl Acad Sci U S A*, *93*(20), 10908-10912. https://doi.org/10.1073/pnas.93.20.10908

Lucchinetti, C. F., Guo, Y., Popescu, B. F., Fujihara, K., Itoyama, Y., & Misu, T. (2014). The pathology of an autoimmune astrocytopathy: lessons learned from neuromyelitis optica. *Brain Pathol*, *24*(1), 83-97. https://doi.org/10.1111/bpa.12099

Luo, J., Beattie, J. A., Fuentes, P., Rizvi, H., Egger, J. V., Kern, J. A., Leung, D. Y. M., Lacouture, M. E., Kris, M. G., Gambarin, M., Santomasso, B. D., Faleck, D. M., & Hellmann, M. D. (2021). Beyond Steroids: Immunosuppressants in Steroid-Refractory or Resistant Immune-Related Adverse Events. *J Thorac Oncol*, *16*(10), 1759-1764. https://doi.org/10.1016/j.jtho.2021.06.024

Luo, J., Xie, C., Zhang, W., Cai, Y., Ding, J., Wang, Y., Hao, Y., Zhang, Y., & Guan, Y. (2020). Experimental mouse model of NMOSD produced by facilitated brain delivery of NMO-IgG by microbubble-enhanced low-frequency ultrasound in experimental allergic encephalomyelitis mice. *Mult Scler Relat Disord*, *46*, 102473. https://doi.org/10.1016/j.msard.2020.102473

Manogaran, P., Traboulsee, A. L., & Lange, A. P. (2016). Longitudinal Study of Retinal Nerve Fiber Layer Thickness and Macular Volume in Patients With Neuromyelitis Optica Spectrum Disorder. *J Neuroophthalmol*, *36*(4), 363-368. https://doi.org/10.1097/wno.0000000000000404

Manogaran, P., Walker-Egger, C., Samardzija, M., Waschkies, C., Grimm, C., Rudin, M., & Schippling, S. (2018). Exploring experimental autoimmune optic neuritis using multimodal imaging. *Neuroimage*, *175*, 327-339.

Marignier, R., Hacohen, Y., Cobo-Calvo, A., Pröbstel, A. K., Aktas, O., Alexopoulos, H., Amato, M. P., Asgari, N., Banwell, B., Bennett, J., Brilot, F., Capobianco, M., Chitnis, T., Ciccarelli, O., Deiva, K., De Sèze, J., Fujihara, K., Jacob, A., Kim, H. J., . . . Hemmer, B. (2021). Myelin-oligodendrocyte glycoprotein antibody-associated disease. *Lancet Neurol*, *20*(9), 762-772. https://doi.org/10.1016/s1474-4422(21)00218-0

Matiello, M., Schaefer-Klein, J., Sun, D., & Weinshenker, B. G. (2013). Aquaporin 4 expression and tissue susceptibility to neuromyelitis optica. *JAMA Neurol*, *70*(9), 1118-1125. https://doi.org/10.1001/jamaneurol.2013.3124

Matsumoto, Y., Kanamori, A., Nakamura, M., Takahashi, T., Nakashima, I., & Negi, A. (2014). Sera from patients with seropositive neuromyelitis optica spectral disorders caused the degeneration of rodent optic nerve. *Experimental Eye Research*, *119*, 61-69.

Matsumoto, Y., Kanamori, A., Nakamura, M., Takahashi, T., Nakashima, I., & Negi, A. (2014). Sera from patients with seropositive neuromyelitis optica spectral disorders caused the degeneration of rodent optic nerve. *Exp Eye Res*, *119*, 61-69. https://doi.org/10.1016/j.exer.2013.12.010

Mazumder, A. G., Julé, A. M., & Sun, D. (2023). Astrocytes of the optic nerve exhibit a region-specific and temporally distinct response to elevated intraocular pressure. *Molecular Neurodegeneration*,

18(1), 68. https://doi.org/10.1186/s13024-023-00658-9

McAllister, A. S. (2013). A review of the vascular anatomy of the optic nerve head and its clinical implications. *Cureus*, *5*(2).

Meffre, E., & O'Connor, K. C. (2019). Impaired B-cell tolerance checkpoints promote the development of autoimmune diseases and pathogenic autoantibodies. *Immunol Rev*, *292*(1), 90-101. https://doi.org/10.1111/imr.12821

Morita, Y., Itokazu, T., Nakanishi, T., Hiraga, S.-i., & Yamashita, T. (2022). A novel aquaporin-4-associated optic neuritis rat model with severe pathological and functional manifestations. *Journal of Neuroinflammation*, *19*(1), 263. https://doi.org/10.1186/s12974-022-02623-7

Morita, Y., Itokazu, T., Nakanishi, T., Hiraga, S. I., & Yamashita, T. (2022). A novel aquaporin-4-associated optic neuritis rat model with severe pathological and functional manifestations. *J Neuroinflammation*, *19*(1), 263. https://doi.org/10.1186/s12974-022-02623-7

Naganuma, T., Furusawa, Y., Hanaoka, A., Takemoto, Y., & Uchida, J. (2021). A case of anti-aquaporin-4 antibody-positive optic neuritis treated by selective immunoadsorption. *Transfus Apher Sci*, *60*(1), 102969. https://doi.org/10.1016/j.transci.2020.102969

Naismith, R. T., Tutlam, N. T., Xu, J., Klawiter, E. C., Shepherd, J., Trinkaus, K., Song, S. K., & Cross, A. H. (2009). Optical coherence tomography differs in neuromyelitis optica compared with multiple sclerosis. *Neurology*, *72*(12), 1077-1082. https://doi.org/10.1212/01.wnl.0000345042.53843.d5

Napoli, I., & Neumann, H. (2009). Microglial clearance function in health and disease. *Neuroscience*, *158*(3), 1030-1038. https://doi.org/10.1016/j.neuroscience.2008.06.046

Newton, B. D., Kantarci, O., & Okuda, D. T. (2020). Atypical Neuromyelitis Optica Spectrum Disorder With Diffuse Cerebral Abnormalities: A Case Report. *J Cent Nerv Syst Dis*, *12*, 1179573520973819. https://doi.org/10.1177/1179573520973819

Ni, Y., Hu, Y., Zhu, L., Jiang, X., Zhang, H., Liu, J., & Zhao, Y. (2024). Lycium Barbarum Polysaccharide-Derived Nanoparticles Protect Visual Function by Inhibiting RGC Ferroptosis and Microglial Activation in Retinal Ischemia–Reperfusion Mice. *Adv Healthc Mater*, *13*(26), e2304285. https://doi.org/10.1002/adhm.202304285

Ochi, H., & Fujihara, K. (2016). Demyelinating diseases in Asia. *Curr Opin Neurol*, *29*(3), 222-228. https://doi.org/10.1097/wco.0000000000000328

Oertel, F. C., Zimmermann, H., Paul, F., & Brandt, A. U. (2018). Optical coherence tomography in neuromyelitis optica spectrum disorders: potential advantages for individualized monitoring of progression and therapy. *Epma j*, *9*(1), 21-33. https://doi.org/10.1007/s13167-017-0123-5

Ohsawa, K., Imai, Y., Sasaki, Y., & Kohsaka, S. (2004). Microglia/macrophage-specific protein Iba1 binds to fimbrin and enhances its actin-bundling activity. *J Neurochem*, *88*(4), 844-856. https://doi.org/10.1046/j.1471-4159.2003.02213.x

Pandit, L., Asgari, N., Apiwattanakul, M., Palace, J., Paul, F., Leite, M. I., Kleiter, I., & Chitnis, T. (2015). Demographic and clinical features of neuromyelitis optica: A review. *Mult Scler*, *21*(7), 845-853. https://doi.org/10.1177/1352458515572406

Papp, V., Magyari, M., Aktas, O., Berger, T., Broadley, S. A., Cabre, P., Jacob, A., Kira, J. I., Leite, M. I., Marignier, R., Miyamoto, K., Palace, J., Saiz, A., Sepulveda, M., Sveinsson, O., & Illes, Z. (2021). Worldwide Incidence and Prevalence of Neuromyelitis Optica: A Systematic Review. *Neurology*, *96*(2), 59-77. https://doi.org/10.1212/wnl.0000000000011153

Perlman, I. (1995). The Electroretinogram: ERG. In H. Kolb, E. Fernandez, B. Jones, & R. Nelson (Eds.), *Webvision: The Organization of the Retina and Visual System*. University of Utah Health Sciences Center

Petzold, A., Fraser, C. L., Abegg, M., Alroughani, R., Alshowaeir, D., Alvarenga, R., Andris, C., Asgari, N., Barnett, Y., Battistella, R., Behbehani, R., Berger, T., Bikbov, M. M., Biotti, D., Biousse, V., Boschi, A., Brazdil, M., Brezhnev, A., Calabresi, P. A., . . . Plant, G. T. (2022). Diagnosis and classification of optic neuritis. *Lancet Neurol*, *21*(12), 1120-1134. https://doi.org/10.1016/s1474-4422(22)00200-9

Phuan, P. W., Ratelade, J., Rossi, A., Tradtrantip, L., & Verkman, A. S. (2012). Complement-dependent cytotoxicity in neuromyelitis optica requires aquaporin-4 protein assembly in orthogonal arrays. *J Biol Chem*, *287*(17), 13829-13839. https://doi.org/10.1074/jbc.M112.344325

Pineles, S. L., Repka, M. X., Liu, G. T., Waldman, A. T., Borchert, M. S., Khanna, S., Heidary, G., Graves, J. S., Shah, V. S., Kupersmith, M. J., Kraker, R. T., Wallace, D. K., Cotter, S. A., & Holmes, J. M. (2020). Assessment of Pediatric Optic Neuritis Visual Acuity Outcomes at 6 Months. *JAMA Ophthalmol*, *138*(12), 1253-1261. https://doi.org/10.1001/jamaophthalmol.2020.4231

Pittock, S. J., Berthele, A., Fujihara, K., Kim, H. J., Levy, M., Palace, J., Nakashima, I., Terzi, M., Totolyan, N., & Viswanathan, S. (2019). Eculizumab in aquaporin-4–positive neuromyelitis optica spectrum disorder. *New England Journal of Medicine*, *381*(7), 614-625.

Poonja, S., Rattanathamsakul, N., & Chen, J. J. (2025). The atypical faces of optic neuritis: neuromyelitis optica spectrum disorder and myelin oligodendrocyte glycoprotein antibody-associated disease. *Curr Opin Neurol*, *38*(1), 96-104. https://doi.org/10.1097/wco.0000000000001335

Qi, Y., Duan, G., Fan, G., & Peng, N. (2022). Effect of Lycium barbarum polysaccharides on cell signal transduction pathways. *Biomed Pharmacother*, *147*, 112620. https://doi.org/10.1016/j.biopha.2022.112620

Ramanathan, S., Brilot, F., Irani, S. R., & Dale, R. C. (2023). Origins and immunopathogenesis of autoimmune central nervous system disorders. *Nature Reviews Neurology*, *19*(3), 172-190. https://doi.org/10.1038/s41582-023-00776-4

Ransohoff, R. M. (2012). Illuminating neuromyelitis optica pathogenesis. *Proc Natl Acad Sci U S A*, *109*(4), 1001-1002. https://doi.org/10.1073/pnas.1119288109

Ratchford, J. N., Quigg, M. E., Conger, A., Frohman, T., Frohman, E., Balcer, L. J., Calabresi, P. A., & Kerr, D. A. (2009). Optical coherence tomography helps differentiate neuromyelitis optica and MS optic neuropathies. *Neurology*, *73*(4), 302-308. https://doi.org/10.1212/WNL.0b013e3181af78b8

Redler, Y., & Levy, M. (2020). Rodent models of optic neuritis. *Frontiers in neurology*, *11*, 580951.

Remlinger, J., Bagnoud, M., Meli, I., Massy, M., Hoepner, R., Linington, C., Chan, A., Bennett, J. L., Enzmann, V., & Salmen, A. (2023). Modeling MOG Antibody-Associated Disorder and Neuromyelitis Optica Spectrum Disorder in Animal Models: Visual System Manifestations. *Neurol Neuroimmunol Neuroinflamm*, *10*(5). https://doi.org/10.1212/nxi.0000000000200141

Rivest, S. (2009). Regulation of innate immune responses in the brain. *Nat Rev Immunol*, *9*(6), 429-439. https://doi.org/10.1038/nri2565

Robinson, A. P., Harp, C. T., Noronha, A., & Miller, S. D. (2014). The experimental autoimmune encephalomyelitis (EAE) model of MS: utility for understanding disease pathophysiology and

treatment. *Handb Clin Neurol*, *122*, 173-189. https://doi.org/10.1016/b978-0-444-52001-2.00008-x

Robson, A. G., Nilsson, J., Li, S., Jalali, S., Fulton, A. B., Tormene, A. P., Holder, G. E., & Brodie, S. E. (2018). ISCEV guide to visual electrodiagnostic procedures. *Doc Ophthalmol*, *136*(1), 1-26. https://doi.org/10.1007/s10633-017-9621-y

Saadoun, S., Waters, P., Bell, B. A., Vincent, A., Verkman, A. S., & Papadopoulos, M. C. (2010). Intra-cerebral injection of neuromyelitis optica immunoglobulin G and human complement produces neuromyelitis optica lesions in mice. *Brain*, *133*(Pt 2), 349-361. https://doi.org/10.1093/brain/awp309

Saadoun, S., Waters, P., Leite, M. I., Bennett, J. L., Vincent, A., & Papadopoulos, M. C. (2013). Neuromyelitis optica IgG causes placental inflammation and fetal death. *J Immunol*, *191*(6), 2999-3005. https://doi.org/10.4049/jimmunol.1301483

Saadoun, S., Waters, P., MacDonald, C., Bell, B. A., Vincent, A., Verkman, A., & Papadopoulos, M. C. (2012). Neutrophil protease inhibition reduces neuromyelitis optica–immunoglobulin G–induced damage in mouse brain. *Annals of neurology*, *71*(3), 323-333.

Saadoun, S., Waters, P., MacDonald, C., Bell, B. A., Vincent, A., Verkman, A. S., & Papadopoulos, M. C. (2012). Neutrophil protease inhibition reduces neuromyelitis optica-immunoglobulin G-induced damage in mouse brain. *Ann Neurol*, *71*(3), 323-333. https://doi.org/10.1002/ana.22686

Sagan, S. A., Winger, R. C., Cruz-Herranz, A., Nelson, P. A., Hagberg, S., Miller, C. N., Spencer, C. M., Ho, P. P., Bennett, J. L., & Levy, M. (2016). Tolerance checkpoint bypass permits emergence of pathogenic T cells to neuromyelitis optica autoantigen aquaporin-4. *Proceedings of the National Academy of Sciences*, *113*(51), 14781-14786.

Saini, H., Rifkin, R., Gorelik, M., Huang, H., Ferguson, Z., Jones, M. V., & Levy, M. (2013). Passively transferred human NMO-IgG exacerbates demyelination in mouse experimental autoimmune encephalomyelitis. *BMC Neurol*, *13*, 104. https://doi.org/10.1186/1471-2377-13-104

Saini, H., Rifkin, R., Gorelik, M., Huang, H., Ferguson, Z., Jones, M. V., & Levy, M. (2013). Passively transferred human NMO-IgG exacerbates demyelination in mouse experimental autoimmune encephalomyelitis. *BMC Neurology*, *13*(1), 104. https://doi.org/10.1186/1471-2377-13-104

Saitakis, G., & Chwalisz, B. K. (2022). Treatment and Relapse Prevention of Typical and Atypical Optic Neuritis. *Int J Mol Sci*, *23*(17). https://doi.org/10.3390/ijms23179769

Schwab, C., & McGeer, P. L. (2008). Inflammatory aspects of Alzheimer disease and other neurodegenerative disorders. *J Alzheimers Dis*, *13*(4), 359-369. https://doi.org/10.3233/jad-2008-13402

Sechi, E., & Flanagan, E. P. (2021). Antibody-Mediated Autoimmune Diseases of the CNS: Challenges and Approaches to Diagnosis and Management. *Front Neurol*, *12*, 673339. https://doi.org/10.3389/fneur.2021.673339

Sekyi, M. T., Lauderdale, K., Atkinson, K. C., Golestany, B., Karim, H., Feri, M., Soto, J. S., Diaz, C., Kim, S. H., Cilluffo, M., Nusinowitz, S., Katzenellenbogen, J. A., & Tiwari-Woodruff, S. K. (2021). Alleviation of extensive visual pathway dysfunction by a remyelinating drug in a chronic mouse model of multiple sclerosis. *Brain Pathol*, *31*(2), 312-332. https://doi.org/10.1111/bpa.12930

Shoenfeld, Y., & Katz, U. (2005). IVIg therapy in autoimmunity and related disorders: our experience with a large cohort of patients. *Autoimmunity*, *38*(2), 123-137.

https://doi.org/10.1080/08916930500059633

Soerensen, S. F., Wirenfeldt, M., Wlodarczyk, A., Moerch, M. T., Khorooshi, R., Arengoth, D. S., Lillevang, S. T., Owens, T., & Asgari, N. (2021). An Experimental Model of Neuromyelitis Optica Spectrum Disorder-Optic Neuritis: Insights Into Disease Mechanisms. *Front Neurol*, *12*, 703249. https://doi.org/10.3389/fneur.2021.703249

Srikajon, J., Siritho, S., Ngamsombat, C., Prayoonwiwat, N., & Chirapapaisan, N. (2018). Differences in clinical features between optic neuritis in neuromyelitis optica spectrum disorders and in multiple sclerosis. *Mult Scler J Exp Transl Clin*, *4*(3), 2055217318791196. https://doi.org/10.1177/2055217318791196

Tambuyzer, B. R., Ponsaerts, P., & Nouwen, E. J. (2009). Microglia: gatekeepers of central nervous system immunology. *J Leukoc Biol*, *85*(3), 352-370. https://doi.org/10.1189/jlb.0608385

Tea, F., Lopez, J. A., Ramanathan, S., Merheb, V., Lee, F. X. Z., Zou, A., Pilli, D., Patrick, E., van der Walt, A., Monif, M., Tantsis, E. M., Yiu, E. M., Vucic, S., Henderson, A. P. D., Fok, A., Fraser, C. L., Lechner-Scott, J., Reddel, S. W., Broadley, S., . . . Brilot, F. (2019). Characterization of the human myelin oligodendrocyte glycoprotein antibody response in demyelination. *Acta Neuropathol Commun*, *7*(1), 145. https://doi.org/10.1186/s40478-019-0786-3

Tian, D. C., Li, Z., Yuan, M., Zhang, C., Gu, H., Wang, Y., & Shi, F. D. (2020). Incidence of neuromyelitis optica spectrum disorder (NMOSD) in China: A national population-based study. *Lancet Reg Health West Pac*, *2*, 100021. https://doi.org/10.1016/j.lanwpc.2020.100021

Tian, L., Ma, L., Kaarela, T., & Li, Z. (2012). Neuroimmune crosstalk in the central nervous system and its significance for neurological diseases. *Journal of Neuroinflammation*, *9*(1), 155. https://doi.org/10.1186/1742-2094-9-155

Tian, L., Rauvala, H., & Gahmberg, C. G. (2009). Neuronal regulation of immune responses in the central nervous system. *Trends Immunol*, *30*(2), 91-99. https://doi.org/10.1016/j.it.2008.11.002

Trewin, B. P., Freeman, I., Ramanathan, S., & Irani, S. R. (2022). Immunotherapy in autoimmune encephalitis. *Curr Opin Neurol*, *35*(3), 399-414. https://doi.org/10.1097/wco.0000000000001048

Uzawa, A., Oertel, F. C., Mori, M., Paul, F., & Kuwabara, S. (2024). NMOSD and MOGAD: an evolving disease spectrum. *Nature Reviews Neurology*, *20*(10), 602-619. https://doi.org/10.1038/s41582-024-01014-1

Vaknin-Dembinsky, A., Karussis, D., Avichzer, J., & Abramsky, O. (2014). NMO spectrum of disorders: a paradigm for astrocyte-targeting autoimmunity and its implications for MS and other CNS inflammatory diseases. *J Autoimmun*, *54*, 93-99. https://doi.org/10.1016/j.jaut.2014.05.004

Wahl, S. M., Wen, J., & Moutsopoulos, N. (2006). TGF-beta: a mobile purveyor of immune privilege. *Immunol Rev*, *213*, 213-227. https://doi.org/10.1111/j.1600-065X.2006.00437.x

Wang, A. Y. M., Wong, V. H. Y., Lee, P. Y., Bui, B. V., Dudczig, S., Vessey, K. A., & Fletcher, E. L. (2021). Retinal ganglion cell dysfunction in mice following acute intraocular pressure is exacerbated by P2X7 receptor knockout. *Sci Rep*, *11*(1), 4184. https://doi.org/10.1038/s41598-021-83669-0

Wingerchuk, D. M., Banwell, B., Bennett, J. L., Cabre, P., Carroll, W., Chitnis, T., de Seze, J., Fujihara, K., Greenberg, B., Jacob, A., Jarius, S., Lana-Peixoto, M., Levy, M., Simon, J. H., Tenembaum, S., Traboulsee, A. L., Waters, P., Wellik, K. E., & Weinshenker, B. G. (2015). International consensus diagnostic criteria for neuromyelitis optica spectrum disorders. *Neurology*, *85*(2), 177-189. https://doi.org/10.1212/wnl.0000000000001729

Wingerchuk, D. M., Hogancamp, W. F., O'Brien, P. C., & Weinshenker, B. G. (1999). The clinical course of neuromyelitis optica (Devic's syndrome). *Neurology*, *53*(5), 1107-1114. https://doi.org/10.1212/wnl.53.5.1107

Wingerchuk, D. M., Lennon, V. A., Lucchinetti, C. F., Pittock, S. J., & Weinshenker, B. G. (2007). The spectrum of neuromyelitis optica. *Lancet Neurol*, *6*(9), 805-815. https://doi.org/10.1016/s1474-4422(07)70216-8

Wingerchuk, D. M., Lennon, V. A., Pittock, S. J., Lucchinetti, C. F., & Weinshenker, B. G. (2006). Revised diagnostic criteria for neuromyelitis optica. *Neurology*, *66*(10), 1485-1489. https://doi.org/10.1212/01.wnl.0000216139.44259.74

Wong, K. A., & Benowitz, L. I. (2022). Retinal Ganglion Cell Survival and Axon Regeneration after Optic Nerve Injury: Role of Inflammation and Other Factors. *Int J Mol Sci*, *23*(17). https://doi.org/10.3390/ijms231710179

Wu, Y., Geraldes, R., Juryńczyk, M., & Palace, J. (2023). Double-negative neuromyelitis optica spectrum disorder. *Mult Scler*, *29*(11-12), 1353-1362. https://doi.org/10.1177/13524585231199819

Wu, Y., Zhang, L., Cao, S., Zhang, J., Li, C., Shan, Y., Liu, Q., Yu, Z., Fang, Q., & Zhang, Y. (2025). Lycium barbarum Glycopeptide Alleviates Neomycin-Induced Ototoxicity by Inhibiting Tryptophan Hydroxylase-Mediated Serotonin Biosynthesis. *Advanced Science*, 2405850.

Wu, Y., Zhang, L., Cao, S., Zhang, J., Li, C., Shan, Y., Liu, Q., Yu, Z., Fang, Q., Zhang, Y., Fu, X., So, K. F., & Chai, R. (2025). Lycium barbarum Glycopeptide Alleviates Neomycin-Induced Ototoxicity by Inhibiting Tryptophan Hydroxylase-Mediated Serotonin Biosynthesis. *Adv Sci (Weinh)*, *12*(29), e2405850. https://doi.org/10.1002/advs.202405850

Wu, Y., Zhong, L., & Geng, J. (2019a). Neuromyelitis optica spectrum disorder: Pathogenesis, treatment, and experimental models. *Mult Scler Relat Disord*, *27*, 412-418. https://doi.org/10.1016/j.msard.2018.12.002

Wu, Y., Zhong, L., & Geng, J. (2019b). Visual impairment in neuromyelitis optica spectrum disorders (NMOSD). *J Chem Neuroanat*, *97*, 66-70. https://doi.org/10.1016/j.jchemneu.2019.01.012

Xiang, W., Xie, C., Luo, J., Zhang, W., Zhao, X., Yang, H., Cai, Y., Ding, J., Wang, Y., Hao, Y., Zhang, Y., & Guan, Y. (2021). Low Frequency Ultrasound With Injection of NMO-IgG and Complement Produces Lesions Different From Experimental Autoimmune Encephalomyelitis Mice. *Front Immunol*, *12*, 727750. https://doi.org/10.3389/fimmu.2021.727750

Xu, L., Yang, L., Xu, H., Li, Y., Peng, F., Qiu, W., & Tang, C. (2024). Lycium barbarum glycopeptide ameliorates motor and visual deficits in autoimmune inflammatory diseases. *Phytomedicine*, *129*, 155610. https://doi.org/10.1016/j.phymed.2024.155610

Yan, Y., Xing, S., Liu, J., Yan, X., Guan, Y., Jiang, Z., Zhang, W., & Li, X. (2025). Lycium barbarum glycopeptide reduces inflammation and fibrosis in corneal injury by modulating the NF-κB/NLRP3/IL-1 β signaling pathway and microRNA-21a-5p/SMAD7. *Exp Eye Res*, 110438. https://doi.org/10.1016/j.exer.2025.110438

Yang, M., Chen, Y., Feng, C., Zhang, M., Wang, H., Zheng, Y., & Li, X. (2024). Single-cell RNA sequencing uncovers molecular mechanisms of intravenous immunoglobulin plus methylprednisolone in Kawasaki disease: attenuated monocyte-driven inflammation and improved NK cell cytotoxicity. *Front Immunol*, *15*, 1455925. https://doi.org/10.3389/fimmu.2024.1455925

Yang, X., Yao, S.-Q., Chan, H. H.-L., & Tan, S. (2025). Dynamic characterization of pathological and

functional deterioration in a mouse model of optic neuritis related to neuromyelitis optica spectrum disorder. *Neural Regeneration Research*, 10.4103/NRR.NRR-D-4124-00898. https://doi.org/10.4103/nrr.Nrr-d-24-00898

Yao, X., Adams, M. S., Jones, P. D., Diederich, C. J., & Verkman, A. S. (2019). Noninvasive, Targeted Creation of Neuromyelitis Optica Pathology in AQP4-IgG Seropositive Rats by Pulsed Focused Ultrasound. *J Neuropathol Exp Neurol*, *78*(1), 47-56. https://doi.org/10.1093/jnen/nly107

Yao, X., & Verkman, A. S. (2017). Marked central nervous system pathology in CD59 knockout rats following passive transfer of Neuromyelitis optica immunoglobulin G. *Acta Neuropathologica Communications*, *5*(1), 15. https://doi.org/10.1186/s40478-017-0417-9

Yick, L. W., Ma, O. K., Ng, R. C., Kwan, J. S., & Chan, K. H. (2018). Aquaporin-4 Autoantibodies From Neuromyelitis Optica Spectrum Disorder Patients Induce Complement-Independent Immunopathologies in Mice. *Front Immunol*, *9*, 1438. https://doi.org/10.3389/fimmu.2018.01438

Yick, L. W., Tang, C. H., Ma, O. K., Kwan, J. S., & Chan, K. H. (2020). Memantine ameliorates motor impairments and pathologies in a mouse model of neuromyelitis optica spectrum disorders. *J Neuroinflammation*, *17*(1), 236. https://doi.org/10.1186/s12974-020-01913-2

You, Y., Barnett, M. H., Yiannikas, C., Parratt, J., Matthews, J., Graham, S. L., & Klistorner, A. (2020). Chronic demyelination exacerbates neuroaxonal loss in patients with MS with unilateral optic neuritis. *Neurol Neuroimmunol Neuroinflamm*, *7*(3). https://doi.org/10.1212/nxi.0000000000000700

You, Y., Klistorner, A., Thie, J., & Graham, S. L. (2011). Latency delay of visual evoked potential is a real measurement of demyelination in a rat model of optic neuritis. *Invest Ophthalmol Vis Sci*, *52*(9), 6911-6918. https://doi.org/10.1167/iovs.11-7434

Yuan, X.-M., Li, W., Dalen, H., Lotem, J., Kama, R., Sachs, L., & Brunk, U. T. (2002). Lysosomal destabilization in p53-induced apoptosis. *Proceedings of the National Academy of Sciences*, *99*(9), 6286-6291.

Zeka, B., Hastermann, M., Kaufmann, N., Schanda, K., Pende, M., Misu, T., Rommer, P., Fujihara, K., Nakashima, I., Dahle, C., Leutmezer, F., Reindl, M., Lassmann, H., & Bradl, M. (2016). Aquaporin 4-specific T cells and NMO-IgG cause primary retinal damage in experimental NMO/SD. *Acta Neuropathol Commun*, *4*(1), 82. https://doi.org/10.1186/s40478-016-0355-y

Zhang, X., Wu, W. K., Xu, W., Man, K., Wang, X., Han, J., Leung, W. Y., Wu, R., Liu, K., & Yu, J. (2017). CXC motif chemokine 10 impairs autophagy and autolysosome formation in non-alcoholic steatohepatitis. *Theranostics*, *7*(11), 2822.

Zhang, Y., Bao, Y., Qiu, W., Peng, L., Fang, L., Xu, Y., & Yang, H. (2018). Structural and visual functional deficits in a rat model of neuromyelitis optica spectrum disorders related optic neuritis. *Exp Eye Res*, *175*, 124-132. https://doi.org/10.1016/j.exer.2018.06.011

Zhao, X., Qiu, W., Zhang, Y., Luo, Y., Zhang, X., Lu, L., & Yang, H. (2018). A prospective case-control study comparing optical coherence tomography characteristics in neuromyelitis optica spectrum disorder- optic neuritis and idiopathic optic neuritis. *BMC Ophthalmol*, *18*(1), 247. https://doi.org/10.1186/s12886-018-0902-3

Zheng, C., Wang, L., Xu, X., Zhou, M., Liu, K., Zhang, Y., Zhao, X., Lu, L., Qiu, W., Zhang, X., & Yang, H. (2022). Different visual evoked potentials in neuromyelitis optica spectrum disorder-related optic neuritis and idiopathic demyelinating optic neuritis: a prospective longitudinal analysis.

BMC Ophthalmol, *22*(1), 376. https://doi.org/10.1186/s12886-022-02595-5

Zhou, X., Zhang, Z., Shi, H., Liu, Q., Chang, Y., Feng, W., Zhu, S., & Sun, S. (2022). Effects of Lycium barbarum glycopeptide on renal and testicular injury induced by di(2-ethylhexyl) phthalate. *Cell Stress Chaperones*, *27*(3), 257-271. https://doi.org/10.1007/s12192-022-01266-0

Zimmerli, S., Majeed, M., Gustavsson, M., Stendahl, O., Sanan, D. A., & Ernst, J. D. (1996). Phagosome-lysosome fusion is a calcium-independent event in macrophages. *Journal of Cell Biology*, *132*(1), 49-61.

Zrzavy, T., Endmayr, V., Bauer, J., Macher, S., Mossaheb, N., Schwaiger, C., Ricken, G., Winklehner, M., Glatter, S., Breu, M., Wimmer, I., Kovacs, G. G., Risser, D. U., Klupp, N., Simonitsch-Klupp, I., Roetzer, T., Rommer, P., Berger, T., Gelpi, E., . . . Höftberger, R. (2021). Neuropathological Variability within a Spectrum of NMDAR-Encephalitis. *Ann Neurol*, *90*(5), 725-737. https://doi.org/10.1002/ana.26223